UNIVERSITÄT BONN
Physikalisches Institut

Study of a Light Standard Model Higgs Boson in the $t\bar{t}H^0$ Channel with ATLAS at LHC and Decay-Mode Independent Searches for Neutral Higgs Bosons with OPAL at LEP

von
Jochen Cammin

Abstract: The production of a light Standard Model Higgs boson in association with a top-quark pair at the LHC is studied in a simulation of the ATLAS detector. The Higgs boson is assumed to decay into $b\bar{b}$, and the top-quark pair to decay into $\ell\nu b$ jjb. Tagging of all four b-jets and the full reconstruction of the final state are necessary to minimize the combinatorial background from assigning two jets to the decay of the Higgs boson and to discriminate the signal process from the large background from top-quark pairs with additional jets. New methods based on likelihood techniques are investigated in order to improve the reconstruction and the signal-background separation. They lead to substantial enhancement of the expected sensitivity of ATLAS to the $t\bar{t}H^0$ channel. Both a fast and the full simulation of the ATLAS detector are used, and a focus is set on the study of the ATLAS b-tagging performance and its parameterization in the fast simulation of the detector.
Further, topological searches for neutral Higgs bosons h^0 produced in e^+e^- collisions at LEP in the process $e^+e^- \to h^0Z^0$ are investigated using data collected at center-of-mass energies of 183–209 GeV with the OPAL detector. These searches are based on studies of the recoil mass spectrum of $Z^0 \to e^+e^-$ and $\mu^+\mu^-$ events. They cover arbitrary decays of the h^0 as well as the possibility that it might be stable. No indication for a signal is found in the data and upper limits on the cross section of h^0Z^0 production are calculated. The results can be interpreted in general scenarios independently of the decay modes of the h^0. The examples considered are the production of a single new scalar particle with a decay width smaller than the detector mass resolution, and, for the first time, two scenarios with continuous mass distributions, due to a single very broad state or several states close in mass.

Post address:
Nussallee 12
53115 Bonn
Germany

BONN-IR-2004-06
Bonn University
March 2004
ISSN-0172-8733

Study of a Light Standard Model Higgs Boson in the $t\bar{t}H^0$ Channel with ATLAS at LHC and Decay-Mode Independent Searches for Neutral Higgs Bosons with OPAL at LEP

Dissertation
zur
Erlangung des Doktorgrades (Dr. rer. nat.)
der
Mathematisch-Naturwissenschaftlichen Fakultät
der
Rheinischen Friedrich-Wilhelms-Universität
zu Bonn

vorgelegt von
Jochen Cammin
aus
Köln

Bonn 2004

Dieser Forschungsbericht wurde als Dissertation von der Mathematisch-Naturwissenschaftlichen Fakultät der Universität Bonn angenommen.

Tag der Promotion:	19. März 2004
Referent:	Prof. Dr. M. Kobel
Korreferent:	Prof. Dr. I. Brock

Abstract: The production of a light Standard Model Higgs boson in association with a top-quark pair at the LHC is studied in a simulation of the ATLAS detector. The Higgs boson is assumed to decay into $\mathrm{b\bar{b}}$, and the top-quark pair to decay into $\ell\nu\mathrm{b}$ jjb. Tagging of all four b-jets and the full reconstruction of the final state are necessary to minimize the combinatorial background from assigning two jets to the decay of the Higgs boson and to discriminate the signal process from the large background from top-quark pairs with additional jets. New methods based on likelihood techniques are investigated in order to improve the reconstruction and the signal-background separation. They lead to substantial enhancement of the expected sensitivity of ATLAS to the $\mathrm{t\bar{t}H^0}$ channel. Both a fast and the full simulation of the ATLAS detector are used, and a focus is set on the study of the ATLAS b-tagging performance and its parameterization in the fast simulation of the detector.

Further, topological searches for neutral Higgs bosons $\mathrm{h^0}$ produced in $\mathrm{e^+e^-}$ collisions at LEP in the process $\mathrm{e^+e^-} \rightarrow \mathrm{h^0Z^0}$ are investigated using data collected at center-of-mass energies of 183–209 GeV with the OPAL detector. These searches are based on studies of the recoil mass spectrum of $\mathrm{Z^0} \rightarrow \mathrm{e^+e^-}$ and $\mu^+\mu^-$ events. They cover arbitrary decays of the $\mathrm{h^0}$ as well as the possibility that it might be stable. No indication for a signal is found in the data and upper limits on the cross section of $\mathrm{h^0Z^0}$ production are calculated. The results can be interpreted in general scenarios independently of the decay modes of the $\mathrm{h^0}$. The examples considered are the production of a single new scalar particle with a decay width smaller than the detector mass resolution, and, for the first time, two scenarios with continuous mass distributions, due to a single very broad state or several states close in mass.

Contents

1 Preamble

The origin of mass of the fundamental particles is an unanswered question in elementary particle physics. The most popular explanation is the Higgs mechanism, where particles acquire mass by interacting with a scalar field which exists everywhere in the universe. The model predicts the existence of a new particle, the Higgs boson, which should manifest itself as the quantum of the scalar Higgs field. The Higgs mechanism completes the Standard Model, the theory which is extremely reliable in the prediction of phenomena related to the elementary particles and their interactions. 40 years have passed since the proposal of the Higgs mechanism, but physicists could neither confirm the Higgs sector of the Standard Model nor of any model beyond it. The missing ingredient is the Higgs boson, which has escaped detection down to the present day. It can help to tell us whether the Standard Model is a suitable theory for the processes observable at present particle colliders and those under construction, or if nature requires a more complex description. Therefore, the Higgs boson is the most-wanted elementary particle in physics.

This thesis presents two searches for Higgs bosons. The first part is dedicated to a study of the Standard Model Higgs boson in the process $\mathrm{pp} \rightarrow \mathrm{t\bar{t}H^0}$ with $\mathrm{t\bar{t}} \rightarrow \ell\nu\mathrm{b\,jjb}$ and $\mathrm{H^0} \rightarrow \mathrm{b\bar{b}}$. The study is based on a simulation of the ATLAS detector, which is currently under construction at the future proton-proton collider LHC. If the mass of the Higgs boson is below 140 GeV, it can be discovered in the $\mathrm{t\bar{t}H^0}$ channel at the LHC. In this thesis a new method is developed to fully reconstruct the final state and to assign the decay products of the two top quarks and the Higgs boson to their mother particles. Also, a new procedure is studied to separate the Higgs signal from the large background. Both methods are based on likelihood techniques and lead to substantial improvements compared to earlier studies of the $\mathrm{t\bar{t}H^0}$, $\mathrm{H^0} \rightarrow \mathrm{b\bar{b}}$ channel. Since there are large uncertainties in the Monte Carlo predictions of the expected background rates, an approach is proposed to measure the background shape and rate directly in data. As the $\mathrm{t\bar{t}H^0}$ channel depends crucially on how well ATLAS can correctly tag jets containing B-hadrons, another focus is the evaluation of the b-tagging parameterization implemented in the fast simulation of the ATLAS detector.

The second part of the thesis is dedicated to a decay-mode independent search for Higgs bosons in $\mathrm{h^0Z^0}$-strahlung in models that contain a more complex Higgs sector than the Standard Model. Data are analyzed at energies of $\sqrt{s} \geq 183$ GeV from the OPAL experiment at the past $\mathrm{e^+e^-}$ LEP accelerator. The analysis developed in this part is unique among the four LEP experiments, in that it makes no assumptions on the decay modes of the Higgs boson. Furthermore, the search is sensitive not only in a mass region of the Higgs boson near the kinematic limit, like most other analyses, but in a broad mass range between $m_{\mathrm{H^0}} = 30$ GeV and $m_{\mathrm{H^0}} \approx 100$ GeV. This allows for interpretation of the results in arbitrary models, including the Standard Model, and in a model independent way. No evidence for the presence of Higgs bosons can be found and limits are set on the parameter space of some selected models. Advanced statistical methods are used for these calculations, based on the likelihood ratio-method to determine confidence levels. For the first time, limits are set on a model predicting a large number of Higgs bosons spread out over a large mass range, and on another model which predicts a very large decay width of the Higgs boson.

The thesis is organized as follows:

Part I contains a short introduction to elementary particle physics (Section 2) and describes the theoretical framework on which the studies presented in this work are based (Section 3).

Part II presents the study of the production of the Standard Model Higgs boson in association with a pair of top-quarks with the ATLAS detector at the LHC.

- Section 4 introduces to the topic and motivates the study of the $t\bar{t}H^0$ channel.
- Section 5 gives a brief overview of the physics goals at the LHC, and Section 6 and 7 describe the LHC accelerator and the ATLAS experiment.
- Section 8 is dedicated to the $t\bar{t}H^0$ channel and describes signal and background properties, the Monte Carlo generators, and details of the simulation.
- Section 9 presents two event reconstruction methods and a method to determine the background directly from data and provides results from the fast simulation of the ATLAS detector at low luminosity conditions.
- Section 10 deals with different parameterizations of the ATLAS b-tagging performance and their impact on the $t\bar{t}H^0$ channel.
- The discovery potential of the $t\bar{t}H^0$ channel under high luminosity conditions is investigated in Section 11.
- In Section 12 the fast simulation is compared to the full simulation and additional information from the b-tagging algorithm in fully simulated events is tested for usability in signal-background separation.
- Finally, Section 13 describes three applications of the results obtained in this thesis.

Part III presents a general search for neutral Higgs bosons with the OPAL detector at LEP.

- An introduction in Section 14 is followed by an overview of Higgs physics at LEP in Section 15.
- The LEP accelerator and the OPAL detector are described in Section 16.
- Section 17 is dedicated to a search for neutral Higgs bosons in the associated production $e^+e^- \to h^0Z^0$. It describes a decay mode independent analysis and presents interpretations of the results in several models.

The results of this thesis are summarized in Section 18.

Part I

Theoretical concepts

2 Introduction

Elementary particle physics studies the constituents of matter and the forces between them. The knowledge gathered over decades from many measurements and theoretical considerations was finally put together into the *Standard Model* of particle physics by Glashow, Weinberg, and Salam in 1967/68. Ever since the model was found to be in perfect agreement with experimental observations.

According to the Standard Model (SM), matter is made of point-like particles with spin $1/2$ (*fermions*). They exist in pairs of three families of leptons and quarks. Altogether there are 24 known fundamental fermions: six leptons $(\nu_\mathrm{e}, \mathrm{e})$, (ν_μ, μ), (ν_τ, τ) and six quarks (u, d), (c, s), (t, b) plus their anti-particles. The leptons e (electron), μ (muon), and τ (tau) have electric charge $Q = -1$, the neutrinos $\nu_\mathrm{e}, \nu_\mu, \nu_\tau$ are electrically neutral. The quarks have fractional electric charge: $+2/3$ for u, c, t-quarks and $-1/3$ for d, s, b-quarks. Only the particles of the first family are stable, and the world around us is composed of up- and down-quarks, forming the nucleons, and the electron.

Interaction between particles is described by four forces: *gravity* which acts on all massive particles, the *electromagnetic force* which is present between particles with electric charge, the *strong force*, interacting on quarks and gluing them together to form bound states, and the *weak force* that acts on all particles. Gravity is not included in the Standard Model. On one hand it is too weak to have observable effects at energies accessible at current particle accelerators. On the other hand there are theoretical problems in formulating a renormalizable quantum field theory for gravity, the basis on which the Standard Model is constructed. The other forces are mediated by *gauge bosons* of spin 1. The gauge boson of the electromagnetic force is the *photon* γ. It couples to the electric charge of a particle and is massless, so the force has infinite range. The exchange bosons of the strong force are the *gluons* which couple to a quantum number called *color*. In total, there are eight massless gluons. Gluons can interact with each other because they also carry color charge (color and anti-color). A quark can have one of three color states: red, green or blue. Unlike leptons, no free quarks have yet been observed. They are tied together to bound states with neutral, 'white' color charge. States composed of two quarks, carrying color and anti-color, are called *mesons*. States containing three quarks with color charge red, green, and blue (or anti-red, anti-green, anti-blue) are called *baryons*. To give an example, the proton is made of two u-quarks and one d-quark, and the net electric charge is $+1$. The neutron contains one u-quark and two d-quarks, and so the neutron has no electric charge.

The weak force is mediated by three gauge bosons W^+, W^-, and Z^0. They are very massive, $m_{\mathrm{W}^\pm} = 80.4$ GeV, $m_{\mathrm{Z}^0} = 91.2$ GeV, and therefore the weak force has very small range. The weak gauge bosons couple to quantum numbers called *weak isospin*, I_W, and *weak hypercharge*, Y_W. The weak force distinguishes left-handed and right-handed states. $\mathrm{W}^\pm$ bosons couple only to left-handed states, Z^0 boson couple to both left-handed and right-handed states. The left-handed states are grouped into doublets, where 'u-quark-like' particles have a component $I_W^3 = 1/2$, 'down-quark-like' particles have $I_W^3 = -1/2$. The fundamental fermions and electroweak gauge bosons, their electroweak quantum numbers and masses are listed in Table 2.1.

Fermion generation			Quantum numbers			
1	2	3	Q	I	I_3	Y_W
	Leptons					
$\begin{pmatrix}\nu_\mathrm{e}\\ \mathrm{e}\end{pmatrix}_L$	$\begin{pmatrix}\nu_\mu\\ \mu\end{pmatrix}_L$	$\begin{pmatrix}\nu_\tau\\ \tau\end{pmatrix}_L$	0 -1	$1/2$ $1/2$	$1/2$ $-1/2$	-1 -1
e_R	μ_R	τ_R	-1	0	0	-2
	Quarks					
$\begin{pmatrix}\mathrm{u}\\ \mathrm{d}\end{pmatrix}_L$	$\begin{pmatrix}\mathrm{c}\\ \mathrm{s}\end{pmatrix}_L$	$\begin{pmatrix}\mathrm{t}\\ \mathrm{b}\end{pmatrix}_L$	$2/3$ $-1/3$	$1/2$ $1/2$	$1/2$ $-1/2$	$1/3$ $1/3$
u_R	c_R	t_R	$2/3$	0	0	$4/3$
d_R	s_R	b_R	$-1/3$	0	0	$-2/3$
Electroweak		W^+	1	1	1	0
gauge bosons		W^-	-1	1	-1	0
		Z	0	0	0	0
		γ	0	0	0	0

Particle	Mass
e	511 keV
μ	106 MeV
τ	1.78 GeV
u	1.5–4.5 MeV
d	5–8.5 MeV
c	1–1.4 GeV
s	0.08–0.15 GeV
t	174 GeV
b	4-4.5 GeV
W	80.4 GeV
Z	91.2 GeV
γ	0

Table 2.1: The fundamental fermions and electroweak gauge bosons, their electroweak quantum numbers and masses. The quark masses are evaluated as described in [1].

The Standard Model is characterized by a high degree of symmetries. For example, the strong force does not distinguish protons and neutrons and treats equally red, green, and blue quarks, and if there was only the weak force, experiments could not tell the difference between an electron and an electron-neutrino. Moreover, the second and third families of leptons and quarks behave like a copy of the first family. However, the copies are not exact, because the particles have very different masses. The electron has a mass of 0.5 MeV, but the mass of the muon is more than 200 times larger, and the mass of the tau is more than 3 000 times larger than that of the electron. The situation is even more extreme in the quark sector, the top quark having a mass four to five orders of magnitude larger than the mass of the u-quark. Although mass is a quantity with which we are most familiar in every day life, it is the property of elementary particles least understood. In the renormalizable quantum field theory of particle physics, explicit mass terms for the fermions and gauge bosons are forbidden by local gauge invariance, a concept that is introduced in the next section. In order to tackle the problem, a scalar field is introduced with a potential whose non-vanishing vacuum expectation value breaks the electroweak symmetry. The fermions and gauge bosons acquire masses by interacting with the scalar field. The mechanism, pioneered by Higgs *et. al.*, also predicts a new fundamental scalar boson, the Higgs boson H^0. The Higgs boson is the last particle of the Standard Model to be discovered. Direct searches at the LEP experiments could not give evidence for its existence, and the legacy of LEP is the certainty that the Standard Model Higgs boson must be heavier than 114.4 GeV at the 95% confidence level. Searches for the Higgs boson are carried on at Fermilab's $\mathrm{p\bar{p}}$-collider, but probably it will not show up before the start of the Large Hadron Collider at CERN. Failing to find the Higgs boson at the LHC will spoil our present picture of the fundamental particles and forces, and new concept will have to be invented.

3 The Standard Model as a gauge theory

The Standard Model is the theoretical framework that describes the fundamental particles and forces, except for gravity. The Standard Model is based on quantum gauge field theory [2] and symmetries. The gauge theories are renormalizable which means that the quantitative features of interactions between the particles can be calculated to arbitrary precision as perturbative expansions in the structure constants, after a few parameters have been measured at some arbitrary energy scale. The structure constants define the strength of the couplings. The invariance of a system of particles, described by a *Lagrangian* $\mathscr{L}$, under continuous symmetry operations is the source of conserved quantities [3], *e.g.* electric charge. Local gauge symmetries, local transformations of the wave functions representing a particle, which leave the Lagrangian unchanged, are building blocks of the theory as they automatically introduce interactions between particles via gauge bosons. The symmetries that are related to a particular force form symmetry groups. The electromagnetic force is related to the group U(1), the weak force to SU(2) and the strong force to SU(3). Despite its power, the Standard Model in its early form was a theory of *massless* particles, contradicting every-day experience. Explicit mass terms in the Lagrangian destroy gauge invariance and make the theory meaningless. There is a way out by introducing a scalar field with a quartic potential and by breaking the symmetry of its ground state. Since the symmetry breaking takes place in the electroweak sector of the Standard Model, the theory is presented here for electromagnetism and the weak forces. For a description of the strong force see for example Refs. [4, 5] and references therein. In the following sections the neutrinos are assumed to be massless, although recent experimental observations support non-vanishing values for neutrino masses [6].

Quantumelectrodynamics

The first and simplest local gauge theory was quantum electrodynamics (QED), based on the U(1) symmetry. The interaction of a spin-1/2 field ψ (fermion) of mass m_f with the electromagnetic field A_μ is described by the Lagrangian

$$\mathscr{L}_{\text{QED}} = \bar{\psi}\left(i\gamma^\mu D_\mu - m_f\right)\psi - \frac{1}{4}F_{\mu\nu}F^{\mu\nu}. \tag{3.1}$$

The tensor of the electromagnetic field strength is $F_{\mu\nu} = \partial_\mu A_\nu - \partial_\nu A_\mu$ and the covariant derivative is $D_\mu = \partial_\mu - ieA_\mu Q$, where e is the electric unit charge, and Q is the charge operator, $Q = -1$ for electrons. The Lagrangian is invariant under the local transformation

$$\psi(x) \quad \rightarrow \quad e^{i\alpha(x)Q}\psi(x), \quad \text{where } A_\mu \text{ transforms as} \tag{3.2}$$

$$A_\mu(x) \quad \rightarrow \quad A_\mu(x) + \frac{1}{e}\partial_\mu\alpha(x), \tag{3.3}$$

and $\alpha(x)$ is a local phase without relevance for observable quantities. From experiments we know that the photon is probably massless, or $m_\gamma < 2 \cdot 10^{-25}$ GeV at most. Local gauge theory sets a more stringent requirement: The photon field A_μ *must* be massless, because an explicit mass term of the form $m_\gamma^2 A_\mu A^\mu$ would not transform into itself.

Weak interactions

The charged weak currents do not distinguish left-handed charged leptons and their associated left-handed neutrino. This suggests to group them into a doublet $\chi_L = \binom{\nu}{\ell^-}_L$ which transforms under the symmetry group $\mathrm{SU}(2)_L$ (the simplified notation ν and ℓ instead of ψ_ν and ψ_ℓ is used now for the spinor fields). The associated inner symmetry is the weak isospin. The right-handed leptons remain singlets, ℓ_R. The Lagrangian

$$\mathscr{L}_W = i\bar{\chi}_L\gamma^\mu D_\mu \chi_L + i\bar{e}_R\gamma^\mu\partial_\mu e_R \tag{3.4}$$

is invariant under transformations

$$\chi_L \to e^{\frac{i}{2}\vec{\alpha}(x)\vec{\tau}}\chi_L, \tag{3.5}$$

if the derivative takes the form

$$D_\mu = \partial_\mu + i\frac{g}{2}\vec{\tau}\vec{W}_\mu(x). \tag{3.6}$$

The Pauli matrices τ_i are generators of SU(2) and g is a coupling constant. Thus, local gauge invariance introduces three vector fields W_1, W_2, W_3. Moreover, due to the non-abelian structure of SU(2), mass terms for the fermions are no longer allowed as they are not gauge invariant.

The new fields W_i can partially be identified with the weak gauge bosons. W_1 and W_2 mix to the physical W bosons:

$$W^\pm_\mu = \frac{1}{\sqrt{2}}\left(W^1_\mu \mp W^2_\mu\right). \tag{3.7}$$

It is alluring to identify the remaining component W^3_μ with the Z^0 boson, but the next section will show that the situation is slightly more complicated.

Electroweak interactions

The photon emerges as the gauge boson of the group $\mathrm{U}(1)_{\mathrm{em}}$ which operates on the wave function of charged fermions. A similar approach does not work with the doublet χ_L, because the corresponding gauge fields couple also to neutrinos which have no electric charge, and none of the field components can be identified with the photon. Instead, electromagnetism and weak interactions must be treated together. The idea is to add a new group, have an additional gauge field, and then let the new field and W^3_μ mix to linear combinations with the desired properties of the photon and the Z^0. In 1961 Glashow [7] postulated a new quantum number, weak hypercharge Y_W, which is related to electric charge and the third component of the weak isospin I_W:

$$Q = \frac{Y_W}{2} + I^3_W. \tag{3.8}$$

The corresponding gauge group is $\mathrm{U}(1)_{Y_W}$ and a gauge transformation is given by $\mathrm{e}_L \to e^{\frac{i}{2}\theta' Y_W}\mathrm{e}_L$. For a common description of electromagnetic and weak interaction, $\mathrm{SU}(2)_\mathrm{I} \times \mathrm{U}(1)_\mathrm{Y}$ is chosen as gauge group.

The Lagrangian is again given by Eq. 3.4, but the covariant derivative is now

$$D_\mu = \partial_\mu + ig\frac{\vec{\tau}}{2}\vec{W}_\mu + ig'\frac{Y_W}{2}B_\mu, \tag{3.9}$$

where g, g' are coupling constants. The Lagrangian is invariant under local gauge transformations of the form

$$\begin{aligned}\chi_L &\to e^{i(\vec{\alpha}(x)\cdot\vec{\tau}+\beta(x)Y_W)/2}\chi_L\\ \mathrm{e}_R &\to e^{i\beta(x)Y_W/2}\mathrm{e}_R,\end{aligned}$$

Multiplying out the derivative, the $\mathrm{SU(2)_I \times U(1)_Y}$ Lagrangian of quantum flavor dynamics (QFD) reads

$$\begin{aligned}\mathscr{L}_{\mathrm{QFD}} &= \bar{\chi}_L\gamma^\mu\left[i\partial_\mu - g\frac{1}{2}\vec{\tau}\cdot\vec{W}_\mu - g'\frac{Y_W}{2}B_\mu\right]\chi_L\\ &\quad + \bar{e}_R\gamma^\mu\left[i\partial_\mu - g'\frac{Y_W}{2}B_\mu\right]e_R - \frac{1}{4}\vec{W}_{\mu\nu}\cdot\vec{W}^{\mu\nu} - \frac{1}{4}B_{\mu\nu}B^{\mu\nu}, \qquad (3.10)\end{aligned}$$

where $B_{\mu\nu} = \partial_\mu B_\nu - \partial_\nu B_\mu$ and $\vec{W}_{\mu\nu} = \partial_\mu\vec{W}_\nu - \partial_\nu\vec{W}_\mu + ig\vec{W}_\mu \times \vec{W}_\nu$. The first two terms describe the kinetic energy of the fermions and their interaction with the gauge fields. The last two terms are the kinetic energy and self-interaction of the gauge fields. Out of the four gauge fields $\vec{W}_\mu$ and B_μ, the components W^3_μ and B_μ mix, because they have the same quantum numbers $I^3_W = 0$ and $Q = 0$. The physical gauge fields are thus $W^\pm_\mu, Z_\mu$, and A_μ, where

$$\begin{pmatrix} W^3_\mu \\ B_\mu \end{pmatrix} = \begin{pmatrix} \cos\theta_W & \sin\theta_W \\ -\sin\theta_W & \cos\theta_W \end{pmatrix}\begin{pmatrix} Z_\mu \\ A_\mu \end{pmatrix}, \qquad (3.11)$$

and θ_W is the weak mixing angle. The quanta of these fields are the gauge bosons $\mathrm{W}^\pm$, Z^0, and γ.

The observed coupling of the photon to fermions holds as realized in nature if in addition to Eq. 3.8 the following relation is fulfilled:

$$e = g\sin\theta_W = g'\cos\theta_W. \qquad (3.12)$$

The formalism presented so far has an important drawback: It does not allow explicit mass terms for gauge bosons and fermions. Terms of the form $\frac{1}{2}M_V^2 V_\mu V^\mu$, $V = \mathrm{W}^\pm, \mathrm{Z}^0$ or $m_f f\bar{f}$ in the Lagrangian break gauge invariance and the theory is no longer renormalizable. Explicit mass terms of gauge bosons are disallowed in any local gauge theory, whereas mass terms for fermions are allowed in QED, but forbidden in $\mathrm{SU(2)_I}$ due to different representations of left-handed fermions (doublets) and right-handed fermions (singlets). On the other hand, experiments demonstrate that the gauge bosons $\mathrm{W}^\pm$ and Z^0 and fermions like the τ lepton and the top quark have large masses, and so Eq. 3.10 is not an acceptable representation of the phenomenology observed in nature. Only the electromagnetic sector of the $\mathrm{U}(1)_Q$ subgroup is described correctly, since the photon is indeed massless.

The next section describes how the introduction of a new fundamental scalar field helps in retaining the concept of local gauge invariance whilst giving mass to the weak gauge bosons and the fermions. The necessity for a new scalar particle is also motivated by unitarity conditions in $\mathrm{W^+W^-}$-scattering: At high energies, the amplitude for longitudinally polarized particles in the elastic scattering $\mathrm{W^+W^-} \to \mathrm{W^+W^-}$ grows indefinitely. The relevant diagrams at Born-level are shown in Figure 3.1a. The terms in the amplitude growing with the fourth power in the energy are canceled due to the non-abelian gauge symmetry, but the s-wave amplitude still diverges quadratically in energy, $A_0 = s\cdot G_F/\left(8\pi\sqrt{2}\right)$. The amplitude can be prevented from diverging by diagrams with exchange of a new scalar

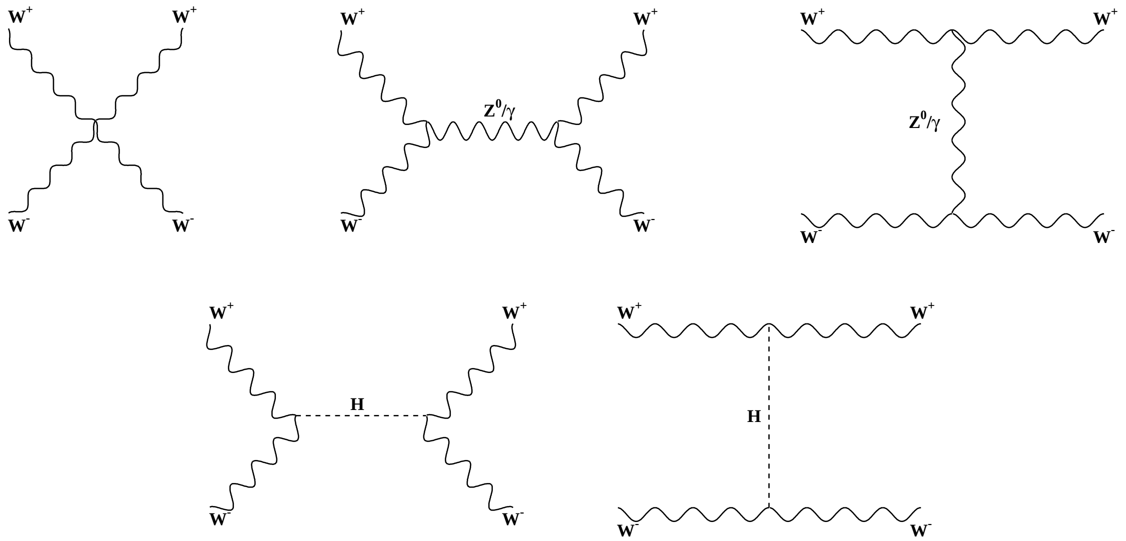

Figure 3.1: Generic diagrams for elastic W^+W^--scattering. a) top row: pure gauge-boson diagrams, b) bottom row: Higgs boson exchange.

particle, see Figure 3.1b. The same argument holds for the amplitude in fermion-pair annihilation $f\bar{f} \to W^+W^-$. The quadratic divergence appears only in theories with massive gauge bosons since massless particles have only transverse polarization. In conclusion, the existence of a new scalar particle is required by unitarity in theories with massive gauge bosons.

3.1 The Higgs mechanism and mass generation

In the Standard Model, generation of mass takes place by introducing a doublet of complex scalar fields with appropriate potential [8]. Interactions of fermions and gauge bosons with this field manifest themselves as masses of the particles. To do so, the vacuum state of the potential must have a smaller degree of symmetry than the Lagrangian. This is called 'spontaneous symmetry breaking'. The following issues must be taken into account when formulating the new Lagrangian:

- The scalar field shall couple to the gauge fields, hence it must carry non-zero hypercharge and weak isospin. The component that contains the vacuum expectation value must have charge $Q = 0$ so that $U(1)_Q$ remains unbroken.
- The self-interaction must be chosen in such a way that it fits into the phenomenology, *i.e.*, it breaks gauge symmetry in the desired way and keeps the theory renormalizable. Therefore, the mass dimension of the self-interaction terms must be smaller than or equal to four.
- The representation of the scalar field must provide a sufficiently large number of degrees of freedom to give mass to the three heavy gauge bosons and the fermions.

The simplest such representation of a scalar field is the following:

$$\Phi = \begin{pmatrix} \Phi^+ \\ \Phi^0 \end{pmatrix} = \begin{pmatrix} \Phi_3 + i\Phi_4 \\ \Phi_1 + i\Phi_2 \end{pmatrix}, \qquad \Phi \text{ real}, Y = 1, I_W = 1/2. \tag{3.13}$$

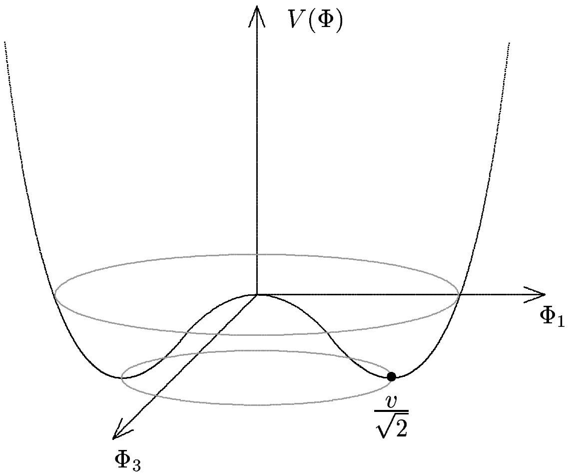

Figure 3.2: The Higgs potential shown as function of two out of the four field components Φ_i.

The appropriate extension to the Lagrangian is given by

$$\mathscr{L}_{\text{Higgs}} = (D_\mu \Phi)^\dagger (D^\mu \Phi) - V(\Phi), \quad \text{where} \tag{3.14}$$

$$V(\Phi) = -\mu^2 \Phi^\dagger \Phi + \lambda \left(\Phi^\dagger \Phi\right)^2, \qquad \mu^2, \lambda > 0 \tag{3.15}$$

$$D_\mu = \partial_\mu + \frac{1}{2} ig\vec{\tau}\vec{\mathrm{W}}_\mu + \frac{1}{2} ig' \mathrm{Y}_W \mathrm{B}_\mu \tag{3.16}$$

The values of λ and μ^2 in the Higgs potential are free real parameters of the theory. λ is chosen positive to make the total field energy bounded from below. If μ^2 is chosen negative, the potential has its minimum for $\Phi = 0$. If, instead, μ^2 is positive, the minimum is not a single point but a circle in the complex plane, as depicted in Figure 3.2. The field $\Phi_{1,2}^{\text{min}}$ in the minimum of the potential is given by:

$$\Phi_{1,2}^{\text{min}} = \sqrt{\frac{-\mu^2}{2\lambda}} e^{i\theta}, \quad 0 \leq \theta \leq 2\pi. \tag{3.17}$$

The equations of motion are obtained by expanding the Lagrangian around the minimum, and so one point Φ^{vac} from Equation (3.17) must be fixed. The common choice is to set $\theta = 0$, which leads to

$$\Phi_{1,2}^{\text{vac}} = \sqrt{\frac{\mu^2}{2\lambda}} := \frac{v}{\sqrt{2}}, \tag{3.18}$$

This equations defines the vacuum expectation value v. The choice of one point from the degenerated minimum breaks the symmetry of the potential. It can be shown that the Higgs field must take the form $\Phi_1 = v/\sqrt{2}$, $\Phi_2 = \Phi_3 = \Phi_4 = 0$ (*unitary gauge*). Non-vanishing values for $\Phi_2, \ldots, \Phi_4$ would result in additional unphysical massless fields, called Goldstone bosons, which can not be identified with existing particles [9]. The degrees of freedom represented by the three Goldstone bosons are absorbed by the additional degree of freedom of longitudinal polarization that the three weak gauge bosons acquire after becoming massive. Also, the expectation value of the upper component Φ^+ must be zero in order to leave U(1), and thus QED, unbroken. Small excitations around Φ^{vac} can then be written as

$$\Phi = \frac{1}{\sqrt{2}} \begin{pmatrix} 0 \\ v + H(x) \end{pmatrix}, \tag{3.19}$$

with the real field $H(x)$.

Inserting Eq. (3.19) into Eq. (3.14) gives, among many others terms, a part that reads

$$\mathscr{L}_{\mathrm{KG}} = \frac{1}{2}\partial^\mu H \partial_\mu H - \lambda v^2 H^2 - \lambda v H^3 - \frac{1}{4}\lambda H^4. \tag{3.20}$$

These terms describe a scalar Klein-Gordon field H with mass $m_H = v\sqrt{2\lambda}$ and self coupling according to the H^3 and H^4 terms (diagrams for the quartic self-coupling are displayed in Figure 3.4). The full Lagrangian contains also products of the Higgs field with the gauge fields, providing mass terms for the gauge bosons. Mass terms for fermions must be introduced 'by hand' via *Yukawa couplings* λ_f of the Higgs field to fermions (shown here for the first generation of leptons and quarks):

$$\mathscr{L}_{\mathrm{Yukawa}} = \lambda_{\mathrm{e}}\chi_{\mathrm{e}}\Phi \mathrm{e}_R + \lambda_{\mathrm{u}}\bar{\mathrm{q}}\tilde{\Phi}\mathrm{u}_R + \lambda_{\mathrm{d}}\mathrm{q}\Phi \mathrm{d}_R + h.c., \tag{3.21}$$

where $\mathrm{q}^T = (\mathrm{u,d})$ and $\tilde{\Phi} = i\tau_2\Phi^*$ is the charged conjugated field which gives mass to quarks with $I_W^3 = +1/2$.

The masses of the fundamental particles are all proportional to the vacuum expectation value of the Higgs field:

$$\begin{aligned} m_{\mathrm{W}^\pm} &= v\frac{g}{2} \qquad (3.22)\\ m_{\mathrm{Z}^0} &= v\frac{\sqrt{g^2+g'^2}}{2} \\ m_f &= v\frac{\lambda_f}{\sqrt{2}} \\ m_{\mathrm{H}^0} &= v\sqrt{2\lambda} = \sqrt{2}\mu. \end{aligned}$$

The vacuum expectation value is related to Fermi's constant:

$$\frac{G_F}{\sqrt{2}} = \frac{1}{2v^2} \rightarrow v = \left(\sqrt{2}G_F\right)^{-1/2} \approx 246 \text{ GeV}. \tag{3.23}$$

The Standard Model now gives an acceptable description of nature. It is a renormalizable quantum gauge theory with massive fermions and massive weak gauge bosons. In total, the Standard Model contains 18 free parameters: 3 charged-lepton masses, 6 quark masses, 4 parameters describing the CKM matrix, the Z^0 mass, Fermi's constant G_F, the structure constants α and α_s, and the mass of the Higgs boson m_{H^0}. A possible CP-violating strong-interaction parameter is sometimes mentioned as 19th parameter [1]. If neutrino masses are included, at least seven more parameters are needed.

The Higgs boson H^0 is a consequence of the mechanism which breaks electroweak symmetry. All its properties are precisely predicted by the model, except for the mass m_{H^0}. The following sections describe how the Higgs boson decays and which bounds can be set on the mass from theoretical arguments and from direct searches.

3.1.1 Decays of the Higgs boson

The coupling of the Higgs boson to fermions and the electroweak gauge bosons $V = \mathrm{W,Z}$ is set by their masses:

$$g_{ff\mathrm{H}^0} = \sqrt{\sqrt{2}G_F}\, m_f \tag{3.24}$$

$$g_{VV\mathrm{H}^0} = 2\sqrt{\sqrt{2}G_F}\, m_V^2. \tag{3.25}$$

At Born-level the decay of the Higgs boson into a pair of fermions is given by:

$$\Gamma(\mathrm{H}^0 \to f\bar{f}) = \frac{N_c G_F}{4\pi\sqrt{2}} m_f^2 m_{\mathrm{H}^0} \beta_f^3, \tag{3.26}$$

where the color factors are $N_c = 1$ for leptons, $N_c = 3$ for quarks, and $\beta = \sqrt{1 - 4m_f^2/m_{\mathrm{H}^0}^2}$ is a phase space factor accounting for the velocity of the fermion in the center-of-mass system. The branching fractions are modified by higher-order QCD and electroweak corrections [10].

The decay into a pair of weak gauge bosons is given by

$$\Gamma(\mathrm{H}^0 \to VV) = \delta_V \frac{G_F}{16\sqrt{2}\pi} m_{\mathrm{H}^0}^3 \left(1 - 4x + 12x^2\right) \beta_V, \tag{3.27}$$

where $x = m_V^2/m_{\mathrm{H}^0}^2$, $\delta_V = 2$ for $V = \mathrm{W}$ and $\delta_V = 1$ for $V = \mathrm{Z}$, and β_V is a phase space factor.

The decay into a pair of gluons or photons proceeds mainly via top- and bottom-quark loops, photonic decays also via W loops. If $m_{\mathrm{H}^0} \ll m_{\mathrm{t}}$, then the partial decay widths can be approximated by

$$\Gamma(\mathrm{H}^0 \to \mathrm{gg}) = \frac{G_F \alpha_s^2(m_{\mathrm{H}^0}^2)}{36\sqrt{2}\pi^3} m_{\mathrm{H}^0}^3 \left(1 + \left(\frac{95}{4} - \frac{7N_f}{6}\right)\frac{\alpha_s}{\pi}\right), \tag{3.28}$$

$$\Gamma(\mathrm{H}^0 \to \gamma\gamma) = \frac{G_F \alpha^2}{128\sqrt{2}\pi^3} m_{\mathrm{H}^0}^3 \left|\frac{4}{3} N_c \mathrm{e}_t^2 - 7\right|^2. \tag{3.29}$$

The branching fractions of the Standard Model Higgs boson into fermions and gauge bosons is shown in Figure 3.3a for Higgs boson masses between 50 GeV and 1 TeV. The decay into $\mathrm{b\bar{b}}$ is dominant up to $m_{\mathrm{H}^0} \sim 135$ GeV. Decays into $\tau^+\tau^-, \mathrm{c\bar{c}}$ and gg are suppressed by one to two orders of magnitude compared to $\mathrm{b\bar{b}}$. Decays into $\gamma\gamma$ (and $\mathrm{Z}^0\gamma$) reach their largest branching ratios of $\mathcal{O}(10^{-3})$ in the range 100 GeV to 150 GeV. Above $m_{\mathrm{H}^0} = 135$ GeV the decay into the heavy gauge bosons $\mathrm{W}^\pm$ and Z^0 becomes kinematically possible, and for $m_{\mathrm{H}^0} > 135$ GeV the decay $\mathrm{H}^0 \to \mathrm{W}^+\mathrm{W}^-$ is preferred. The decay fraction into a pair of Z^0 bosons is only about half of that into a pair of $\mathrm{W}^\pm$ bosons. If $m_{\mathrm{H}^0} \gtrsim 2m_{\mathrm{t}}$ the decay into $\mathrm{t\bar{t}}$ is possible, but it never reaches the the same strength as the decays into the weak gauge bosons (c.f. Eq. 3.24 and 3.25).

Figure 3.3b shows the total decay width of the Standard Model Higgs boson. For a mass below ~ 150 GeV the decay width is below 10^{-2} GeV, thus much smaller than current and expected future experimental mass resolutions. Above 150 GeV, the width grows rapidly, $\Gamma_{\mathrm{H}^0} \sim {m_{\mathrm{H}^0}}^3$. At $m_{\mathrm{H}^0} = 500$ GeV the Higgs boson has a width of ~ 65 GeV.

3.2 Mass bounds from theory and direct searches

The mass of the Higgs boson is not predicted by the Standard Model, but it can be constraint by requiring that the theory remains self-consistent.

Unitarity bounds

The introduction of a new scalar particle was motivated above by divergences in scattering of longitudinal polarized $\mathrm{W}^\pm$ bosons in the high energy limit. The amplitude can be

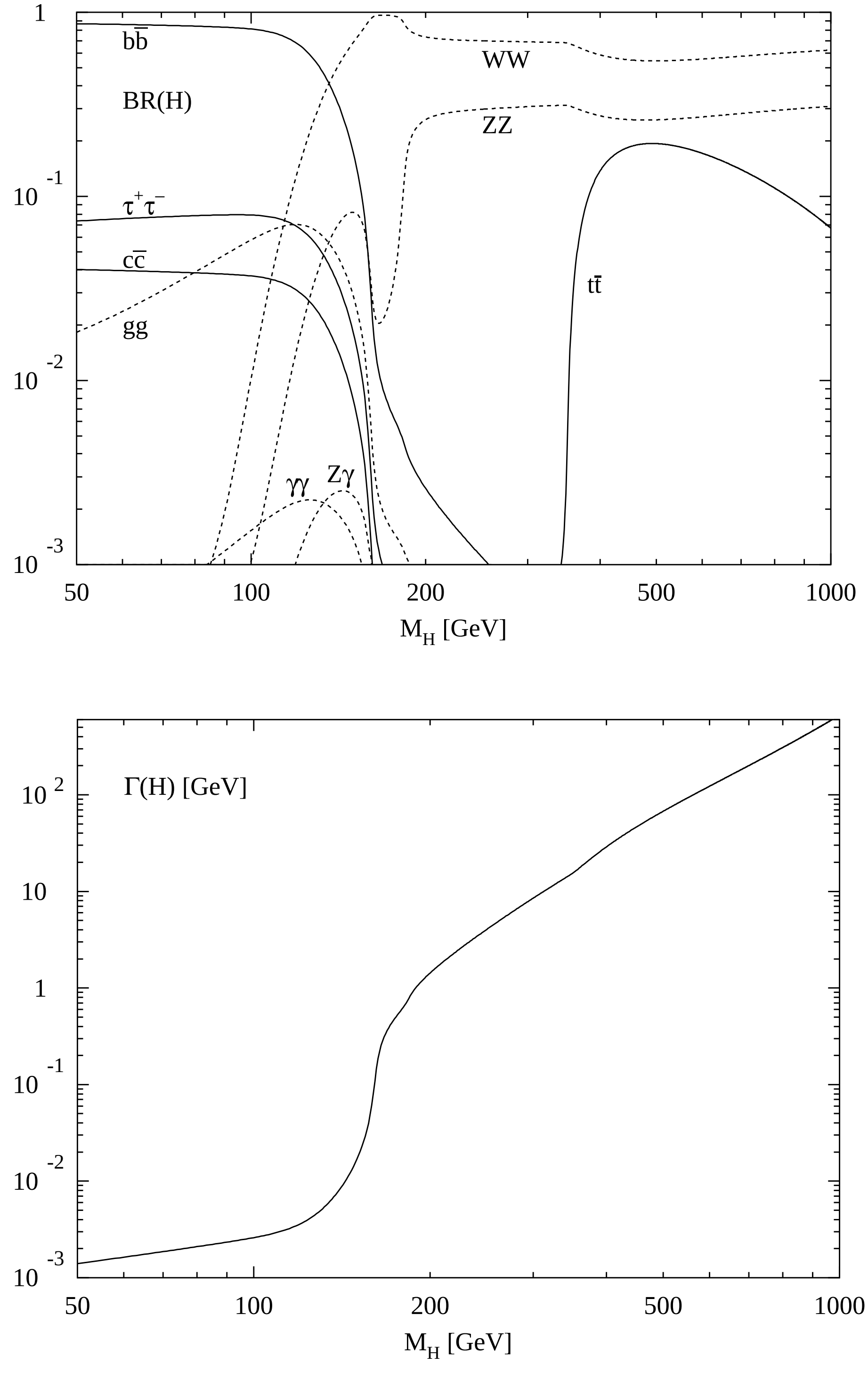

Figure 3.3: (a) Branching ratios of the dominant decay modes of the SM Higgs boson. (b) Total decay width of the SM Higgs boson. All relevant higher-order corrections are taken into account [11, 12].

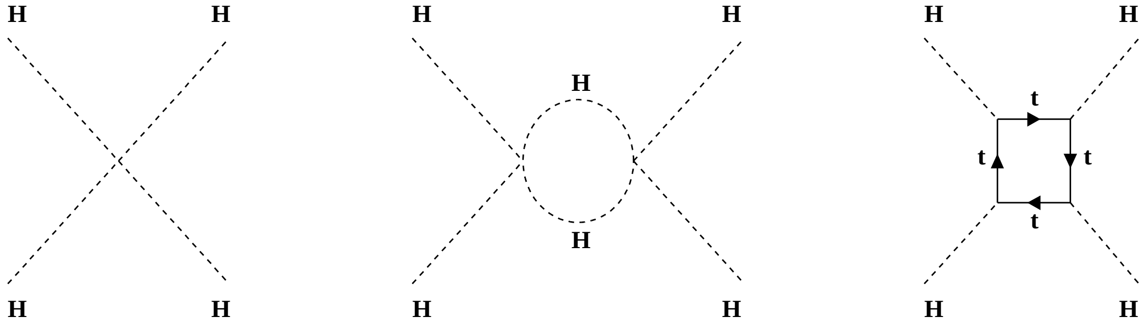

Figure 3.4: Dominant diagrams for Higgs self coupling.

expanded into Legendre polynomials. In the high energy limit, the lowest order polynomial (the s-wave amplitude) for $\mathrm{W}^{\pm}$ scattering is given by

$$A_{\text{s-wave}} = -\frac{G_F m_{\mathrm{H}^0}^2}{4\sqrt{s}\pi}. \tag{3.30}$$

If the amplitude $A_{\text{s-wave}}$ respects unitarity, the Higgs boson must fulfill:

$$m_{\mathrm{H}^0}^2 \leq \frac{2\sqrt{2}\pi}{G_F} \sim (850\ \mathrm{GeV})^2. \tag{3.31}$$

Similar bounds are obtained for other scattering processes, *e.g.*, $\mathrm{e}^+\mathrm{e}^- \to \mathrm{f}\bar{\mathrm{f}}, \mathrm{W}^+\mathrm{W}^-, \mathrm{Z}^0\mathrm{Z}^0$, and they all constrain the mass of the Higgs boson to values below 1 TeV [11]. However, these bounds should be taken with care because they are obtained from high energy limits of perturbative expansions.

Bounds from perturbation theory and stability of the vacuum

Stronger upper and lower bounds on the Higgs boson mass can be derived from the energy scale up to which the Standard Model should be valid without the necessity of introducing new physics.

Figure 3.4 shows the dominant diagrams for the Higgs self coupling λ. The energy dependence $\lambda(Q^2)$ can be derived from the renormalization group equations. Neglecting the graph with top-quark loops, it is given by:

$$\lambda(Q^2) = \frac{\lambda(v^2)}{1 - \frac{3\lambda(v^2)}{8\pi^2}\ln\frac{Q^2}{v^2}}. \tag{3.32}$$

There is a pole where the self coupling becomes infinite. This *Landau pole* is reached at smaller energy scales Λ if the Higgs boson mass increases. Requiring that the self coupling λ remains finite for arbitrary values of Q implies $\lambda(v) = 0$. Since $\lambda(v^2) = m_{\mathrm{H}^0}^2/v^2$ this would result in a non-interacting *trivial* theory. If, instead, λ is required to be finite only up to a scale Λ_{NP} where new physics sets in, equivalent to the requirement $\lambda(\Lambda_{\mathrm{NP}}) \leq 1$, the mass bound reads:

$$m_{\mathrm{H}^0}^2 < \frac{8\pi^2 v^2}{3\ln\Lambda_{\mathrm{NP}}^2/v^2}. \tag{3.33}$$

However, to derive meaningful mass bounds, contributions to the Higgs self coupling from graphs with top-quark loops and higher-order contributions must be included.

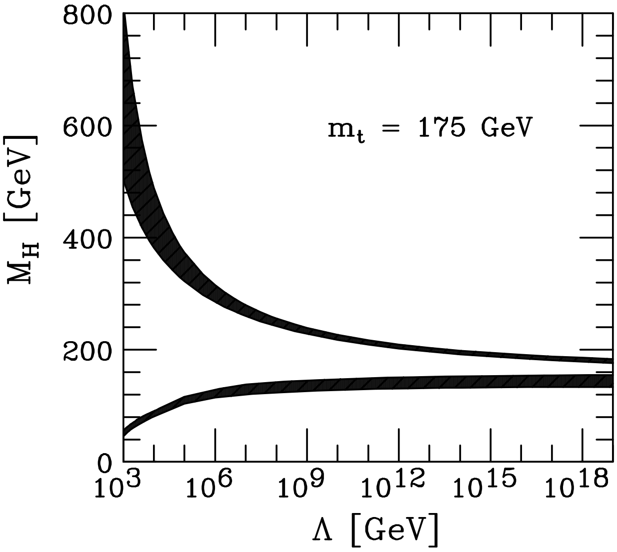

Figure 3.5: Theoretically allowed range for the mass of the Standard Model Higgs boson depending on the scale Λ where new physics occurs. The requirement of avoiding a Landau pole provides the upper bound and stability of the vacuum provides the lower bound [13].

Lower bounds can be obtained from considering stability of the electroweak vacuum in the minimum of the Higgs potential. If the quartic self coupling is small, the vacuum could take negative values due to the large top-quark Yukawa coupling. This would destabilize the Higgs potential. Requiring $\lambda(Q^2) > 0$ for all $Q < \Lambda_{\mathrm{NP}}$ yields a lower bound on the Higgs boson mass which increases when the cut-off Λ_{NP} grows.

The results of these considerations are visualized in Figure 3.5. It is assumed that perturbative calculations are meaningful up to the scale Λ_{NP} where new physics shows up (just termed Λ in the figure). Assuming this scale is the Planck scale, $\Lambda_{\mathrm{Pl}} = 10^{19}$ GeV, the Higgs boson mass is bound to 130 GeV $< m_{\mathrm{H}^0} <$ 190 GeV.

Bounds from precision measurements

The Higgs boson contributes via loop diagrams to radiative corrections of fundamental parameters of the Standard Model, *e.g.*, m_{Z^0}, $\Gamma_{\mathrm{Z}^0}, m_{\mathrm{W}^\pm}$. Many of these parameters have been measured with high precision, and so a global fit to these electroweak observables with the Higgs boson mass as a free parameter sets limits on m_{H^0}. Unfortunately, the general form of the corrections is

$$\Delta \sim g^2 \left(\ln \frac{m_{\mathrm{H}^0}}{m_{\mathrm{W}^\pm}} + g^2 \frac{{m_{\mathrm{H}^0}}^2}{{m_{\mathrm{W}^\pm}}^2} \right) , \tag{3.34}$$

so there is only weak, logarithmic dependence on m_{H^0} in leading corrections and corrections quadratic in m_{H^0} are suppressed by additional factors of g^2. This is known as Veltman's screening theorem [14]: the leading contributions to the radiative corrections of the Higgs boson mass cancel out because of SU(2) symmetry. Large uncertainties on the fitted m_{H^0} are the consequence. The χ^2 of the electroweak fit is displayed in Figure 3.6, left. The best value of the Higgs boson mass is $m^{\mathrm{fit}}_{\mathrm{H}^0} = 96^{+60}_{-38}$ GeV and the 95% CL upper bound is $m^{\mathrm{fit}}_{\mathrm{H}^0} < 219$ GeV ([15], December 2003). The fitted value of m_{H^0} is very sensitive to the top quark mass, the dependence is shown in Figure 3.6, right. The top quark mass used

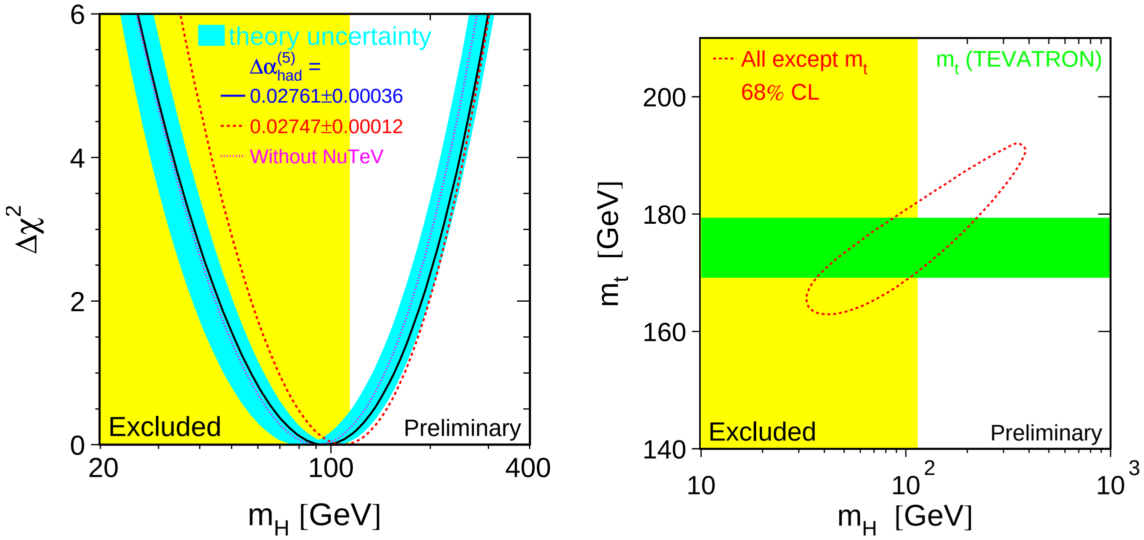

Figure 3.6: Left: the χ^2 distribution of the global fit to parameters of the Standard Model, depending on m_{H^0}. Right: The 68% confidence level contour in m_t for the fit to all electroweak data except the direct measurement of m_t [15].

in the fit for m_{H^0} is $m_t = (174.3 \pm 5.1)$ GeV. If m_t increased by just 2 GeV, the best value for m_{H^0} would increase by approximately 18 GeV.

Bounds from direct searches

At present, the best experimental lower limit on the mass of the Standard Model Higgs boson stems from direct searches with the four LEP experiments. The production modes and search strategies for Higgs bosons at LEP are detailed in Section 15 of Part III. In data from e^+e^--collisions at center-of-mass energies up to 209 GeV no evidence for a signal was observed, and a lower limit $m_{H^0} > 114.4$ GeV for the mass of the Standard Model Higgs boson was obtained from the combination of data from the four experiments [16].

3.3 Extensions to the Standard Model

The Higgs sector of the Standard Model with one complex scalar doublet is the smallest possible realization of electroweak symmetry breaking. However, a more involved Higgs sector would also do, with no contradiction to present experimental data. A minimal extension is obtained by adding a second complex doublet:

$$\Phi_1 = \begin{pmatrix} \Phi_3 + i\Phi_4 \\ \Phi_1 + i\Phi_2 \end{pmatrix}, \qquad \Phi_2 = \begin{pmatrix} \Phi_7 + i\Phi_8 \\ \Phi_5 + i\Phi_6 \end{pmatrix}. \tag{3.35}$$

There is some degree of freedom in how the fields are chosen to couple to fermions. Common realizations are the so called 'Type 1' to 'Type 4' Two-Higgs-doublet models (2HDM) with couplings according to the following table:

	type of 2HDM			
couples to	Type 1	Type 2	Type 3	Type 4
Down-type leptons	Φ_2	Φ_1	Φ_2	Φ_1
Up-type quarks	Φ_2	Φ_2	Φ_2	Φ_2
Down-type quarks	Φ_2	Φ_1	Φ_1	Φ_2

The particle spectrum is obtained, like in the Standard Model, by expanding the fields Φ_1 and Φ_2 around a minimum of the potential. Only the essence is mentioned here, because a special but very popular manifestation of a 2HDM Type 2 model is described in the next sections. The outcome are five Higgs bosons: two neutral CP-even bosons h^0 and H^0, one neutral CP-odd boson A^0, and two charged bosons H^+ and H^-. In addition, there are again three massless Goldstone bosons which represent degrees of freedom absorbed by the longitudinal polarizations of the massive gauge bosons after spontaneous symmetry breaking. Reference [17] discusses in more detail general 2HDMs.

3.3.1 Problems of the Standard Model

The Standard Model gives an amazingly accurate description of present experimental results, with agreement between prediction and observation at a level up to 10^{-6}. But despite having numerous virtues, there are also some unsatisfactory issues, and the Standard Model is commonly regarded to be a low-energy approximation of a more fundamental theory. Some deficits of the Standard Model are discussed below.

- The Standard Model leaves unexplained why the strong and the electroweak gauge structure is $\mathrm{SU}(3)_\mathrm{C} \times \mathrm{SU}(2)_\mathrm{I} \times \mathrm{U}(1)_\mathrm{Y}$ with different gauge couplings and fermionic quantum number whose values are not predicted by the model. Efforts are done to unify the gauge groups and have only one coupling above the energy scale of *Grand Unification* [18]. This is not possible in the SM because for large energy scales the coupling constants do not meet in a single point, c.f. Section 3.3.2 and Figure 3.7. The unification scale could be as large as the Planck scale, $\Lambda_\mathrm{Pl} \sim 10^{19}$ GeV.

- The mass m_Φ of the scalar field Φ is not stable against quantum fluctuations, and the renormalization of m_Φ^2 is quadratically divergent. The same is true for the vacuum expectation value of the potential, and affects therefore the masses of fermions and gauge bosons. A cut-off must be chosen at some (large) mass scale $M_X \gg m_\Phi$ where new physics is supposed to emerge. The fact that the masses m_{H^0}, m_{Z^0}, $m_{\mathrm{W}^\pm}$ are at the electroweak scale, but the scale for new physics is many orders of magnitudes larger is called the *hierarchy problem*.

  The hierarchy problem becomes crucial if one considers that the mass of the Higgs boson is required to be at the electroweak scale ($\mathcal{O}(m_{\mathrm{W}^\pm})$) so that diagrams in perturbation theory cancel at sufficiently low energy scales to satisfy unitarity. But without radiative corrections, m_{H^0} would be at scale M_X. To bring back m_{H^0} to the electroweak scale, the loop corrections CM_X^2 on the right-hand side of Eq. 3.36 must almost cancel the 'bare mass' $m_{\mathrm{H}^0}^2(M_X)$,

  $$m_{\mathrm{H}^0}^2(m_{\mathrm{W}^\pm}) \sim m_{\mathrm{H}^0}^2(M_X) - CM_X^2. \tag{3.36}$$

  This requires *fine-tuning* of parameters to an accuracy of order 10^{-26} in each order of perturbation theory. Such extreme fine-tuning is unnatural.

- The Standard Model does not contain gravity.

3.3.2 Supersymmetry

Some of the problems mentioned before can be solved by introducing a new symmetry, which relates fermions to bosons. Every Standard Model fermion has a bosonic partner, and every Standard Model boson has a fermionic partner. A new symmetry operation is introduced which transforms a fermion into a boson and vice versa. This symmetry unifies the particles at a fundamental level and is called *Supersymmetry* (SUSY). The new supersymmetric particles ('sparticles') cannot be identified with particles from the Standard Model, and so Supersymmetry at least doubles the particle content. Moreover, no SUSY particle has been observed at the same mass as its SM partner, so SUSY must be a broken symmetry. The SUSY particle spectrum is listed below for the specific case of the *Minimal Supersymmetric Standard Model* (MSSM), which includes two Higgs doublets and thus five physical Higgs bosons. The partners of the charged gauge bosons and the charged Higgs bosons mix to charginos $\tilde{\chi}^{\pm}_{1,2}$ and the partners of the neutral gauge bosons and CP-even Higgs bosons mix to neutralinos $\tilde{\chi}^{0}_{1,2,3,4}$. For introductions to Supersymmetry see Refs. [19, 20].

$$\begin{array}{lllllll}
(\mathrm{u,d,c,s,t,b})_{L,R} & (\mathrm{e},\mu,\tau)_{L,R} & (\nu_{\mathrm{e},\mu,\tau})_L & \mathrm{g} & \underbrace{\mathrm{W}^{\pm},\mathrm{H}^{\pm}} & \underbrace{\gamma,\mathrm{Z},\mathrm{h}^0,\mathrm{H}^0} & \mathrm{A}^0 \\
(\tilde{\mathrm{u}},\tilde{\mathrm{d}},\tilde{\mathrm{c}},\tilde{\mathrm{s}},\tilde{\mathrm{t}},\tilde{\mathrm{b}})_{L,R} & (\tilde{\mathrm{e}},\tilde{\mu},\tilde{\tau})_{L,R} & (\tilde{\nu}_{\mathrm{e},\mu,\tau})_L & \tilde{\mathrm{g}} & \tilde{\chi}^{\pm}_{1,2} & \tilde{\chi}^{0}_{1,2,3,4} & \text{—}
\end{array}$$

The MSSM introduces a new conserved quantum number, since the Lagrangian contains only terms with even number of SUSY particles. The new symmetry is called R-parity, which is defined as $R \equiv (-1)^{3B+L+2S}$, where B is the baryon number, L the lepton number, and S the spin, so that all SM particles have even R parity and all SUSY particles have odd R parity. R parity conservation was originally introduced to prohibit the decay of the proton. As a consequence of R parity conservation, SUSY particles can only be produced in pairs, and the decay of a SUSY particle into SM particles will always include an odd number of SUSY particles so that there is a stable lightest supersymmetric particle ('LSP') which is neutral and uncolored, leaving no traces in collider detectors.

Supersymmetry naturally solves the hierarchy problem because radiative corrections containing SUSY particles cancel the divergences originating from loop corrections with SM particles. No artificial fine-tuning is necessary to keep the mass of the Higgs bosons at the electroweak scale, if the SUSY mass scale is of order 1 TeV. Also, SUSY unifies the gauge coupling constants at a scale $m_{\mathrm{SUSY}} \lesssim \Lambda_{\mathrm{Pl}}$. The running of the coupling constants $\alpha_1, \alpha_2, \alpha_3$ is shown in Figure 3.7 for the Standard Model and the MSSM. The gauge groups can be embedded into a higher 'Grand Unification' symmetry, *e.g.* in SO(10), they split into the known SM symmetry groups below the energy scale of Grand Unification. Finally, *local* Supersymmetry generates a particle that has all characteristics of the graviton, and so SUSY points a way to the unification of gravity and the other forces.

3.3.3 The Higgs sector of the MSSM

The MSSM is the simplest supersymmetric extension of the Standard Model. Spontaneous symmetry breaking with just one Higgs doublet is no longer possible for several reasons: The supersymmetric partners of the Higgs bosons, the Higgsinos, introduce gauge anomalies, which can only be restored by supersymmetric partners of a second scalar doublet. Within SUSY it is not possible to give mass to quarks with $I^3_W = 1/2$ with the help of the charge-conjugated Higgs-field. Therefore, the Higgs sector must consist of at least two complex scalar fields:

$$H_1 = \begin{pmatrix} H_1^1 \\ H_1^2 \end{pmatrix} \qquad H_2 = \begin{pmatrix} H_2^1 \\ H_2^2 \end{pmatrix}. \tag{3.37}$$

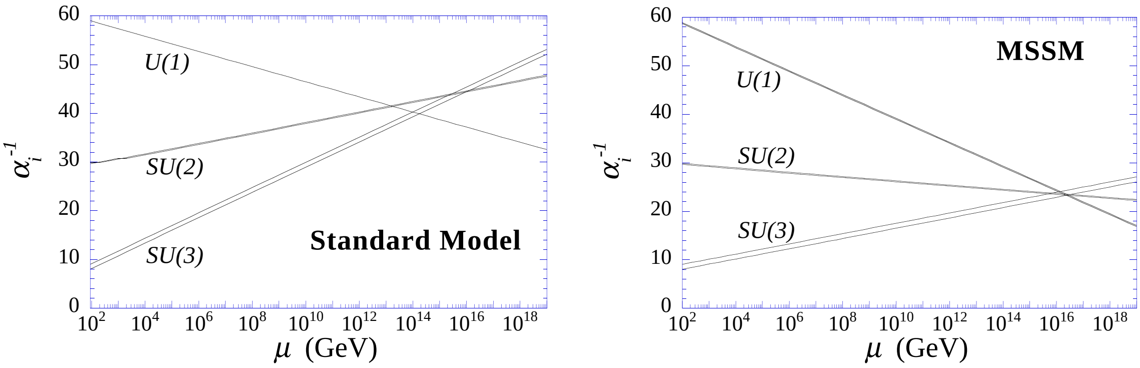

Figure 3.7: Running of the inverse coupling constants in the SM and the MSSM [21].

The MSSM Higgs potential is given by

$$V = \mu^2(|H_1|^2 + |H_2|^2) + \frac{g^2 + g'^2}{8}(|H_1|^2 - |H_2|^2)^2 + \frac{1}{2}g^2|H_1^* H_2|^2. \tag{3.38}$$

There is no symmetry breaking here, because the minimum of the potential is at $H_1 = H_2 = 0$. To break SU(2) × U(1) symmetry it is essential to break Supersymmetry. One way to accomplish this, whilst retaining a physically acceptable theory, is to introduce ‘soft breaking terms’ [22, 23, 24]:

$$\begin{aligned} V &= (\mu^2 + m_1^2)|H_1|^2 + (\mu^2 + m_2^2)|H_2|^2 - \mu B(\epsilon_{ij} H_1^i H_2^j + h.c.) \\ &+ \frac{1}{8}(g^2 + g\prime^2))(|H_1|^2 - |H_2|^2)^2 + \frac{1}{2}g^2|H_1^* H_2|^2, \end{aligned} \tag{3.39}$$

where $\epsilon_{12} = -\epsilon_{21} = 1$, $\epsilon_{11} = \epsilon_{22} = 0$ and $m_1, m_2, \mu B$ being soft SUSY breaking mass parameters. Non-vanishing vacuum expectation values of the neutral components of the two Higgs doublet break the electroweak symmetry in the desired way:

$$\langle H_1 \rangle = \frac{1}{\sqrt{2}}\begin{pmatrix} v_1 \\ 0 \end{pmatrix}, \qquad \langle H_2 \rangle = \frac{1}{\sqrt{2}}\begin{pmatrix} 0 \\ v_2 \end{pmatrix} \tag{3.40}$$

The two vacuum expectation values v_1 and v_2 define one parameter of the MSSM,

$$\tan\beta \equiv \frac{v_2}{v_1} \qquad \text{with } \sqrt{v_1^2 + v_2^2} \approx 246 \text{ GeV}. \tag{3.41}$$

The requirement for a minimum, $\partial V/\partial H_1^0 = \partial V/\partial H_2^0 = 0$, reads

$$\begin{aligned} \mu^2 + m_1^2 &= \tilde{m}_3^2 \tan\beta + \frac{g + g'^2}{4}\left(v_1^2 - v_2^2\right), \\ \mu^2 + m_2^2 &= \tilde{m}_3^2 \cot\beta + \frac{g + g'^2}{4}\left(v_1^2 - v_2^2\right), \end{aligned}$$

with $\tilde{m}_3^2 \equiv -B\mu$. Thus, the Higgs sector is fixed by just two parameters, $\tan\beta$ and $\tilde{m}_3$.

It was already mentioned in the introduction of Section 3.3 that the eight parameters of the two complex doublets correspond to three Goldstone bosons $G^0, G^\pm$ and five Higgs bosons $\mathrm{h}^0, \mathrm{H}^0, \mathrm{A}^0, H^\pm$. More specific, the mass eigenstates arise from mixtures of the eight components with the same Q and CP quantum numbers:

$$\begin{aligned}
\begin{pmatrix} G^- \\ H^- \end{pmatrix} &= \begin{pmatrix} \cos\beta & -\sin\beta \\ \sin\beta & \cos\beta \end{pmatrix} \begin{pmatrix} H_1^2 \\ H_2^1 \end{pmatrix}, \\
\begin{pmatrix} G^0 \\ \mathrm{A}^0 \end{pmatrix} &= \sqrt{2} \begin{pmatrix} \cos\beta & -\sin\beta \\ \sin\beta & \cos\beta \end{pmatrix} \begin{pmatrix} \Im(H_1^1) \\ \Im(H_2^2) \end{pmatrix}, \\
\begin{pmatrix} \mathrm{h}^0 \\ \mathrm{H}^0 \end{pmatrix} &= \sqrt{2} \begin{pmatrix} \cos\alpha & -\sin\alpha \\ \sin\alpha & \cos\alpha \end{pmatrix} \begin{pmatrix} \Re(H_2^2) - v_2 \\ \Re(H_1^1) - v1 \end{pmatrix}
\end{aligned}$$

and $G^+ = (G^-)^\dagger$, $H^+ = (H^-)^\dagger$. The angle α describes the mixing between the CP-even Higgs bosons and is another parameter of the model. The Born-level masses of the Higgs bosons are obtained by expanding the potential around the minimum:

$$M^2_{\mathrm{H}^\pm} = \frac{1}{4}\left(g^2 + 2\frac{\tilde{m}_3^2}{v_1 v_2}\right)(v_1^2 + v_2^2), \tag{3.42}$$

$$M^2_{\mathrm{A}^0} = \frac{\tilde{m}_3^2}{v_1 v_2}(v_1^2 + v_2^2) = \tilde{m}_3^2(\tan\beta + \cot\beta) = M^2_{\mathrm{H}^\pm} - M^2_{\mathrm{W}^\pm}, \tag{3.43}$$

$$M^2_{\mathrm{H}^0,\mathrm{h}^0} = \frac{1}{2}\left[M^2_{\mathrm{A}^0} + M^2_{\mathrm{Z}^0} \pm \sqrt{(M^2_{\mathrm{A}^0} + M^2_{\mathrm{Z}^0})^2 - 4M^2_{\mathrm{Z}^0} M^2_{\mathrm{A}^0}\cos^2 2\beta}\right] \tag{3.44}$$

The masses of the $\mathrm{W}^\pm$ and the Z^0 can be read off the Lagrangian after symmetry breaking:

$$\begin{aligned}
M^2_{\mathrm{W}^\pm} &= \frac{g^2}{4}(v_1^2 + v_2^2) \\
M^2_{\mathrm{Z}^0} &= \frac{g^2 + g'^2}{4}(v_1^2 + v_2^2) \\
m_\ell &= \frac{\lambda_\ell}{\sqrt{2}} v_1 \\
m_d &= \frac{\lambda_d}{\sqrt{2}} v_1 \\
m_u &= \frac{\lambda_u}{\sqrt{2}} v_2.
\end{aligned} \tag{3.45}$$

From Eq. 3.44 one can derive that $m_{\mathrm{h}^0} \leq m_{\mathrm{Z}^0} \cos 2\beta$, so that the MSSM predicts at least one Higgs boson being lighter than the Z^0. But the relation holds only at Born-level and higher-order corrections shift m_{h^0} to significantly higher values. Still, the MSSM predicts $m_{\mathrm{h}^0} < 130$ GeV.

The couplings of the neutral MSSM Higgs bosons to fermions and weak gauge bosons are modified with respect to Standard Model couplings. Depending on α and β the Yukawa couplings can be smaller or larger than the SM values. The Higgs-gauge couplings are always suppressed. At Born-level there is no coupling between A^0 and gauge bosons due to CP-invariance. The Born-level couplings are listed in Table 3.1.

Experimental constraints

The MSSM with SUSY breaking terms in the Lagrangian has more than 100 free parameters, but on Born-level, all Higgs boson masses and couplings can be expressed by just two

Table 3.1: Yukawa and weak gauge boson couplings to the Higgs boson normalized to the Standard Model couplings.

Φ		$g_{\mathrm{u\bar{u}}\Phi}$	$g_{\mathrm{d\bar{d}}\Phi}$	$g_{\mathrm{VV}\Phi}$
MSSM	h^0	$\dfrac{\cos\alpha}{\sin\beta}$	$-\dfrac{\sin\alpha}{\cos\beta}$	$\sin(\beta-\alpha)$
	H^0	$\dfrac{\sin\alpha}{\sin\beta}$	$\dfrac{\cos\alpha}{\cos\beta}$	$\cos(\beta-\alpha)$
	A^0	$\dfrac{1}{\tan\beta}$	$\tan\beta$	0

parameters. The common choice of parameters is $\tan\beta$ and m_{A^0}. However, radiative loop corrections containing top quarks or SUSY particles substantially alter the Born-level formulae. In order to make comparable predictions and measurements in the MSSM Higgs sector, several benchmark scenarios have been developed in which results are given depending on $\tan\beta$ and m_{A^0} with other MSSM parameters fixed. Out of several existing benchmark scenarios, only two are discussed here: In the m_{h^0}-max scenario the parameters are chosen such that the maximum possible Higgs boson mass is obtained as a function of $\tan\beta$, with other MSSM parameters fixed as described in [26]. These are the most conservative assumptions on the $\tan\beta$ range for fixed values of the mass of the top quarks and the SUSY mass scale. The no-mixing scenario is similar to the m_{h^0}-max scenario, but it assumes that there is no mixing between the scalar partners of the left-handed and right-handed top quarks.

Limits on the two scenarios in the $(m_{\mathrm{A}^0}, \tan\beta)$-plane from the LEP experiments are shown in Figure 3.8 as 95% confidence-level exclusion contours. For the m_{h^0}-max scenario, values of $\tan\beta$ between 0.5 and 2.4 are excluded, and for the no-mixing scenario values of $\tan\beta$ between 0.7 and 10.5 are excluded. The LHC will be sensitive to much larger areas of the MSSM parameter space, and expected discovery contours are discussed in Section 13.3.

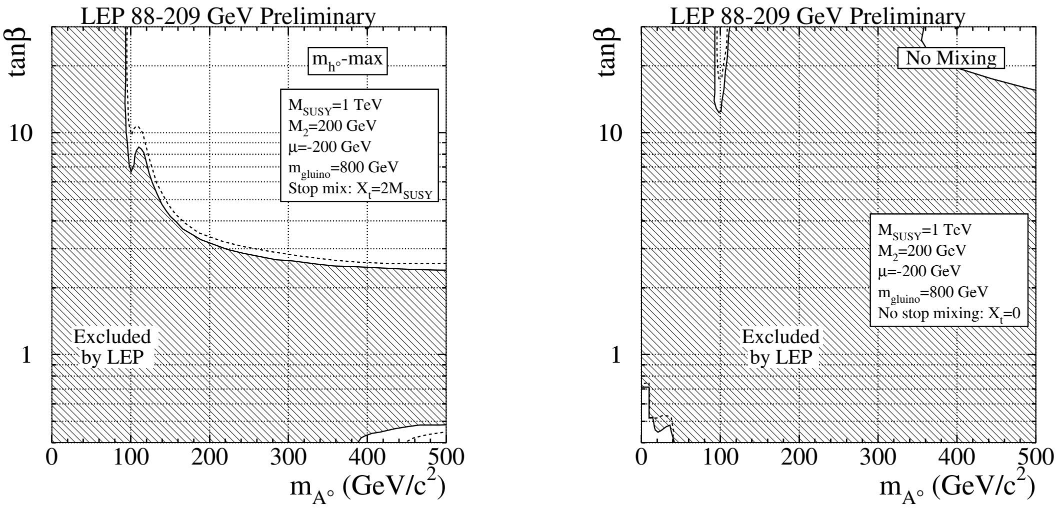

Figure 3.8: Experimental constraints on the parameters space of the MSSM Higgs sector for the m_{h^0}-max and the no-mixing scenario [25].

Part II

The ATLAS discovery potential for the channel $t\bar{t}H^0$, $H^0 \rightarrow b\bar{b}$ at the LHC

4 Introduction

This part of the thesis describes a study of the discovery potential of the ATLAS experiment for a Standard Model Higgs boson in a mass range where the decay $\mathrm{H}^0 \rightarrow \mathrm{b\bar{b}}$ is dominant. As will be discussed in Section 5.6.1, to our present knowledge, this final state will only be observable if the Higgs boson is produced in association with a pair of top-quarks. If the mass of the Higgs boson is smaller than about 130 GeV, then $\mathrm{t\bar{t}H}^0$, $\mathrm{H}^0 \rightarrow \mathrm{b\bar{b}}$ is one of the most promising channels to observe the Standard Model Higgs boson at the LHC [27], and it is the only channel to measure the Yukawa coupling of the b-quark.

The $\mathrm{t\bar{t}H}^0$ channel is quite demanding. It requires excellent performance of the entire detector and elaborate treatment in the selection of signal events: Apart from two b-jets expected from the decay of the Higgs boson, there is an additional pair of b-jets from the decay of the top quarks. Thus, reconstruction of the Higgs boson mass from the invariant mass of the $\mathrm{b\bar{b}}$-pair suffers from combinatorics when selecting two out of four b-jets. But the background to the $\mathrm{t\bar{t}H}^0$ signal is huge, and mass information from the Higgs boson is an essential tool for rejecting a substantial fraction of unwanted processes.

The $\mathrm{t\bar{t}H}^0$, $\mathrm{H}^0 \rightarrow \mathrm{b\bar{b}}$ channel was already studied for the ATLAS Technical Design Report (TDR) [27, 28]. It was shown that the signal from the Higgs boson can be observed as a peak in the m_{bb} mass spectrum if the combinatorial background is minimized by a full reconstruction of the final state. The full final state reconstruction aims at minimizing the combinatorics by assigning two of the four b-jets to the decays of the top quarks with the help of information about the kinematics of the event. In the TDR study a significance of signal over square root of the background, $S/\sqrt{B} = 5.0$ for $m_{\mathrm{H}^0} = 100$ GeV and $S/\sqrt{B} = 3.6$ for $m_{\mathrm{H}^0} = 120$ GeV was predicted for an integrated luminosity of 30 fb^{-1}.

Since publication of the TDR in 1999, a lot of progress has been made in both the theoretical prediction of signal and background properties and in the simulation of the final detector configuration. Advanced calculations of the signal cross section and a new Monte Carlo generator for the dominant background are available. In addition, there were significant changes in the layout of some parts of the ATLAS detector and some disadvantageous effects on the observability of the Higgs boson in the $\mathrm{t\bar{t}H}^0$ channel are expected. Therefore, this analysis reviews the discovery potential of the channel and seeks for advanced methods in the event analysis and selection.

This part of the thesis is organized as follows: Chapter 5 gives an overview of the physics program at the upcoming LHC proton-proton collider. The next two chapters portray the experimental environment at the *Conseil Européen pour la Recherche Nucléaire* (CERN). A brief description of the accelerator is followed by an overview of the ATLAS experiment. The main part (Chapters 8 to 13) is then dedicated to a description of the channel $\mathrm{t\bar{t}H}^0$ with $\mathrm{H}^0 \rightarrow \mathrm{b\bar{b}}$. After a discussion of the general aspects, two event reconstruction methods are presented. The studies include simulations of the physics processes with both a fast and a detailed full simulation of the ATLAS detector. For the fast simulation, two scenarios with low and high luminosity conditions at the LHC are taken into account ($\mathcal{L} \sim 10^{33}$ $\mathrm{cm}^{-2}\mathrm{s}^{-1}$ and $\mathcal{L} \sim 10^{34}$ $\mathrm{cm}^{-2}\mathrm{s}^{-1}$, respectively). At low luminosity conditions, the study focuses on the b-tagging performance of ATLAS, because good flavor-tagging capabilities are crucial for the discovery of a low mass Higgs boson at the LHC.

5 Physics goals at the LHC

The high energy and luminosity of the LHC offer unique opportunities to answer questions from the forefront of particle physics. Hence, the ATLAS physics program is very rich, and an extensive overview can be found in the ATLAS Detector and Physics Performance Technical Design Report [27]. The most important topics are mentioned below with a focus on searches for Higgs bosons.

5.1 QCD processes

Studies of QCD processes are used to test predictions from perturbative QCD and to perform precision measurements. The strong coupling constant α_s can be measured at various scales in connection with the gluon distribution. Knowledge of the parton distribution functions (PDF) is essential for all processes at the LHC, both signals and backgrounds. They can be determined by global fits to data from deep-inelastic scattering, Drell-Yang, jet and direct photon production. QCD processes provide huge backgrounds to other Standard Model processes and signals of new physics. It is therefore of prime importance to measure and understand precisely QCD events.

Inelastic collisions ('minimum-bias events'), underlying the processes of interest, are unavoidable at the high luminosity of the LHC. At design luminosity on average 23 minimum-bias events are expected per bunch-crossing. The modeling of these events by the generators and their impact on the detector and reconstruction performance must be studied so that the generators and detector simulation can be tuned accordingly.

5.2 Electroweak gauge bosons

The high production rate of electroweak gauge bosons allows for measurements which supersede those from existing accelerators. The W mass is a fundamental parameter of the Standard Model. It is related to other parameters of the theory, most notably, corrections to the W mass depend on the masses of the top quark ($\sim m_\mathrm{t}^2$) and the Higgs boson ($\sim \log m_{\mathrm{H}^0}$). The W mass is currently known with a precision of 39 MeV [1], and improving the uncertainty will therefore put more stringent constraints on m_{H^0}. The aim of the LHC is to determine the top mass with a precision of about 2 GeV (see Section 5.4, the current error is 5.1 GeV [1]), and so $m_{\mathrm{W}^\pm}$ should be known with an error less than 15 MeV so that it is not the dominant error in the estimation of the Higgs boson mass. To measure the W boson mass at the LHC, the leptonic decays of the W boson must be used, and due to the neutrino only the transverse mass can be reconstructed. In one year of data taking at low luminosity the LHC will produce about 300 million W+X, W$\to \ell\nu$ events. The mass measurement will therefore be dominated by systematic uncertainties.

Models beyond the Standard Model may result in couplings different from those in the Standard Model. A sensitive test to the model is provided by the measurement of gauge boson couplings of $\mathrm{W}^\pm$, Z^0, and γ bosons. These can be either Triple Gauge-boson Couplings (TGC), *e.g.*, WWγ, WWZ, or Quartic Gauge-boson couplings (QGC), *e.g.*, $\gamma\gamma$WW, ZγWW, ZZWW, WWWW.

Finally, the production of Z^0 bosons is important for the *in situ* calibration of the detector, *e.g.*, by constraining the invariant mass of the lepton pair in $Z^0 \to \ell^+\ell^-$ decays to the well-known Z^0 mass.

5.3 B-physics

The LHC will produce a plethora of B-hadrons. The B-physics program will focus on the study of CP-violation in the B-system, B-oscillations, rare B-decays (*e.g.*, $B_d^0 \to K^{*0}\mu\mu$, $B_d^0 \to \rho^0\mu\mu$, $B_s^0 \to \phi^0\mu\mu$) involving flavor-changing neutral currents, precision measurements of B-hadrons for confirming the Standard Model or finding hints of new physics, and on constraining the CKM matrix angles $\sin 2\alpha$ and $\sin 2\beta$. Events containing b-quarks will be triggered at the Level 1 stage by B-decays with muons in the central region $|\eta| < 2.4$.

5.4 The top-quark

The LHC will also be a top-quark factory, producing more than 8 million $t\bar{t}$ pairs per year at low luminosity. This provides a playground for a large variety of top physics studies. The top quark is of special interest because it is the only fundamental fermion with a mass at the electroweak scale. It is so heavy that it decays before hadronization can take place, offering the unique opportunity to study the decay of a 'bare' quark.

If the top quark mass can be measured with a precision of about 2 GeV, the mass of the Standard Model Higgs boson can be constrained to a level of 30% (if $m_{W^\pm}$ can be measured to ±15 MeV). Precision measurements of the top quark production cross section and decay modes are tests of the Standard Model and deviations may point to new physics. Moreover, pairs of top quarks, $t\bar{t}$, are important backgrounds to many searches for new particles, and so good knowledge of the top quark properties is mandatory.

Examination of top quark decays provides information on the CKM matrix element V_{tb} from a direct measurement. In the Standard Model, the top quark decays almost exclusively into Wb. Such a measurement is also sensitive to the existence of a fourth generation of quarks. The coupling strength of the W-t-b vertex can directly be measured in electroweak single-top production. Searches for rare decays of the top quark may reveal deviations from the Standard Model predictions, *e.g.*, the decay into charged Higgs bosons in the MSSM ($t \to H^+b$, see also Section 5.6.3) or flavor-changing neutral current decays $t \to Z^0q$, $t \to \gamma q$, $t \to gq$, which are strongly suppressed in the Standard Model.

5.5 Supersymmetry and other physics beyond the Standard Model

Supersymmetry (SUSY) [19, 20] is a prominent extension to the Standard Model because it solves some of its drawbacks. Discovery of SUSY signatures should be straightforward at the LHC if SUSY exists at a scale $m_{\mathrm{SUSY}} \sim 1$ TeV. Since the lightest supersymmetric particles, which do not interact with the detector, can occur in the final state of particle decays, SUSY exhibits itself as events with large missing transverse energy. In addition, SUSY events often contain a considerable number of high-p_T jets, multiple leptons with same sign charge, and spherical event shape.

There are many SUSY models around, each of them introduces a set of new model parameters. It is beyond the scope of this section to give a detailed overview of all scenarios, and the main search strategies can be found in [27]. Since it is impossible to do scans over the whole multi-dimensional parameter space, a few benchmark scenarios were developed for each model, and many detailed studies were performed in ATLAS to estimate the sensitivity to Supersymmetry. The main conclusion is that regardless of the model, SUSY will easily be discovered at the LHC with just a few amount of data.

There are a lot of other extensions to the Standard Model to which ATLAS is sensitive. Technicolor [29] provides breaking of electroweak symmetry without the need of the Higgs sector, it can still generate masses for fermions and gauge bosons. Other phenomena are mentioned here as keywords only, with more details to be found, again, in the TDR. There are: compositeness, excited quarks and leptons, leptoquarks, new gauge bosons, majorana neutrinos, extra dimensions, monopoles, and black holes.

5.6 Searches for Higgs bosons at the LHC

This section reports how Higgs bosons can be discovered with ATLAS in the framework of the Standard Model and of the Minimal Supersymmetric Standard Model, MSSM.

5.6.1 The Standard Model Higgs boson

At the LHC there are four important production mechanisms for the Standard Model Higgs boson, whose cross sections are shown in Figure 5.2:

- Gluon-gluon-fusion (Figure 5.1a): The Higgs boson is produced in the fusion of two gluons via a heavy-quark loop. The loop is dominated by top quarks. This production mode has by far the largest cross section over the allowed mass range of the Higgs boson. Higher order QCD corrections are significant, *e.g.*, $\mathrm{gg} \rightarrow \mathrm{H(g)}$, $\mathrm{gq} \rightarrow \mathrm{Hq}$, $\mathrm{q\bar{q}} \rightarrow \mathrm{Hg}$. Including next-to-leading order calculations, the cross section is enhanced by $\approx 50\%$.
- Vector-boson-fusion (Figure 5.1b): The Higgs boson production proceeds via fusion of two $\mathrm{W}^{\pm}$ or Z^0 bosons which were radiated off incident quarks. The quarks can be detected as jets in the forward direction at large values of pseudorapidity. This is the process with second largest cross section. It is about one order of magnitude smaller than gluon fusion in the low Higgs mass region and becomes comparable for $m_{\mathrm{H}^0} > 800$ GeV.
- Associated production $\mathrm{W}^{\pm}\mathrm{H}^0$, $\mathrm{Z}^0\mathrm{H}^0$ (Figure 5.1c): The cross section for the process where the Higgs boson is radiated off a $\mathrm{W}^{\pm}$ or a Z^0 boson falls rapidly with increasing m_{H^0}. For $m_{\mathrm{H}^0} = 150$ GeV the cross section of $\mathrm{W}^{\pm}\mathrm{H}^0$ production is $\approx 1/20$ of that for gluon fusion. However, this mode is of interest in the intermediate mass range $m_{\mathrm{H}^0} < 2m_{\mathrm{Z}^0}$.
- Associated production $\mathrm{t\bar{t}H}^0$ (Figure 5.1d): The production rate of the Higgs boson in association with a pair of top quarks has a cross section about five times smaller than $\mathrm{W}^{\pm}\mathrm{H}^0$ production for $m_{\mathrm{H}^0} < 200$ GeV and becomes competitive for $m_{\mathrm{H}^0} > 500$ GeV. For light Higgs bosons, $\mathrm{t\bar{t}H}^0$ production is expected to be the only mode where the decay $\mathrm{H}^0 \rightarrow \mathrm{b\bar{b}}$ is observable.

The Standard Model Higgs boson can be discovered at the LHC in the whole mass range between the LEP 2 limit (114.4 GeV) and theoretical upper bounds (≈ 1 TeV) after a few years of data taking. Expected significances for the discovery in various search channels

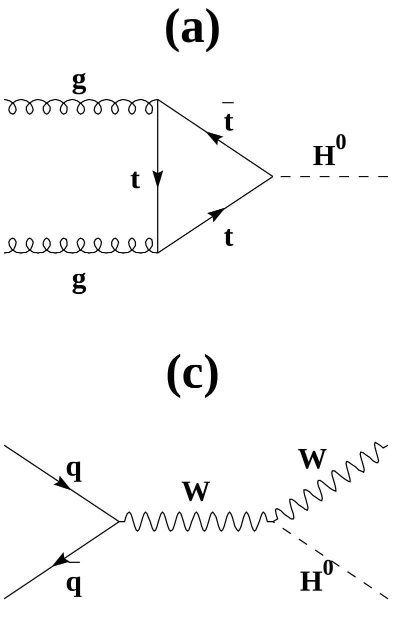

Figure 5.1: Higgs boson production at the LHC: Dominant diagrams in leading order.

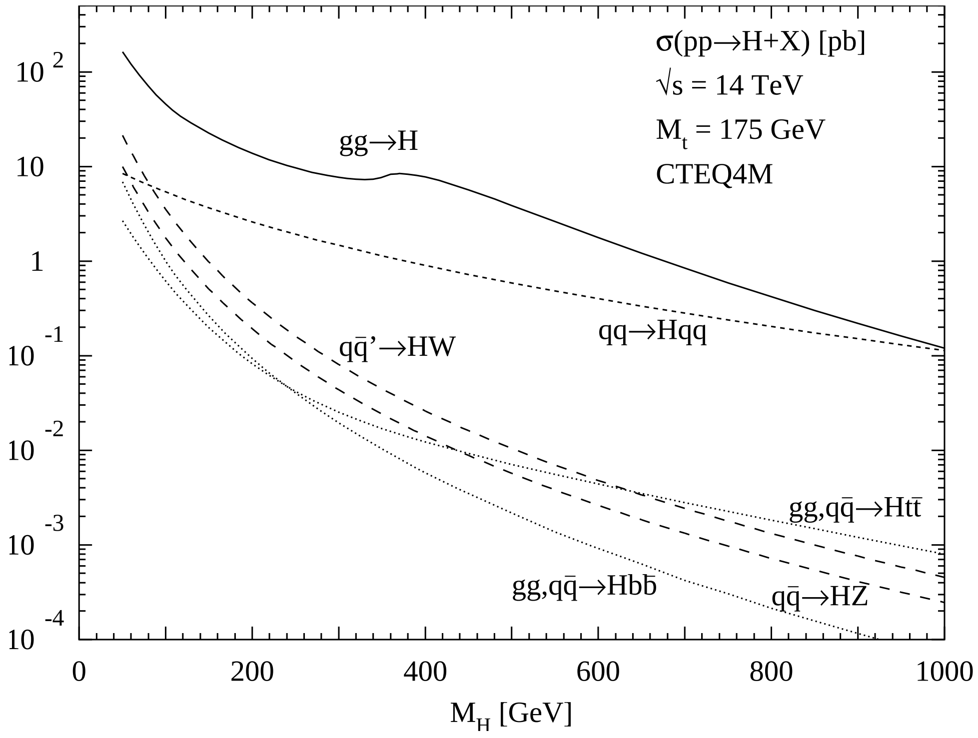

Figure 5.2: Cross sections for Standard Model Higgs boson production at the LHC [30].

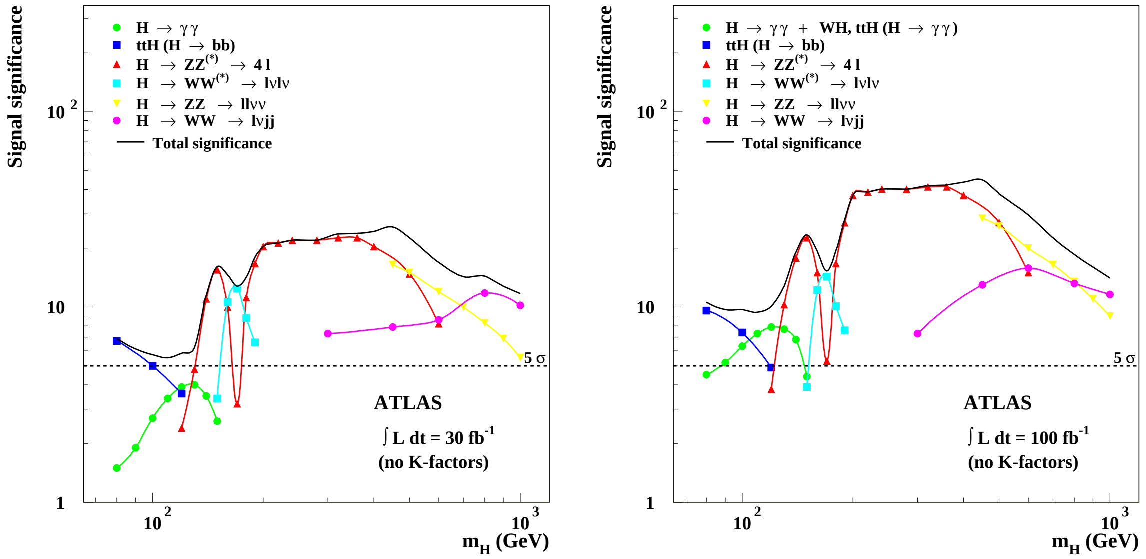

Figure 5.3: ATLAS discovery potential for the Standard Model Higgs boson with 30 fb^{-1} (left) and 100 fb^{-1} (right) as of 1999 [27].

are displayed in Figure 5.3. Typically several production channels and decay modes must be analyzed to establish a signal over usually large backgrounds. The following sections present the search strategies for a Standard Model Higgs boson H^0 at the LHC. Many of these analyses are detailed in Ref. [27].

110 GeV $< m_{\mathrm{H}^0} <$ 130 GeV

The low mass region is difficult, and several channels must be combined to guarantee discovery of the Higgs boson. The dominant decay mode is $\mathrm{H}^0 \to \mathrm{b}\bar{\mathrm{b}}$, but there is no trigger for dijet final states which would be needed to detect the direct production $\mathrm{gg} \to \mathrm{H}^0 \to \mathrm{b}\bar{\mathrm{b}}$. Moreover, it would be impossible in the gluon fusion to extract the signal from huge QCD backgrounds. A trigger is needed, *e.g.*, isolated leptons. They are provided by processes containing $\mathrm{W}^\pm$ or Z^0 bosons, *e.g.*, $\mathrm{W}^\pm\mathrm{H}^0$, $\mathrm{Z}^0\mathrm{H}^0$ and $\mathrm{t}\bar{\mathrm{t}}\mathrm{H}^0$ production. The channels $\mathrm{WH}^0 \to \ell\nu\mathrm{b}\bar{\mathrm{b}}$ and $\mathrm{Z}^0\mathrm{H}^0 \to \ell^+\ell^-\mathrm{b}\bar{\mathrm{b}}$ were studied in [27] with updates in [31]. It was found that they suffer from large $\mathrm{W}^\pm$+jets and Z^0+jets backgrounds, and the signal significance is below two standard deviations with an integrated luminosity of 30 fb^{-1}. More promising is $\mathrm{t}\bar{\mathrm{t}}\mathrm{H}^0$ production in the final state $\ell\nu\mathrm{b}$ jjb $\mathrm{b}\bar{\mathrm{b}}$. Despite the smaller cross section, tagging of four b-jets helps to reduce backgrounds from $\mathrm{t}\bar{\mathrm{t}}$+jets, $\mathrm{W}^\pm$+jets, and Z^0+jets.

The rare decay $\mathrm{H}^0 \to \gamma\gamma$ offers another possibility to look for the Higgs boson. The branching fraction into two photons is in the order of only 10^{-3}, but thanks to the clean and unique signature it can be observed in direct Higgs boson production via gluon fusion. The existence of the Higgs boson is visible in the di-photon mass spectrum as a narrow peak on top of a large but well controlled background. This channel needs good energy and angular resolution of the electromagnetic calorimeters and good photon identification with small fake rates of electrons and jets. Significances between three and four standard deviations in the range 110 GeV $< m_{\mathrm{H}^0} <$ 140 GeV are expected for 30 fb^{-1}.

The most promising channel in the mass region up to $m_{\mathrm{H}^0} =$ 180 GeV is the production of the Higgs boson in the fusion of two gauge bosons, $\mathrm{W}^\pm$ or Z^0. This production mode is characterized by two opposite, high-p_T jets in the forward region and little jet activity in the central region. The principle decay modes in this channel are $\mathrm{H}^0 \rightarrow \tau^+\tau^- \rightarrow \ell\nu\nu\ell\nu\nu$, $\mathrm{H}^0 \rightarrow \tau^+\tau^- \rightarrow \ell\nu\nu\mathrm{h}\nu$, $\mathrm{H}^0 \rightarrow \mathrm{W}^+\mathrm{W}^- \rightarrow \ell\nu\ell\nu$, and $\mathrm{H}^0 \rightarrow \mathrm{W}^+\mathrm{W}^- \rightarrow \ell\nu\mathrm{jj}$ [32].

130 GeV $< m_{\mathrm{H}^0} <$ 180 GeV

The intermediate mass range is covered by vector-boson-fusion with $\mathrm{H}^0 \rightarrow \mathrm{W}^+\mathrm{W}^-$ and direct production with subsequent decays $\mathrm{H}^0 \rightarrow \mathrm{ZZ}^*$ and $\mathrm{H}^0 \rightarrow \mathrm{WW}^*$. Useful final states are $\mathrm{ZZ}^* \rightarrow 4\ell$ and $\mathrm{WW}^* \rightarrow \ell\nu\ell\nu$, the leptons being electrons or muons. The decay $\mathrm{H}^0 \rightarrow \mathrm{WW}^*$ has larger branching fraction but is more difficult to detect because of the two neutrinos occurring in the decay of the W bosons, and only transverse masses can be reconstructed. Significances way above five standard deviations for 30 fb^{-1} are expected if both channels are combined.

180 GeV $< m_{\mathrm{H}^0} <$ 1 TeV

If the Higgs boson mass is large enough to allow for the decay into a pair of on-shell Z^0 bosons, the mode $\mathrm{gg} \rightarrow \mathrm{H}^0 \rightarrow \mathrm{Z}^0\mathrm{Z}^0 \rightarrow 4\ell$ is the 'golden channel' to discover the Standard Model Higgs boson at the LHC. The signature of four isolated, high-p_T leptons is straightforward to identify. The signal-to-background ratio is larger than one, and the significance is larger than 10 in the range 180 GeV $< m_{\mathrm{H}^0} <$ 500 GeV. It will be possible to observe the Higgs boson in this channel up to a mass of 800 GeV. The width of the Higgs boson increases rapidly with higher masses, and it dominates the experimental resolution for $m_{\mathrm{H}^0} >$ 300 GeV.

For Higgs boson masses above 800 GeV the signal rate is too small to be observed in the four lepton final state. Decay modes with larger branching fraction must be used, but they are more difficult to separate from the background, *e.g.*, the $\mathrm{H}^0 \rightarrow \mathrm{Z}^0\mathrm{Z}^0 \rightarrow \ell\ell\nu\nu$ mode has a rate six times larger than the four-lepton mode, $\mathrm{H}^0 \rightarrow \mathrm{W}^+\mathrm{W}^- \rightarrow \ell\nu\mathrm{jj}$ has a rate 150 times larger and $\mathrm{H}^0 \rightarrow \mathrm{Z}^0\mathrm{Z}^0 \rightarrow \ell\ell\mathrm{jj}$ has a rate 25 times larger. Excellent detector performance to reconstruct missing transverse energy and $\mathrm{W}^\pm/\mathrm{Z}^0 \rightarrow \mathrm{jj}$ decays is mandatory to reject the large QCD background.

At those high masses the production of the Higgs boson via fusion of two gauge bosons becomes important and contributes to the discovery potential for heavy Higgs bosons.

Results from most recent sensitivity studies in the range $m_{\mathrm{H}^0} <$ 200 GeV [32] for an integrated luminosity of 30 fb^{-1} are shown in Figure 5.4. With 30 fb^{-1} the Higgs boson can be discovered with a statistical significance much larger than five standard deviations in the mass range from 110 GeV to 200 GeV. Typically, at least two channels contribute to the discovery which provides robustness and the possibility of cross checks between channels. The most difficult regime is the low mass region. Several channels with either small branching ratio or complicated final states must be combined to claim discovery.

5.6.2 Properties of the Higgs boson

Proofing whether there is a signal from a Higgs boson is the first duty of the LHC experiments. Once this has succeeded, more detailed investigations about the characteristics of the new particle must be started. Its mass, CP-quantum number, decay width, production rate, and branching ratios will be studied. High statistics are needed for a precise determination of these parameters and so most of the studies must be performed in the high luminosity phase in order to reach the desired accuracy.

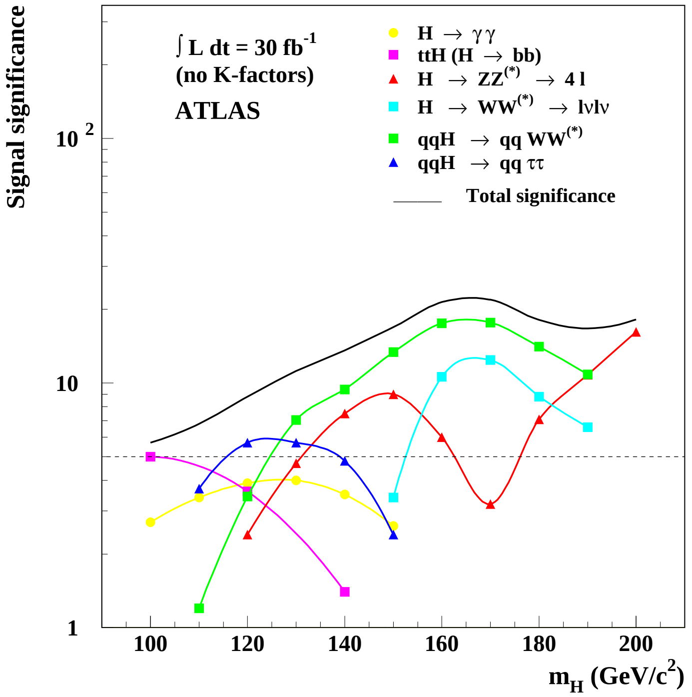

Figure 5.4: ATLAS sensitivity for the discovery of a Standard Model Higgs boson in the low mass and intermediated range as of spring 2003.

The expected precision $\Delta m_{H^0}/m_{H^0}$, combining CMS and ATLAS, is shown in Figure 5.5 for an integrated luminosity of 300 fb^{-1} per experiment. Over almost the entire mass range the precision is dominated by the $H^0 \rightarrow ZZ^{(*)} \rightarrow 4\ell$ channel and is in the order of 10^{-3} up to a Higgs mass of 400 GeV. Above this value the precision decreases due to the increasing decay width and is in the order of 10^{-2} for $m_{H^0} = 800$ GeV. To reach this goal, the absolute energy scale must be know to 0.1%. The ATLAS goal is to determine the lepton energy scale to even 0.02%.

Direct measurement of the width of the Higgs boson is possible for $m_{H^0} > 200$ GeV, when the decay width becomes comparable to or larger than the detector mass resolution. Figure 5.6 shows that a precision of the order of 6% can be reached with 300 fb^{-1} in the range 300 GeV $< m_{H^0} <$ 700 GeV.

The coupling of the Higgs boson to other particles determines the production rate and decay ratios. The Standard Model can be disentangled from other models by verifying that the production and decay rates are consistent with the model expectations. However, depending on the parameters, other models may mimic the Standard Model, and deviations may arise only at energies beyond the range of the LHC. The relative precision of the production modes times branching ratios is displayed in Figure 5.7 for the low and intermediate mass range. Assuming a 10% systematic uncertainty, the average accuracy is about 20%.

The coupling of the Higgs boson to fermions and bosons can be extracted from the study of production rates times branching ratios. Without further theoretical input it is only possible to measure relative couplings for different channels. The advantage is that some systematic uncertainties, such as errors on the luminosity, cancel in the ratios. Figure 5.8 shows the expected accuracies for the coupling to bosons and fermions.

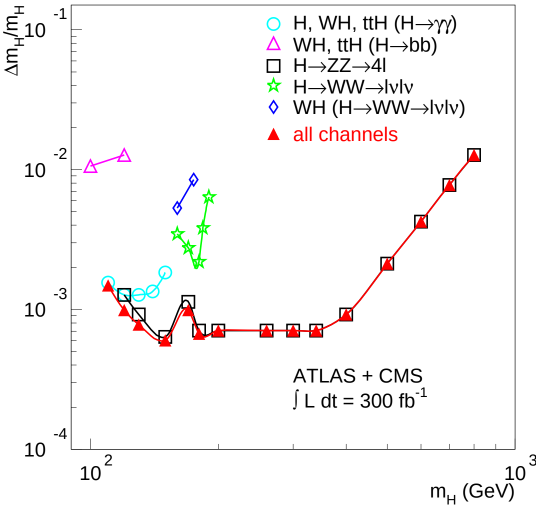

Figure 5.5: Relative precision on the measured Higgs boson mass as a function of m_{H^0} from the combination of CMS and ATLAS with an integrated luminosity of 300 fb^{-1} each.

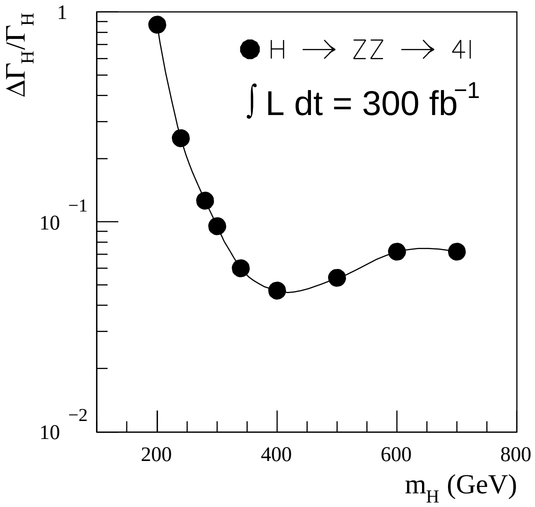

Figure 5.6: Relative precision on the measured Higgs boson width as a function of m_{H^0} from the combination of CMS and ATLAS with an integrated luminosity of 300 fb^{-1} each.

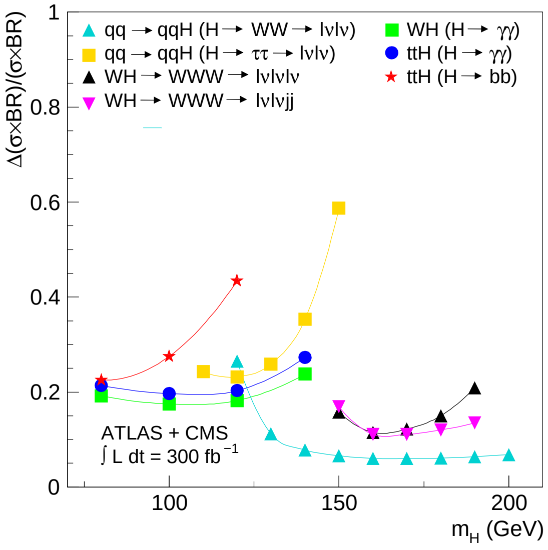

Figure 5.7: Relative precision on the measured Higgs boson production rates as a function of m_{H^0} from the combination of CMS and ATLAS with an integrated luminosity of 300 fb^{-1} each.

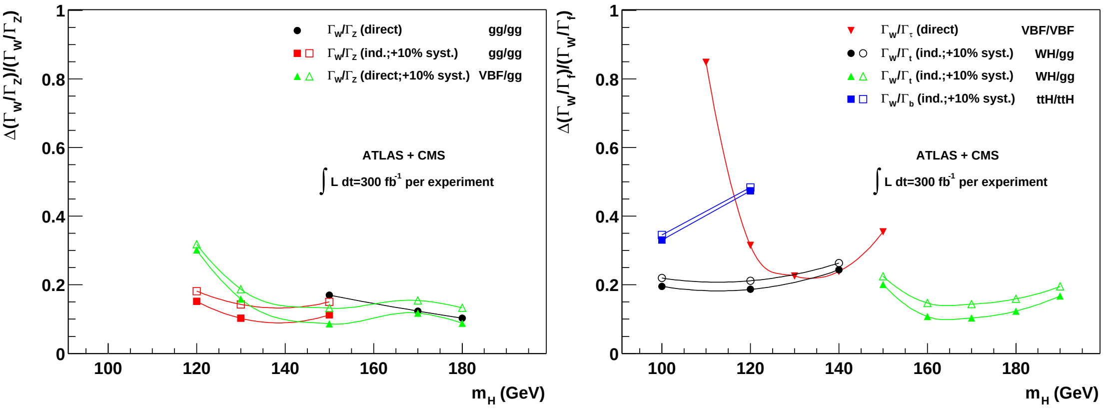

Figure 5.8: Relative precision on the measured Higgs boson couplings as a function of m_{H^0} from the combination of CMS and ATLAS with an integrated luminosity of 300 fb^{-1} each. Left: coupling to the Z^0 boson, right: coupling to fermions.

5.6.3 The Minimal Supersymmetric Standard Model

The MSSM opens up many new search channels for Higgs bosons. There are three neutral states h^0, H^0, and A^0 and two charged states H^+ and H^-. In general, the h^0 is similar to the Standard Model Higgs boson. Besides Standard Model-like production and decay channels of the neutral Higgs bosons, one has to take into account new decay modes such as the decay of $\mathrm{A}^0/\mathrm{H}^0$ into $\mathrm{Z}^0\mathrm{h}^0$ or $\mathrm{h}^0\mathrm{h}^0$, and decays of the charged Higgs bosons. The couplings depend on the parameters $\tan\beta$ and m_{A^0} (on Born level), and thus many final states must be analyzed to guarantee discovery of the MSSM Higgs bosons. The spectrum of channels studied in ATLAS is rich and includes:

- h^0, H^0, $\mathrm{A}^0 \to \gamma\gamma$ in direct and associated production with a $\mathrm{W}^\pm$ boson or a pair of top quarks,
- $\mathrm{h}^0 \to \mathrm{b}\bar{\mathrm{b}}$ in association with $\mathrm{t}\bar{\mathrm{t}}$,
- h^0, $\mathrm{H}^0 \to \mathrm{ZZ}^{(*)} \to 4\ell$,
- $\mathrm{H}^0, \mathrm{A}^0 \to \tau^+\tau^-$ (in $\mathrm{b}\bar{\mathrm{b}}\mathrm{H}^0/\mathrm{A}^0$ production) and $\mathrm{t}\bar{\mathrm{t}}$, which is enhanced for large parts of the parameter space because the HZZ and HWW couplings are suppressed and even absent for A^0,
- $\mathrm{b}\bar{\mathrm{b}}\mathrm{H}^0$ and $\mathrm{b}\bar{\mathrm{b}}\mathrm{A}^0$, which is enhanced at large $\tan\beta$, followed by H^0, $\mathrm{A}^0 \to \tau^+\tau^-, \mu^+\mu^-$ or $\mathrm{b}\bar{\mathrm{b}}$, depending on the model parameters,
- $\mathrm{H}^0 \to \mathrm{h}^0\mathrm{h}^0$ with $\mathrm{h}^0\mathrm{h}^0 \to \mathrm{b}\bar{\mathrm{b}}\mathrm{b}\bar{\mathrm{b}}, \mathrm{b}\bar{\mathrm{b}}\gamma\gamma$ and $\mathrm{A}^0 \to \mathrm{Z}^0\mathrm{h}^0$ with $\mathrm{Z}^0\mathrm{h}^0 \to \mathrm{b}\bar{\mathrm{b}}\mathrm{b}\bar{\mathrm{b}}$, $\ell^+\ell^-\mathrm{b}\bar{\mathrm{b}}$, $\ell^+\ell^-\gamma\gamma$,
- $\mathrm{H}^\pm \to \tau\nu, \mathrm{tb}, \mathrm{cs}, \mathrm{cb}, \mathrm{h}^0/\mathrm{A}^0\mathrm{W}^{\pm *}, bt^*$, where the charged Higgs boson is produced in the decay $\mathrm{t} \to \mathrm{H}^+\mathrm{b}$ or in $\mathrm{pp} \to \mathrm{tH}^\pm$ and $\mathrm{pp} \to \mathrm{tbH}^\pm$.

For purely hadronic final states (*e.g.*, $\mathrm{b}\bar{\mathrm{b}}\mathrm{H}^0/\mathrm{A}^0 \to \mathrm{b}\bar{\mathrm{b}}\mathrm{b}\bar{\mathrm{b}}$) very high jet-$p_T$ thresholds must be set.

The predicted sensitivity to MSSM Higgs bosons is shown in Figure 5.9 as discovery contours in the $(\tan\beta, m_{\mathrm{A}^0})$-plane of the Maximal Mixing Scenario [26], assuming 300 fb^{-1} and using analyses as of autumn 2001. The left-hand figure shows the regions in which

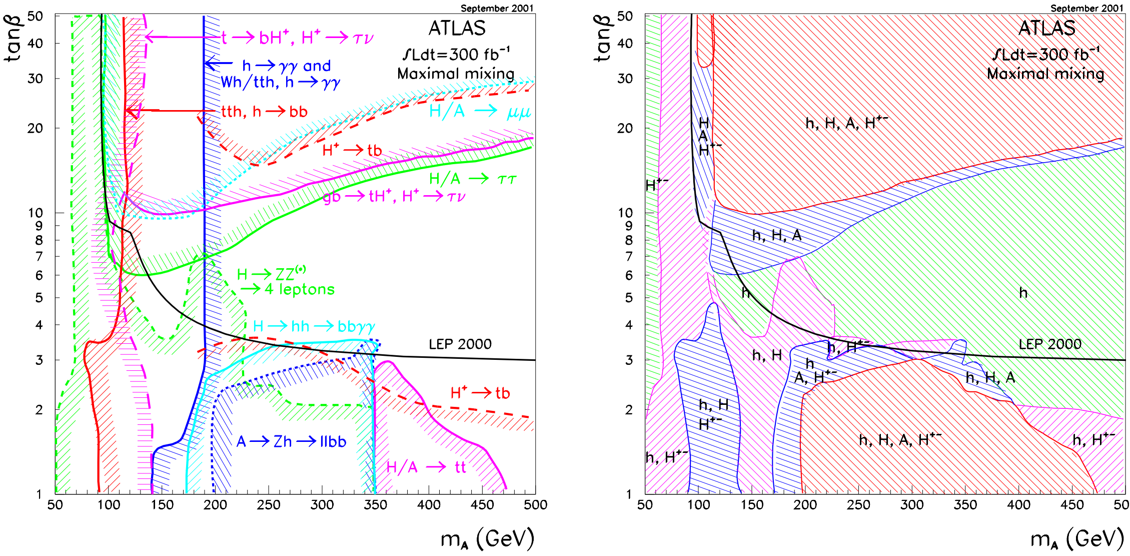

Figure 5.9: ATLAS sensitivity for the discovery of MSSM Higgs bosons in the Maximal Mixing Scenario. Values below the black curve are excluded by the LEP experiments at the 95% confidence level. Left: observability of different production and decay channels. Right: observability of different MSSM Higgs bosons.

different production and decay modes can be observed. Some modes are already excluded by limits from the LEP experiments. Other modes are very powerful and can be discovered in large areas of the parameter space, *e.g.*, $H^0/A^0 \to \tau^+\tau^-$, $t\bar{t}h^0$ with $h^0 \to b\bar{b}$, and the $h^0 \to \gamma\gamma$ channels. The right-hand figure demonstrates that with 300 fb^{-1} at least one MSSM Higgs boson can be discovered, regardless of the parameter values, and in most areas at least two Higgs bosons are observable. Updated MSSM scans, which include results from this thesis, are discussed in Section 13.3.

6 The Large Hadron Collider

The Large Hadron Collider (LHC) is a proton-proton collider currently under construction at CERN. It is being built into the tunnel of the former LEP accelerator. The LHC will accelerate two beams of protons in opposite directions in a 27 km long ring up to a beam energy of 7 TeV. Operation with heavy ions is foreseen as well. The beams, each containing about 3×10^{14} protons, are brought to collisions at four interaction points. The design luminosity is 10^{34} $\mathrm{cm}^{-2}\mathrm{s}^{-1}$. To keep the particles on track, the LHC will be equipped with high-field superconducting NbTi dipole magnets (up to 8.34 T), which are operated in superfluid helium. The main parameters of the LHC are listed in Table 6.1.

The LHC will benefit from existing accelerator facilities at CERN, namely the LINAC, the BOOSTER, the PROTON SYNCHROTRON, and the SUPER PROTON SYNCHROTRON, Figure 6.1. The protons are obtained from a hydrogen source, and they are pre-accelerated in the LINAC to energies of 50 MeV. Then they enter the BOOSTER which increases the energy to 1.4 GeV. Successive acceleration of the protons takes place in the PS and SPS to energies of 25 GeV and 450 GeV, before they are injected into the LHC.

The particles are accelerated by an RF system which operates at a temperature of 4.5 K and at 400.8 MHz, the second harmonic of the SPS frequency. Superconduction cavities are used which are sputtered with a thin film of niobium. The design voltage of the RF system is 16 MV per beam, providing an average bunch length of 7.5 cm. The bunch spacing is 25 ns, *i.e.* ten RF periods.

Since two beams of particles with same charge must be accelerated in opposite directions, two independent magnetic channels are needed. However, they will be housed in the same yoke and cryostat system. A cross-sectional view on the LHC dipole system located inside the cryogenic system is shown in Figure 6.2. The magnet coils are made of copper-clad niobium-titanium cables. They are operated at 1.9 K with a current of 15 000 A, and have to withstand forces of some hundred tons per meter during ramping of the magnetic field. There will be 1 232 main dipoles and 392 main quadrupoles, the latter producing gradients of 233 T/m. In case of quenches the stored energy must safely be released from

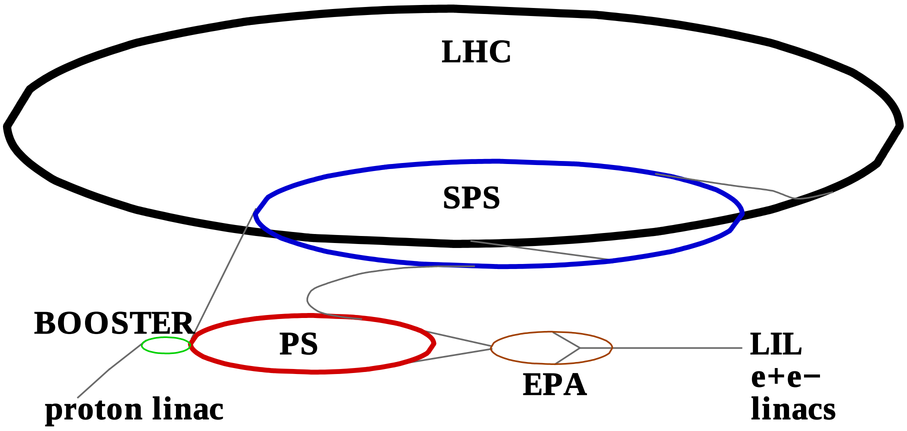

Figure 6.1: The accelerator system of the LHC.

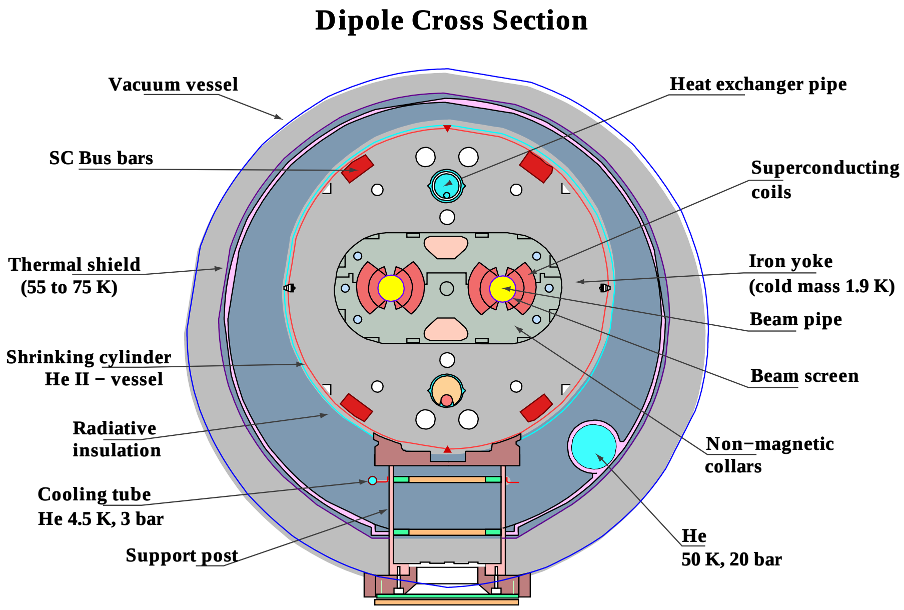

Figure 6.2: View on a dipole system of the LHC.

the magnets. The energy is absorbed by resistors which can be switched into the circuit, heating eight tons of steel to about 300 °C.

The LHC is the first accelerator with a vacuum system at cryogenic temperature, so that a number of novel design requirements must be fulfilled. For instance, precaution must be taken to protect the cryogenic system from 0.2 W/m of synchrotron radiation per beam.

Table 6.1: Main parameters of the LHC.

Quantity	Value	Unit
Energy at collision	7	TeV
Energy at injection	0.45	TeV
Circumference	26 658	m
Dipole field at 7 TeV	8.34	T
Luminosity	10^{34}	$\mathrm{cm}^{-2}\mathrm{s}^{-1}$
Luminosity lifetime	10	h
Protons per bunch	1.1×10^{11}	
Bunches per beam	2 808	
Nominal bunch spacing	25	ns
Distance between beams (arc)	194	mm
DC beam current	0.56	A
Energy loss per turn/proton/7 GeV	6.7	keV
Radiated power per beam/7 TeV	3.8	kW
Stored energy per beam/7 TeV	350	MJ
Stored energy in magnets/7 TeV	11	GJ

7 The ATLAS detector at the LHC

The ATLAS detector is one of the four detectors at the LHC. The name is an acronym for 'A Toroidal LHC ApparatuS'. ATLAS, like CMS [33], is an omni purpose detector, designed to explore the full physics program of the LHC. The two experiments LHCb [34] and ALICE [35] will focus on more specific topics, *i.e.*, b-physics and heavy ion collisions.

7.1 Introduction

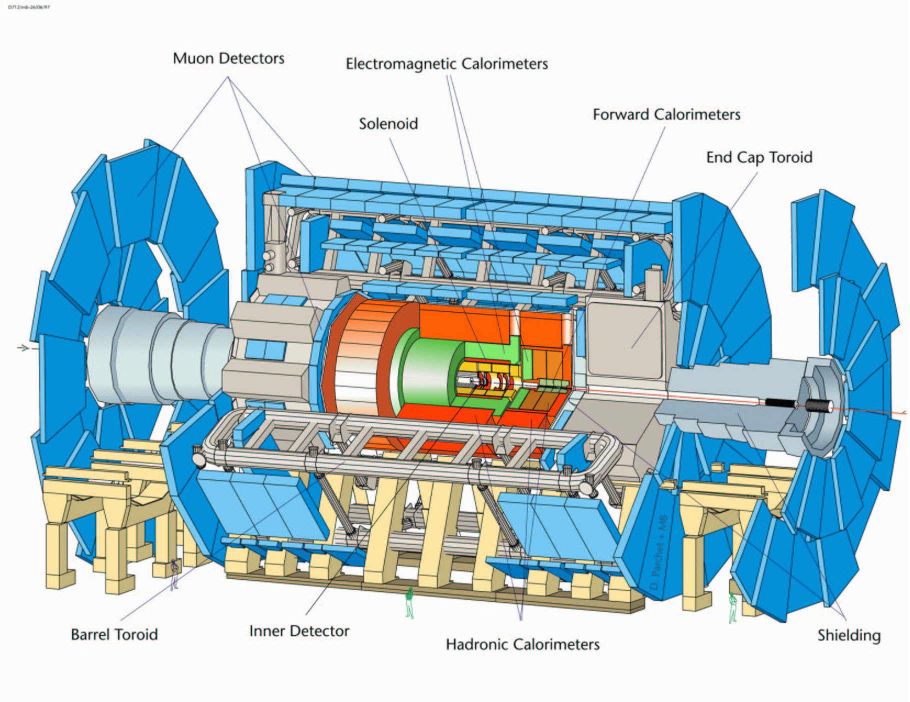

Figure 7.1: The ATLAS detector.

A sketch of the ATLAS detector is shown in Figure 7.1. The detector has cylindrical symmetry with a height (diameter) of 22 m, a length of 42 m, and a weight of almost 7 000 tons.

The parameters of the LHC and the challenging physics program put high demands on the components of ATLAS: A powerful tracking system is needed which can resolve even low p_T tracks in the dense environment expected at design luminosity, hermetic calorimeters with very good energy resolution for electrons and photons, and a precise spectrometer for measuring the momenta of muons. ATLAS will have a large acceptance in pseudorapidity. After a brief description of the coordinate system used in ATLAS, the detector sub-systems are described in more detail.

The coordinate system

A cylindrical system like the ATLAS detector is naturally described by cylinder coordinates (R, ϕ, z), where R is the radius, ϕ the azimuthal angle and z the coordinate along the cylinder axis. However, at hadron colliders, a more useful and common description of highly relativistic particles uses transverse momentum p_T, pseudorapidity η, and azimuth ϕ. The pseudorapidity is related to the angle θ between a particle and the z-axis by Equation (7.1),

$$\eta = -\ln\left(\tan\left(\theta/2\right)\right). \tag{7.1}$$

The trajectory of charged particles inside the uniform solenoid field of ATLAS is described by five helix parameters. Three of these describe the velocity vector at the point of closest approach (p.c.a) of the track to the primary vertex. The remaining two parameters, d_0 and z_0, are the transverse and longitudinal coordinates of the p.c.a.

7.2 The Inner Detector

The Inner Detector (ID) reconstructs tracks of charged particles and measures their momentum (above 0.5 GeV) from the track's curvature in the magnetic solenoid field of 2 T. The ID is contained inside a cylinder of 7 m length and radius 1.15 m, covering an acceptance of $|\eta| < 2.5$, and consists of three parts: A high resolution Pixel Detector with 123 million read-out channels, a microstrip Semi Conductor Tracker (SCT) with 6.2 million channels, and a Transition Radiation Tracker (TRT) made of straw tubes with 420 000 channels.

The concept was chosen to meet the demands of high-precision measurements of momentum and the reconstruction of vertices in an environment with a large track density. The performance of the Inner Detector is important for the $\mathrm{t\bar{t}H^0}$, $\mathrm{H^0 \rightarrow b\bar{b}}$ channel because the reconstructed tracks provide information about secondary vertices expected from jets with b-quarks. The silicon detectors provide only a small number of space points per track (three in the PIXEL and four in the SCT), but they are precisely known. More layers would result in too much material and high costs. The TRT provides on average 36 points for tracks in $|\eta| < 2.5$ with much less material involved as in the silicon detectors and at lower costs.

The characteristics of the Inner Detector components are listed in Table 7.1.

7.2.1 Pixel detector

The pixel detector measures tracks precisely and as close to the beam pipe as possible. This helps to identify tracks originating from secondary vertices, which is needed to tag jets with B-hadrons.

The pixel detector is made of 1 500 barrel and 700 disk modules, each of which contains 61 440 pixel elements. A pixel covers an area of $400 \times 50\mathrm{m}^2$.

The detector consists of three layers of modules, which are arranged as shown in Figure 7.2, right. The innermost layer (B-layer) is located at a radius of 5.05 cm, Layer 1 at 8.85 cm, and Layer 2 at 12.25 cm. The thickness of each layer corresponds to about 1.7% of a radiation length. On each side of the barrel pixel modules, there are three disks with pixel modules. They are located at $z = 49.5$ cm, $z = 58.0$ cm, and $z = 65.0$ cm.

The silicon sensor on a module is read out by 16 chips, each of which processes information from 24×160 pixels. A pixel cell acts as a diode. If a charged particle traverses the material, it creates ionization charges in the substrate which are then collected at the edges by an electric field.

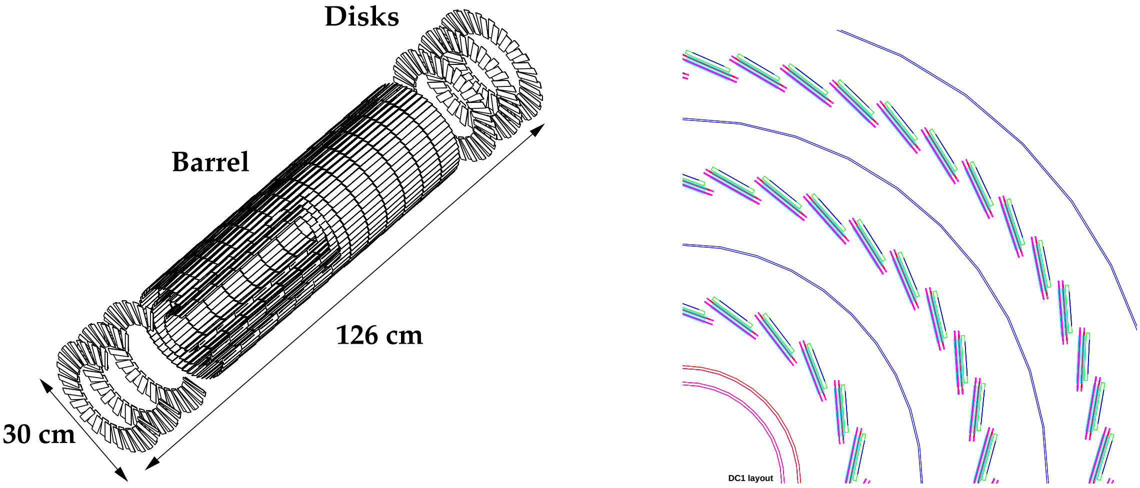

Figure 7.2: Left: 3D view on the pixel detector, right: transverse view on a quarter of the pixel barrel.

7.2.2 Semiconductor tracker

The Semi Conductor Tracker (SCT) is comprised of silicon microstrip modules, and provides four measurements per track in the barrel region. Each silicon detector covers $6.36 \times 6.40\ \text{cm}^2$, segmented into 768 strips with a pitch of 80 µm. There are four single-sided silicon detectors on each module. On each side, two detectors are wire-bonded together to form 12.8 cm long strips. Then two such systems are arranged back-to-back at a 40 mrad stereo angle in order to allow for determination of the z coordinate of tracks.

In the barrel the SCT is arranged in four double-layers at radii between 30 cm and 52 cm. They are complemented by nine disks at each side of the barrel to allow for measurement of tracks at large η. The layout of the SCT is shown in Figure 7.3.

7.2.3 Transition radiation tracker

The transition radiation tracker (TRT) provides a large number of measurements per track (36 on average). It is build from straw tube detectors with diameters of 4 mm and maximal length of 144 cm in the barrel. The tubes are filled with a gas mixture of 70% Xe, 20% CO_2, and 10% CF_4 with a total volume of $3\ \text{m}^3$. The sensitive element is a 30 m gold-plated W-Re wire at the center of the straws. The barrel contains about 50 000 straws arranged in three rings with a total of 73 layers and grouped in modules with 329 to 793 axial straws, covering radii from 56 to 107 cm.

The two end-caps each consist of 18 wheels which are grouped into wheel ‘A’ (6 disks), wheel ‘B’ (8 disks), and wheel ‘C’ (4 disks). The TRT layout is displayed in Figure 7.4.

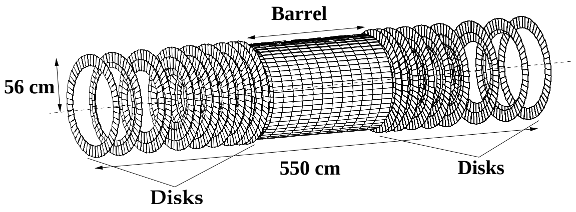

Figure 7.3: The silicon strip detector.

Table 7.1: Characteristics of the Inner Detector. Typical resolutions are quoted.

System	Position	Area (m^2)	Typ. resolution $\sigma(\mu\mathrm{m})$	Channels (10^6)	η coverage
Pixels	1 removable barrel layer	0.2	$R\phi = 12, z = 66$	16	±2.5
	2 removable barrel layers	1.4	$R\phi = 12, z = 66$	81	±1.7
	3 end-cap disks (each side)	0.4	$R\phi = 12, z = 77$	26	±1.7–2.5
SCT	4 barrel layers	34.4	$R\phi = 16, z = 580$	3.2	±1.4
	9 end-cap wheels (each side)	26.7	$R\phi = 16, z = 580$	3.0	1.4–2.5
TRT	Axial barrel straws		170 per straw	0.1	±0.7
	Radial end-cap straws		170 per straw	0.32	0.7–2.5

7.3 The Calorimeters

The calorimeters primarily provide energy measurement of electrons, photons, jets, and missing energy. They also give information about position and angle, and particle identification. There are three types of detectors: An electromagnetic calorimeter covering the region $|\eta| < 3.2$, hadronic calorimeters in the barrel, $|\eta| < 1.7$, and in the end-caps, $1.5 < |\eta| < 3.2$, and forward calorimeters covering $3.1 < |\eta| < 4.9$. Hermetic calorimetry and very good energy resolution for electrons and photons is essential for many searches, *e.g.*, for signatures of supersymmetry and for the Higgs boson discovery channels $\mathrm{H} \rightarrow \gamma\gamma$ and $\mathrm{H} \rightarrow \mathrm{ZZ}^* \rightarrow \mathrm{eeee}$. Figure 7.5 shows a view on the calorimeter system. More detailed descriptions of the different parts are given in the following sections.

7.3.1 Electromagnetic calorimeter

The electromagnetic calorimeter (EM) consists of liquid argon (LAr) as active material with an accordion-like structure of Kapton electrodes and lead as absorber. Incoming electrons lose energy in the lead absorbers and emit bremsstrahlung photons. Photons

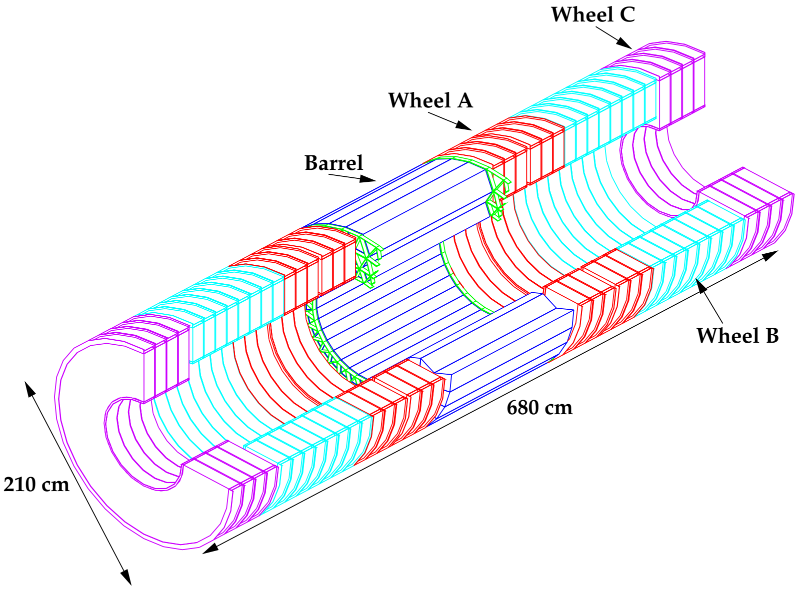

Figure 7.4: The transition radiation tracker.

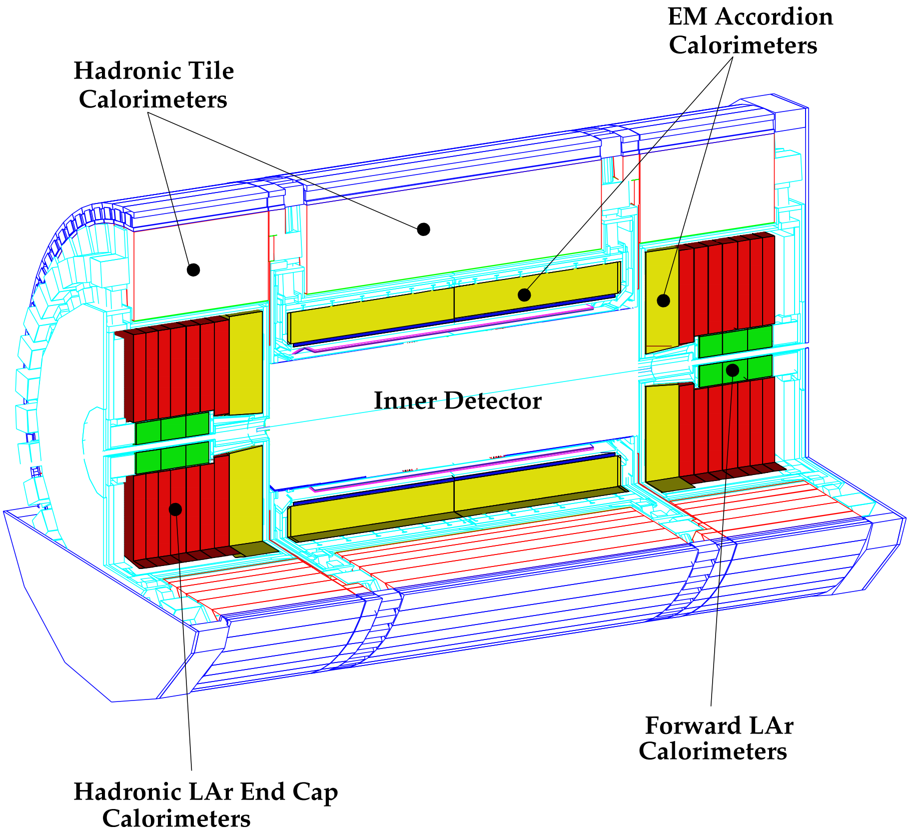

Figure 7.5: The calorimeter system.

convert into electron-positron pairs, and in this way a shower cascade is initiated. The secondary particles ionize the liquid argon. Free electrons from the ionization are drawn off to electrodes by a high-voltage field. The calorimeter is divided into several samplings, each has varying granularity in η and ϕ, depending on the range in pseudorapidity. The number of read-out channels is $\sim 190\,000$. The total radiation length is larger than 24 X_0 in the barrel and larger than 26 X_0 in the end-caps.

When particles enter the EM calorimeter they already penetrated through the Inner Detector, the superconducting coil, and the cryostat which corresponds to a thickness of 2.3 X_0 (for $\eta = 0$). To correct for the energy loss, a presampler precedes the EM calorimeter over the range $|\eta| < 1.8$. The presampler consists of a LAr layer of thickness 1.1 cm in the barrel and 0.5 cm in the end-caps. In the transition region between the barrel and end-cap cryostat the equivalent material is $\sim$ 7 X_0. In this region ($1.0 < |\eta| < 1.6$) a scintillator slab complements the presampler.

Coverage, granularity, and segmentation of the EM calorimetry and the presampler are listed in Table 7.2. The design goal for the energy resolution is:

$$\frac{\sigma_E}{E} = \frac{0.1}{\sqrt{E}} \oplus \frac{0.3}{E} \oplus 0.01.$$

7.3.2 Hadronic calorimeters

Hadronic calorimeters are needed to measure the energy of jets and hadronic particles in cooperation with the electromagnetic calorimeters. The system consists of a central

Table 7.2: Pseudorapidity coverage, granularity, and longitudinal segmentation of the electromagnetic calorimeter and the presampler.

EM calorimeter	Barrel	End-cap	
Coverage	$\lvert\eta\rvert < 1.475$	$1.375 < \lvert\eta\rvert < 3.2$	
Longitud. segm.	3 samplings	3 samplings	$1.5 < \lvert\eta\rvert < 2.5$
		2 samplings	$1.375 < \lvert\eta\rvert < 1.5$
			$2.5 < \lvert\eta\rvert < 3.2$
Granularity ($\Delta\eta \times \Delta\phi$)			
Sampling 1	0.003×0.1	0.025×0.1	$1.375 < \lvert\eta\rvert < 1.5$
		0.003×0.1	$1.5 < \lvert\eta\rvert < 1.8$
		0.004×0.1	$1.8 < \lvert\eta\rvert < 2.0$
		0.006×0.1	$2.0 < \lvert\eta\rvert < 2.5$
		0.1×0.1	$2.5 < \lvert\eta\rvert < 3.2$
Sampling 2	0.025×0.025	0.025×0.025	$1.375 < \lvert\eta\rvert < 2.5$
		0.1×0.1	$2.5 < \lvert\eta\rvert < 3.2$
Sampling 3	0.05×0.025	0.05×0.025	$1.5 < \lvert\eta\rvert < 2.5$
Presampler	Barrel	End-cap	
Coverage	$\lvert\eta\rvert < 1.52$	$1.5 < \lvert\eta\rvert < 1.8$	
Longitud. segm.	1 sampling	1 sampling	
Granularity ($\Delta\eta \times \Delta\phi$)	0.025×0.1	0.025×0.1	

barrel part ($|\eta| < 1.0$) and two identical extended barrels ($0.8 < |\eta| < 1.7$) based on an alternating structure of plastic scintillator plates (tiles) and iron absorbers. Traversing particles initiate showers in the absorbers, and the secondary particles excite the atoms in the scintillator which then emit light. The light is transmitted inside wavelength shifting fibers to photomultipliers which convert the light into an electronic signal. At larger pseudorapidity ($1.5 < |\eta| < 3.2$, end-cap), where large radiation density is expected, the hadronic calorimeters are made from intrinsically radiation-hard LAr detectors).

The very forward region, $3.1 < |\eta| < 4.9$ is covered by LAr detectors. For good hermetic coverage the forward calorimeters are placed at about 4.7 m from the interaction point, and so they have to deal with very high rates of radiation. They consist of three sections. The first is made of copper and the last two are made of tungsten. The metal has longitudinal channels which house rods, which are at high positive voltage, and tubes which are grounded. The gaps are filled with LAr which serves as active material. The presence of the forward calorimeters allows for detecting jets at large η, which is important, for instance, for Higgs searches in the weak-boson fusion channels, and for measurement of missing energy.

The characteristics of the hadronic and forward calorimeters are specified in Table 7.3. The design goal for the energy resolution is:

$$\frac{\sigma_E}{E} = \frac{0.5}{\sqrt{E}} \oplus 0.03.$$

7.4 The Muon Spectrometer

The muon system is an outstanding feature of ATLAS. It serves as trigger for many signatures and provides measurement of muon momenta. Muons are contained, *e.g.*, in signals

Table 7.3: Pseudorapidity coverage, granularity, and longitudinal segmentation of the hadronic and forward calorimeters.

Hadronic tile	Barrel	Extended barrel	
Coverage	$\|\eta\| < 1.0$	$0.8 < \|\eta\| < 1.7$	
Longitud. segm.	3 samplings	3 samplings	
Granularity ($\Delta\eta \times \Delta\phi$)			
Samplings 1 and 2	0.1×0.1	0.1×0.1	
Sampling 3	0.2×0.1	0.2×0.1	
Hadronic LAr		**End-cap**	
Coverage		$1.5 < \|\eta\| < 3.2$	
Longitud. segm.		4 samplings	
Granularity ($\Delta\eta \times \Delta\phi$)		0.1×0.1	$1.5 < \|\eta\| < 2.5$
		0.2×0.2	$2.5 < \|\eta\| < 3.2$
Forward calorimeter		**Forward**	
Coverage		$3.1 < \|\eta\| < 4.9$	
Longitud. segm.		3 samplings	
Granularity ($\Delta\eta \times \Delta\phi$)		$\sim 0.2 \times 0.2$	

from Higgs bosons ($H \rightarrow ZZ^* \rightarrow \mu\mu\mu\mu$) and in many processes predicted by models beyond the Standard Model.

The muon spectrometer measures the deflection of muon tracks in superconducting air-core toroid magnets. They are equipped with trigger chambers and high-precision tracking chambers. The system covers the region $|\eta| < 1.0$, using magnetic bending by large barrel toroids, and the region $1.4 < |\eta| < 2.7$ using two smaller end-cap magnets which are located in both sides of the barrel toroid. In the transition region $1.0 < |\eta| < 1.4$ magnetic deflection is covered by a combination of barrel and end-cap fields. The geometry of the magnetic field is designed to be orthogonal for most of the muon trajectories. The magnet system is shown in Figure 7.6 and the arrangement of the chambers can be seen from Figure 7.7.

7.4.1 Muon precision system

The precision measurement of muon trajectories is realized by two types of chambers, Monitored Drift Tubes, MDT and Cathode Strip Chambers, CSC. There are three cylindric layers in the barrel, located at radii of about 5, 7.5, and 10 m. The end-cap chambers in the range $1 < |\eta| < 2.7$ are located at distances of 7, 10, 14, and 21–23 m from the interaction point.

MDTs cover most of the η range. The chambers consist of aluminum tubes with a diameter of 3 cm. They are filled with 98% Argon and 7% CO_2 at a pressure of 3 bar. The 50 µm sense wire is made of tungsten-rhenium and provides a single wire resolution of $\sim$ 80 µm. The total tube volume is 800 m^3.

CSCs with higher granularity are used in the innermost plane and cover $2 < |\eta| < 2.7$, where large rates and background put high demands on the system. They are multiwire proportional chambers with anode wires of tungsten-rhenium. The segmented cathode strips and charge interpolation between neighboring strips provide good spatial resolution of 60 µm. The total of 1.1 m^3 gas volume is filled with 30% Ar, 50% CO_2, and 20% CF_4.

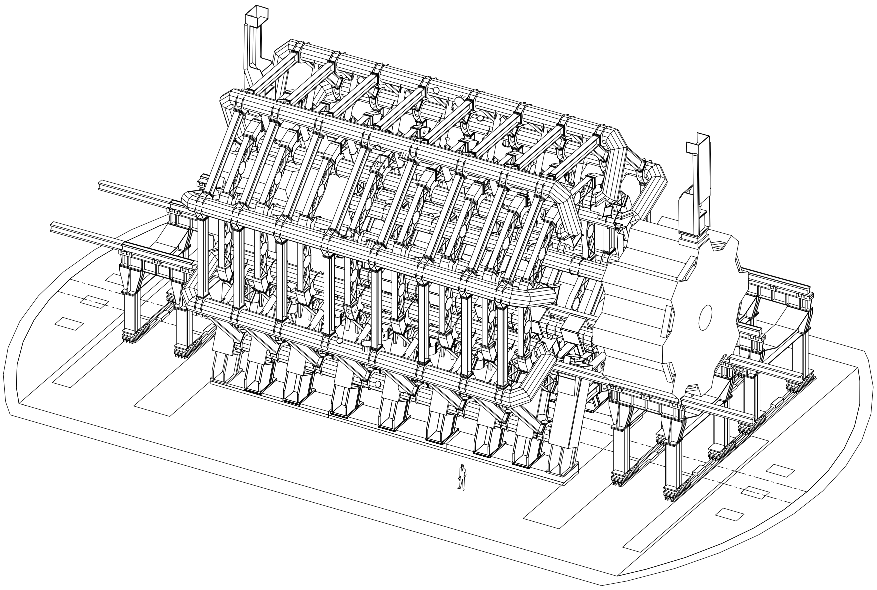

Figure 7.6: The magnet system of the muon spectrometer.

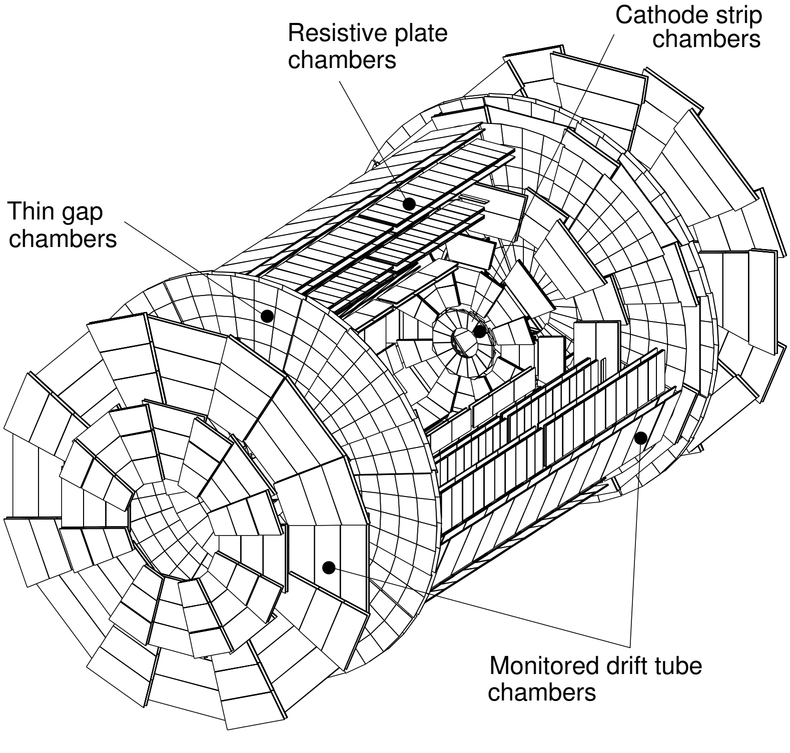

Figure 7.7: Geometry of the muon chambers.

Table 7.4: Muon chamber instrumentation.

	Precision chambers		Trigger chambers	
	CSC	MDT	RPC	TGC
Number of chambers	32	1 194	596	192
Number of readout channels	67 000	370 000	355 000	440 000
Area covered (m^2)	27	5 500	3 650	2 900

7.4.2 Muon trigger system

Three layers of Resistive Plate Chambers, RPCs, provide trigger functionality in the barrel region. They are situated on both sides of the middle MDT layer, and inside the outer MDT layer. Thin Gap Chambers TGCs are used in the end-caps. They are arranged in three layers near the middle MDT layer.

The RPCs consist of two parallel resistive plates, separated by insulating spacers. The volume in between is filled with a gas mixture based on $C_2H_2F_4$. An electric field of some kV/mm multiplies electrons originating from the ionization of the gas by traversing muons, via the avalanche effect. Quick response of the cells is requested for trigger purpose, and the typical space-time resolution is 1 cm×1 ns. The design of the TGCs is similar to multiwire proportional chambers. The cells are operated in saturation mode with a mixture of 55% CO_2 and 45% n-pentane, n-C_5H_{12}. The gas volume is 16 m^3. Good time resolution of 2 ns for the RPCs and 5 ns for the TGCs is achieved by the electric field configuration and small drift times due to small wire distances. The desired granularity is defined by grouping several anode wires together, usually between 4 and 20. The combined signal forms the trigger information. Both RPCs and TGCs provide also measurements of the second coordinate of the trajectories.

Information about the muon instrumentation is available from Table 7.4.

7.5 Trigger and Data Acquisition

The LHC proton bunches will cross at a rate of 40 MHz. At design luminosity of 10^{34} $cm^{-2}s^{-2}$ there will be on average 23 inelastic pp collisions per bunch crossing, leading to an event rate of almost 1 GHz. A multiple-stage trigger system is required to reduce the data to a manageable amount and to filter for interesting events [36]. In ATLAS, the Level-1 trigger (LVL1) performs the initial event selection and reduces the rate to less than about 75 kHz. The LVL1 identifies regions in the detector with interesting features, so-called Regions of Interest (RoIs). Information from all RoIs are combined and passed to the Level-2 trigger (LVL2), which applies a series of optimized selection algorithms to the event. The Event Filter (EF) processes the output from LVL2 with more sophisticated reconstruction and trigger algorithms using tools similar to the offline software. The EF then takes the final decision if the event is discarded or written to tape. Level-2 trigger and Event Filter form the High Level Trigger (HLT). The output rate from the HLT is in the order of 100 Hz, and selected events have an average size of $\sim$ 1.5 Mbyte. The mass storage system therefore must be capable of recording a few hundred Mbytes per second.

The selection criteria of the trigger system must be designed to cover the physics aspects of proton-proton collision at $\sqrt{s}$ =14 TeV, ranging from b-physics with low-p_T tracks to new processes with typically high-p_T signatures. Thus, the online event selection must reduce the output rate, efficiently reject fake events and background processes and guaran-

Table 7.5: Trigger menu for physics triggers. 'e' stands for electron, 'γ' for photon, 'μ' for muon, 'τ' for tau, 'j' for jet, 'xE' for missing transverse energy, 'E' for total transverse energy, 'jE' for total transverse energy using only jets, and 'i' indicates an isolation requirement.

Selection signature	Example of physics coverage
e25i	$W \to e\nu$, $Z \to ee$, top production, $H \to WW^{(*)}/ZZ^{(*)}$, W', Z'
2e15i	$Z \to ee$, $H \to WW^{(*)}/ZZ^{(*)}$
μ20i	$W \to \mu\nu$, $Z \to \mu\mu$, top production, $H \to WW^{(*)}/ZZ^{(*)}$, W', Z'
2μ10	$Z \to \mu\mu$, $H \to WW^{(*)}/ZZ^{(*)}$
γ60i	direct photon production, $H \to \gamma\gamma$
2γ20i	$H \to \gamma\gamma$
j400	QCD, SUSY, new resonances
2j350	QCD, SUSY, new resonances
3j165	QCD, SUSY
4j110	QCD, SUSY
τ60i	charged Higgs
μ10+e15i	$H \to WW^{(*)}/ZZ^{(*)}$, SUSY
τ35i+xE45	$qqH(\tau\tau)$, $W \to \tau\nu$, $Z \to \tau\tau$, SUSY at large $\tan\beta$
j70+xE70	SUSY
xE200	new phenomena
E1 000	new phenomena
jE1 000	new phenomena
2μ6+$\mu^+\mu^-$+mass cuts	rare b-hadron decays

tee optimal acceptance for processes comprising the physics program of ATLAS. A trigger menu, presented in Table 7.5 with typical applications, has been established to cover most of these processes. In addition, there exist less inclusive triggers for more specialized questions, *e.g.*, for invisible Higgs decays, b-hadron physics, monitoring, calibration or determination of trigger efficiencies.

7.6 Detector deferrals and impact on the physics program

When the LHC starts in 2007, ATLAS will not be complete [37]. Due to funding restrictions, some parts of the detector will have to be deferred. The Pixel sub-detector will initially be missing Layer 1 (the middle layer) and the TRT will not have the two end-cap 'C'-wheels. The Gap Scintillator will also be missing. Deferrals in the Inner Detector are shown in Figure 7.8. Eight chambers per end-cap of the muon CSC sub-system will be staged, as will be half of the Digital Signal Processor boards of the LAr instrumentation. Deferrals in the High Level Trigger and data acquisition force the LVL1 trigger rate to be reduced from 75 kHz down to 40 kHz.

The parts of ATLAS which have to be staged were chosen in such a way as to keep the impact on the physics program small, but the impact is not negligible. Most important are the deferrals in the trigger and DAQ, because the reduced acceptance rate leaves no safety margin to account for the large uncertainties on the predicted rates of QCD processes. B-physics is compromised by the Trigger/DAQ removals as there will be no trigger for b-physics in the initial phase, and trigger threshold must be raised in general. The removal of pixel Layer 1 degrades track and vertex reconstruction, and therefore deteriorates the b-tagging performance. The channel $t\bar{t}H^0$ with $H^0 \to b\bar{b}$, $t\bar{t} \to \ell\nu b jjb$, investigated in this thesis, involves four b-jets, and therefore this channel is very sensitive to how well

Full Inner Detector

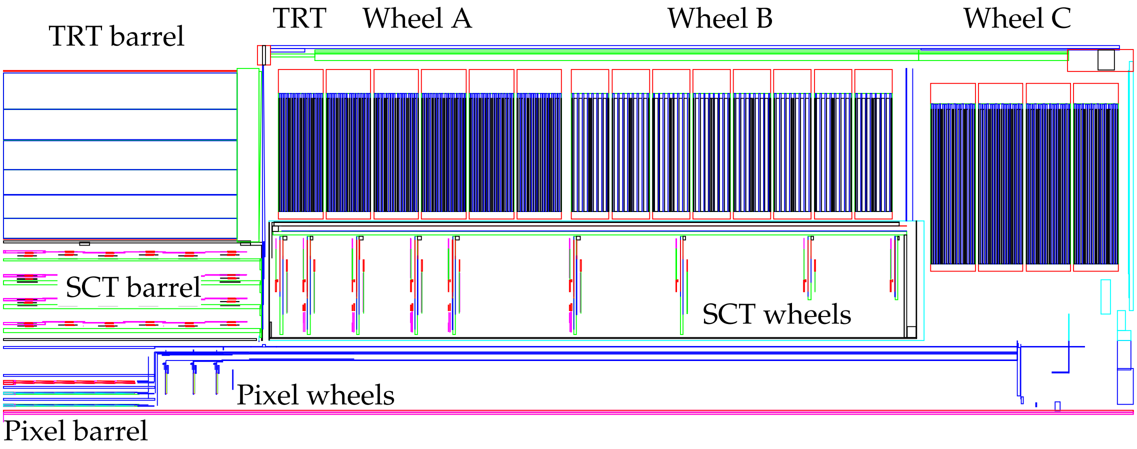

Staged Inner Detector

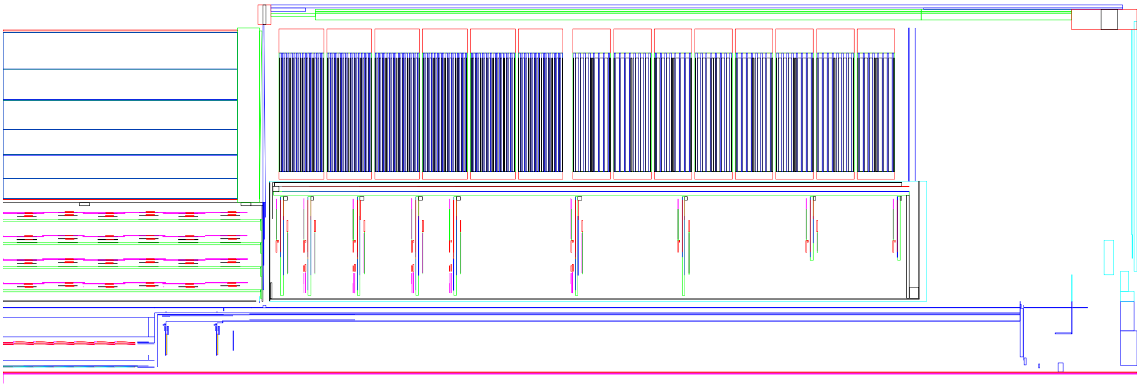

Figure 7.8: Longitudinal view of the top-right quarter of the Inner Detector.

ATLAS performs in flavor-tagging. Part of this thesis is dedicated to an investigation of the impact of the reduced layout of the pixel detector on the discovery potential of the $t\bar{t}H^0$ channel (Chapter 10).

7.7 Simulation of the ATLAS detector

The physics processes that are expected at the LHC are simulated in order to investigate the requirement to the experiments and explore their physics potential. For a realistic description the response of the ATLAS detector to particles penetrating its components must be simulated as detailed as possible. The simulations are based on the GEANT 3 package [38]. If a description of the detector geometry and materials is provided the package calculates the interaction of charged and neutral particles on their flight through the detector, *e.g.*, multiple scattering, energy loss, electromagnetic or hadronic showering or bending inside the magnetic field.

Since ATLAS is a huge and complicated detector, these simulations are very CPU time consuming, in particular for events with high particle multiplicities. On state-of-the-art PCs the simulation of all components takes several minutes per event. Studies of physics channels of interest and the associated background usually require the generation and simulation of millions of events. This is not feasible with the full simulation of the ATLAS detector. Therefore, a fast simulation was developed (ATLFAST [39]) in which the detector response is parametrized as functions of p_T and η. Energy and momentum of the particles are smeared according to values which are obtained from studies of representative events in full simulation. Since no modeling of the detector-particle interactions needs to be performed, huge numbers of events can be processed in a short amount of time. The fast simulation is only an approximation of the real detector, but it has been and is being validated in many studies. ATLFAST was mainly designed to treat jet reconstruction efficiencies, flavor labeling, resolution of missing transverse energy, and isolated leptons and photons. A parameterization is also available of photon, electron and muon momentum resolution, hadronic calorimeter energy resolution, the effect of the magnetic field on jet reconstruction, and the reconstruction of helix track parameters in the Inner Detector.

Most of the signal processes which are of interest at the LHC contain jets. There are several effects that result in reconstructed jet energies much smaller than the energy of the original parton, they can be divided into losses due to detector effects and losses from physics effects. Detector effects arise from non-compensating calorimeters, dead material, mismeasurement, and missing low-p_T particles swept out by the magnetic field. Physics effects are due to fragmentation, minimal-interacting particles in the decay chains (neutrinos), 'out-of-cone' losses, when particles are emitted at large distances to the jet axis and are therefore not associated to the jet, and radiation of hard gluons which are reconstructed as separate jets. Mass measurements can only be accurate if these effects are compensated by calibrating the jet energy scale. In ATLFAST only the physics effects need to be calibrated, because the detector response is not simulated in full detail. The calibration was obtained from the dijet mass in $\mathrm{W}^{\pm}\mathrm{H}^0$ events with $\mathrm{H} \rightarrow \mathrm{u\bar{u}}, \mathrm{gg}$ and $\mathrm{b\bar{b}}$. Calibration factors $K_{\text{jet}} = p_T^{\text{parton}}/p_T^{\text{jet}}$ were derived separately for b-jets and u-jets (gluon jets show similar behavior as b-jets). The calibration as provided by ATLFAST is designed to give proper mass scales but not necessarily proper energy scales.

8 Study of the channel $t\bar{t}H^0$, $H^0 \rightarrow b\bar{b}$

The process $t\bar{t}H^0$ with $H^0 \rightarrow b\bar{b}$ is an important and challenging channel, and contributes to the discovery potential for a light Standard Model Higgs boson at the LHC. The ATLAS Technical Design Report concludes that this channel alone would account for half of the Higgs boson discovery potential of ATLAS in the low mass range, the second discovery channel being direct production with $H^0 \rightarrow \gamma\gamma$. Meanwhile, the analysis of the weak boson fusion processes has shown that these channels have a significant contribution as well [32]. Still, $t\bar{t}H^0$ production is the only channel where the decay $H^0 \rightarrow b\bar{b}$ can be observed. Also, it is a benchmark channel for the overall performance of ATLAS and for the tracking and flavor-tagging performance in particular. The $t\bar{t}H^0$, $H^0 \rightarrow b\bar{b}$ channel is studied in this section based on Monte Carlo simulations of the ATLAS detector.

8.1 Signal and background processes

The signal process $t\bar{t}H^0$ is depicted in Figure 8.1 a). At the LHC, the $t\bar{t}H^0$ state is produced via gluon-gluon interaction in about 90 % and in quark-quark interaction in 10 % of all cases.

Top quarks decay almost exclusively into Wb, and W bosons decay hadronically in about $2/3$ of all cases, and into lepton plus neutrino in about $1/3$ of all cases. Table 8.1 lists the relevant branching ratios. The $t\bar{t}$ final state with the highest branching fraction is jjb jjb. Including $H^0 \rightarrow b\bar{b}$ this would result in a purely hadronic multi-jet final state with moderate transverse momentum of the jets for which no trigger is foreseen in ATLAS (c.f. Table 7.5 on page 48). To have a handle for triggering $t\bar{t}H^0$ events, one requires one top quark to decay semileptonically, leading to a final state of $\ell\nu$b jjb bb with 6 jets (4 of which are b-jets), 1 lepton and missing transverse momentum. Concerning the lepton, only electrons (e) and muons (μ) are considered. The main background to the signal process arises from QCD processes with a top-quark pair and additional jets from initial or final state gluon radiation, Figure 8.1 b). The cross section for the $t\bar{t}$+jets background is about 900 times larger than that of the signal. But the additional jets are by far dominated by light flavors, so only a small fraction consists of true $t\bar{t}b\bar{b}$ events. Requiring four b-jets in the final state can effectively suppress large parts of this background. Therefore,

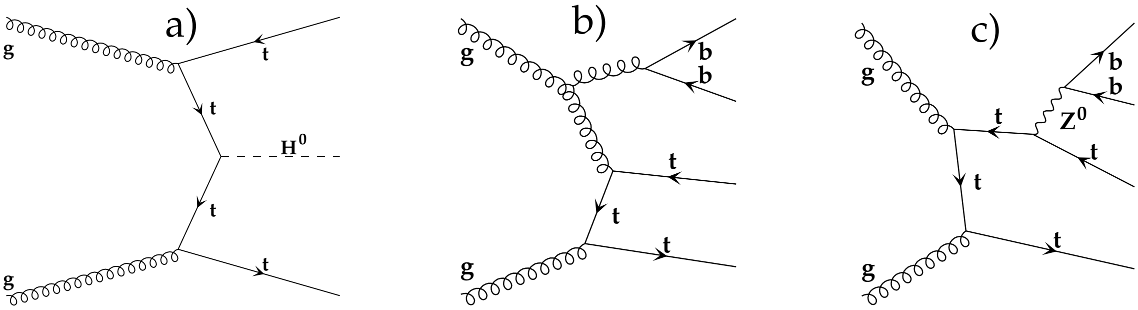

Figure 8.1: a) $t\bar{t}H^0$ signal process, b) QCD $t\bar{t}b\bar{b}$ background, c) electroweak $t\bar{t}b\bar{b}$ background.

Table 8.1: Branching ratios of top quarks and W bosons. The figures for the W boson decays are the world averages from [1].

$t^+ \to Wb$	$> 99.8\%$ (SM prediction)
$W^+ \to \ell^+\nu$	$(10.68 \pm 0.12)\%$ per lepton family
$W^+ \to$ hadrons	$(67.96 \pm 0.35)\%$

a high-performance b-tagging algorithm which efficiently tags b-jets and strongly rejects non-b-jets is crucial for this analysis.

Differentiation between b-jets and jets from lighter quark flavors is possible by exploiting life-time and decay information of the original quarks. Hadrons containing b-quarks have substantially larger life-times than hadrons without b-quarks, so that at LHC energies b-hadrons travel a few millimeters before decaying. With a high precision tracking system it is possible to measure the distance between the primary interaction vertex and the decay vertex of b-hadrons. Semi-leptonic decays of the b-quark provide another means to identify b-hadrons by tagging soft leptons (electrons or muons). However, due to mismeasurements, tracks from jets from lighter quarks can fake secondary vertices, or tracks from b-hadrons may be measured with too small distances to the primary vertex, and so it is not possible to tag b-jets with 100% efficiency without misidentifying jets from lighter quarks as b-jets. The b-tagging approach used in this work is discussed in Section 8.3 and the algorithm applied to fully simulated events is described in Section 12.2.

There is also a less severe $t\bar{t}b\bar{b}$ background which is mediated by electroweak gauge bosons, $gg \to Z/\gamma^*/W \to t\bar{t}b\bar{b}$ (also denoted as '$t\bar{t}b\bar{b}$ (EW)' in the text), Figure 8.1 c). The cross section for these processes is nine times smaller than $t\bar{t}b\bar{b}$ production from QCD. More leading-order diagrams for the signal and the $t\bar{t}b\bar{b}$ background are printed in Appendix A. Other backgrounds are negligible as long as four tagged b-jets are required. Potentially dangerous processes may arise from $W^\pm$+jets and single-top+W production, the former having a huge cross section, the latter almost resembling the final state of the signal. The importance of these processes is discussed in Section 9.2.5.

8.2 Monte Carlo generators and cross sections

Signal events are generated with PYTHIA 6.203 [40] for Higgs boson masses of 80 GeV to 140 GeV in steps of 10 GeV. All $t\bar{t}b\bar{b}$ background events are generated with AcerMC 1.0 [41]. AcerMC calculates the hard $t\bar{t}b\bar{b}$ process based on matrix element calculations, and the events are then interfaced to PYTHIA for simulation of decays, hadronization and initial- and final state radiation. In all cases the CTEQ5L structure functions are used. It was argued before that $t\bar{t}$+light jets events are another important source of background, if the light jets are misidentified as b-jets. At the time of preparation of this thesis no matrix element based generator for $t\bar{t}+n\cdot$jets was available. The process $t\bar{t}jj$ (+additional jets) is therefore generated with PYTHIA using the parton shower approach [42, 43].

The cross sections for the signal process are calculated with the HQQ program [44], and the branching ratios of $H^0 \to b\bar{b}$ are calculated with the HDECAY program [12]. Cross sections for the background processes are used as provided by the event generators. The renormalization and factorization scales Q^2_{QCD} are taken to be the same and are set to $Q^2_{\mathrm{QCD}} = (m_t + m_{H^0}/2)^2$ for signal and $t\bar{t}b\bar{b}$ background. In the case of background events $m_{H^0} = 120$ GeV is used. Since this scale can not be chosen in PYTHIA, the $t\bar{t}jj$

Table 8.2: Inclusive signal cross sections and branching ratios.

m_{H^0} (GeV)	$\sigma_{\mathrm{incl.}}$ (pb)	BR(H→b$\bar{\mathrm{b}}$)
100	0.84	0.82
110	0.66	0.79
120	0.52	0.70
130	0.42	0.56
140	0.34	0.37

Table 8.3: Monte Carlo samples and generators used in this analysis.

Process	Generator	$\sigma_{\mathrm{incl.}}$ (pb)	Generated Events
$\mathrm{t\bar{t}H^0}$	PYTHIA 6.203	see Tab.8.2	1 M
gg→ $\mathrm{t\bar{t}b\bar{b}}$	AcerMC 1.0	8.1	2 M
$\mathrm{q\bar{q}}$ → $\mathrm{t\bar{t}b\bar{b}}$	AcerMC 1.0	0.5	2 M
gg→Z/γ/W→ $\mathrm{t\bar{t}b\bar{b}}$	AcerMC 1.0	0.9	1 M
$\mathrm{t\bar{t}jj}$	PYTHIA 6.203	474	19.3 M

cross section is calculated with the default setting $Q^2_{\mathrm{QCD}} = \left(m_{\mathrm{t}}^2 + p_T^2\right)$, where p_T is the transverse momentum of the scattering process. The leading-order cross sections and the number of generated Monte Carlo events are listed in Tables 8.2 and 8.3.

Higher order corrections

The predicted leading order cross sections for the $\mathrm{t\bar{t}H^0}$ signal process and the relevant background processes are subject to large uncertainties from the choice of the renormalization and factorization scales. This indicates significant contribution of higher order QCD corrections, and next-to-leading order calculations can help to reduce the scale dependence of the cross section predictions. The ratio between leading order and next-to-leading order cross sections is usually termed K,

$$\mathrm{K} := \frac{\sigma_{\mathrm{NLO}}(\mathrm{pp} \to \mathrm{t\bar{t}H^0})}{\sigma_{\mathrm{LO}}(\mathrm{pp} \to \mathrm{t\bar{t}H^0})}. \tag{8.1}$$

Virtual and real $\mathcal{O}(\alpha_s^3)$ corrections to the parton level processes $\mathrm{q\bar{q}} \to \mathrm{t\bar{t}H^0}$ and $\mathrm{gg} \to \mathrm{t\bar{t}H^0}$ have been calculated in Refs. [45, 46]. The results are shown in Figure 8.2 and 8.3 for a Higgs boson mass of 120 GeV. For a central factorization and renormalization scale $\mu = m_{\mathrm{t}} + m_{\mathrm{H}^0}/2$ the cross section is enhanced by 20% when NLO corrections are taken into account. The scale dependence of the $\mathrm{t\bar{t}H^0}$ cross section is significantly reduced with the NLO result.

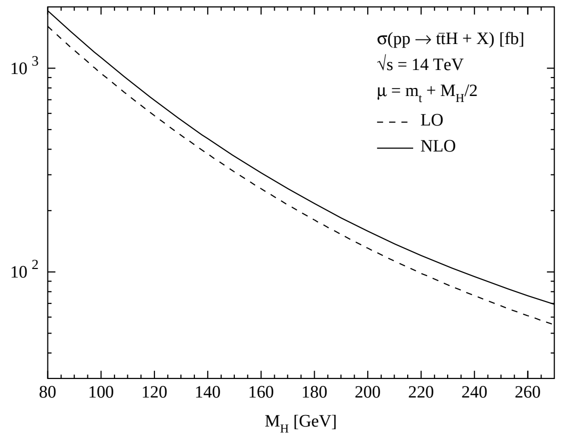

Figure 8.2: Leading order and next-to-leading order cross sections for pp → $\mathrm{t\bar{t}H^0}$ [45].

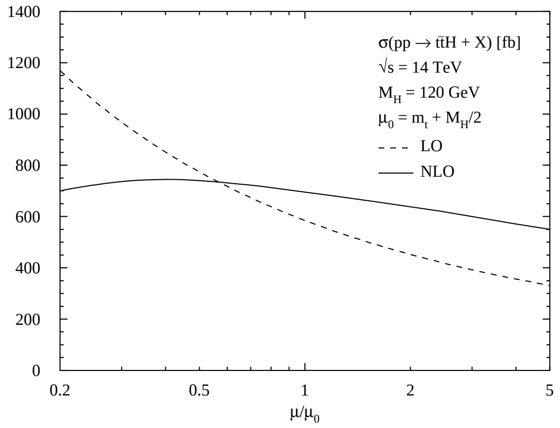

Figure 8.3: Scale dependence of the production cross section [45].

In contrast to the $t\bar{t}H^0$ signal process, there are so far no higher order corrections available for the $t\bar{t}$+jets background. Consequently, no K-factors are applied in this analysis. Concerning the signal, this leads to conservative results, because for the central scale $\mu = m_t + m_{H^0}/2$ used in this study the K-factor is larger than 1.

8.3 Characteristics of signal and background processes

This section discusses some properties of the signal and background processes. Figure 8.4 shows p_T- and η distributions of the lepton, b-jets and light-quark jets at generator level before any cuts.

a) and b) p_T and η of the lepton: the mean value of the transverse momentum is 57 GeV in $t\bar{t}H^0$, 53 GeV in $t\bar{t}b\bar{b}$, and 50 GeV in $t\bar{t}jj$ events. The shape is very similar for signal and background events, except for a slightly more pronounced tail in $t\bar{t}H^0$ events. The η distribution has an RMS of ~ 1.4 for all three processes.

c) and d) p_T and η of b-jets from decays of the top quarks: the mean value of the transverse momentum is 78 GeV in $t\bar{t}H^0$, 75 GeV in $t\bar{t}b\bar{b}$, and 71 GeV in $t\bar{t}jj$ events. Again, the p_T distribution of $t\bar{t}H^0$ events has a slightly more pronounced tail. The RMS of the η distribution is the same as for Figure b).

e) and f) p_T and η of b-jets originating from the decay of the Higgs boson and from gluon radiation, respectively: These distributions can only be shown for the matrix element based $t\bar{t}H^0$ and $t\bar{t}b\bar{b}$ processes. The mean value of the transverse momentum is 71 GeV in $t\bar{t}H^0$ and 38 GeV in $t\bar{t}b\bar{b}$ events. The p_T distribution in signal events is a bit softer as that of b-jets from top-quark decays. The much softer p_T spectrum in $t\bar{t}b\bar{b}$ events and the η distribution with larger contribution of the forward region reflects the different origin of the $b\bar{b}$-pair in $t\bar{t}b\bar{b}$ events.

Figures 8.5 and 8.6 show event displays of a fully simulated and reconstructed signal event $t\bar{t}H^0 \to \mu\nu b$ jjb bb. The generated Higgs boson mass is $m_{H^0} = 120$ GeV. Figure 8.5 is a projection to the xy-plane, which is perpendicular to the beam axis. The top figure a) gives a view on the complete detector. One observes a reconstructed muon track in the lower left quarter of the muon system. Energy depositions in the calorimeters are shown as light rectangles. The electromagnetic calorimeter is labeled 'LAr', and the hadronic calorimeter is labeled 'Tile'. In the Inner Detector only the reconstructed tracks are shown. Figure b) zooms into the Inner Detector and shows both hits and the reconstructed tracks. The large number of hits reveals the position of the detectors: One can see three pixel layers ('PIXEL') and four silicon strip layers ('SCT'). The large number of hits in the TRT makes possible to visually identify tracks even without reconstruction. In this display, reconstructed tracks are shown only if they have a transverse momentum larger than 1 GeV. Figure 8.6 shows the same event in the ρz-plane, where ρ is the radial distance of a point to the beam axis in the xy-plane. The total view a) offers more details of the components of the muon system (MDTs, RPCs, and CSCs). Figure b) magnifies the calorimeters and the Inner Detector.

8.4 Simulation, reconstruction and b-tagging procedure in the fast simulation

In the fast simulation, ATLFAST, no interaction of particles with the detector, no particle reconstruction and no particle identification is simulated. Instead, the four vectors of the

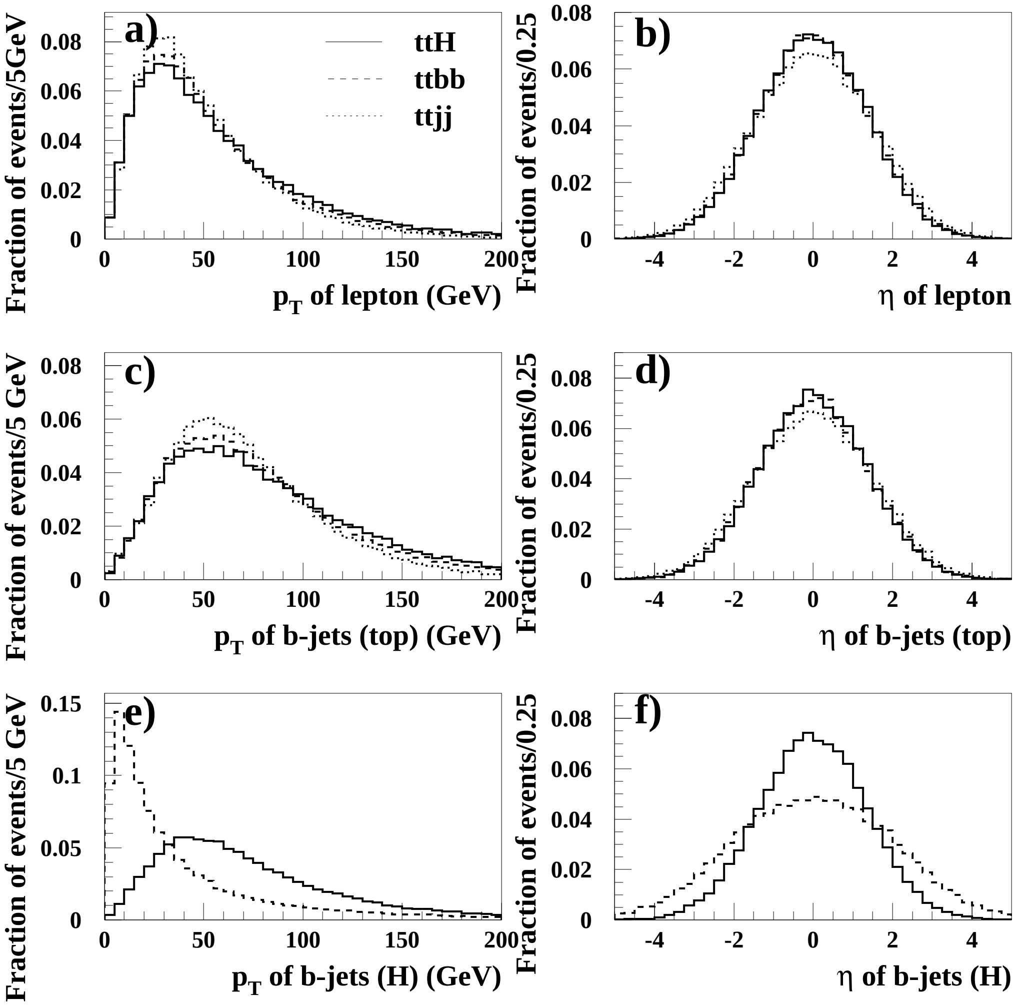

Figure 8.4: Characteristic p_T and η distributions in signal and background events.

stable particles, produced by a Monte Carlo generator, are smeared according to energy and momentum resolutions obtained from studies with the full simulation of the detector. The bending of the ϕ angle of charged particles due to the magnetic field is simulated for particles with $p_T > 0.5$ GeV.

To simulate calorimeter clusters needed for the reconstruction of jets, ATLFAST uses a simplified geometry of the calorimeters cells. The granularity is 0.1×0.1 in $\eta \times \phi$ for $|\eta| < 3.2$ and 0.2×0.2 in $3.2 < |\eta| < 5.0$. No distinction is made between the electromagnetic and the hadronic calorimeters. The transverse energy of all undecayed particles, except for neutrinos and muons, are summed up in the calorimeter cells corresponding to the directions of the particles.

The $\eta \times \phi$ matrix is then scanned for cells with transverse energy $E_T > 1.5$ GeV. They are used as seeds for clusters. Cells around a seed in a cone $\Delta\mathrm{R} < 0.4$ are summed up. If the total energy inside the cone is above 5 GeV, the system of cells is marked as cluster.

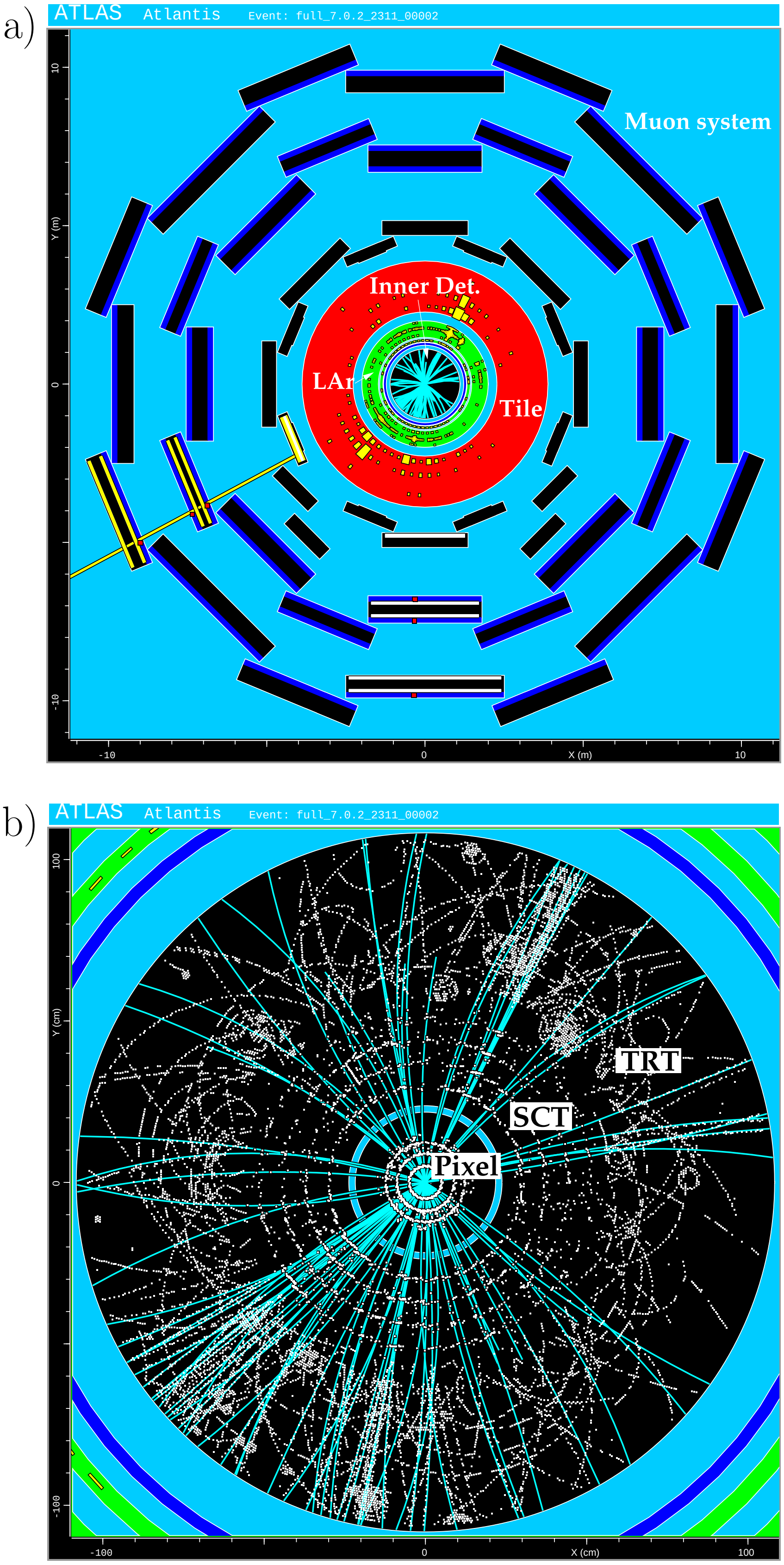

Figure 8.5: Event display of a simulated $t\bar{t}H^0$ event in the xy-plane.

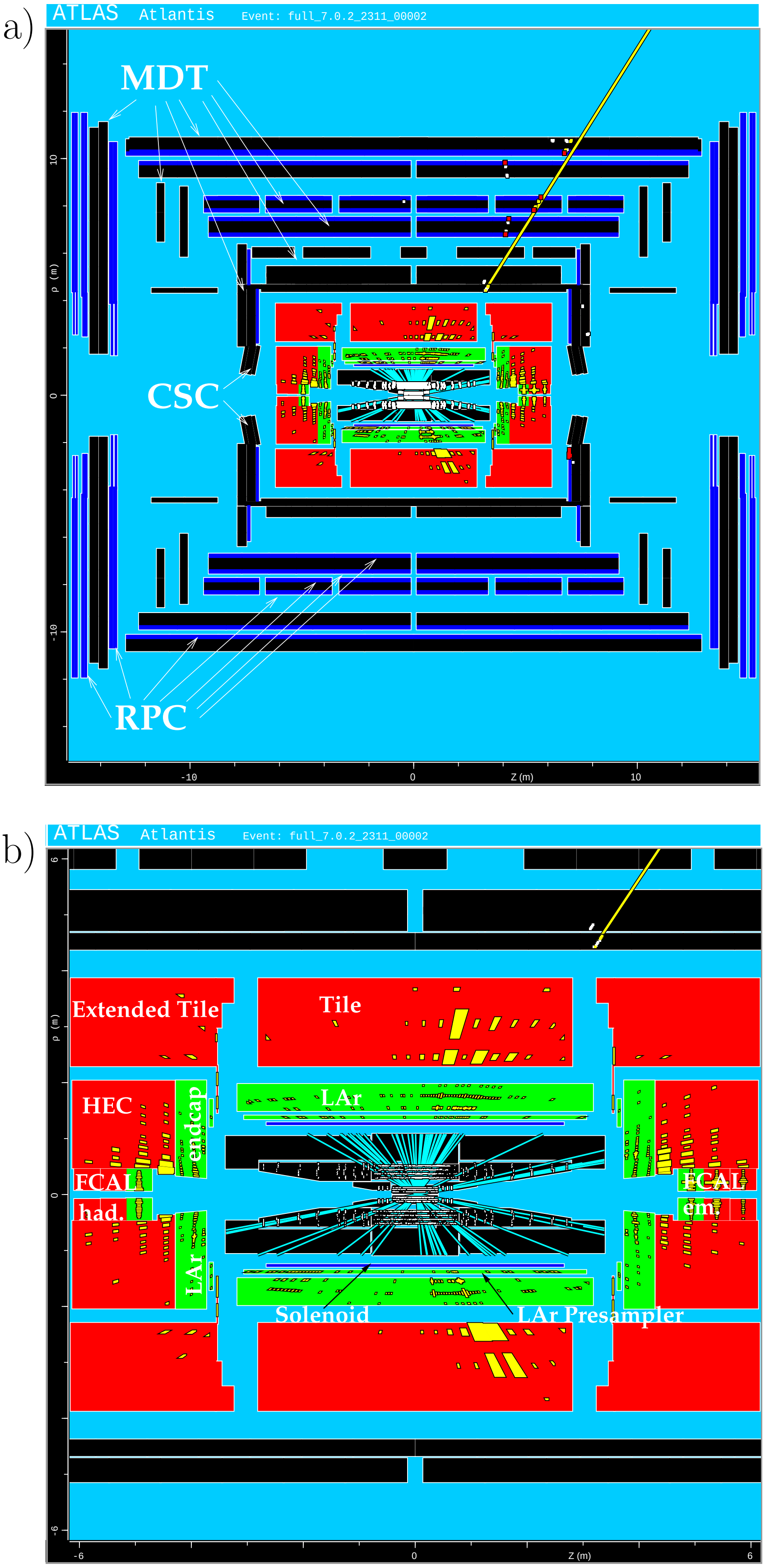

Figure 8.6: Event display of a simulated $t\bar{t}H^0$ event in the ρz-plane.

Clusters are associated to electrons, photons, and muons if $\Delta\mathrm{R}_{\mathrm{e}/\gamma/\mu-\mathrm{cluster}} < 0.1$. The particles are marked as isolated if they have $|\eta| < 2.5$, $p_T > 5$ GeV, if there is no additional cluster in a cone $\Delta\mathrm{R} < 0.4$, and if the energy E_T of cells inside a cone of $\Delta\mathrm{R} < 0.2$ around the particle is less than 10 GeV. ATLFAST does not include efficiencies for the reconstruction of electrons, photons, and muons. A reconstruction efficiency of 90% is therefore assumed in this work (this is the value commonly used within ATLAS).

Clusters not associated to the generated and smeared electrons, muons or photons are used as seeds for jets. The energy of non-isolated muons which fall inside the cone of $\Delta\mathrm{R} < 0.4$ is added to the jet-candidate. The jet is kept if it has transverse energy $E_T > 10$ GeV, where $E_T = E \cdot \sin\theta$. Jets with $|\eta| < 2.5$ are labeled as b-jets or c-jets if there is a b-quark or c-quark with $p_T > 5$ GeV (after final state radiation, FSR) inside a cone with $\Delta\mathrm{R} < 0.2$.

The components of the missing transverse momentum, p_x^{miss} and p_y^{miss}, are reconstructed from the sum of isolated electrons, photons, muons, and jets, unassociated calorimeter clusters and cells not used for cluster reconstruction.

The flavor-labeling procedure described above does not reflect the expected flavor-tagging performance of ATLAS. In data, algorithms based on the lifetime-information of heavy quarks will be used as well as soft-lepton tags. These algorithms have limited efficiency to tag true b-jets, and they will erroneously tag light-quark jets and c-jets as b-jets. This behavior is simulated by randomly tagging b-labeled jets with an efficiency ε_{b}, and mistagging light jets and c-jets with efficiencies of $\varepsilon_j = 1/\mathrm{R_j}$ and $\varepsilon_c = 1/\mathrm{R_c}$. Usually, a fixed efficiency ε_{b} is chosen as working-point and associated rejections factors $\mathrm{R_j}$ and $\mathrm{R_c}$ are used which were obtained from full simulation studies. The parameter set commonly used in ATLAS is $\varepsilon_{\mathrm{b}} = 60\%, \mathrm{R_j} = 100, \mathrm{R_c} = 10$, and these values were also applied in the TDR study, Ref. [28]. Therefore, this set of parameters is used as reference point in Section 9 to compare the results of this thesis to the earlier analysis. More advanced parameterizations are investigated in Section 10. They are derived from performance studies with the latest detector layout and include p_T-dependent rejection factors $\mathrm{R_j}$ and $\mathrm{R_c}$.

9 Reconstruction of the final state

The channel $\mathrm{t\bar{t}H^0}$ with $\mathrm{H^0 \to b\bar{b}}$ was considered for the first in ATLAS time in Ref. [47]. Events with three or four b-tagged jets were selected and some straightforward p_T and η cuts were applied. All possible combinations of two b-jets were taken into account. The signature from the Higgs boson would appear as a mass peak in the combinatorial spectrum of invariant $\mathrm{b\bar{b}}$ masses. This procedure results in rather small purities of b-jets from the decay of the Higgs boson in the $\mathrm{b\bar{b}}$ mass distribution: the combinatorial probability of finding the two correct b-jets from all four b-jets is $\binom{4}{2}^{-1} \approx 17\%$. In reality, the probability is even smaller in the presence of additional b-jets, *e.g.*, if a light-quark jet is mistagged as b-jet. Some refined procedures were tried, *e.g.*, by choosing the two b-jets with smallest p_T, but only little improvement was gained. The work concludes that a full reconstruction of the final state would be needed to reduce the combinatorial choices by assigning two of the b-jets to the decays of the top quarks.

Partial and full event reconstruction was first implemented in Ref. [28]. It was demonstrated that four b-tagged jets and full reconstruction are needed to observe a pronounced peak in the m_{bb} spectrum and to keep the $\mathrm{t\bar{t}}$+jets background under control.

The final-state reconstruction of [28] is reviewed in Section 9.1 using updated and new Monte Carlo generators, and more sophisticated methods are developed in Section 9.2.

Parton-Jet matching

There is no direct link between the generated partons (the 'Monte Carlo truth') and the reconstructed jets and leptons. In order to gather information about correct jet pairing it is therefore necessary to match the partons to the jets. This is done via a simple $\Delta\mathrm{R}$ matching criterion: For each parton the jet with the smallest distance $\Delta\mathrm{R}$ is matched to the parton, and a jet is matched to only one parton. The distance $\Delta\mathrm{R}$ must be less than 1.0. If no associated jet exists within $\Delta\mathrm{R} < 1.0$ then no parton-jet matching is possible. For all the six initial quarks in signal events (2 b-quarks from the Higgs boson decay, 3 quarks from the hadronic top-quark decay, and 1 b-quark from the semileptonic top-quark decay) an associated jet can be found in 78% of all cases.

It should be noted that this procedure can lead to incorrect assignment if the direction of the jet differs significantly from that of the initial parton, *e.g.*, if after final state radiation of gluons the decay products of the parton are reconstructed by the jet finder as several jets. As a matter of fact the quoted 78% efficiency for the parton-jet matching is high compared to the efficiency for single jet reconstruction given in the ATLFAST manual [39] (around 80%, but for $\Delta\mathrm{R} < 0.4$). This indicates that there is a substantial amount of incorrect parton-jet associations due to the relatively high jet multiplicity from initial state radiation (ISR) and final state radiation (FSR).

9.1 'TDR' analysis of the $\ell\nu$b jjb bb final state

The same event reconstruction procedure as in Ref. [28] was applied in order to achieve an adequate comparison between the TDR results and the present situation with new Monte

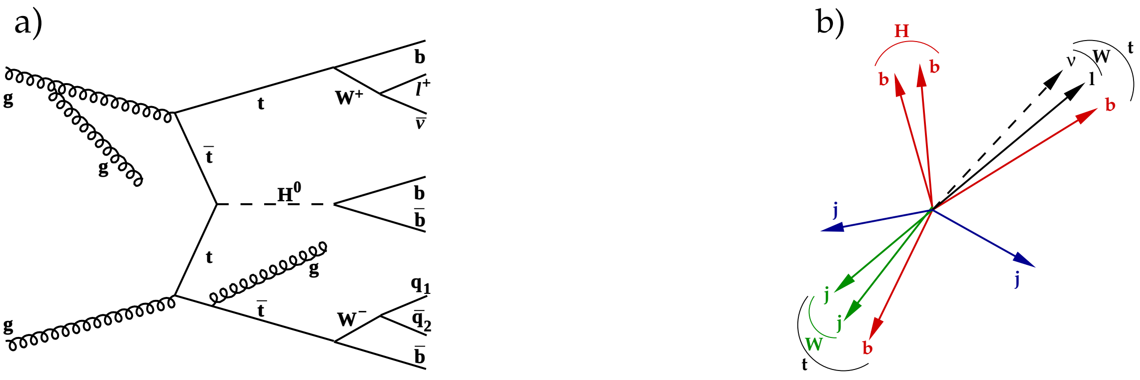

Figure 9.1: a) Feynman diagram for the signal process, including decays and additional gluon radiation. b) Sketch of reconstructed objects.

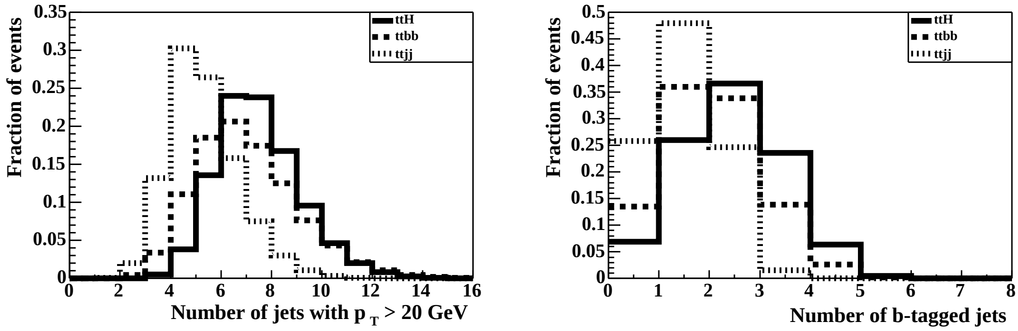

Figure 9.2: Left: Number of jets with $p_T > 20$ GeV after jet calibration. Right: Number of b-tagged jets using $\varepsilon_b = 60\%$, $R_c = 10$, $R_j = 100$. The histograms are normalized to Unity.

Carlo generators and updated cross sections. This procedure is referred to as the 'TDR method' in the following (although some of the cut values are different from those in the TDR analysis). It aims at reconstructing the complete final state of the event to minimize the combinatorial background when assigning two of the four b-jets to the Higgs boson decay. The TDR method consists of three steps: A preselection, the reconstruction of the $t\bar{t}H^0 \rightarrow t\bar{t}b\bar{b}$ final state, and cuts on the reconstructed top quark and Higgs boson masses.

9.1.1 Preselection

A preselection is applied to select only events which are compatible with the signal topology of four b-jets, two non-b-jets and one lepton. This preselection reduces the size of the background event samples, primarily the $t\bar{t}$+jets events. The preselection requires

- at least 1 isolated lepton (ℓ = e or μ) with transverse momentum $p_T^e > 25$ GeV, $p_T^\mu > 20$ GeV and pseudorapidity $|\eta| < 2.5$,
- at least 6 jets with $p_T > 20$ GeV and $|\eta| < 5$,
- at least 4 of these jets must be tagged as b-jets.

After the preselection the signal to background ratio is enhanced by a factor of 50.

In addition to jets originating from the hard process, there can be jets from initial- or final-state gluon radiation, Figure 9.1 a). This increases the combinatorial problems when

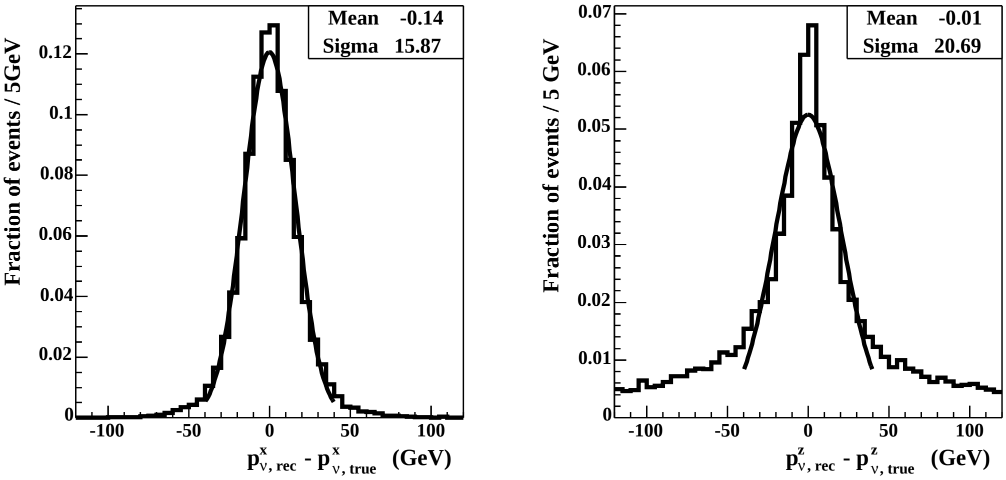

Figure 9.3: Resolution of the reconstructed neutrino momentum (left: x-component [same for $\mathrm{p_y}$], right: z-component) in $\mathrm{t\bar{t}H}$ events with $m_{\mathrm{H}^0} = 120$ GeV. The distributions are shown for events after the reconstruction of the final state where one solution for p^z_ν has been chosen. The histograms are normalized to Unity.

assigning the objects reconstructed in an event to the hard-process particles, Figure 9.1 b). Figure 9.2 shows the number of jets with $p_T > 20$ GeV and the number of jets tagged as b-jets for signal events and the main backgrounds. In signal events, the mean number of jets with $p_T > 20$ GeV is 7.5.

The next step is the reconstruction of the two W bosons, W → $\ell\nu$ and W → jj. After that two out of all b-jets are assigned to the two top quark decays by a minimization procedure which involves the reconstructed W bosons and the b-jets. The Higgs boson in signal events is reconstructed from the remaining b-jets.

9.1.2 Reconstruction of W→ $\ell\nu$

To fully reconstruct the leptonic W decay, one needs to reconstruct the four-vector of the neutrino momentum (the neutrino mass is neglected, $m_\nu = 0$, so that $E_\nu = |\vec{p}_\nu|$). In contrast to p^ν_x and p^ν_y, which are identified with p^{miss}_x and p^{miss}_y, one cannot measure p^z_ν in the detector, because the momentum along the z-direction of the initial state is unknown. Instead, it can be calculated by constraining the invariant mass of the lepton-neutrino system to the W mass. In the rare case of two or more isolated leptons the one with the largest value of p_T is chosen. Hence, the missing part of the neutrino momentum is obtained by solving Equation 9.1 for p^z_ν.

$$m^2_{\mathrm{W}^\pm} = (E_\nu + E_\ell)^2 - (p^x_\nu + p^x_\ell)^2 - \left(p^y_\nu + p^y_\ell\right)^2 - (p^z_\nu + p^z_\ell)^2 . \tag{9.1}$$

Solving this equation results in 0, 1 or 2 solutions:

$$\begin{aligned} \beta &:= m^2_{\mathrm{W}^\pm} - \left(E^{\ell 2} - p^{\ell\,2}_x - p^{\ell\,2}_y - p^{\ell\,2}_z\right) + 2p^{\mathrm{miss}}_x p^\ell_x + 2p^{\mathrm{miss}}_y p^\ell_y, \\ p^\nu_{z\,1,2} &= \frac{1}{2} \cdot \frac{\beta p^\ell_z \pm E^\ell \sqrt{\beta^2 + \left(2p^\ell_z p^{\mathrm{miss}}_T\right)^2 - \left(2E^\ell p^{\mathrm{miss}}_T\right)^2}}{E^{\ell 2} - p^{\ell\,2}_z}. \end{aligned} \tag{9.2}$$

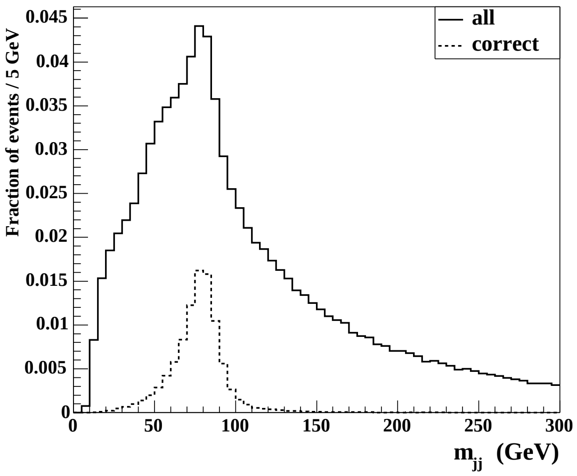

Figure 9.4: Distribution of the invariant jet-jet mass for non-b-jets with $p_t > 20$ GeV in $t\bar{t}$H events with $m_{H^0} = 120$ GeV. The dashed histogram shows the contribution for the correct jet-pair found by the parton-jet matching. The full histogram is normalized to Unity.

No solution can be found if there is a significant mismeasurement of p_T^{miss} or of the jet energies and momenta. Events are kept only if there exists at least one solution. This condition is satisfied for about 75% of the events in signal and background. For almost all of these events there are two solutions, and both are kept for further evaluation in the top quark reconstruction.

The resolution of the reconstructed neutrino momentum is shown in Figure 9.3 for p_x^ν and p_ν^z for fully reconstructed signal events. A Gaussian is fitted to the peak of the distribution, and a width of $\sigma = 15.9$ GeV is obtained for $p_\nu^{x,y}$ and $\sigma = 20.7$ GeV for p_ν^z. The resolution for p_ν^z is worse because its calculation introduces measurement errors from six variables ($E_\ell, p_x^{\text{miss}}, p_y^{\text{miss}}, p_\ell^x, p_\ell^y, p_\ell^z$, neglecting the natural width of $m_{W^\pm}$). One observes large tails from events where the wrong out of the two solutions for p_ν^z was chosen in the process of the top quark reconstruction (cf. section 9.1.4).

9.1.3 Reconstruction of W→ jj

To reconstruct the hadronic W decay, a list of jet-pairs is established. Only jets which are not tagged as b-jets, and which have $p_T > 20$ GeV are taken into account. In the list, only jet-pairs with $m_{\text{jj}} = m_{W^\pm} \pm 25$ GeV are kept. For all jet-jet-pairs which fulfill these requirements, the jet four-momenta are rescaled with a single factor so that m_{jj} equals $m_{W^\pm}$. In about 20% of the signal events no jet-pair candidate can be found that passes these requirements. These events are rejected. Figure 9.4 shows the invariant jet-jet masses for all pairs (without constraining the invariant mass of the jj-candidates to the W mass). On average there are 2.5 jet-pairs in signal events that lie inside the mass window, 3.0 such pairs for the irreducible $t\bar{t}b\bar{b}$ background and 1.6 pairs for the reducible $t\bar{t}$jj background. The jet multiplicity in the $t\bar{t}$jj events is smaller since in PYTHIA only the top quark pair is produced in the hard process, and additional jets emerge from the parton shower which produces 'softer' jets with smaller p_T and larger pseudorapidity. In $t\bar{t}b\bar{b}$ events, generated with AcerMC and interfaced to PYTHIA, these jets are produced in addition to the final state with two top quarks and two b-quarks.

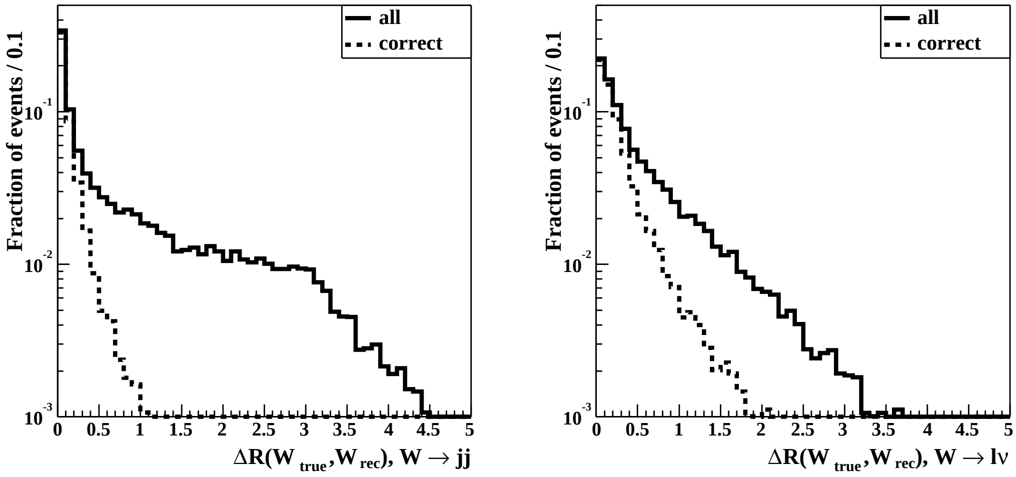

Figure 9.5: Difference ΔR between the generated and the reconstructed W bosons. The definition of 'correct' in the right-hand plot is such that the solution for p^z_ν which is used in the reconstruction must be the one which is closer to the generated p^z_ν. The distributions are normalized to Unity.

At this stage the complete list of jet-pairs inside the acceptance window is kept, and the decision which pair is chosen for the reconstruction of the hadronic W decay is made in the process of the top quark reconstruction (cf. next section).

The angular difference ΔR between the generated and the reconstructed W bosons is shown in Figure 9.5 for the leptonic and the hadronic W decay.

9.1.4 Reconstruction of two top quarks

After reconstruction of the leptonic W decay, and building the list of jet-pair candidates for the hadronic W decay, one needs to find the appropriate b-jets from the decay of the top quark. This is done simultaneously for both top quarks by finding the combination of one charged lepton, the solution for p^z_ν, two b-jets and two non-b-jets from the list of jet-pairs which minimizes

$$\Delta^2 = (m_{\ell\nu\mathrm{b}} - m_\mathrm{t})^2 + (m_\mathrm{jjb} - m_\mathrm{t})^2. \tag{9.3}$$

After this procedure two b-jets, two non-b-jets, the lepton, and one of the solutions for p^z_ν are selected for the top quark decays. The top quark masses are identified with the invariant masses of the $\ell\nu$b and the jjb system. The distributions of m_jjb and $m_{\ell\nu\mathrm{b}}$ are shown in Figures 9.6 and 9.7. The resolution of the top quark mass reconstruction is obtained from a Gaussian fit in the range 160–190 GeV. The values are $\sigma_{\ell\nu\mathrm{b}} = 8.6$ GeV and $\sigma_\mathrm{jjb} = 7.7$ GeV in signal events with $m_{\mathrm{H}^0} = 120$ GeV. Similar resolutions are obtained for other masses of the Higgs boson and for the background processes. The tails of the distribution are dominated by events with incorrect pairing. Such events are rejected by requiring that the reconstructed top quark masses lie in the range $m_\mathrm{t} \pm 20$ GeV.

The angular difference ΔR between the generated and the reconstructed top quarks is shown in Figure 9.8 for the semileptonic and the hadronic top quark decay.

Since two of the b-jets are now assigned to the top quark decays, the remaining b-jets can be assigned to the Higgs boson candidate. In the rare case that more than two b-jets are left, the two with highest p_T are chosen.

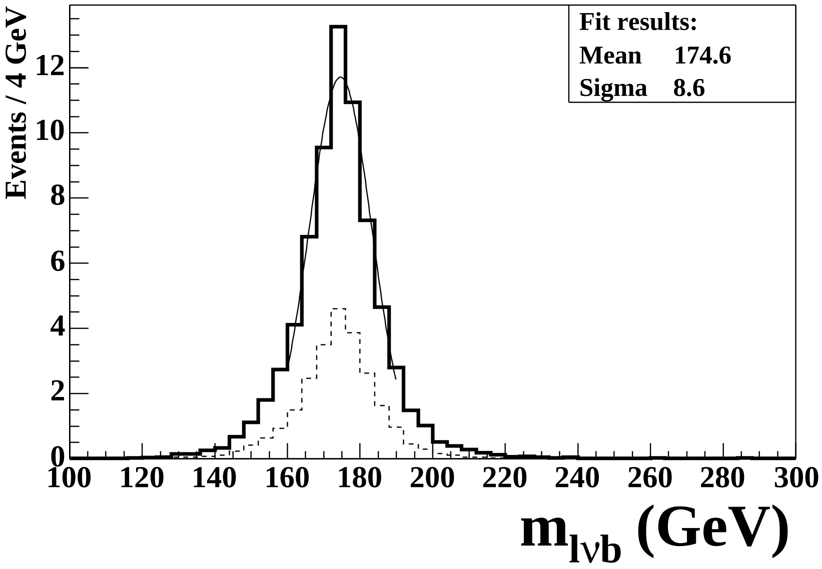

Figure 9.6: The reconstructed $m_{\ell\nu\mathrm{b}}$ for signal events with $m_{\mathrm{H}^0} = 120$ GeV. The distribution is normalized to the rate of expected events for $\mathcal{L} = 30\ \mathrm{fb}^{-1}$. The dashed histogram shows the fraction of correctly reconstructed top quarks. The wrong combinations also peak at the top-quark mass, since Equation 9.3 biases them towards m_{t}.

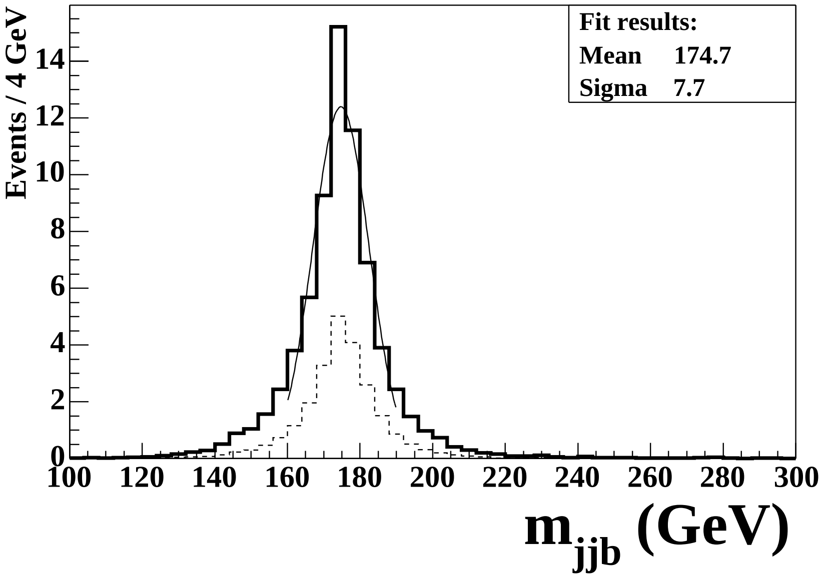

Figure 9.7: The reconstructed m_{jjb} for signal events with $m_{\mathrm{H}^0} = 120$ GeV. The distribution is normalized to the rate of expected events for $\mathcal{L} = 30\ \mathrm{fb}^{-1}$. The dashed histogram shows the fraction of correctly reconstructed top quarks.

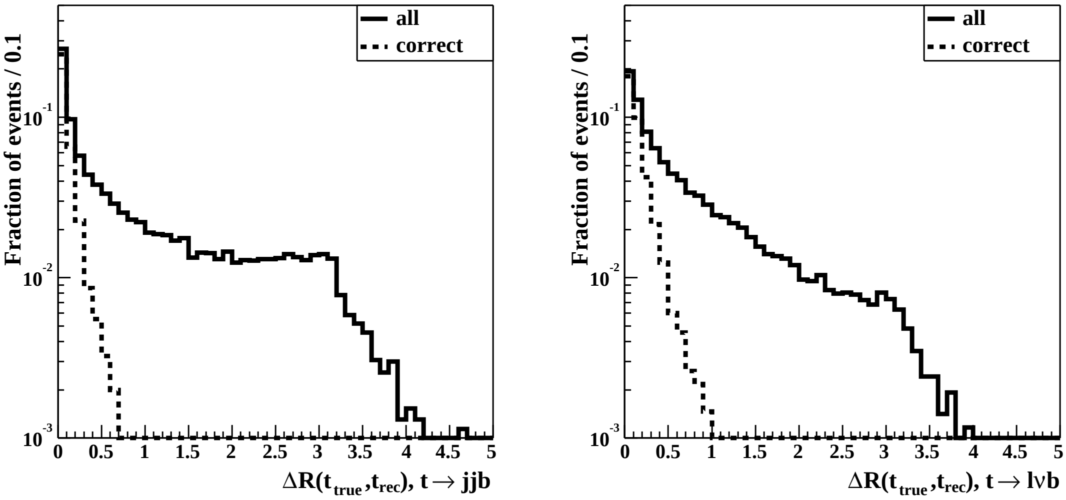

Figure 9.8: Difference ΔR between the generated and the reconstructed top quarks. The histograms are normalized to Unity.

9.1.5 The reconstructed m_{bb} spectra

The Higgs boson mass for $m_{\mathrm{H}^0} = 120$ GeV, reconstructed from the two remaining b-jets, is shown in Figure 9.9. For the background the reconstructed m_{bb} spectra are shown separately for each contribution in Figure 9.10.

In signal events, the m_{bb} spectrum shows a peak near the simulated Higgs boson mass, but it reveals also large tails from events where the wrong b-jets are chosen. A Gaussian is fitted to the peak in order to determine the value and resolution of the reconstructed Higgs boson mass. This is accomplished by fitting a combination of a polynomial and an exponential function, to account for the combinatorial part, plus a Gauss function for the peak, see Equation 9.4. The fit is applied in the mass range 10 GeV $< m_{\mathrm{bb}} <$ 300 GeV.

$$\text{fit function} = \left(a_0 + a_1 x + a_2 x^2\right) \cdot e^{-bx} + \mathrm{Gauss}(\mathrm{A}_0, \sigma, \mathrm{m}^{\mathrm{fit}}_{\mathrm{H}^0}) \qquad (9.4)$$

The fits are shown in Figure 9.11 for Higgs boson masses of 80, 100, 120, and 140 GeV, and the fit parameters describing the Gaussian part are listed in Table 9.1. One thing to notice is that the peak appears at slightly lower masses than the generated mass. The shift is 4%–8%, depending on m_{H^0}. This behavior can be attributed to a non-optimal jet calibration within ATLFAST and is investigated further in Section 9.1.5.2. The width of the peak is 10.6 GeV for $m_{\mathrm{H}^0} = 80$ GeV and increases to 15.2 GeV for $m_{\mathrm{H}^0} = 140$ GeV. The distribution of the QCD $\mathrm{t\bar{t}b\bar{b}}$ background clusters at masses below 90 GeV while the $\mathrm{t\bar{t}b\bar{b}}$ (EW) background peaks at the Z^0 mass. To reject background, a mass cut is introduced to select only events around the signal mass peak. Thus, the selection becomes dependent on the signal mass hypothesis. Selected events must lie within $m^{\mathrm{fit}}_{\mathrm{H}^0} \pm 30$ GeV, where $m^{\mathrm{fit}}_{\mathrm{H}^0}$ is the position of the mass peak from Table 9.1.

The figures of reconstructed masses show as dashed lines the fraction of events with correct assignment of the reconstructed particles to the original partons. For a single top quark, the correct b-jet is found in about 50% of all cases. The two correct b-jets from the decay of the Higgs boson are found in about 27% and corresponds to the fraction of events in which the correct b-jets are found for *both* top quarks. This purity is larger for events

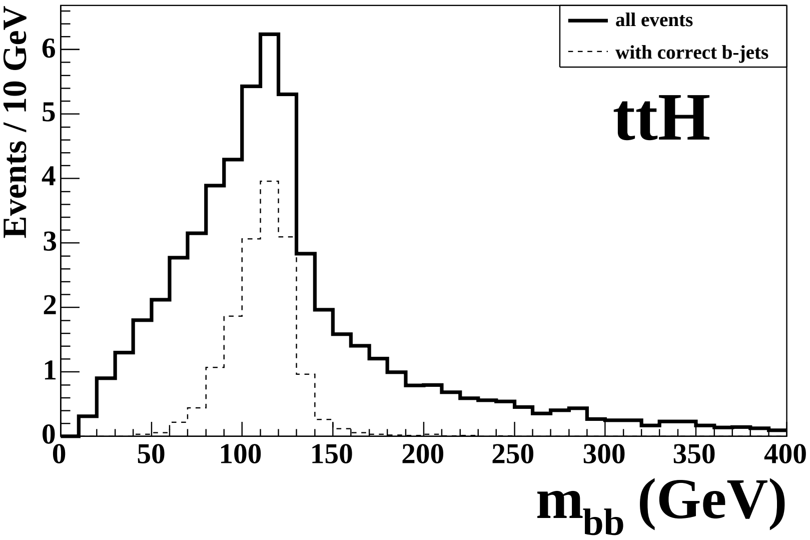

Figure 9.9: The reconstructed Higgs boson mass for $m_{H^0} = 120$ GeV. The distribution is normalized to the rate of expected events for $\mathcal{L} = 30$ fb^{-1}. The dashed line indicates the fraction of events where both b-jets actually stem from the Higgs boson decay.

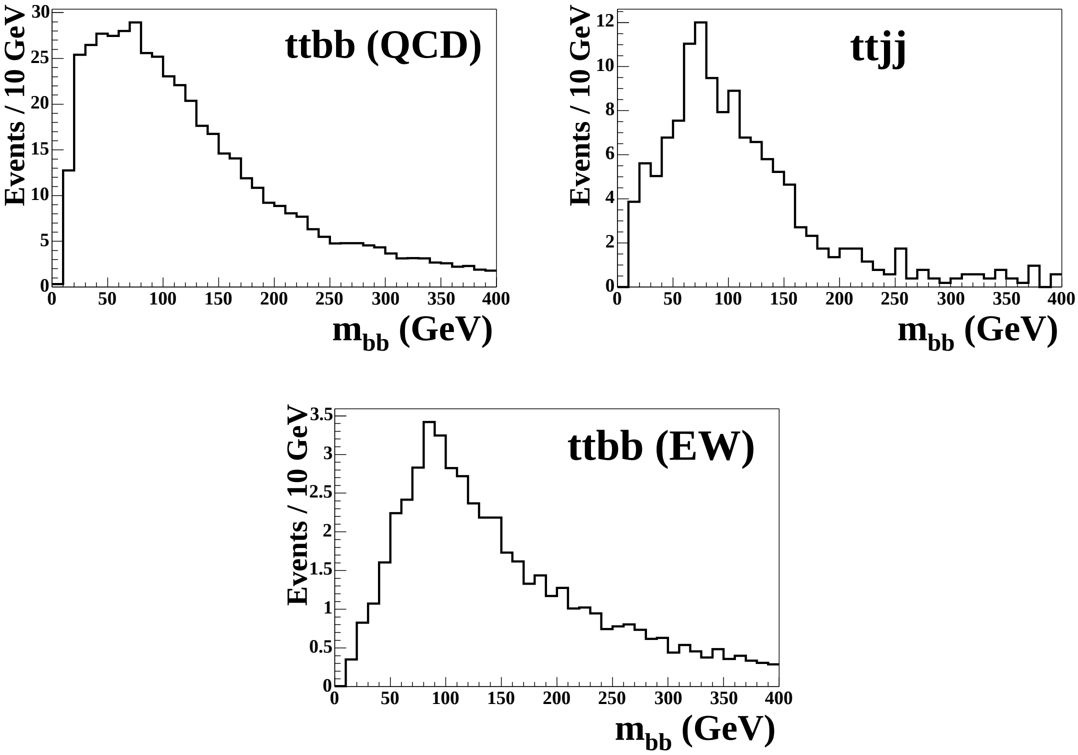

Figure 9.10: The reconstructed m_{bb} spectra for the background contributions. The distributions are normalized to the rate of expected events for $\mathcal{L} = 30$ fb^{-1}.

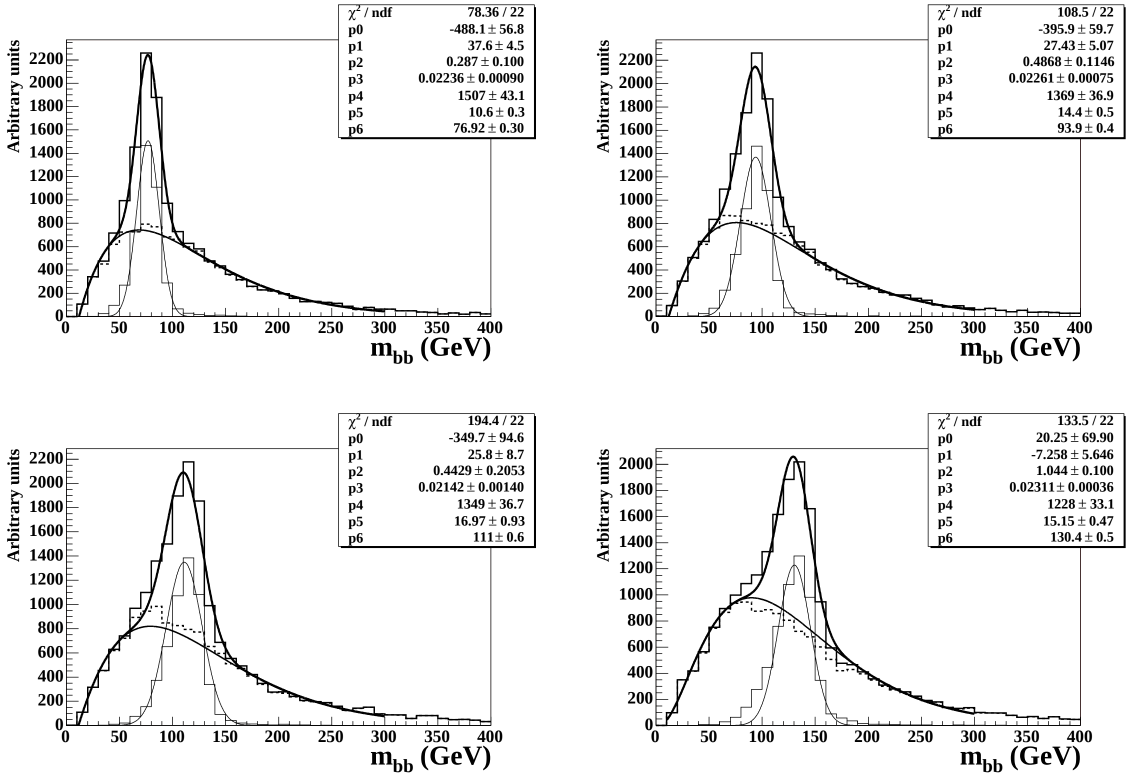

Figure 9.11: Fitted mass spectra of signal events for TDR reconstruction for $m_{\mathrm{H}^0} = 80, 100, 120, 140$ GeV. The thick line is the resulting fit to the complete spectrum in the range 10 GeV $< m_{\mathrm{bb}} <$ 300 GeV. The two thin lines show the fits to the combinatorial permutations (dashed histogram) and to the correctly reconstructed events (Gaussian-shaped histogram with thin line). The fit parameters p0–p6 correspond to the parameters in Equation (9.4) in the same order.

Table 9.1: Results for the parameters describing the Gaussian part of Equation 9.4 in signal events.

TDR method, low luminosity				
m_{H^0}(GeV)	$m^{\mathrm{fit}}_{\mathrm{H}^0}$(GeV)	$\Delta m^{\mathrm{fit}}_{\mathrm{H}^0}$(GeV)	σ(GeV)	$\Delta\sigma$(GeV)
80	76.9	0.3	10.6	0.3
90	85.7	0.3	13.1	0.4
100	93.9	0.4	14.4	0.5
110	103.3	0.4	14.5	0.6
120	111.0	0.6	17.0	0.9
130	120.5	0.5	15.8	0.6
140	130.4	0.5	15.2	0.5

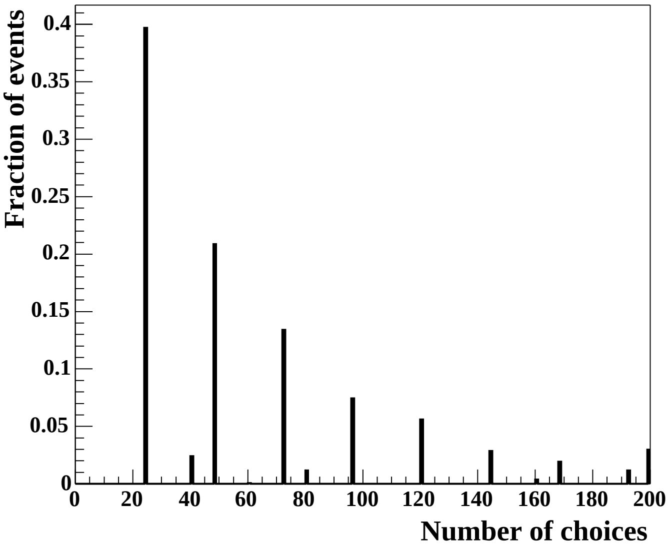

Figure 9.12: Number of choices in the TDR event reconstruction. The histogram is normalized to Unity. Events with more than 200 choices are accumulated in the last bin.

inside the m_{bb} window and amounts to about 50% for the b-jets assigned to the Higgs boson candidate. These numbers should be compared to the purities one would get if no reconstruction of the final state were done: The probability of selecting two correct b-jets out of four b-jets is $1/6 \approx 17\%$ which is much less than 27% obtained after reconstruction. Nevertheless, this figure seems to be small, but one has to keep in mind that the situation is complicated by possible mistag of light jets from the decay of the W boson or from gluon radiation and by the ambiguity in the solutions for the neutrino momentum. The total number n_c of choices to find the b-jets for the top quark decays, the light jets for the hadronic W decay and the solution for p_ν^z is given by

$$n_c = \frac{n_{\text{b-jet}}!}{(n_{\text{b-jet}} - 2)!} \cdot n_{jj} \cdot n_{\mathrm{sol}}, \tag{9.5}$$

where $n_{\text{b-jet}}$ is the number of b-tagged jets in the event, n_{jj} is the number of jet-pair candidates for the hadronic W decay in the acceptance window, and n_{sol} is the number of solutions for p_ν^z (usually two). Most events have four b-tagged jets which leads to a series of $n_{jj} \cdot 24$ possible choices. Some events have five b-tagged jets which gives $n_{jj} \cdot 40$ possible choices. The spectrum of choices is shown in Figure 9.12. While in most of the events there are 24 possibilities, there is a substantial fraction with more than 100 possible choices.

The sum spectra of all backgrounds and a signal from a 120 GeV Higgs boson are shown in Figure 9.13, normalized to expected event rates for an integrated luminosity of 30 fb^{-1}. The signal sits on the shoulder of a much larger background distribution. Obviously, even a modest increase in the prediction of the background rate would complicate establishing the signal peak.

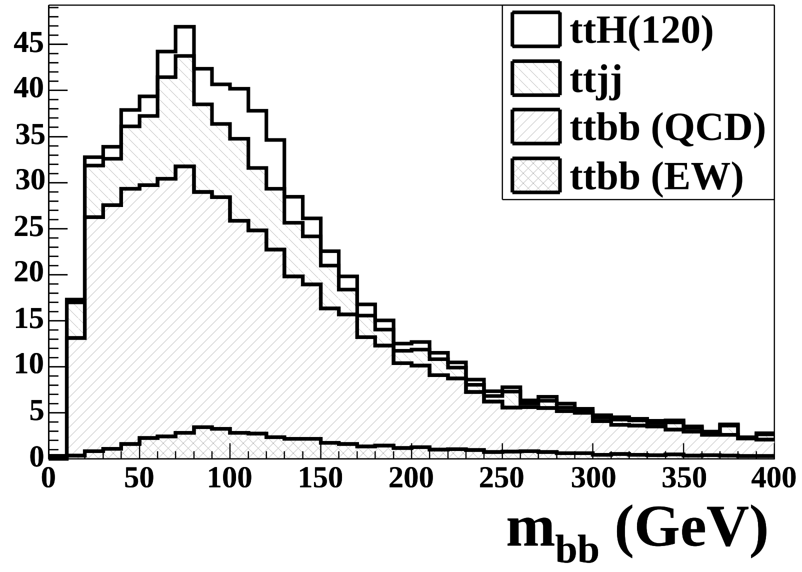

Figure 9.13: The sum of the reconstructed m_{bb} spectra for signal and background normalized to the rate of expected events for $\mathcal{L} = 30\ \mathrm{fb}^{-1}$.

9.1.5.1 Combinatorics in the reconstructed mass spectra

The shapes of the reconstructed mass spectra are significantly different from the distributions at parton level. This is not only due to effects from the detector energy and mass resolution. An important role plays the misidentification of light jets as b-jets and the incorrect association of b-jets from the decay of the Higgs boson to the hadronic and the semi-leptonic top quark decay. These two effects have a big impact on the shape of the background.

In order to investigate this issue the $\mathrm{t\bar{t}b\bar{b}}$ background and the signal are studied in more detail. The samples are divided into two complementary subsamples:

1. A subset where at least on light jet is misidentified as a b-jet or at least one b-jet is misidentified as a light jet ('fake jets').

2. A subset with correct identification of the jet flavors ('true jets').
   This sample is further split into two subsets

   a) with correct association of the b-jets and light jets to the top quark decays ('correct pairing'),

   b) with at least one incorrect association ('wrong pairing').

The resulting distributions are plotted in Figure 9.14. There is a significant shift towards higher masses due to the contribution of events with fake jets, which make about 40% out of all events. This fraction has of course a strong dependence on the b-tagging performance, and the numbers given here are valid for $\varepsilon_{\mathrm{b}} = 0.6$, $\mathrm{R_j} = 100$, $\mathrm{R_c} = 10$.

The fraction of events with 'true jets' follows closer the shape of the original partons, although the tail to higher masses is more pronounced due to incorrect jet pairing. The

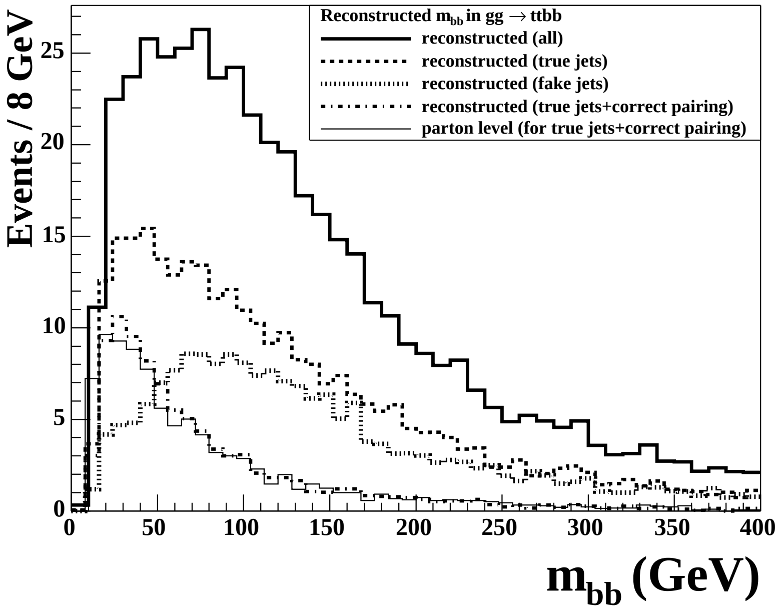

Figure 9.14: The main $t\bar{t}b\bar{b}$ background and the contribution with true jets, fake jets, and correct pairing. The histograms are normalized to the expected rate for $\mathcal{L} = 30\ \text{fb}^{-1}$.

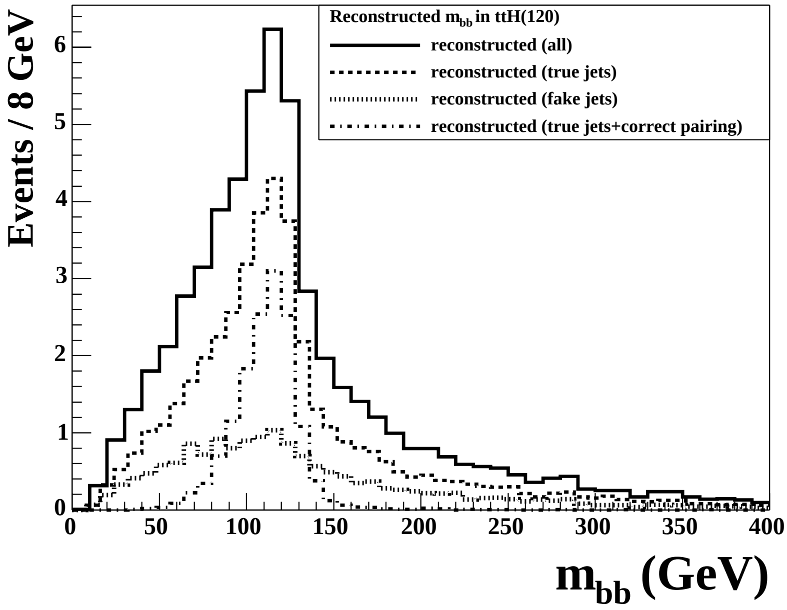

Figure 9.15: Same as Figure 9.14 but for the signal with $m_{H^0} = 120$ GeV. The parton level distribution for a 120 GeV Higgs boson is very narrow and is not shown. The histograms are normalized to the expected rate for $\mathcal{L} = 30\ \text{fb}^{-1}$.

fraction of events with correct pairing is only about 32% of the events with true jets, but it is close to the parton distribution.

For the signal the effect of fake jets and incorrect pairing is less distinct, but nevertheless visible in larger tails and as an accumulation of events on the left side of the peak as shown in Figure 9.15.

This overall shift to higher masses of the background and the broadening of the signal distribution has a negative impact on the signal to background ratio in the region of the Higgs boson peak. The fraction of fake jets can be reduced by selecting a b-tag with higher rejection power against light and c-jets, but this is always at the cost of efficiency for finding true b-jets. As will be shown in Section 10.1 the choice of $\varepsilon_{\mathrm{b}} = 60\%$ is optimal in terms of $S/\sqrt{B}$.

9.1.5.2 Jet calibration and impact on reconstructed masses

The reconstructed mass of the Higgs boson, m_{bb}, peaks at 4%–8% smaller values than the simulated mass. For instance, for a simulated mass $m_{\mathrm{H}^0} = 120$ GeV the peak appears at ~ 111 GeV. The reason for the shift is the jet calibration in ATLFAST which gives good results for light jets, but too small energies for b-jets in $\mathrm{t\bar{t}H}^0$ events.

Figure 9.16 stresses this point. The first two rows show the invariant mass of jet-pairs from hadronic $\mathrm{W}^{\pm}$ decays and of b-jet-pairs from the decay of the Higgs boson before and after jet calibration, normalized to the generated masses. To clean the samples, only jets were used with parton-jet matching in $\Delta\mathrm{R} < 0.2$. The invariant jj-mass is centered around 1.0 after calibration, but the invariant $\mathrm{b\bar{b}}$ mass has its mean at 0.93. One can conclude that the calibration of b-jets, derived from rather clean $\mathrm{W}^{\pm}\mathrm{H}^0$ events [39], slightly underestimates the b-jet energy in the more crowded environment of $\mathrm{t\bar{t}H}^0$ events. A different approach to optimize the b-jet calibration is performed in Ref. [48] using $\mathrm{t\bar{t}H}^0$ and $\mathrm{t\bar{t}b\bar{b}}$ events and Neural Networks. The study applies isolation cuts of $\Delta\mathrm{R} > 0.7$ around jets in order to clean the samples. The improvement is rather small, still. Applying the same isolation requirement $\Delta\mathrm{R} > 0.7$ to the analysis described in this section gives somewhat better reconstructed masses of the Higgs boson, with a mean of 0.97 (bottom row of Figure 9.16). However, the more stringent isolation reduces the selection efficiency significantly and the resulting significances are not acceptable. Therefore, the current analysis stays with the jet calibration implemented in ATLFAST.

9.1.6 Results for the TDR reconstruction method

The steps of the classical analysis are briefly summarized in the following:

1. selection of events with $\geq$1 isolated lepton, at least 6 jets, 4 of which are tagged as b-jets,
2. reconstruction of the neutrino four-vector,
3. establishing a list of non-b-jet pairs with $|m_{\mathrm{jj}} - m_{\mathrm{W}^{\pm}}| < 25$ GeV,
4. finding the combination of p_{ν}^{z}, 4 b-jets and 2 non-b jets which gives invariant masses $m_{\ell\nu\mathrm{b}}$ and m_{jjb} closest to m_{t}, keeping only events with $|m_{\ell\nu\mathrm{b}} - m_{\mathrm{t}}| < 20$ GeV and $|m_{\mathrm{jjb}} - m_{\mathrm{t}}| < 20$ GeV.
5. calculating m_{bb} of the remaining b-jets with largest p_T and keeping events with $|m_{\mathrm{bb}}^{\mathrm{fit}} - m_{\mathrm{H}^0}| < 30$ GeV.

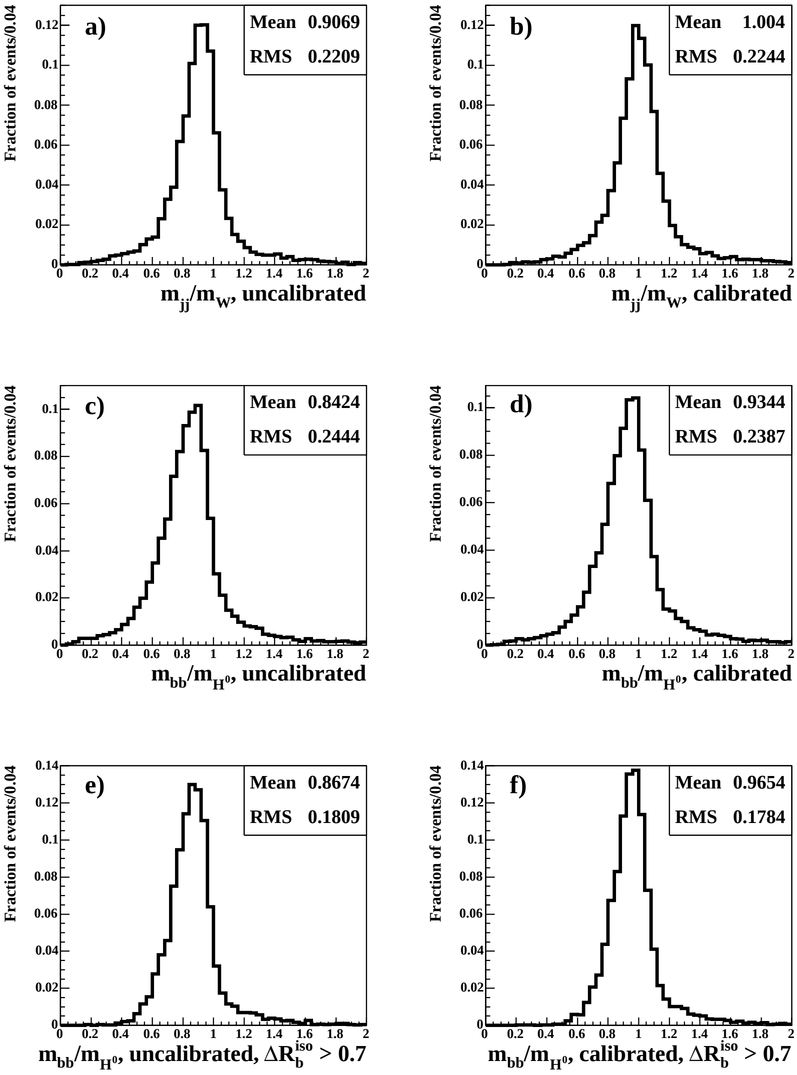

Figure 9.16: Comparison of jet calibration for light-jets and for b-jets. Signal events with $m_{\mathrm{H}^0} =$ 120 GeV are used.

The efficiencies and the number of expected events for a luminosity of 30 fb^{-1} for these steps of the analysis are reported in Table 9.2 and 9.3 for the selection of a Higgs boson with a mass of 120 GeV. The signal efficiency is 0.9%, and 28 signal events and 193 background events are expected after three years of running at low luminosity (10 fb^{-1} per year). The irreducible $\mathrm{t\bar{t}b\bar{b}}$ background accounts for 69% of the total background (for the b-tag parametrization described in Section 8.4).

The results for other Higgs boson masses are given in Table 9.4 for $m_{\mathrm{H}^0} = 80$ GeV to $m_{\mathrm{H}^0} = 140$ GeV. Although the existence of a Standard Model Higgs boson below 114.4 GeV has been ruled out by the LEP experiments at the 95% confidence level [16], the signal efficiency and expected background rates for masses below this limit are of interest for scans of the parameter space in models beyond the Standard Model, *e.g.*, in the Minimal Supersymmetric Standard Model. Such a scan, using results from this work, is described in Section 13.3. The significance for a 120 GeV Higgs boson is $S/\sqrt{B} = 2.0$

Table 9.2: Efficiencies after each step of the analysis for $m_{\mathrm{H}^0} = 120$ GeV. The relative efficiencies with respect to the previous step are given in parenthesis.

Cut	$\mathrm{t\bar{t}H^0}$(120) (%)	$\mathrm{t\bar{t}b\bar{b}}$(QCD) (%)	$\mathrm{t\bar{t}jj}$ (%)	$\mathrm{t\bar{t}b\bar{b}}$(EW) (%)
1ℓ and 6 jets	46.2	36.9	15.4	34.7
4 b-jets	3.8 (8.1)	1.5 (4.0)	0.01 (0.1)	1.5 (4.3)
2 tops reconstructed	2.3 (60.0)	0.9 (59.8)	4.7×10^{-3} (45.6)	0.9 (59.2)
m_{t} inside mass window	1.8 (79.2)	0.7 (76.8)	3.1×10^{-3} (65.3)	0.7 (77.7)
m_{bb} inside mass window	0.9 (49.0)	0.2 (26.0)	1.0×10^{-3} (34.1)	0.2 (30.1)

Table 9.3: Expected events after the steps of the analysis for $m_{\mathrm{H}^0} = 120$ GeV and $\mathcal{L} = 30$ fb^{-1}.

Cut	$\mathrm{t\bar{t}H^0}$(120)	$\mathrm{t\bar{t}b\bar{b}}$(QCD)	$\mathrm{t\bar{t}jj}$	$\mathrm{t\bar{t}b\bar{b}}$(EW)	$\sum$Bkg
1ℓ and 6 jets	1 471	27 802	661 783	2 701	692 286
4 b-jets	119.1	1 100.7	441.3	116.7	1 658.7
2 tops reconstructed	71.5	658.9	201.2	69.1	929.2
m_{t} inside mass window	56.6	505.9	131.3	53.7	690.9
m_{bb} inside mass window	27.8	131.2	44.7	16.6	192.5

Table 9.4: Expected events for the analysis of Higgs boson masses between 80 GeV and 140 GeV for an integrated luminosity of 30 fb^{-1}.

m_{H^0} (GeV)	80	90	100	110	120	130	140
$\varepsilon_{\mathrm{t\bar{t}H^0}}$ (%)	0.75	0.82	0.84	0.86	0.88	0.87	0.91
$\mathrm{t\bar{t}H^0}$	78.4	64.6	50.5	39.2	27.8	17.7	9.3
$\mathrm{t\bar{t}b\bar{b}}$ (QCD)	155.3	150.3	146.5	137.8	131.2	123.4	113.9
$\mathrm{t\bar{t}jj}$	57.7	57.1	54.2	48.6	44.7	41.4	38.0
$\mathrm{t\bar{t}b\bar{b}}$ (EW)	16.7	17.3	17.5	17.1	16.6	15.4	13.9
total bkg.	229.7	224.7	218.2	203.5	192.5	180.2	165.8
$S/\sqrt{B}$	5.2	4.3	3.4	2.7	2.0	1.3	0.7
$\sigma_{\mathrm{Poisson}}$	4.9	4.1	3.2	2.6	1.9	1.2	0.6

and falls rapidly for higher masses due to both the decreasing $\mathrm{t\bar{t}H^0}$ cross section and the smaller branching ratio $\mathrm{H{\rightarrow}b\bar{b}}$. In Table 9.4 the significances are expressed both as $S/\sqrt{B}$ and as Poissonian significances $\sigma_{\mathrm{Poisson}}$. The Poissonian significances are calculated with the program `UWStatTools` [49].

Table 9.5: Settings and inclusive cross sections in the TDR and the current analysis. The $\mathrm{t\bar{t}}$+jets stands for $\mathrm{t\bar{t}}$ with additional jets of any flavor, including $\mathrm{t\bar{t}b\bar{b}}$. In the TDR analysis, $\mathrm{t\bar{t}b\bar{b}}$ events are generated with PYTHIA, and in 'this analysis' the AcerMC generator is used.

	TDR	this analysis
PDF	CTEQ4L	CTEQ5L
Q^2_{QCD}	$(m_{\mathrm{t}}^2 + p_T^2)$	$(m_{\mathrm{t}} + m_{\mathrm{H}^0}/2)^2$, except $\mathrm{t\bar{t}}$+jets
Generators	PYTHIA 5.7	PYTHIA 6.2 AcerMC 1.0
$\mathrm{t\bar{t}H^0}$ (100)	1.20 pb	0.84 pb
$\mathrm{t\bar{t}H^0}$ (120)	0.72 pb	0.52 pb
$\mathrm{t\bar{t}}$+jets	600 pb	491 pb
$\mathrm{t\bar{t}Z} \rightarrow \mathrm{t\bar{t}b\bar{b}}$	0.57 pb	
$\mathrm{t\bar{t}b\bar{b}}$ (EW)		0.89 pb

9.1.7 Comparison with results from the TDR

The results obtained in this analysis are different from those in the ATLAS Detector and Physics Technical Design Report (TDR). In this section the changes in the $\mathrm{t\bar{t}H^0}$, $\mathrm{H}\rightarrow\mathrm{b\bar{b}}$ channel with respect to the TDR analysis [28] are described. The focus in the TDR analysis is on a Higgs boson mass of 100 GeV, and so the same mass is used in this comparison. Further on, the cut on m_{bb} is applied to a central value of $m_{\mathrm{H}^0} = 100$ GeV, and not around $m_{\mathrm{bb}}^{\mathrm{fit}}$.

Changes have taken place in the cross section calculations, in the Monte Carlo generators and detector simulation, and in the preselection.

9.1.7.1 Cross sections

The TDR cross sections were calculated with CTEQ4L parton density functions. The change to the CTEQ5L PDFs results in a general decrease of the cross sections by about 20%. The leading order cross sections show a strong dependence on the choice of the Q^2_{QCD} scale. The TDR analysis used the default choices in PYTHIA (which in general depend on the process) whereas the scale in the current analysis is set to $Q^2_{\mathrm{QCD}} = (m_{\mathrm{t}} + m_{\mathrm{H}^0}/2)^2$, with the exception of the $\mathrm{t\bar{t}jj}$ background where the PYTHIA default is used as well. The signal cross sections and branching ratios for $\mathrm{H}\rightarrow\mathrm{b\bar{b}}$ are now taken from dedicated programs, HQQ [44] and HDECAY [12], which give more accurate results.

The cross sections quoted in the TDR were obtained for the leptonic decay of one W ($\ell = \mathrm{e}$ or μ) and arbitrary decay of the other W. They are normalized to the inclusive cross sections and are compared in Table 9.5 to the numbers of the cross sections from Tables 8.2 and 8.3.

9.1.7.2 Monte Carlo generators

In both analyses the signal events and the reducible $\mathrm{t\bar{t}jj}$ background are generated with PYTHIA (version 5.7 and 6.2). In the TDR the irreducible QCD $\mathrm{t\bar{t}b\bar{b}}$ background and electroweak $\mathrm{t\bar{t}Z}$ events are generated with PYTHIA, whereas these samples are generated by AcerMC in the current analysis. Significant changes are expected for the $\mathrm{t\bar{t}b\bar{b}}$ background in particular, because the parton shower approach in PYTHIA tends to underestimate this background. Figure 9.17 demonstrates that the events generated with the matrix element

Table 9.6: Cuts in the TDR and in the current analysis.

	TDR	this analysis
Preselection		
1 lepton	$p_{T_e} > 20$ GeV	$p_{T_e} > 25$ GeV
	$p_{T_\mu} > 6$ GeV	$p_{T_\mu} > 20$ GeV
	$\|\eta\| < 2.5$	$\|\eta\| < 2.5$
≥ 6 jets	$p_T > 15$ GeV	$p_T > 20$ GeV
	$\|\eta\| < 5$	$\|\eta\| < 5$
four b-jets	$\|\eta\| < 2.5$	$\|\eta\| < 2.5$
Cuts on reconstructed masses		
$m_{\ell\nu\mathrm{b}}$	$m_\mathrm{t} \pm 20$ GeV	
m_jjb	$m_\mathrm{t} \pm 20$ GeV	
m_bb	$m_{\mathrm{H}^0} \pm 30$ GeV	

Table 9.7: Width of reconstructed masses obtained from fits to t$\bar{\mathrm{t}}$H events with $m_{\mathrm{H}^0} = 100$ *GeV* and for a b-tag performance of $\varepsilon_\mathrm{b} = 60\%$, $\mathrm{R_c} = 10$, $\mathrm{R_j} = 100$.

	TDR	this analysis
$\sigma_{m_{\ell\nu\mathrm{b}}}$ (GeV)	8.6	8.5
σ_{m_jjb} (GeV)	9.8	7.6
σ_{m_bb} (GeV)	16.1	14.4

calculations in AcerMC have a slightly harder p_T spectrum of the b-jets, and a higher multiplicity of jets, shown here for jets with $p_T > 20$ GeV.

The TDR analysis takes into account only the resonant contribution from t$\bar{\mathrm{t}}$Z →t$\bar{\mathrm{t}}$b$\bar{\mathrm{b}}$ events. In this analysis the full contribution from electroweak gg→Z/γ^*/W→ t$\bar{\mathrm{t}}$b$\bar{\mathrm{b}}$ processes is used which are available with the advent of the AcerMC generator.

9.1.7.3 Reconstruction and event selection

The same reconstruction procedure is used for the TDR and the current analysis, but different p_T cuts are applied to account for the increased trigger thresholds in ATLAS. The changes are summarized in Table 9.6.

Table 9.7 compares the properties of the reconstructed top-quark and Higgs boson masses in t$\bar{\mathrm{t}}$H^0 events with $m_{\mathrm{H}^0} = 100$ GeV. The same mass resolution is achieved for the reconstruction of the semi-leptonic top-quark decay. A slightly better resolution is observed for m_jjb and m_bb with the current analysis due to an updated parametrization in the jet calibration [50].

The total selection efficiencies cannot be compared directly since the TDR analysis starts from a wider set of decay modes (one leptonic W decay is required with arbitrary decay of the other W). Thus, the efficiencies of the mass cuts on $m_{\ell\nu\mathrm{b}}$, m_jjb, and m_bb in the selection for a 100 GeV Higgs boson are compared here.

Table 9.8: Efficiencies of the mass cuts in the TDR and in the current analysis.

	$m_{\ell\nu\mathrm{b}}$, m_jjb in mass window	m_bb in mass window
	TDR	
t$\bar{\mathrm{t}}$H^0 (100)	38%	44%
t$\bar{\mathrm{t}}$+jets	23%	25%
	this analysis	
t$\bar{\mathrm{t}}$H^0 (100)	48%	51%
t$\bar{\mathrm{t}}$b$\bar{\mathrm{b}}$ (QCD)	46%	28%
t$\bar{\mathrm{t}}$jj	30%	39%

The efficiencies of the $m_{\ell\nu\mathrm{b}}$ and m_jjb cuts are 30% larger (relative) in the current analysis

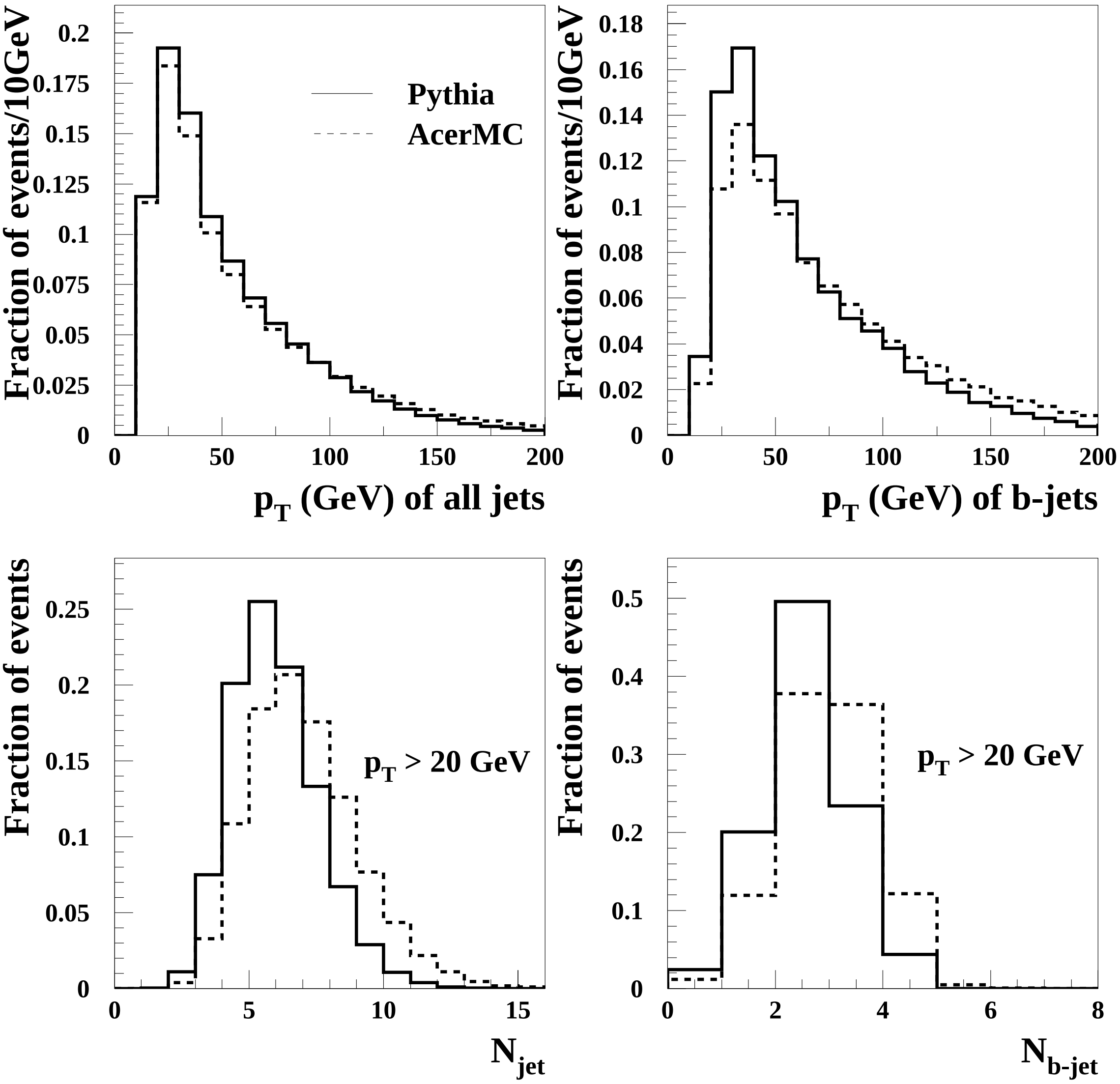

Figure 9.17: Comparison between the parton shower approach and the matrix element calculation for the $t\bar{t}b\bar{b}$ background. Shown is the p_T spectrum for all jets and for b-jets (top row), and the number of jets and b-jets with $p_T > 20\ GeV$ after jet calibration (bottom row). The histograms are normalized to Unity.

than in the TDR analysis. This increase in the efficiency corresponds to the smaller width of the reconstructed top-quark masses (Table 9.7). Since topological and kinematic properties of the irreducible background generated by AcerMC are much closer to the ones of the signal process, the efficiency of the $t\bar{t}b\bar{b}$ background is almost the same as for $t\bar{t}H^0$ events. A better mass resolution of m_{bb} yields also higher efficiency for the m_{bb} cut, most significant in the case of the $t\bar{t}jj$ background.

Finally, the TDR analysis selects 61 signal events and expects 150 events from background (dominated by 130 events from $t\bar{t}$+jets). With the current analysis 49 signal events and 211 background events (159 events from $t\bar{t}b\bar{b}$) are expected. These numbers refer to the selection for a 100 GeV Higgs boson with a cut $m_{H^0} \pm 30$ GeV on m_{bb}. The significant increase in the background arises from the more reliable prediction of the irreducible $t\bar{t}b\bar{b}$ background based on matrix element calculations and from the inclusion of the complete $t\bar{t}b\bar{b}$ background mediated by weak gauge bosons. The loss in signal events is due to smaller cross sections obtained with the CTEQ5L parton distribution functions.

9.1.8 Conclusions on the TDR reconstruction method

It has been shown that with the current knowledge the sensitivity of the channel $t\bar{t}H^0$, $H\rightarrow b\bar{b}$ is smaller than the results given in the TDR. For $m_{H^0} = 100$ GeV the expected significance is 3.4 compared to 5.0 in the TDR. For $m_{H^0} = 120$ GeV the expected significance is 2.0 compared to 3.6 in the TDR. These changes are due to a more precise estimate of the irreducible $t\bar{t}b\bar{b}$ background and changes in the cross section for both signal and background with the introduction of the CTEQ5L structure functions and the choice of a different default Q^2_{QCD} scale.

It has also been noted that the influence of the light-quark jet rejection and the jet pairing on the reconstructed distributions of m_{bb} is significant. The jet pairing is studied in the next section, where new methods are developed to reconstruct the final state and to improve the separation of the signal from the background.

9.2 Improved analysis

This thesis concentrates on possible improvements of the reconstruction and analysis procedure in the $\mathrm{t\bar{t}H^0}$ channel. An investigation of the ATLAS b-tagging performance is subject of Ref. [51]. Three fields for optimization of the reconstruction seem to be promising:

Neutrino reconstruction: As described in section 9.1.2, about 25% of all events are lost because the z-component of the neutrino momentum and therefore the semileptonic top quark decay can not be reconstructed. A method to determine or approximate p_ν^z, if the calculation from Equation 9.1 fails, could recover these events.

Jet pairing: The jet multiplicity in both the signal and background events is high, and so is the number of combinatorial choices to match six jets to the decay products of the two top quarks and the Higgs boson. More details can be found in Section 9.1.5 on page 68. With the TDR reconstruction method the two b-jets assigned to the Higgs boson actually stem from the Higgs boson decay for only 27% of the reconstructed signal events in the whole m_{bb} mass range. This is still an improvement considering the fact that without the reconstruction of the top quarks the probability to select the correct b-jets out of all b-jets is much less than 17%. For events inside the mass window $m_{\mathrm{H^0}}^{\mathrm{fit}} \pm 30$ GeV the correct b-jet fraction increases to about 50% in the TDR method. An improved jet pairing would sharpen the signal peak and bring the background shape closer to the true shape where the bulk of the distribution is located at masses below 80 GeV, cf. Figures 9.14 and 9.15.

Final event selection for events inside the m_{bb} acceptance window: The cut on m_{bb} reduces the background by 70–80% (depending on $m_{\mathrm{H^0}}$). This is to be compared to a loss in the signal efficiency of about 55%. Exploring differences in the event topology for the events surviving this mass cut may provide further means to discriminate signal from background.

9.2.1 Top quark reconstruction

The same preselection as described in section 9.1.1 is used.

The problem that p_ν^z can not be calculated arises for those 25% of the events, where the measured transverse mass of the lepton-neutrino system is larger than the W mass. This happens mainly due to a significant mismeasurement of p_x^{miss} or p_y^{miss}. For such events (denoted in the following as events with no solution, $n_{\mathrm{sol}} = 0$) the neutrino and the lepton are close in the z-direction but separated in x and y. For events with $n_{\mathrm{sol}} \geq 1$ the situation is vice versa, as is depicted in Figure 9.18.

To recover events with $n_{\mathrm{sol}} = 0$ the approximation $p_\nu^z = p_\ell^z$ is made (collinear approximation). To constrain the invariant mass $m_{\ell\nu}$ to the W mass, the neutrino four-momentum is scaled so that $m_{\ell\nu} = m_{\mathrm{W^\pm}}$. The resolution of p_ν^z after scaling is shown in Figure 9.19. This procedure increases the efficiency for the reconstruction of the leptonic W decay to 100%. Only a small degradation of the mass resolution of the reconstructed semileptonic top quark decay is observed. Including the events with $n_{\mathrm{sol}} = 0$ the resolution degrades from 8.6 GeV to 9.1 GeV.

9.2.2 Jet pairing

In the TDR method the combination which minimizes the expression $\Delta = (m_{\ell\nu\mathrm{b}} - m_{\mathrm{t}})^2 + (m_{\mathrm{jjb}} - m_{\mathrm{t}})^2$ is chosen in order to find the correct jets from the top-quark decays. This

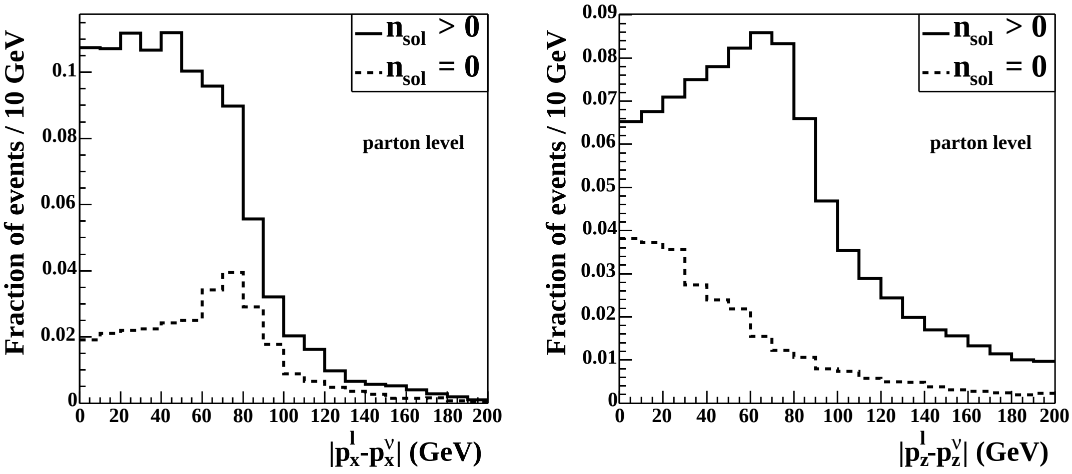

Figure 9.18: The differences between the neutrino and the lepton momentum components for events with $n_{sol} \geq 1$ and for events with $n_{sol} = 0$. Left: difference in p_x. Right: difference in p_z. The full histograms are normalized to Unity, and the dashed histograms according to the ratio of events with $n_{sol} = 0$ to events with $n_{sol} > 0$.

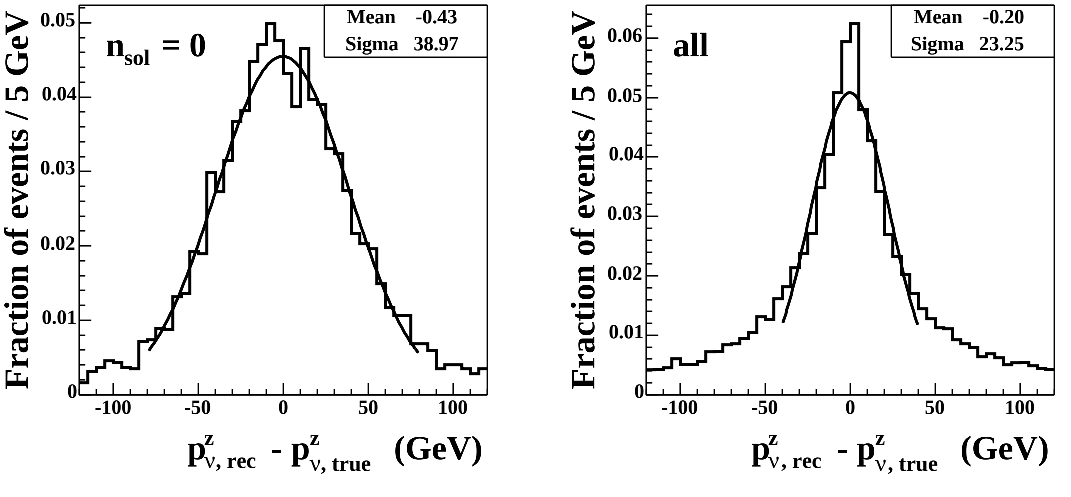

Figure 9.19: Resolution of the reconstructed neutrino momentum with the collinear approximation method. Left: Resolution for the subset of events where the approximation $p^z_\nu = p^z_\ell$ is applied. Right: All events. The histograms are normalized to Unity.

recipe only makes use of the invariant top-quark masses and does not take into account additional information like, for example, spatial distances between jets.

The jet pairing can possibly be improved by using additional information from the event topology. The most promising variables are

1. m_{jj}: the invariant mass of the pair of light jets from the hadronic W decay,
2. m_{jjb}: the invariant mass of the two light jets and one b-jet from the hadronic top quark decay,
3. $\Delta\mathrm{R}(\ell, \mathrm{b})$: the distance in R between the lepton and the b-jet assumed to originate from the same top quark,
4. $m_{\ell\nu\mathrm{b}}$: the invariant mass of the lepton, the reconstructed neutrino and one b-jet coming from the semileptonic top quark decay,
5. ΔR (b,jj): the distance in R between the b-jet and the system of light jets from the hadronic top quark decay,
6. $\angle$(j,j): the angle between the two light jets from the hadronic W decay,

These variables are shown in Figure 9.20. The reference distributions are created from signal events for correct and all wrong combinations of the jet pairing. If there is more than one solution for p_ν^z the one which minimizes $|m_{\ell\nu\mathrm{b}} - m_{\mathrm{t}}|$ is selected. In the analysis for each possible combination a pairing likelihood is calculated from these distributions, and the combination with the highest likelihood is chosen. The likelihood technique is explained in Appendix B, and the distribution of the likelihood output pLH for correct and wrong combinations in signal events is displayed in Figure 9.21. Events are kept only if $pLH > 0.7$ to assure a good quality of the jet pairing. If both distributions are normalized to Unity (not shown in Figure 9.21) the normalized pLH distribution of the correct pairing is dominating over the distribution of wrong pairings for values larger than 0.7. The efficiency for this cut is about 88% for the $\mathrm{t\bar{t}H^0}$ signal and the $\mathrm{t\bar{t}b\bar{b}}$ backgrounds, and about 70% for the $\mathrm{t\bar{t}jj}$ background.

The likelihood method is compared to the TDR method in Figure 9.22 and in Table 9.9. With the likelihood method the peak of the top quark masses is being reconstructed at slightly lower masses, and the width increases by about 2.0 GeV. However, the purity of the jet pairing is higher for the likelihood reconstruction (the purity $\mathcal{P}^b$ given in Table 9.9 refers only to the b-jets in the top quark decays). This means that the simple matching criterion used in the TDR method introduces a small bias in the mass distributions towards the expected top quark mass. As a consequence, no cut is applied on the reconstructed top quark masses any longer, thus gaining another 20% of efficiency. On the other hand, loosening cuts on the reconstructed masses could introduce additional backgrounds which do not contain a pair of top-quarks. This issue is discussed in section 9.2.5.

The likelihood output distributions have a sharp peak at 0 for wrong combinations and at 1 for correct combinations. Nevertheless, the gain in purity with the likelihood pairing is rather small (a few percent). This can be explained by the large number of wrong combinations. The absolute normalization in Figure 9.21 is arbitrary, but the relative normalization between correct and wrong combinations is conserved. For 64% of the selected events there exists a wrong combination with a likelihood higher than the one of the correct combination. In most of these cases the superior wrong combination has one b-quark from the Higgs boson decay assigned to the top quark decay and vice

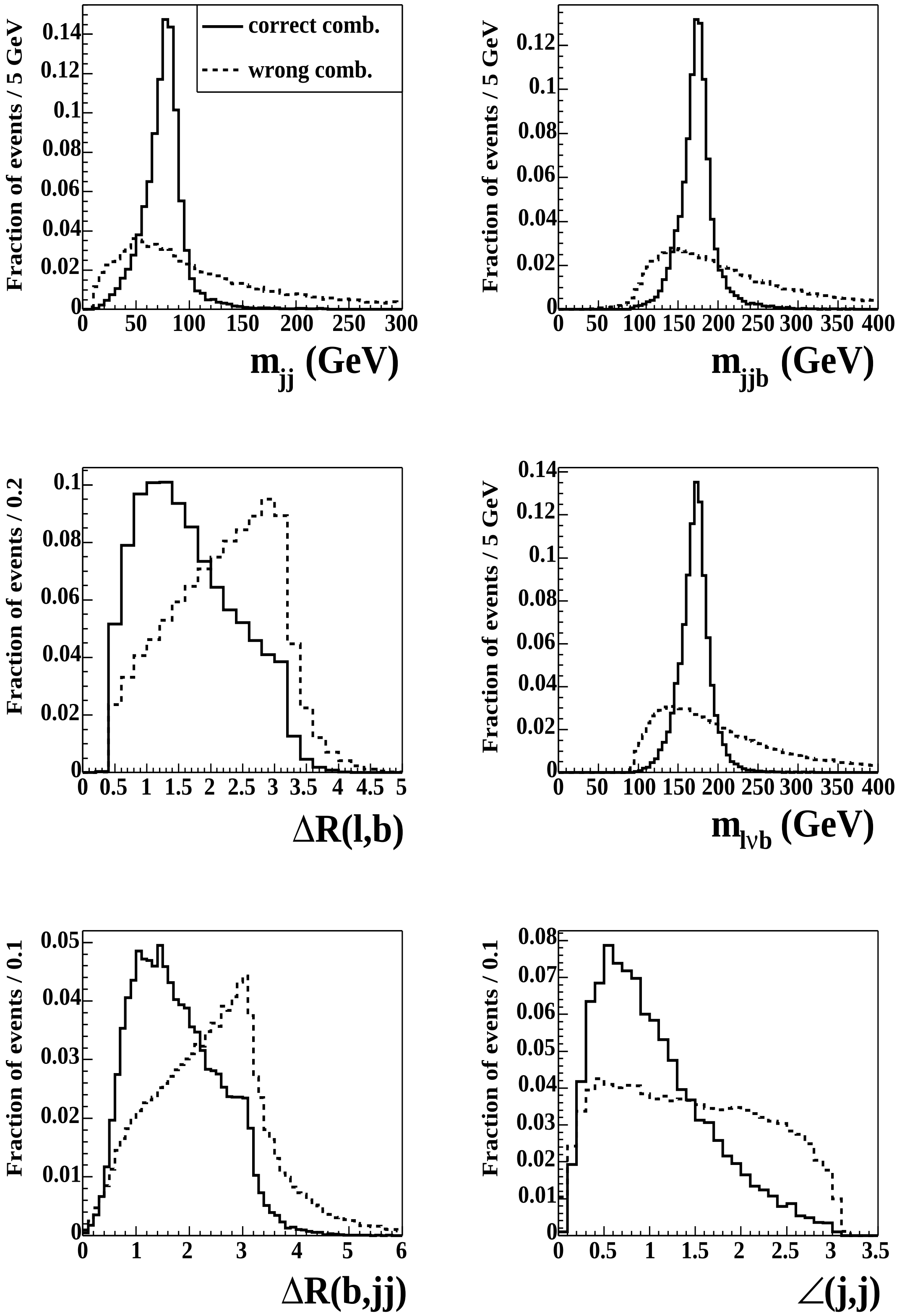

Figure 9.20: Input variables to the pairing likelihood for correct and wrong combinations of the jet pairing. Signal events are used to generate these reference distributions. The histograms are normalized to Unity.

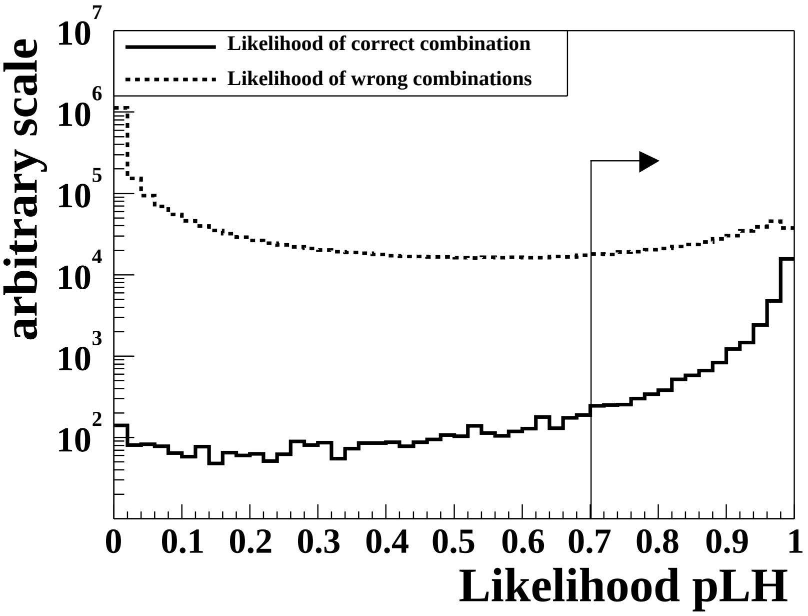

Figure 9.21: Jet-pairing: the likelihood output for correct and wrong combinations in signal events. The absolute normalization is arbitrary, but the relative normalization between correct and wrong combinations is conserved.

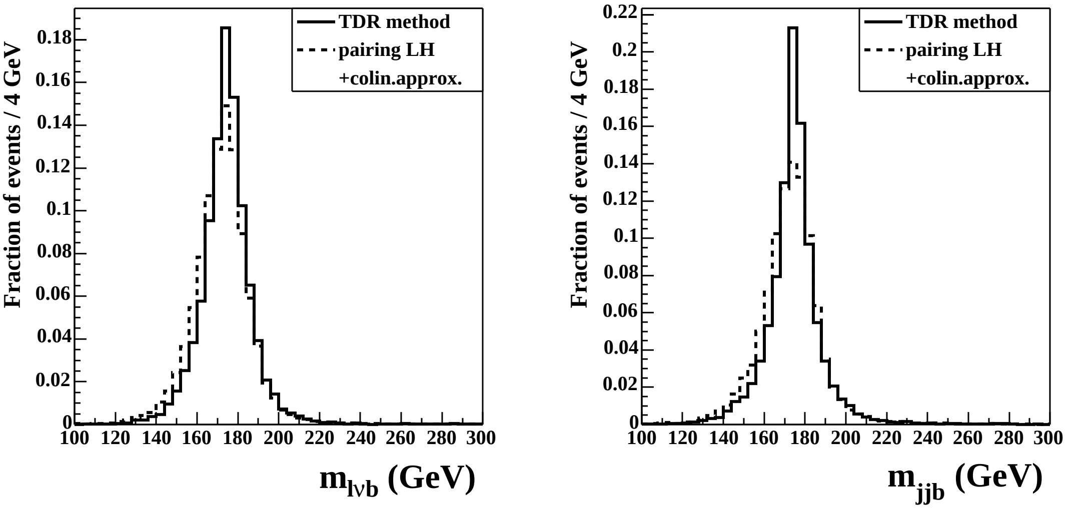

Figure 9.22: Comparison of the reconstructed top quark masses for the TDR method and the likelihood technique for signal events with $m_{H^0} = 120$ GeV. Each histogram is normalized to Unity.

Table 9.9: Peak position m, resolution σ, efficiency ε, and purity $\mathcal{P}$ of the b-jets of the reconstructed top quarks for signal events with $m_{\mathrm{H}^0} = 120$ GeV. Events from the whole m_{bb} spectrum are used. $\varepsilon_{\mathrm{sol}}$ is the efficiency to calculate p_ν^z. $\varepsilon_{\mathrm{jj}}$ is the efficiency to find at least one jj-candidate inside the acceptance window $m_{\mathrm{W}} \pm 25$ GeV. No such acceptance window is used in the likelihood method.

Method	$< m_{\ell\nu\mathrm{b}} >$ (GeV)	$\sigma_{\ell\nu\mathrm{b}}$ (GeV)	$\varepsilon_{\mathrm{sol}}$ (%)	$\mathcal{P}^b_{\ell\nu\mathrm{b}}$ (%)	$< m_{\mathrm{jjb}} >$ (GeV)	σ_{jjb} (GeV)	$\varepsilon_{\mathrm{jj}}$ (%)	$\mathcal{P}^b_{\mathrm{jjb}}$ (%)
TDR	174.6	8.6	74.8	49.9	174.7	7.7	80.2	48.2%
Colin. approx. +likelihood	172.9	10.4	100.	54.6	173.8	10.4	100.	49.8%

versa. The correct pairing is then the one with second highest likelihood. Nevertheless, the analysis benefits from the likelihood pairing method, because the sequent cuts on m_{jj}, $m_{\ell\nu\mathrm{b}}$, and m_{jjb} are replaced by a single cut on the pairing likelihood. This enhances the efficiency of the selection by almost 20% as mentioned above, and increases slightly the amount of correct pairing after all cuts. The sum spectra of all backgrounds and the signal is shown in Figure 9.23 for an integrated luminosity of 30 fb^{-1}. Figure 9.24 gives a comparison of the reconstructed m_{bb} between the TDR method and the collinear approximation with likelihood pairing in events from the signal, the irreducible $\mathrm{t\bar{t}b\bar{b}}$ and the reducible $\mathrm{t\bar{t}jj}$ background. The two methods lead to similar results, but the improved method reconstructs a bit less events in the high mass tail which corresponds to the slight increase of the reconstruction purity (c.f. Table 9.9).

Figure 9.25 shows fits to the reconstructed m_{bb} spectrum for $m_{\mathrm{H}^0} = 80$, 100, 120, and 140 GeV, and the fit parameters for all masses are listed in Table 9.10. On average, the width of the peak in the m_{bb} distribution is about 0.5 GeV broader with the likelihood based pairing.

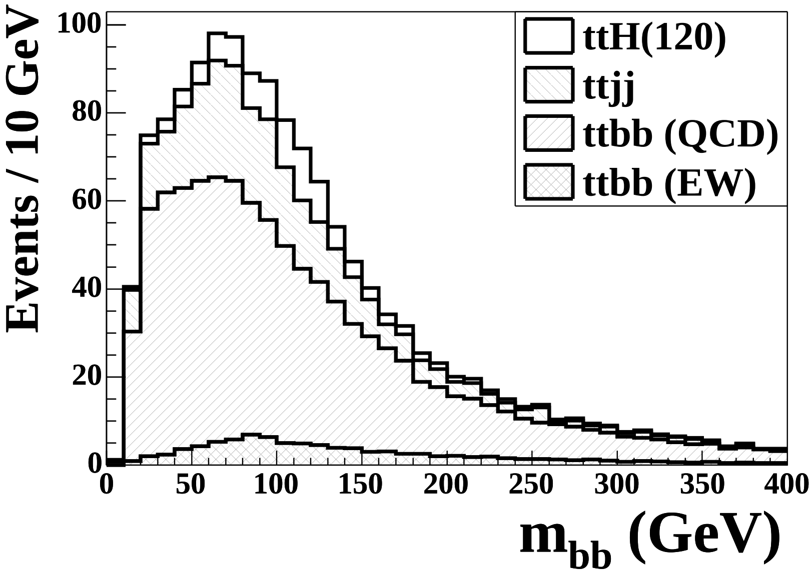

Figure 9.23: Reconstructed masses in the improved analysis. The sum of the reconstructed m_{bb} spectra for signal and background normalized to the rate of expected events for $\mathcal{L} = 30$ fb^{-1}.

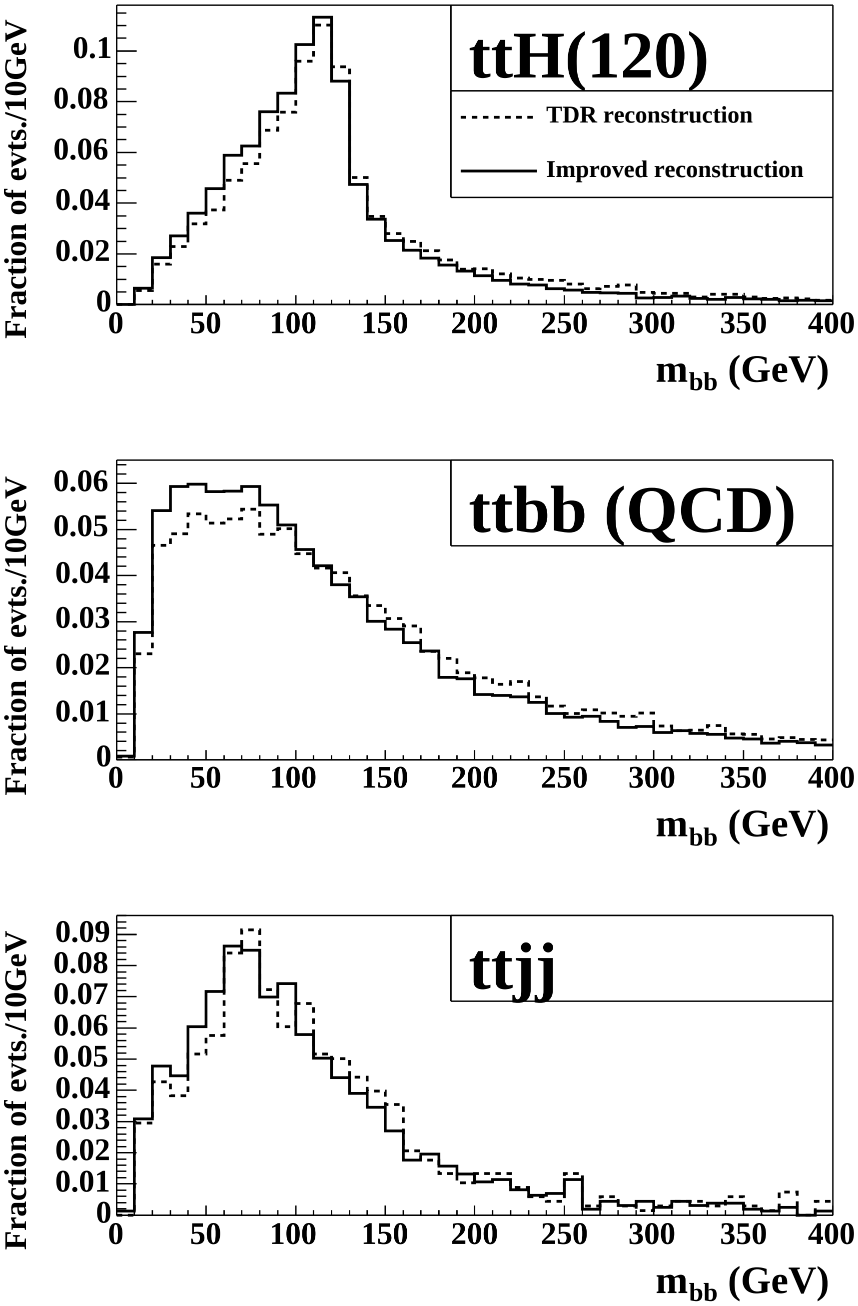

Figure 9.24: Comparison of reconstructed masses m_{bb} in the TDR and the improved reconstruction method. The histograms are normalized to Unity.

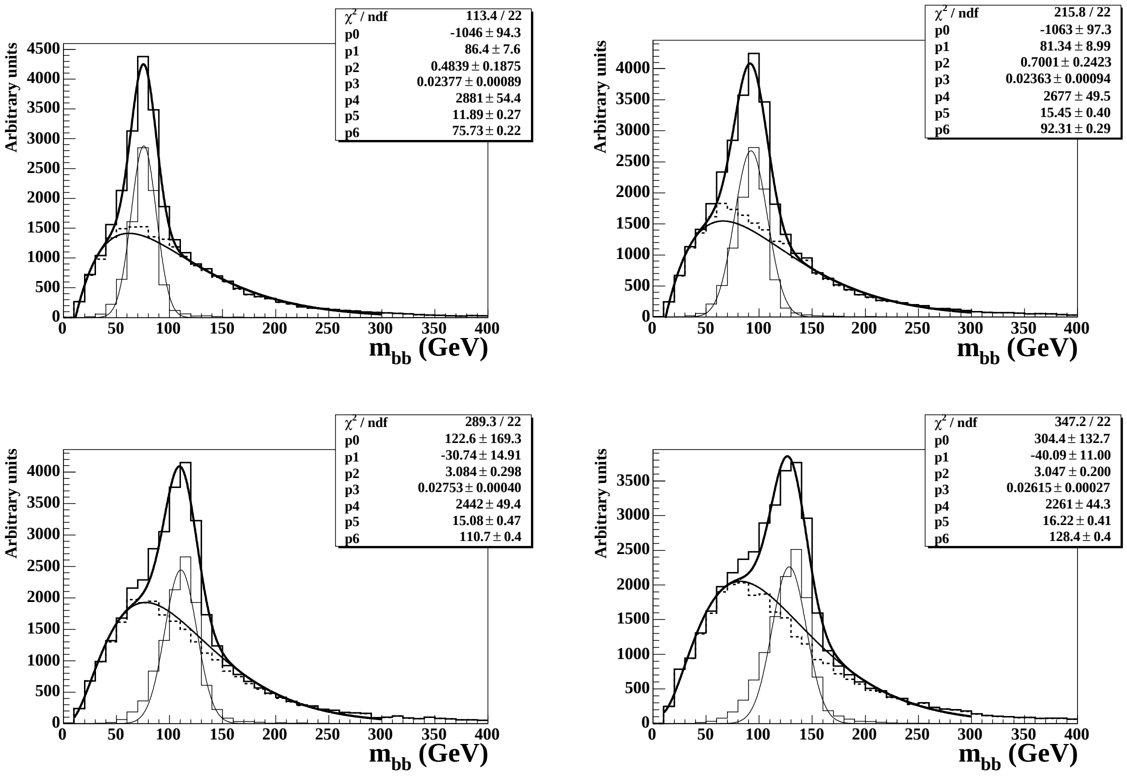

Figure 9.25: Fitted mass spectra of signal events in the improved reconstruction for $m_{\mathrm{H}^0} = 80, 100, 120, 140$ GeV. The thick line is the resulting fit to the complete spectrum in the range 10 GeV $< m_{\mathrm{bb}} <$ 300 GeV. The two thin lines show the fits to the combinatorial permutations (dashed histogram) and to the correctly reconstructed events (Gaussian-shaped histogram with thin line). The fit parameters p0–p6 correspond to the parameters in Equation (9.4) in the same order.

Table 9.10: Results for the parameters describing the Gaussian part of Equation 9.4 in signal events.

Improved method, low luminosity				
m_{H^0}(GeV)	$m_{\mathrm{H}^0}^{\mathrm{fit}}$(GeV)	$\Delta m_{\mathrm{H}^0}^{\mathrm{fit}}$(GeV)	σ(GeV)	$\Delta\sigma$(GeV)
80	75.8	0.2	11.9	0.3
90	84.5	0.2	13.6	0.3
100	92.3	0.3	15.5	1.4
110	101.1	0.3	16.3	0.5
120	110.7	0.4	15.1	0.5
130	120.3	0.4	15.1	0.4
140	128.4	0.4	16.2	0.4

9.2.3 Final event selection

A final event selection is applied after the reconstruction of the top quarks to events which are within the acceptance window $m_{\mathrm{bb}} = m^{\mathrm{fit}}_{\mathrm{H}^0} \pm 30$ GeV. The selection makes use of a set of variables for which differences in the shape between signal and background are observed. However, these differences are rather small, and cutting on each variable separately would reduce the efficiency by too much. Therefore, the variables are combined into a likelihood, and a cut is applied only on the likelihood output. The variables used for the final event selection are:

1. m_{bb}: the invariant mass of the two b-jets assigned to the Higgs boson, which has a peak in signal events and a fading shape in background events,
2. $\Delta\eta(\mathrm{t}_{\mathrm{near}}, \mathrm{bb})$: the difference in pseudo rapidity between the bb-system and the reconstructed top quark nearest in ΔR.
3. $\cos\theta^*_{\mathrm{b,b}}$: the cosine of the decay angle of the two b-jets associated to the Higgs boson in the rest frame of the bb-system, making use of different decay distributions of spin-0 (Higgs boson) and spin-1 particles (gluons),
4. $\Delta\eta(\mathrm{b,b})$: the difference in pseudo rapidity between the two b-jets associated to the Higgs boson. In background events these b-jets are expected to be less central,
5. $m^{(1)}_{\mathrm{bb}}$: the combination with the smallest invariant mass m_{bb} out of the six combinations which are possible when selecting two b-jets out of four b-jets.
6. $m^{(2)}_{\mathrm{bb}}$: the combination with the second smallest invariant mass m_{bb} out of the six combinations which are possible when selecting two b-jets out of four b-jets,
7. $\phi_{\mathrm{t}_1} - \phi_{\mathrm{t}_2}$: the difference in phi between the reconstructed top quarks,
8. $p_T^{\mathrm{t}_1} + p_T^{\mathrm{t}_2}$: the sum of the transverse momenta of the reconstructed top quarks, which is slightly higher in signal events due to the emission of the massive Higgs boson.

These variables are shown in Figure 9.26 for the signal $\mathrm{t\bar{t}H}^0$, the irreducible $\mathrm{t\bar{t}b\bar{b}}$, and the reducible $\mathrm{t\bar{t}jj}$ background. A 3-class likelihood is used to combine the distributions into a single output (there is no separate class for the $\mathrm{t\bar{t}b\bar{b}}$ (EW) background).

The output distributions of the final likelihoods, *fLH*, for a 120 GeV signal and for the irreducible $\mathrm{t\bar{t}b\bar{b}}$ and the reducible $\mathrm{t\bar{t}jj}$ background are shown in Figure 9.27. A cut is placed at 0.35, and only events with a likelihood above this threshold are selected. The position of the cut is optimized for the best value of $S/\sqrt{B}$. The sum of the likelihood distributions for all backgrounds and the signal is shown in Figure 9.28 normalized to the expected event rate for a luminosity of 30 fb^{-1}.

The likelihood input distributions are determined separately for each Higgs boson mass. The optimal position of the likelihood cut is also explored for each mass separately, but it turns out that a cut at 0.35 is optimal for all masses between 80 and 140 GeV.

The efficiency of this cut in the selection for a 120 GeV Higgs boson is 85% for the signal and 63% for the total background. This reflects in a relative increase of the significance by 8% after the cut on *fLH*. Figure 9.29 shows the reconstructed m_{bb} for signal and background events in the acceptance window $m_{\mathrm{H}^0} \pm 30$ GeV before and after the final likelihood. An improvement in the signal to background ratio is visible after the cut on *fLH*.

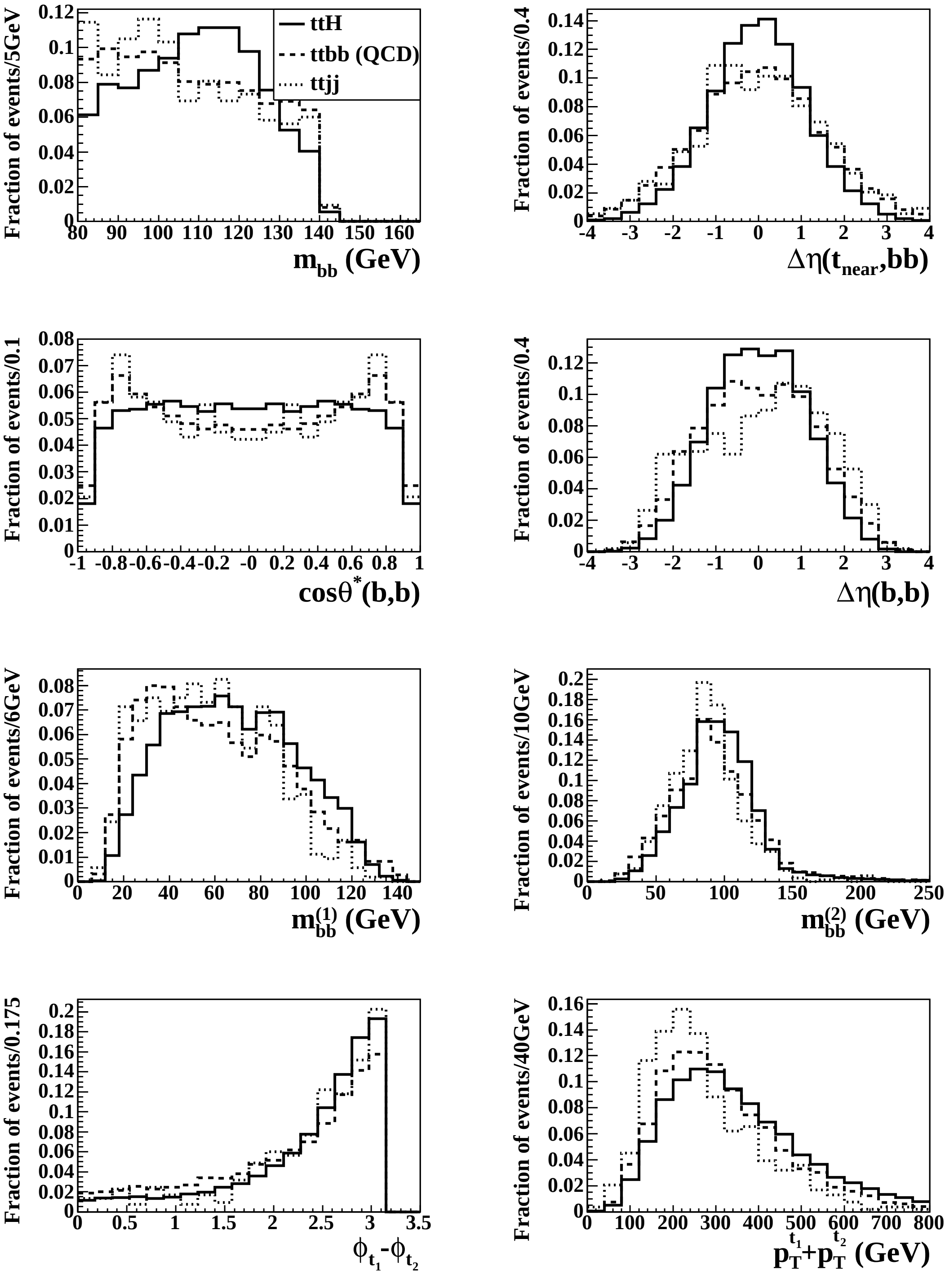

Figure 9.26: Input variables to the likelihood in the final event selection. The histograms are normalized to Unity.

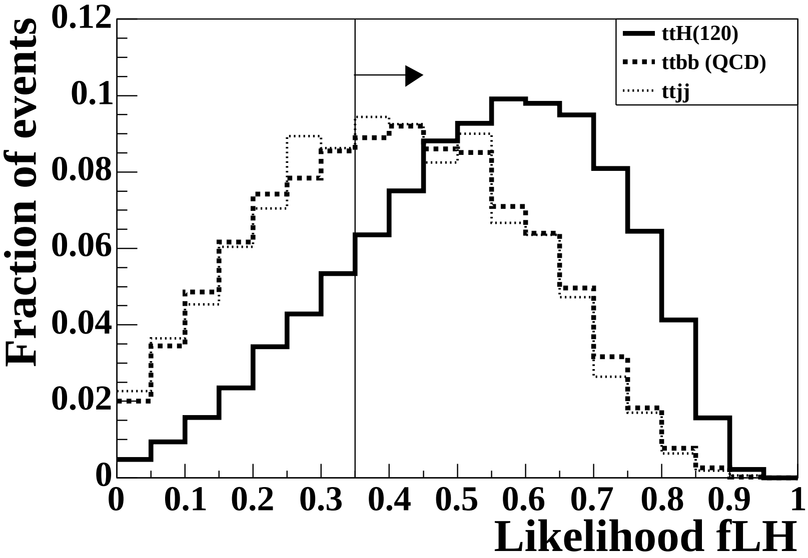

Figure 9.27: The likelihood output for the final event selection normalized to Unity.

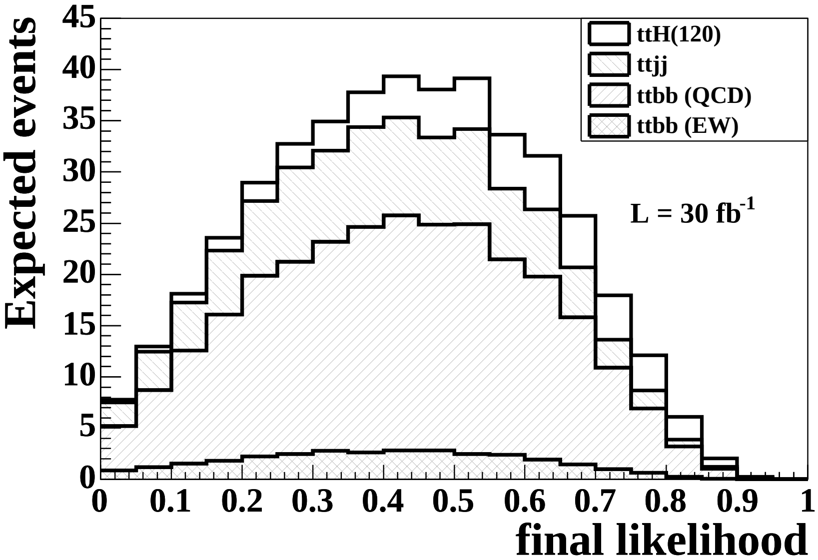

Figure 9.28: The sum of the final likelihood distribution for signal and background normalized to the expected rate of events for $\mathcal{L} = 30$ fb^{-1}.

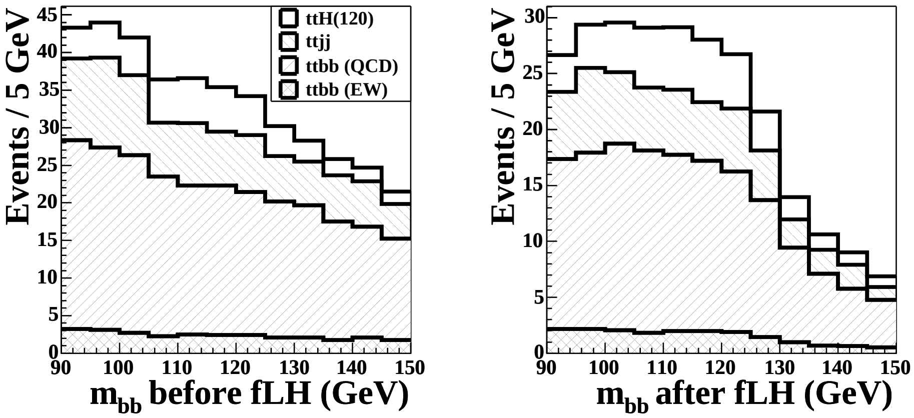

Figure 9.29: The distribution of m_{bb} for events inside the acceptance window $m_{H}^{fit} \pm 30$ GeV before and after the final likelihood. The histograms are normalized to the expected rate for $\mathcal{L} = 30$ fb^{-1}.

Table 9.11: Efficiencies after each step of the improved analysis for $m_{H^0} = 120$ GeV. The relative efficiencies with respect to the previous step are given in parenthesis.

Cut	$t\bar{t}H^0(120)$ (%)	$t\bar{t}b\bar{b}$(QCD) (%)	$t\bar{t}jj$ (%)	$t\bar{t}b\bar{b}$(EW) (%)
1ℓ+6j(4b)	3.8	1.5	0.01	1.5
2 tops reconstructed	3.3 (88.0)	1.3 (87.2)	0.01 (69.7)	1.3 (85.9)
m_{bb} inside mass window	1.7 (50.9)	0.3 (26.6)	2.3×10^{-3} (33.5)	0.4 (31.4)
$fLH > 0.35$	1.5 (85.6)	0.2 (64.9)	1.4×10^{-3} (61.2)	0.3 (66.9)

Table 9.12: Expected events after each step of the improved analysis for $m_{H^0} = 120$ GeV and $\mathcal{L} = 30$ fb^{-1}.

Cut	$t\bar{t}H^0(120)$	$t\bar{t}b\bar{b}$(QCD)	$t\bar{t}jj$	$t\bar{t}b\bar{b}$(EW)	$\sum$Bkg
1ℓ+6j(4b)	119.1	1100.7	441.3	116.7	1658.7
2 tops reconstructed	104.8	959.8	307.6	100.2	1367.6
m_{bb} inside mass window	53.3	255.3	103.0	31.5	389.8
$fLH > 0.35$	45.6	166.0	63.1	21.0	250.2

9.2.4 Results for the improved analysis

The efficiency and number of expected events for each consecutive step of the improved analysis are given in Tables 9.11 and 9.12 for the selection of a 120 GeV Higgs boson. The average overall gain compared to the TDR method amounts to about 45% in $S/\sqrt{B}$. The results for Higgs boson masses between 80 and 140 GeV are summarized in Table 9.13.

The significances for the observation of the signal, expressed as $S/\sqrt{B}$, are plotted in Figure 9.30 versus the Higgs boson mass in the range $m_{H^0} = 100$–140 GeV. Curves are shown for the TDR method and the improved likelihood reconstruction methods as discussed in sections 9.1 and 9.2. A clear improvement in the expected significances with the collinear approximation and the likelihood methods can be observed compared to the reconstruction procedure used in the TDR. For a 120 GeV Higgs boson the significance can be raised by 45% from 2.0 to 2.9. In addition to the significances obtained with the analysis presented in this thesis, also the original numbers for $m_{H^0} = 100$ GeV and $m_{H^0} = 120$ GeV from the TDR are shown. There the expected significances where 5.0 and 3.6.

Table 9.13: Signal efficiency and expected events in the improved analysis for $\mathcal{L} = 30$ fb^{-1} and for various Higgs boson masses.

m_{H^0} (GeV)	80	90	100	110	120	130	140
$\varepsilon_{\mathrm{t\bar{t}H}^0}$ (%)	1.28	1.36	1.35	1.34	1.32	1.25	1.21
$\mathrm{t\bar{t}H}^0$	136.9	110.7	86.2	65.1	45.6	28.2	15.0
$\mathrm{t\bar{t}b\bar{b}}$ (QCD)	211.3	206.2	198.0	185.5	166.0	146.9	131.7
$\mathrm{t\bar{t}jj}$	104.2	100.9	87.3	76.3	63.1	50.9	40.9
$\mathrm{t\bar{t}b\bar{b}}$ (EW)	23.0	24.5	24.6	23.7	21.0	17.9	15.6
total bkg.	338.5	331.65	309.9	285.5	250.1	215.7	188.2
$S/\sqrt{B}$	7.4	6.1	4.9	3.9	2.9	1.9	1.1
$\sigma_{\mathrm{Poisson}}$	7.0	5.7	4.6	3.7	2.7	1.8	1.0

The comparison with the current status for the TDR reconstruction method (significances of 3.4 and 1.9) stresses the large impact of the choice of the parton distribution functions and the Q^2 scale, and the more precise description of the irreducible $\mathrm{t\bar{t}b\bar{b}}$ background. To illustrate the effect of the smaller cross section, the numbers from the TDR have been scaled according to the CTEQ5L structure functions and the choice $Q^2_{QCD} = (m_{\mathrm{t}} + m_{\mathrm{H}^0}/2)^2$ but with the same composition of the background (*i.e.*, the complete $\mathrm{t\bar{t}}$+jets background is generated with PYTHIA). One observes a degradation of the expected $S/\sqrt{B}$ by about 20%. The remaining difference between the scaled TDR numbers and the results from the TDR reconstruction method in this analysis arises from the higher jet multiplicity and the harder p_T spectrum of the $\mathrm{t\bar{t}b\bar{b}}$ background estimated with the AcerMC generator instead of PYTHIA, and from the inclusion of non-resonant electroweak $\mathrm{t\bar{t}b\bar{b}}$ background.

The evolution of the expected signal and background events, the signal to background ratio, the purity of correct reconstruction, and the significances are detailed in Table 9.14 for the selection of a 120 GeV Higgs boson. Both the pairing likelihood and the final likelihood increase the fraction of events where the correct b-jets are assigned to the decay of the Higgs boson. The signal to background ratio is enhanced from 0.14 to 0.18 with the final likelihood. The significance is enhanced with each step of the improvements. The collinear approximation increases the significance by 15%. Replacing the TDR reconstruction method by the pairing likelihood gains another 16%. The final likelihood enhances the significance by 8%. The total improvement on the significance is 45%.

9.2.5 Discussion of mass cuts in the improved analysis

The improved analysis benefits mostly from an increased efficiency due to the collinear approximation and the introduction of likelihoods in the jet-pairing and in the final event selection. In the likelihood jet-pairing there is no a-priori restriction on the invariant mass of the jet-pair candidate supposed to originate from the hadronic W decay. It is left to the pairing likelihood to find the best combination out of all possible ones. The cut $pLH > 0.7$ ensures that events are rejected if no combination is found that resembles the characteristics of events with a top-quark pair.

No cut on the reconstructed top-quark masses is applied, since the fraction of correctly reconstructed events after all selection steps is found to be comparable to or even higher than the purity of the TDR reconstruction method. Figure 9.31 shows the reconstructed hadronic W and the two top-quark masses in the improved analysis for events with $pLH > 0.7$ (*i.e.*,

Table 9.14: Consecutive changes for the steps of the improvements. The table shows the purities, and the expected number of events for $\mathcal{L} = 30$ fb^{-1} in the selection for a 120 GeV Higgs boson. $\mathcal{P}_{bb}$ is the purity that the correct b-jets are assigned to the decay of the Higgs boson ('all' for events from the whole mass spectrum, and 'window' for the events in the mass window around the expected signal mass peak).

	TDR method	TDR + col. approx.	col. approx. + pairing LH	col. approx + pairing LH + final LH
$\mathcal{P}_{bb}$ all	27.2%	27.1%	28.9%	28.9%
$\mathcal{P}_{bb}$ window	50.4%	50.1%	50.7%	53.5%
$t\bar{t}H^0$ (120)	27.8	35.8	53.4	45.6
$t\bar{t}b\bar{b}$ (QCD)	131.2	167.8	264.7	166.0
$t\bar{t}jj$	44.7	54.9	106.7	63.1
$t\bar{t}b\bar{b}$ (EW)	16.6	21.1	32.6	21.0
total bkg.	192.5	243.8	404.0	250.1
S/B	0.14	0.15	0.13	0.18
$S/\sqrt{B}$	2.0	2.3	2.7	2.9
σ_{Poisson}	1.9	2.2	2.5	2.7

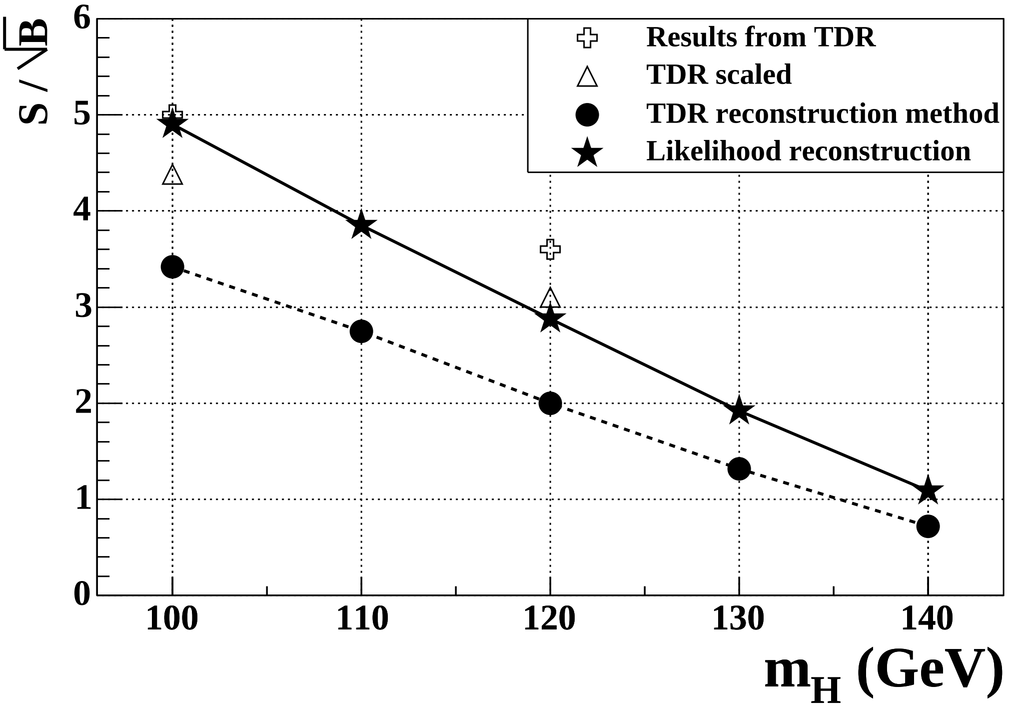

Figure 9.30: Expected significances for $\mathcal{L} = 30$ fb^{-1}. See the text for an explanation of the 'TDR scaled' values.

before the m_{bb} cut and the final event selection), including the true distributions. The masses m_{jj}, $m_{\ell\nu\mathrm{b}}$, and m_{jjb} are reconstructed at the expected masses $m_{\mathrm{W}^\pm}$ and m_{t}. Only small tails are observed, and they are not significantly larger than in the TDR reconstruction method which includes cuts on m_{jj}. This indicates that the pairing likelihood reconstructs the top quark masses in a reliable way and that it is robust against possible blur from the collinear approximation or from including the whole m_{jj} mass range.

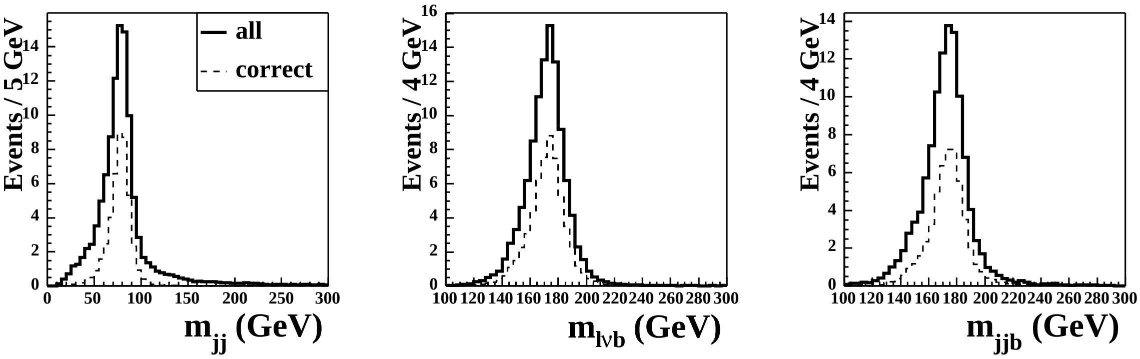

Figure 9.31: Reconstructed masses in the improved analysis. The dashed histograms show the fraction of events with correct reconstruction. The histograms are normalized to the expected rate for $\mathcal{L} = 30\ \mathrm{fb}^{-1}$.

Nevertheless, there is no explicit cut requiring that the reconstructed masses $m_{\ell\nu\mathrm{b}}$ and m_{jjb} are close to the expected top mass. All events with a lepton, missing transverse momentum and six jets of which four are tagged as b-jets might be reconstructed, and it is not obvious that background processes *not* containing a pair of top-quarks are negligible. Thus, it is verified with W+jets and tW events if those backgrounds need to be taken into account.

W+jets events are very unlikely to pass the preselection requirement of six jets and four b-jets, but this process has a huge cross section of $\sigma \times \mathrm{BR}_{\mathrm{W}\to\ell\nu} = 14\,470\,\mathrm{pb}$. The required number of b-tagged jets can be reached with real b-jets from gluon splitting or fake b-jets from the mis-tag of light jets. A control sample of 60 million W+jets event is generated with PYTHIA.

Single top events have a much smaller cross section $\sigma \times \mathrm{BR}_{\mathrm{tW}\to\ell\nu\mathrm{jjb}} \approx 11\,\mathrm{pb}$, but the event topology is closer to the required one with two top-quarks. In particular this is true for the process gb→tW, where there is a top-quark and a W boson in the final state, and only one additional (fake) b-jet is necessary to mimic the final state of a pair of top-quarks. But still three mistagged jets are necessary in total for tW events to pass the preselection cuts. About 275 k tW events are generated with ONETOP [52] and 100 k events with TOPREX [53].

Since up to four mistagged light jets are needed in the W+jets events in order to survive the preselection cuts, the size of the Monte Carlo sample would be reduced by several orders of magnitude after applying the b-tagging procedure from ATLFAST. Instead, a random mis-tag is applied to the W+jets and tW events, so that each event contains four b-tagged jets. The events are reweighted (c.f. Section 12.3) to correspond to a b-tagging performance with $\varepsilon_{\mathrm{b}} = 0.6$, $\mathrm{R_j} = 100$, $\mathrm{R_c} = 10$. The full chain of reconstruction and selection is then applied to these events. Figure 9.32 shows the reconstructed masses m_{jjb} and $m_{\ell\nu\mathrm{b}}$ in tW events with W→jj, t→ $\ell\nu$b after reconstruction of the complete final state. Since there is only one top quark, the attempt to reconstruct a second top quark results in a very broad mass distribution. Hence, single top events are unlikely to pass the

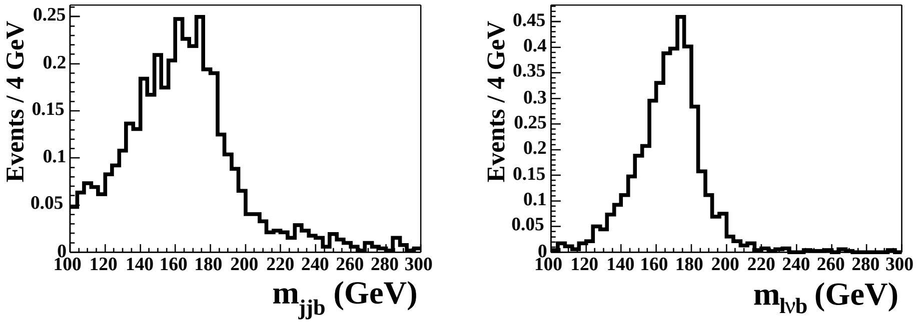

Figure 9.32: Reconstructed masses in tW events with W→jj, t→ $\ell\nu$b. The histograms are normalized to the expected rate for $\mathcal{L} = 30$ fb^{-1}.

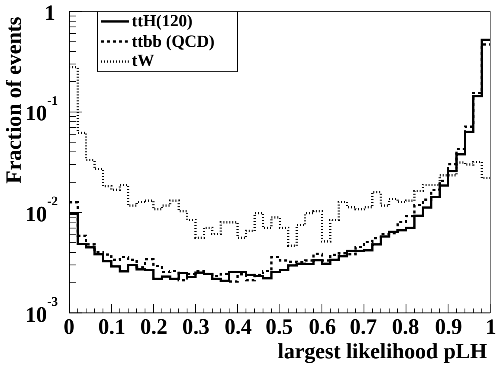

Figure 9.33: Distribution of the pairing likelihood for signal, irreducible background and single top events. The histograms are normalized to Unity.

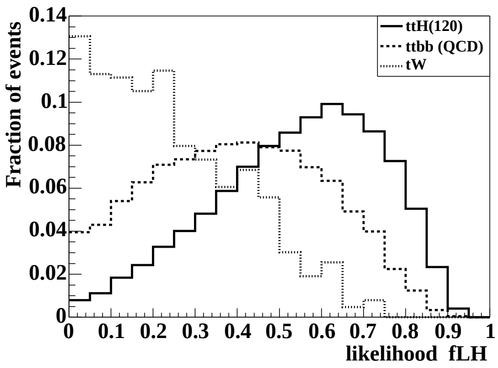

Figure 9.34: Distribution of the final likelihood for signal, irreducible background and single top events. The histograms are normalized to Unity.

cut on pLH. The distribution of the pairing likelihood output is displayed in Figure 9.33. Only 29% of the tW events fulfill $pLH > 0.7$ to be compared to an efficiency of 89% for the signal and events from the irreducible $\mathrm{t\bar{t}b\bar{b}}$ background. The final likelihood selection provides further means to suppress this kind of background (Figure 9.34). The efficiency to pass the cut $fLH > 0.35$ is 27% and thus only one third of the efficiency for backgrounds with two top quarks.

After all steps of the improved analysis the expected event rate for the W+jets and tW process for $\mathcal{L} = 30$ fb^{-1} is below the level of one event. Both ONETOP and TOPREX give comparable results for single-top events. This small number is mainly due to the fact that the required number of b-labeled jets can only be reached from mistagged light- or c-jets. Even if the mis-tag rate was two or three times higher than the selected $\mathrm{R_j} = 100$, $\mathrm{R_c} = 10$, these backgrounds are still negligible compared to the other backgrounds.

This section has demonstrated that despite of omitting cuts on m_{jj}, $m_{\ell\nu\mathrm{b}}$ and m_{jjb} the improved analysis reconstructs and selects correctly events with two top-quarks. Processes with only one or no top-quark have a negligible contribution and can clearly be identified with both the pairing likelihood and the final likelihood.

9.3 Conclusions on the reconstruction and selection methods

In Section 9.1 the channel $\mathrm{t\bar{t}H^0}$, $\mathrm{H^0 \rightarrow b\bar{b}}$ was reinvestigated. With a more precise prediction of the irreducible background and updated cross sections for the signal and the background the significance of this channel is considerably smaller than the expectations in the ATLAS TDR. Therefore, an attempt was made in Section 9.2 to improve the reconstruction and analysis procedure, leading to a substantial enhancement in the expected significances. On average, the expected $S/\sqrt{B}$ with the improved selection is 45% higher than with the TDR method. The proposed improvements to achieve this enhancement are

1. a collinear approximation if the equation for p_ν^z can not be solved,
2. a likelihood for the jet pairing,
3. a final likelihood for events inside the m_{bb} mass window.

The collinear approximation recovers 25% of the events, while the width of the reconstructed semileptonically decayed top quark increases by only 0.5 GeV. The pairing likelihood combines several kinematic variables into a single likelihood output. The jet combination with the highest likelihood is taken to be the correct combination. Instead of cutting on three masses m_{jj}, m_{jjb}, and $m_{\ell\nu\mathrm{b}}$ there is only one cut on the pairing likelihood to ensure that events with two top quarks are reconstructed. The efficiency for this cut is around 88%, and the efficiency for a successful reconstruction of two top quarks and two remaining b-jets is augmented by 50%. It has been demonstrated that background processes not containing a pair of top quarks, like $\mathrm{W}^{\pm}$+jets or single top events, are not dangerous as they have small likelihood values. In total, the collinear approximation and the pairing likelihood lead to an increase of the mass resolution of the reconstructed top masses, from about 8 GeV with the TDR reconstruction method to about 10 GeV. However, the purity of correctly reconstructed events is slightly better than in the TDR reconstruction and the significance is increased by 35%. One should also keep in mind that the TDR reconstruction method biases the reconstructed top quark masses to the mass m_{t} used as input in the minimization procedure, Equation 9.3. The final likelihood explores differences between the signal and background process for events inside the m_{bb} mass window around the hypothetical Higgs mass. The efficiency of the cut on the final likelihood distribution is 85% for the signal and 64% for the background. The significance is increased by 8% by this cut. The aforementioned numbers hold for $m_{\mathrm{H}^0} = 120$ GeV.

9.3.1 Comparison with results from the CMS collaboration

The CMS collaboration has also investigated the channel $\mathrm{t\bar{t}H}^0$, $\mathrm{H}^0 \rightarrow \mathrm{b\bar{b}}$ and obtains a significance of $S/\sqrt{B} = 5.3$ for $m_{\mathrm{H}^0} = 115$ GeV and $\mathcal{L} = 30\ \mathrm{fb}^{-1}$, using a K-factor of 1.5 [54]. The ATLAS analysis, presented in this thesis, yields $S/\sqrt{B} = 2.4$ with the TDR reconstruction method and for the same mass of the Higgs boson. The source of the large difference between the discovery potential at CMS and ATLAS was studied in detail in Ref. [55]. Therefore, only a brief summary is presented here.

Although the CMS analysis has a different strategy in reconstructing the final state, the largest impact could be traced back to different assumptions on the cross sections:

- CMS uses CTEQ4L structure functions which give 20% larger cross sections than the newer CTEQ5L structure functions used in ATLAS.
- CMS applies a K-factor of 1.5 to the $\mathrm{t\bar{t}H}^0$ signal and the $\mathrm{t\bar{t}Z}$ background, ATLAS does not apply K-factors. According to Section 8.2 and Refs. [45, 46], a value of 1.5 appears to be too optimistic.

- Different Monte Carlo generators and different Q^2_{QCD} scales are used in CMS and ATLAS. It was pointed out before that the calculation of cross sections is very sensitive to choice of the Q^2_{QCD} scale if no higher-order corrections are implemented.
- The p_T and η cuts which are applied in the CMS analysis to the $\mathrm{t\bar{t}b\bar{b}}$ background at generator level seem to underestimate the irreducible background. Only the resonant contribution of the $\mathrm{t\bar{t}Z}$ background was considered, whereas the ATLAS analysis takes into account also the non-resonant part.

If the CMS cross sections and K-factors are used in this thesis, the TDR reconstruction methods results in comparable significances to the CMS values (ATLAS: $S/\sqrt{B} = 4.8$, CMS: $S/\sqrt{B} = 5.3$, this comparison does not take into account the more complete set of background processes in ATLAS). These numbers are even surpassed if the likelihood analysis is applied.

9.4 Systematic uncertainties

The analysis of the $\mathrm{t\bar{t}H^0}$ channel suffers mainly from the large uncertainty in the prediction of the background from top quark pairs with additional jets. The leading-order cross section calculation is very sensitive to the choice of the Q^2_{QCD} scale. This indicates significant contribution from higher order corrections which are not available at present. Therefore, it is essential to *measure* the rate of the $\mathrm{t\bar{t}}$+jets background from real data and to tune the Monte Carlo generators accordingly. For an extraction of the $\mathrm{t\bar{t}H^0}$ signal peak in the m_{bb} mass spectrum it is likewise important to know the shape of the background, especially that of the $\mathrm{t\bar{t}b\bar{b}}$ background. It was emphasized in section 9.1.5.1 that the shape is influenced to a large extend by the rate of mistagged jets and the quality of the jet pairing to identify the correct decay products of the top quarks. In the following, a recipe is derived how to measure the $\mathrm{t\bar{t}}$+jets background in the $\mathrm{t\bar{t}H^0}$ channel.

9.4.1 Determining the shape

The first step is to determine the shape of the background. If this is done from the data, no or only little contribution from the $\mathrm{t\bar{t}H^0}$ signal is allowed. To do so, the preselection described in Section 9.1.1 is applied to the $\mathrm{t\bar{t}}$+jets sample but with the following change: Instead of selecting events with at least four tagged b-jets, only events with exactly two b-jets are selected. The parametrization $\varepsilon_{\mathrm{b}} = 0.6$, $\mathrm{R_j} = 100$, $\mathrm{R_c} = 10$ is used. The efficiency for this selection is 18.5% for $\mathrm{t\bar{t}H^0}$ events, and the ratio of $\mathrm{t\bar{t}H^0}$ to $\mathrm{t\bar{t}}$+jets events after this modified preselection is 2.7×10^{-3}.

Two non-b-jets with $p_T > 20$ GeV are chosen by random and are labeled as b-jets. This sample is denoted as '$\mathrm{t\bar{t}jj}$' in the following. Then the top reconstruction in the '$\mathrm{t\bar{t}jj}$' sample is done in the usual way, and the m_{bb} mass spectrum is calculated from the remaining two b-jets. In Figure 9.35 this spectrum is compared to the m_{bb} spectrum obtained in the default selection from $\mathrm{t\bar{t}}$+bb events (true and fake, generated by PYTHIA). Although the shapes are similar the peak region 20 GeV $< m_{\mathrm{bb}} <$ 125 GeV is not well described by the $\mathrm{t\bar{t}jj}$ control sample, and the spectrum cannot be used directly as an estimate for the $\mathrm{t\bar{t}b\bar{b}}$ background mass spectrum (the background in the selection for $m_{\mathrm{H^0}} = 120$ GeV would be underestimated by 8.5% in the cut window $m_{\mathrm{bb}} \pm 30$ GeV). Therefore, a calibration function C is introduced to normalize the m_{bb} distribution from the $\mathrm{t\bar{t}jj}$ control sample to the m_{bb} spectrum from the $\mathrm{t\bar{t}b\bar{b}}$ sample: $C = H^{\mathrm{t\bar{t}b\bar{b}}}_{m_{\mathrm{bb}}} / H^{\mathrm{t\bar{t}jj}}_{m_{\mathrm{bb}}}$, where $H^{\mathrm{t\bar{t}b\bar{b}}}_{m_{\mathrm{bb}}}$ and $H^{\mathrm{t\bar{t}jj}}_{m_{\mathrm{bb}}}$ are

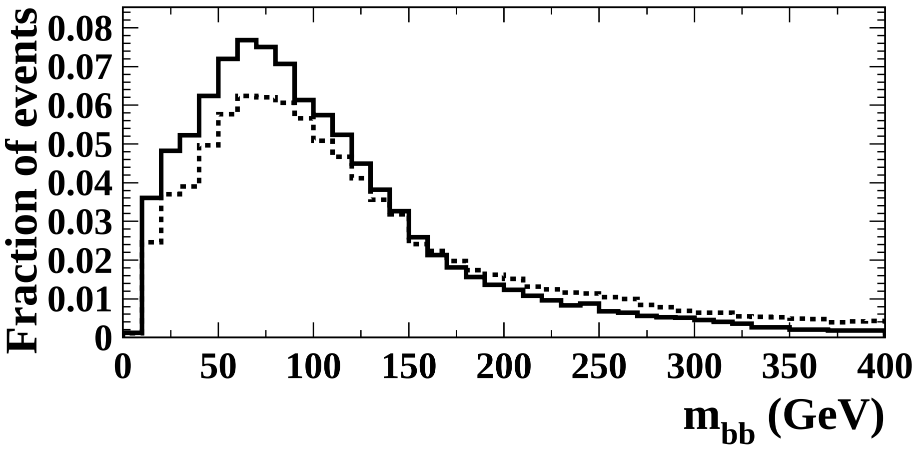

Figure 9.35: Comparison of the mass spectra in the analysis for the $\ell\nu$b jjb bb final state and in the control sample with the $\ell\nu$b jjb jj final state. In both cases the events are generated with Pythia only. The histograms are normalized to Unity.

the histogrammed mass spectra. The shape can then be determined by measuring from data the mass spectrum in a control sample of events with two b-jets and at least four additional non-b-jets and multiplying the obtained spectrum by the calibration function C. This method is less sensitive to the modeling of the background in the MC generators since only the ratio of the shapes is used. The expected statistical error for the procedure for 30 fb^{-1} of collected data can be estimated as follows: In the whole m_{bb} mass range there are about 58 000 events expected for the t$\bar{\mathrm{t}}$jj control sample. The efficiency for the mass cut $|m_{\mathrm{bb}} - m_{\mathrm{H}^0}| < 30$ GeV is $\approx 28\%$ which leads to a relative statistical uncertainty for the cut of

$$\left(\frac{\Delta\varepsilon}{\varepsilon}\right)_{\mathrm{stat.}} \approx 1\%. \tag{9.6}$$

The contamination from t$\bar{\mathrm{t}}$H^0 signal events inside the mass window is only 4×10^{-4}.

9.4.2 Absolute normalization

The absolute normalization for the background can be determined in this analysis from the m_{bb} mass spectrum in side-bands were a negligible amount of signal events is expected. The side-bands with $m_{\mathrm{bb}} < 50$ GeV and $m_{\mathrm{bb}} > 250$ GeV are chosen, based on the distribution of the m_{bb} spectrum of signal events with $m_{\mathrm{H}^0} = 120$ GeV. Due to the tails of the reconstructed m_{bb} in signal events (see Fig. 9.9) it is not possible to choose side-bands which are completely signal-free and have sufficient statistics in the background samples at the same time. For $\mathcal{L} = 30$ fb^{-1} and $m_{\mathrm{H}^0} = 120$ GeV there are 10.5 signal events and 245 events from the total background expected in the chosen side-band.

The m_{bb} spectrum (measured from the data as described in the previous section) can then be normalized to contain $N_{\mathrm{Bkg_{tot}}} = N_{\mathrm{sb}}^{\mathrm{t\bar{t}b\bar{b}}}/\varepsilon_{\mathrm{sb}}^{\mathrm{t\bar{t}jj}}$ events, where $N_{\mathrm{sb}}^{\mathrm{t\bar{t}b\bar{b}}}$ is the number of events in the side-bands $m_{\mathrm{bb}} < 50$ GeV and $m_{\mathrm{bb}} > 250$ GeV in the t$\bar{\mathrm{t}}$b$\bar{\mathrm{b}}$ distribution, and $\varepsilon_{\mathrm{sb}}^{\mathrm{t\bar{t}jj}}$ is the fraction of events in these side-bands in the m_{bb} mass spectrum obtained from the t$\bar{\mathrm{t}}$jj control sample.

The accuracy of the absolute normalization will be dominated by the statistical error of N_{sb}. From Monte Carlo simulation and the TDR reconstruction method one expects $N_{\mathrm{sb}} \sim 245$ events in the t$\bar{\mathrm{t}}$b$\bar{\mathrm{b}}$ sample for $\mathcal{L} = 30$ fb^{-1}, and about 20 000 events in the side-bands of the m_{bb} mass spectrum of the $\mathrm{t\bar{t}jj}$ control sample with $\varepsilon_{\mathrm{sb}} = 33\%$. This leads to a total statistical error of

$$\left(\frac{\Delta N_{\mathrm{bkg.}}}{N_{\mathrm{bkg.}}}\right)_{\mathrm{stat.}} \approx 6.5\%. \tag{9.7}$$

It was mentioned before that there is a small contribution from the signal process in the side-band $m_{\mathrm{bb}} < 50$ GeV and $m_{\mathrm{bb}} > 250$ GeV. So the measured background cross section is systematically too high in the presence of the signal. For $m_{\mathrm{H}^0} = 120$ GeV this introduces a systematic uncertainty:

$$\left(\frac{\Delta N}{N}\right)_{\mathrm{sys.}} \approx 4\%. \tag{9.8}$$

9.4.3 Conclusion on systematic uncertainties

In the beginning of data taking, the systematic uncertainties in the $\mathrm{t\bar{t}H^0}$, $\mathrm{H^0} \rightarrow \mathrm{b\bar{b}}$ channel will be dominated completely by the imperfect knowledge of the $\mathrm{t\bar{t}}$+jets background. There are large uncertainties in the theoretical predictions from Monte Carlo generators as long as higher order calculations are not available. Therefore, it is important to get an estimate of the background directly from the data. While this is straightforward for the normalization, some Monte Carlo information is still necessary for the determination of the shape. With the two methods described above it should be possible to measure the background to an accuracy of better than 10% with 30 fb^{-1}.

In the following, the impact of systematic uncertainties in the background prediction is investigated. Only the errors from the absolute normalization are considered here, since they are much larger than the estimated uncertainty from the determination of the shape. The statistical component of 6.5% is independent of the Higgs boson mass, but it varies with the luminosity, $(\Delta N/N)_{\mathrm{stat.}} \sim 1/\sqrt{\mathcal{L}}$. Thus, for the improved likelihood reconstruction method, which has higher efficiency, the statistical error will reduce to 4.5%. The systematic component of 4% does depends on the amount of expected signal events, hence, it depends on m_{H^0}. The shape of the signal distributions in the side-bands is dominated by wrong combinatorial choices, and this shape is almost independent of the Higgs boson mass. Therefore, the efficiency of the requirement '$m_{\mathrm{bb}} < 50$ GeV or $m_{\mathrm{bb}} > 250$ GeV' is taken to be the same as for $m_{\mathrm{H}^0} = 120$ GeV. The systematic shift of 4% due to the presence of signal events in the mass side-bands is then scaled according to the expected signal rates after full reconstruction of the final states.

The total uncertainty is obtained by adding $(\Delta N/N)_{\mathrm{stat.}}$ and $(\Delta N/N)_{\mathrm{syst.}}$ in quadrature. The program from Ref. [49] is used to incorporate the uncertainty into the Poissonian probability functions, following the 'Cousins & Highland' approach described in [56] and generalized in [57, 58]. Table 9.15 shows the resulting uncertainties and compares the expected Poissonian significances with and without a systematic uncertainty in the TDR method and the improved analysis for $\mathcal{L} = 30\ \mathrm{fb}^{-1}$. The values of $S/\sqrt{B}$ are listed, too (calculated without systematics uncertainties).

The figures demonstrate that uncertainties between 5% and 12% on the background have a dramatic impact on the expected significances, which decrease by ≈ 20% to 50%. This scenario is still optimistic, because no additional uncertainties are taken into account, *e.g.*, systematic uncertainties from the imperfect knowledge of the detector, from b-tagging, and uncertainties on the signal prediction. Hence, for the $\mathrm{t\bar{t}H^0}$ channel with $\mathrm{H^0} \rightarrow \mathrm{b\bar{b}}$ to contribute to the discovery of a light Standard Model Higgs boson at the LHC, it will

Table 9.15: Comparison of significances $S/\sqrt{B}$ and σ_{Poisson} without systematic uncertainties and including systematic uncertainties on the background prediction. The uncertainties are calculated for $\mathcal{L} = 30$ fb^{-1}.

TDR method

m_{H^0} (GeV)	80	90	100	110	120	130	140
$S/\sqrt{B}$	5.2	4.3	3.4	2.7	2.0	1.3	0.7
σ_{Poisson}	4.9	4.1	3.2	2.6	1.9	1.2	0.6
$\Delta_{\text{syst.}}$	12.1%	10.6%	9.4%	8.5%	7.6%	7.0%	6.7%
Syst. σ_{Poisson}	2.4	2.2	1.9	1.7	1.3	0.9	0.5

Improved method

m_{H^0} (GeV)	80	90	100	110	120	130	140
$S/\sqrt{B}$	7.4	6.1	4.9	3.9	2.9	1.9	1.1
σ_{Poisson}	7.0	5.7	4.6	3.7	2.7	1.8	1.0
$\Delta_{\text{syst.}}$	11.1%	9.5%	8.1%	7.1%	6.1%	5.3%	4.8%
Syst. σ_{Poisson}	3.2	2.9	2.7	2.4	2.0	1.4	0.8

be necessary to understand very well the detectors and to have precise predictions for the signal and background rates obtained from data or from improved calculations which include higher order corrections.

10 Results with new b-tag parameterizations

The results in Sections 9.1 and 9.2 are derived using a b-tag parameterization of $\varepsilon_\mathrm{b} = 60\%$ and constant rejection factors $\mathrm{R_j} = 100, \mathrm{R_c} = 10$. Jets are tagged or mistagged as b-jets on a random basis corresponding to the constant efficiencies ε_b, $\varepsilon_\mathrm{c} = 1/\mathrm{R_j}$, and $\varepsilon_\mathrm{j} = 1/\mathrm{R_c}$. This is clearly a simplified model of the ATLAS b-tagging performance, not taking into account p_T and η dependences or recent changes in the detector layout. In the real experiment the discriminating variable which distinguishes between b-jets and non-b-jets is built from impact parameter significances of tracks in the jets (and additional information, depending on the algorithm). This quantity and the precision with which it can be measured depends on the jet's transverse momentum and on the direction of the jet in the detector. Consequently, $\mathrm{R_j}$ and $\mathrm{R_c}$ are not at all constant, but functions of p_T and η. A realistic simulation of the $\mathrm{t\bar{t}H^0}$, $\mathrm{H^0 \to b\bar{b}}$ channel therefore needs an adequate parameterization of the b-tagging performance within the fast simulation of the ATLAS detector.

The quality of b-tagging depends on the performance of the Inner Detector Tracker (ID tracker), and on the performance of the Pixel Detector in particular. The design of this detector has undergone several changes since the Technical Design Report in 1999: the radius of the innermost layer (b-layer) was increased from 4.3 cm to 5.0 cm, the radius of Layer 1 decreased from 11.0 cm to 8.85 cm, and the radius of Layer 2 decreased from 14.2 cm to 12.25 cm. Tilt angles and pixel pitches were modified, the sensor thickness grew from 150 µm to 200 µm, and the number of wheels was reduced from four to three. Modifications affect also the SCT and TRT. The material budget of the Inner Detector in terms of radiation length increased due to a more detailed description of the layout in the simulation. There is also an important change in the layout of the pixel detector in the LHC starting phase: Due to restricted resources, ATLAS will start with one layer of the pixel detector missing, the second barrel layer and the second wheel on both sides will be deferred as well. The staging of some parts of ATLAS and its impact on the physics potential is discussed in [37].

In Reference [51] extensive studies have been performed on the ATLAS b-tagging potential, considering the present detector layout. In addition, new b-tagging parameterizations have been evaluated for ATLFAST at low luminosity conditions. The study takes into account the current detector layout with all pixel layers ('complete' layout) and with only two layers ('reduced' layout). The TDR layout is also available ('perfect' layout). For each layout a p_T dependent parameterization is derived from the full simulation and reconstruction of several processes, using an impact-parameter based b-tagging algorithm. The largest set of parameterizations is available from $\mathrm{W^\pm H^0}$ events with leptonic decay of the $\mathrm{W^\pm}$ and $\mathrm{H^0 \to b\bar{b}, u\bar{u}, c\bar{c}}$. $\mathrm{W^\pm H^0}$ events provide a rather clean sample of b-jets (or u, c-jets). Contrary, the signal channel of this work, $\mathrm{t\bar{t}H^0}$ with main background from $\mathrm{t\bar{t}}$, contains at least six jets, so that the jets are much less isolated. The event displays in Figure 10.1 reveal this issue. The b-weight of a jet, used for flavor-tagging, is calculated from the impact parameter significances of its tracks, and can be disturbed by other jets which are close by. A parameterization from $\mathrm{W^\pm H^0}$ events only would therefore not be adequate to simulate the expected b-tagging performance in $\mathrm{t\bar{t}H^0}$ and $\mathrm{t\bar{t}}$ events. To ac-

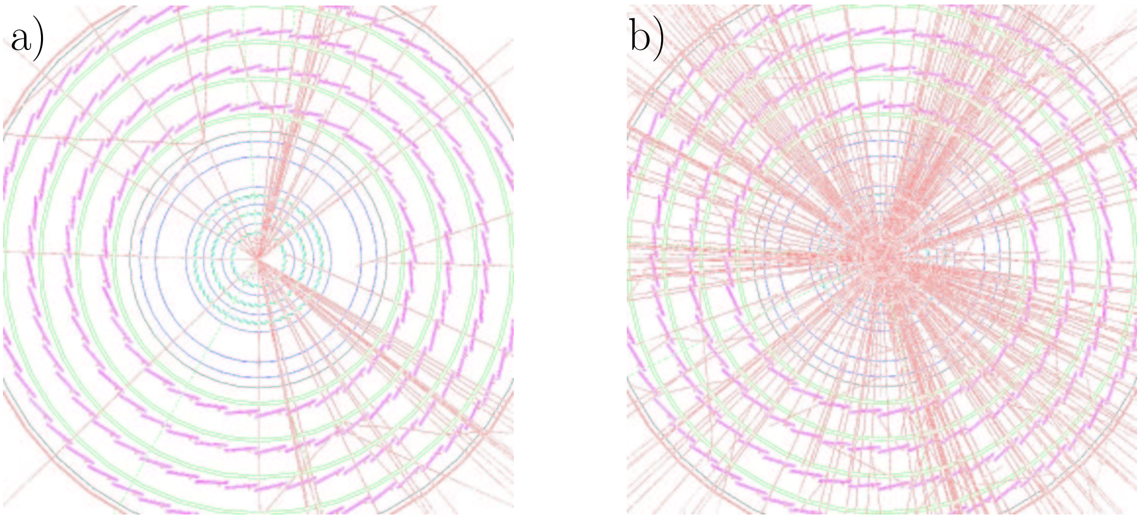

Figure 10.1: Event display of a) $W^{\pm}H^0 \rightarrow \ell\nu b\bar{b}$ and b) $t\bar{t}H^0 \rightarrow \ell\nu b\, jjb\, b\bar{b}$ as seen by the SCT and the Pixel Detector (from [59]).

complish this task, the b-tagging conditions were investigated in [51] in fully simulated $t\bar{t}H^0$ and $t\bar{t}$ events as well, and special sets of parameterizations were obtained. A parameterization in both p_T and η was not possible due to lacking statistics in the Monte Carlo samples. A two-dimensional parameterization will be prepared in the future when larger fully simulated Monte Carlo samples are available.

In the following sections the p_T-dependent parameterization, provided by the authors of Ref. [51], is applied to the $t\bar{t}H^0$ analysis. The parameterization covers several detector layouts. It describes the 'perfect', the 'complete', and the 'reduced' layout, includes module and chip inefficiencies, with and without including the effect of low luminosity pile-up and from $W^{\pm}H^0$ and $t\bar{t}H^0/t\bar{t}$ events. In this way it is possible to monitor the changes and to compare the results to those obtained from the simple p_T-independent parameterization used in Sections 9.1 and 9.2. The b-tagging is done in such a way that the efficiency ε_b is kept at a constant level over the p_T range and the rejections R_j and R_c are determined for nine non-equidistant bins in the whole p_T range. Examples for the rejection factors are shown in Figure 10.2. Compared to the constant rejections $R_j = 100$ and $R_c = 10$, one observes considerable smaller rejection against light jets in the range $p_T < 60$ GeV, which provides a source for an increased fake rate in the reducible $t\bar{t}$+jets background. The rejection against c-jets is 50%–20% smaller than the assumption in the TDR analysis.

Table 10.1 details the conditions from which the different configurations are deduced. Configuration '∅' corresponds to the parameterization commonly used in ATLAS and in Sections 9.1 and 9.2. The next set (A to C2) stems from $W^{\pm}H^0$ events and does not take into account the effect from event pile-up. The B-sets are available for different efficiencies ε_b and allow for a scan for the optimal value of ε_b, maximizing the expected statistical significance of finding a signal over the background. Most of the configurations include the effect that 1% of the modules and 2% of the chips are expected to be inoperable. A two-dimensional b-tagging algorithm with impact-parameter information in the plane perpendicular to the beam pipe was used ('2D' in the 'b-tag' column). The configurations A' to C' include the effect from low luminosity pile-up. The 'D' and 'E' sets account for a larger z-pitch of the pixels. A pitch of 400 microns will eventually be used in ATLAS. 'D2' and 'E2' incorporate a three-dimensional b-tagging algorithm which in addition makes use

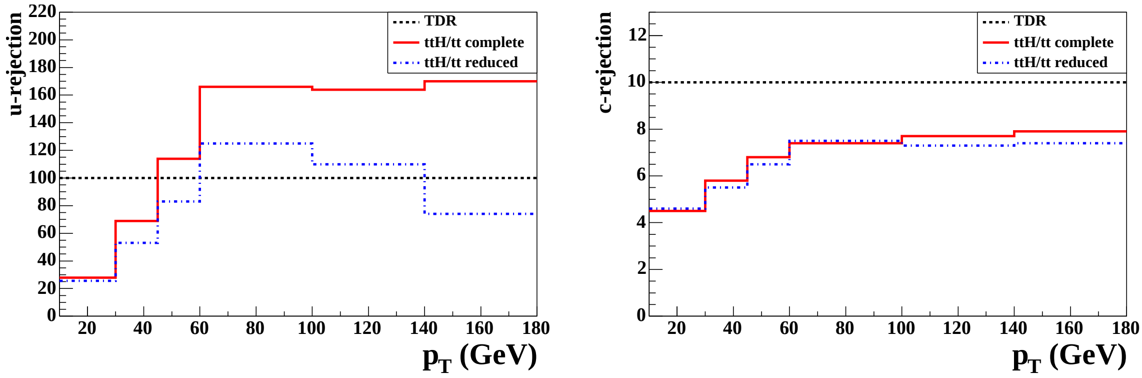

Figure 10.2: Rejections R_j and R_c as functions of p_T of the jet as obtained from the full simulation of $t\bar{t}H^0/t\bar{t}$ events.

of the z-information of the track impact parameters. Finally, configurations F and G stem from $t\bar{t}H^0/t\bar{t}$ events. These sets do not include pile-up or inefficiencies.

For all configurations listed in Table 10.1 the complete analysis chain is repeated for the TDR reconstruction and the improved analysis in the mass range 80 GeV $\leq m_{H^0} \leq$ 140 GeV.

Table 10.1: The detector configurations used for the new b-tagging parameterization. If not mentioned otherwise the z-pitch of the pixels in the b-layer is 300 µm.

Configuration	Layout	ε_b (%)	module/chip inefficiencies	b-tag
∅	TDR	60%	—	$R_j = 100$, $R_c = 10$
		from $W^{\pm}H^0$, no pile-up		
A	perfect	60%	—	2D
B1	complete	50%	1%/2%	2D
B2	complete	60%	1%/2%	2D
B3	complete	70%	1%/2%	2D
B4	complete	80%	1%/2%	2D
C1	reduced	60%	—	2D
C2	reduced	60%	1%/2%	2D
		from $W^{\pm}H^0$, low luminosity pile-up		
A'	perfect	60%	—	2D
B'	complete	60%	1%/2%	2D
C'	reduced	60%	1%/2%	2D
		from $W^{\pm}H^0$, low luminosity pile-up, 400 μm pitch		
D1	complete	60%	1%/2% (0.5%/1%)	2D
D2	complete	60%	1%/2% (0.5%/1%)	3D
E1	reduced	60%	1%/2% (0.5%/1%)	2D
E2	reduced	60%	1%/2% (0.5%/1%)	3D
		from $t\bar{t}H^0/t\bar{t}$, no pile-up		
F	complete	60%	—	2D
G	reduced	60%	—	2D

10.1 Optimal working point

The choice of the working point for the b-tagging algorithm is a compromise between high efficiency for identifying true b-jets and high rejection factors against udsg-jets and c-jets. If ε_b is large, then also the probability of mistagging light- and c-jets is large. On the other hand, requiring high rejections $\mathrm{R_j}$ and $\mathrm{R_c}$ results in small efficiencies ε_b. The optimal working point is defined to maximize the expected significance $S/\sqrt{B}$.

Figures 10.3 and 10.4 show the significances $S/\sqrt{B}$ for b-tagging efficiencies ε_b between 50% and 80% (configuration B1 to B4) for all available masses of the Higgs boson. In all cases the significance is maximized for $\varepsilon_\mathrm{b} = 60\%$, justifying the choice of ε_b in the previous chapters. Table 10.2 presents the result of the scan in more detail, by showing the selection efficiency, the purities of the b-jet assignment to the top quarks and the Higgs boson, and the expected event rates for signal and background processes. As expected, the reconstruction purities are higher for smaller efficiencies ε_b. But the efficiency enters in the total selection efficiency by powers of four, and so a value of $\varepsilon_\mathrm{b} = 50\%$ does not yield the best significance. Stepping through the efficiencies from $\varepsilon_\mathrm{b} = 50\%$ to $\varepsilon_\mathrm{b} = 80\%$ the signal expectation increases roughly by factors of two. The increase for the irreducible $\mathrm{t\bar{t}b\bar{b}}$ background is a bit larger but comparable to the signal. In contrast, the reducible $\mathrm{t\bar{t}jj}$ background grows three times faster than the signal with increasing ε_b. The signal over background ratio, S/B, decreases almost linearly with increasing ε_b.

10.2 Significances with different detector configurations

On pages 106–112 graphical and numerical results for the parameterization from different detector configurations and event samples are shown. The b-tagging efficiency is 60% in all cases. In the graphical representations the changes are expressed as relative changes of $S/\sqrt{B}$ with respect to configuration '$\emptyset$' (TDR detector). Tables 10.3 and 10.4 contain details for all configurations in the analysis for $m_{\mathrm{H}^0} = 120$ GeV. Tables 10.5 and 10.6 specify for all masses and configurations the significances $S/\sqrt{B}$. For the sake of clarity, the graphs are divided into three categories:

Category I: Stepwise approach from a perfect detector to the realistic situation with pile-up and inefficiencies. Both the complete and the reduced (initial) detector layouts are used. The parameterization is deduced from $\mathrm{W^\pm H^0}$ events (Figs. 10.5 and 10.6).

Category II: Comparison between parameterizations from $\mathrm{W^\pm H^0}$ and $\mathrm{t\bar{t}H^0/t\bar{t}}$ events (Figs. 10.7 and 10.8).

Category III: Improvement of 3D b-tagging over 2D b-tagging (Figs. 10.9 and 10.10). The parameterization is derived from $\mathrm{W^\pm H^0}$ events.

In general, the figures show that the decrease in significance for the TDR method is almost independent of the mass of the Higgs boson. For the improved method a stronger mass dependence is observed, and smaller masses m_{H^0} are more affected than larger masses. In the following, the three categories are discussed for $m_{\mathrm{H}^0} = 120$ GeV.

Category I

Application of the 'perfect' detector layout, but with p_T-dependent $\mathrm{R_j}$ and $\mathrm{R_c}$, gives a decrease of $\approx 20\%$. Inclusion of pile-up reduces the significances by another 3%. With

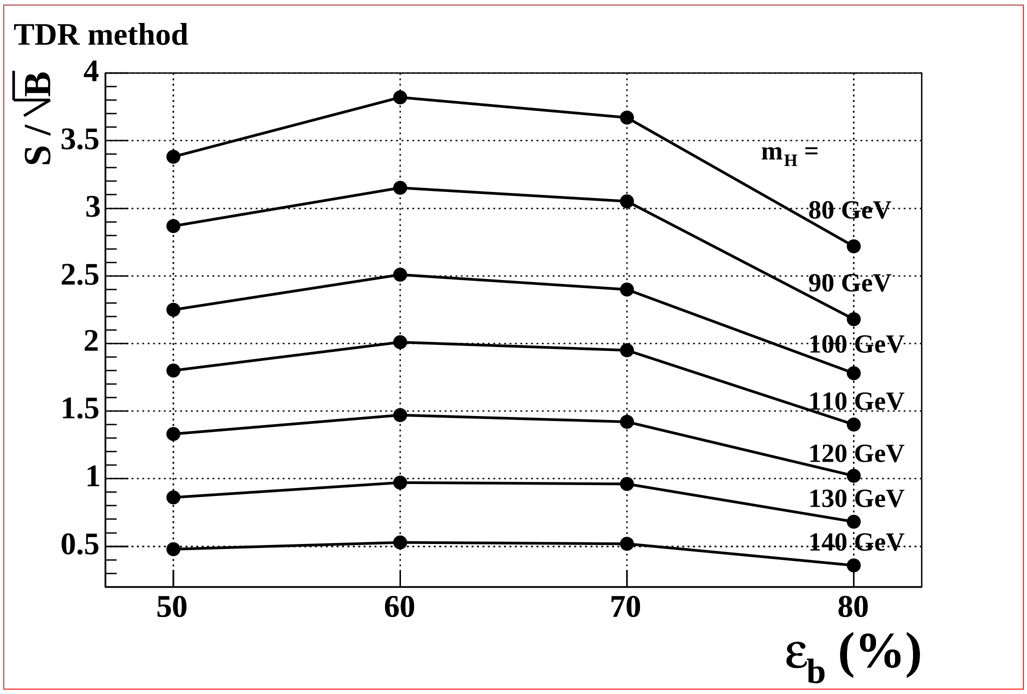

Figure 10.3: Significances for different b-tagging efficiencies using a parameterization for the 'complete layout' (configuration B1–B4) in the TDR reconstruction method.

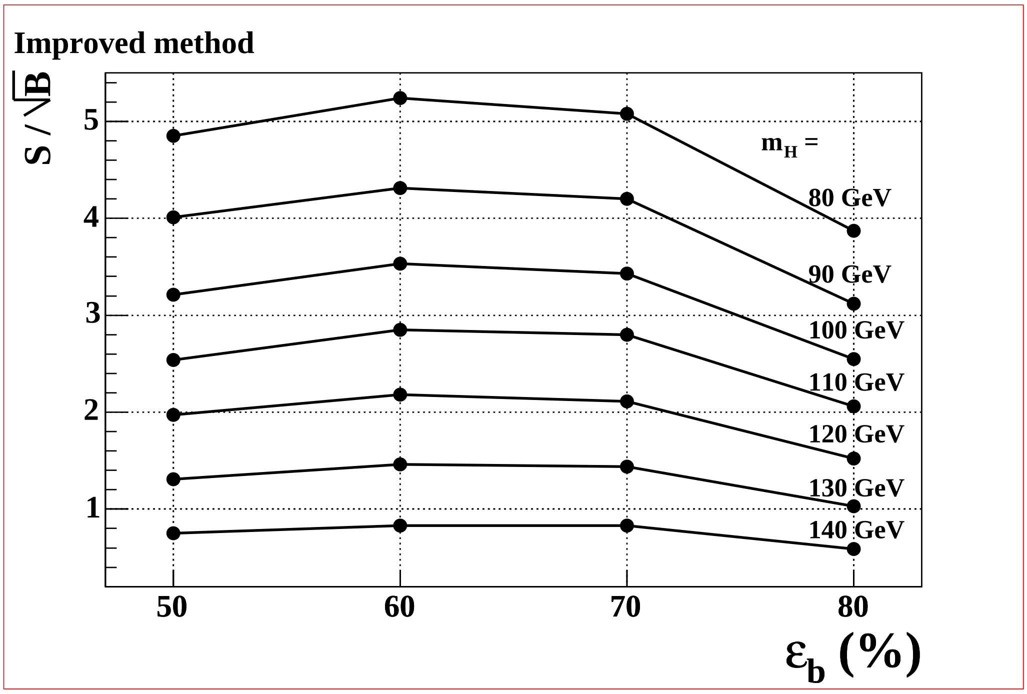

Figure 10.4: Significances for different b-tagging efficiencies using a parameterization for the 'complete layout' (configuration B1–B4) in the improved reconstruction method.

Table 10.2: Expected events for an integrated luminosity of 30 fb^{-1} and reconstruction purities for the assignment of b-jets. Numbers are given for the complete layout without pile-up, with 1%/2% module/chip inefficiencies and for various efficiencies ε_b.

TDR-Method

Configuration	B1	B2	B3	B4
ε_b	50%	60%	70%	80%
$\varepsilon_{\mathrm{t\bar{t}H^0}}$ (%)	0.47	1.03	2.03	3.51
$\mathcal{P}^b_{\mathrm{jjb}}$ (win)	57.8	53.3	48.6	37.6
$\mathcal{P}^b_{\ell\nu\mathrm{b}}$ (win)	59.5	57.1	54.4	46.9
$\mathcal{P}^b_{\mathrm{H^0\to b\bar{b}}}$ (all)	25.0	22.0	18.8	13.7
$\mathcal{P}^b_{\mathrm{H^0\to b\bar{b}}}$ (win)	47.1	43.3	38.2	29.2
$\mathrm{t\bar{t}H^0}$	14.8	32.9	64.7	111.6
$\mathrm{t\bar{t}b\bar{b}}$ (QCD)	75.4	196.4	461.9	1104.7
$\mathrm{t\bar{t}jj}$	38.7	280.9	1557.7	9400.6
$\mathrm{t\bar{t}b\bar{b}}$ (EW)	9.4	23.4	52.3	115.4
total bkg.	123.5	500.7	2071.9	10620.7
S/B	0.12	0.06	0.03	0.01
$S/\sqrt{B}$	1.33	1.47	1.42	1.08
$\sigma_{\mathrm{Poisson}}$	1.22	1.41	1.39	1.07

Improved method

Configuration	B1	B2	B3	B4
ε_b	50%	60%	70%	80%
$\varepsilon_{\mathrm{t\bar{t}H^0}}$ (%)	0.77	1.75	3.52	6.67
$\mathcal{P}^b_{\mathrm{jjb}}$ (win)	60.8	55.2	49.5	37.2
$\mathcal{P}^b_{\ell\nu\mathrm{b}}$ (win)	65.6	63.5	60.0	53.3
$\mathcal{P}^b_{\mathrm{H^0\to b\bar{b}}}$ (all)	26.6	23.1	19.5	14.1
$\mathcal{P}^b_{\mathrm{H^0\to b\bar{b}}}$ (win)	47.7	43.4	38.2	29.3
$\mathcal{P}^b_{\mathrm{H^0\to b\bar{b}}}$ (LH)	50.4	46.5	41.1	31.2
$\mathrm{t\bar{t}H^0}$	24.2	55.6	111.8	212.0
$\mathrm{t\bar{t}b\bar{b}}$ (QCD)	93.2	265.1	658.0	1818.4
$\mathrm{t\bar{t}jj}$	46.3	357.2	2073.9	14986.9
$\mathrm{t\bar{t}b\bar{b}}$ (EW)	12.2	30.9	72.3	179.1
total bkg.	151.7	653.2	2804.2	16984.4
S/B	0.16	0.08	0.04	0.01
$S/\sqrt{B}$	1.97	2.18	2.11	1.63
$\sigma_{\mathrm{Poisson}}$	1.84	2.11	2.08	1.62

the ‘complete’ layout including inefficiencies but no pile-up the significance changes by 24% w.r.t. the reference configuration ‘$\emptyset$’. Effects from pile-up bring a further decrease of 2%–3%. The ‘reduced’ layout, which represents the ATLAS detector in the starting phase, leads to 28%–29% smaller significances, and again the addition of pile-up changes the result by 2%–3%. Thus, with the initial detector, the significances are expected to be smaller by about one third compared to the simulation of a perfect detector and simplified parameterization of the b-tagging performance.

Category II

The parameterization from $\mathrm{t\bar{t}H^0/t\bar{t}}$ events is available only without pile-up and inefficiencies, and so the performance is compared to the same detector conditions in $\mathrm{W^{\pm}H^0}$ events. The parameterization from $\mathrm{t\bar{t}H^0/t\bar{t}}$ events gives $\approx 3\%$ better results than the parameterization from $\mathrm{W^{\pm}H^0}$ events. This behavior may contradict the expectations, since $\mathrm{t\bar{t}H^0/t\bar{t}}$ events have much larger track multiplicities than $\mathrm{W^{\pm}H^0}$ events. But it is shown in Ref. [51] that b-jets from $\mathrm{t\bar{t}H^0}$ and $\mathrm{t\bar{t}}$ events have slightly larger p_T than b-jets from $\mathrm{W^{\pm}H^0}$ events ($m_{\mathrm{H^0}} = 120$ GeV) and a more central η-distribution. This results in fewer multiple-scattering and an improved b-tagging performance. Furthermore, the $\mathrm{t\bar{t}H^0/t\bar{t}}$ samples were ‘cleaned’ by an isolation requirement to the jets in order to build the likelihood reference distributions.

Category III

These configurations shed light on the effect of a modified size of the pixels in the b-layer (300 µm versus 400 µm) and the improvement of a three-dimensional b-tagging algorithm over a two-dimensional algorithm. The graphs ‘300 µm’ denote the simulation with 400 µm pitch in Layer 1 and Layer 2 and 300 µm pitch in the B-Layer. Module/chip inefficiencies of 1%/2% are assumed. Unification of the pixel modules implies also 400 µm pixels in the B-Layer. A small degradation is expected from the increased z-pitch. On the other hand, it is then possible to select the best modules for assembly of the B-Layer, and less inefficiencies are expected. Therefore, the simulation was performed assuming smaller inefficiencies of 0.5%/1% for the innermost modules. The graphs ‘400 µm’ demonstrate that the degradation of the 400 µm pitch is compensated by higher quality of the B-Layer modules, and the significances are even better by about 2%.

Figures 10.9 and 10.10 also show that a three-dimensional b-tagging algorithm, which includes information from the impact parameter along the z-direction can enhance the performance significantly. Although at the time of writing the 3D-btag was in a preliminary stage, one can expect that it can compensate for much of the drop in significance [51].

An interesting result of these studies is the expected degradation of the b-tagging performance of the reduced detector layout, with those parts of the detector deferred as described in Section 7.6 (most important the second pixel layer and one disk), and the impact on the discovery potential of the $\mathrm{t\bar{t}H^0}$ channel. I turns out that with the staged detector the reducible $\mathrm{t\bar{t}jj}$ background increases by 20%–30%. Since $\mathrm{t\bar{t}jj}$ is not the main background, this has a moderate effect on the expected significances which is decreased by 4%–7%, depending on the parameterization used. An additional 8%–15% amount of data is needed to compensate the detector deferrals. However, it should be noted that the parameterization from $\mathrm{t\bar{t}H^0/t\bar{t}}$ events includes neither inefficiencies nor pile-up, and larger discrepancies between the complete and the reduced layout are expected if these effects are included.

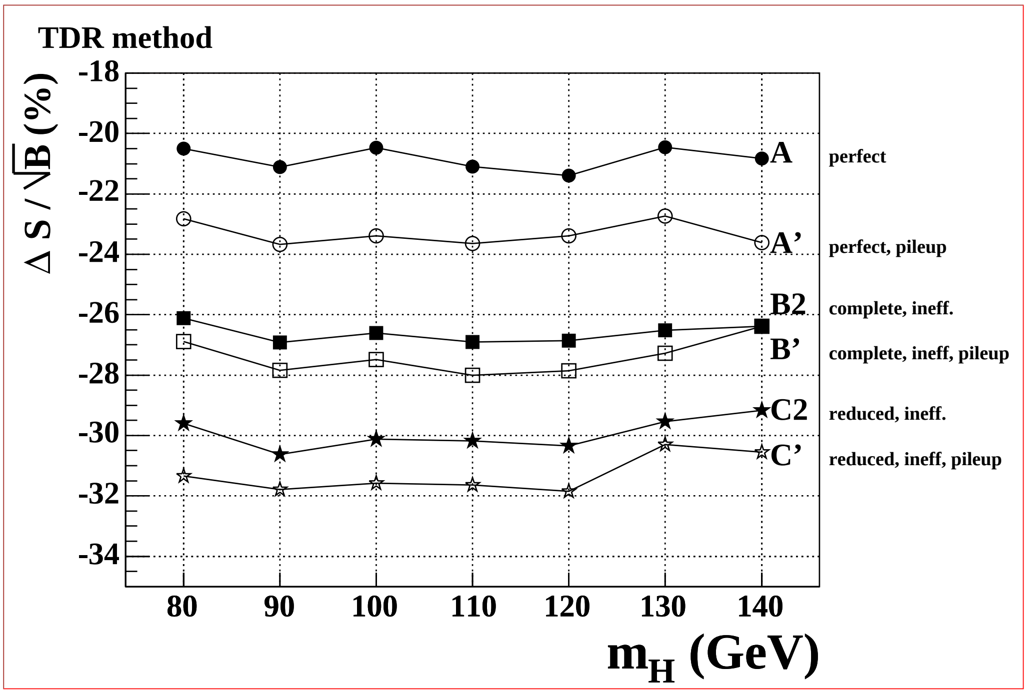

Figure 10.5: Category I—Significances relative to the 'perfect layout' (configuration ∅) for the TDR reconstruction method.

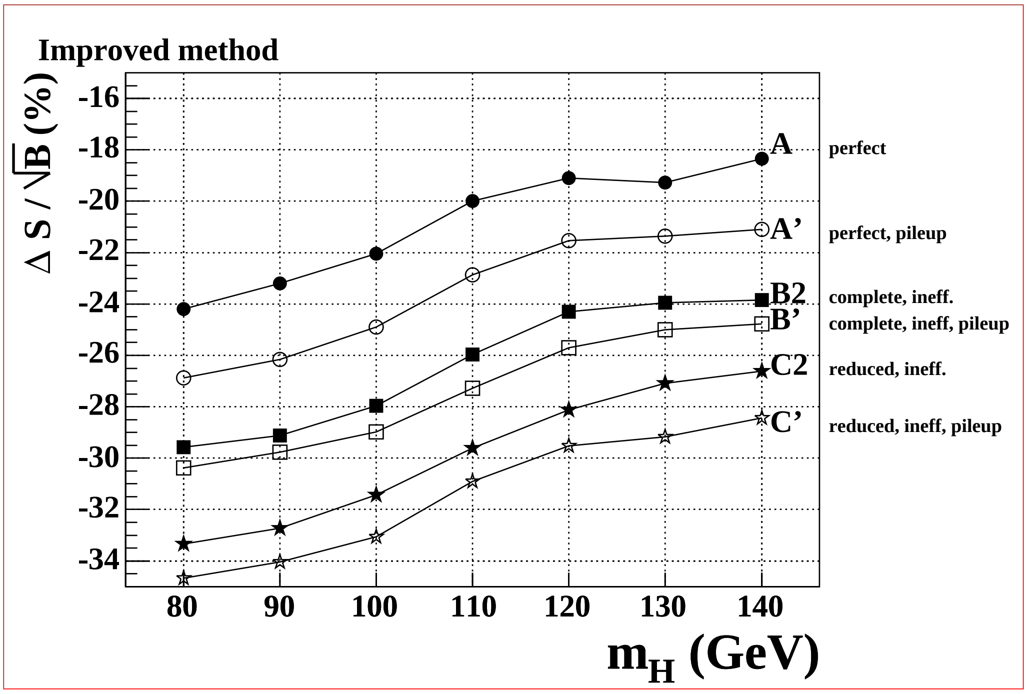

Figure 10.6: Category I—Significances relative to the 'perfect layout' (configuration ∅) for the improved analysis.

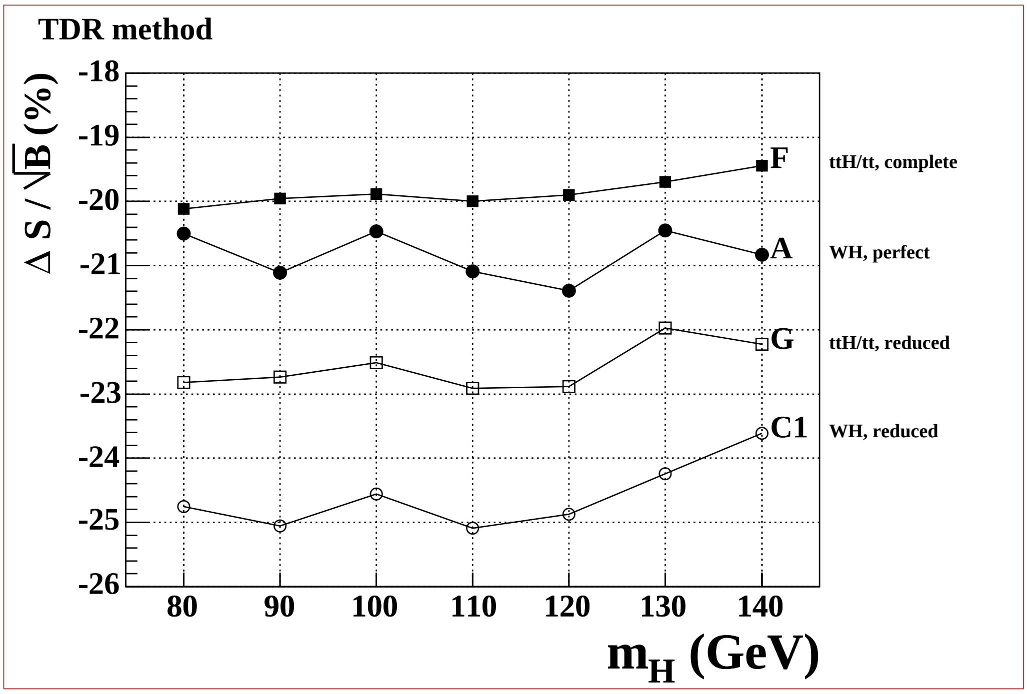

Figure 10.7: Category II—Significances relative to the 'perfect layout' (configuration ∅) for the TDR reconstruction method.

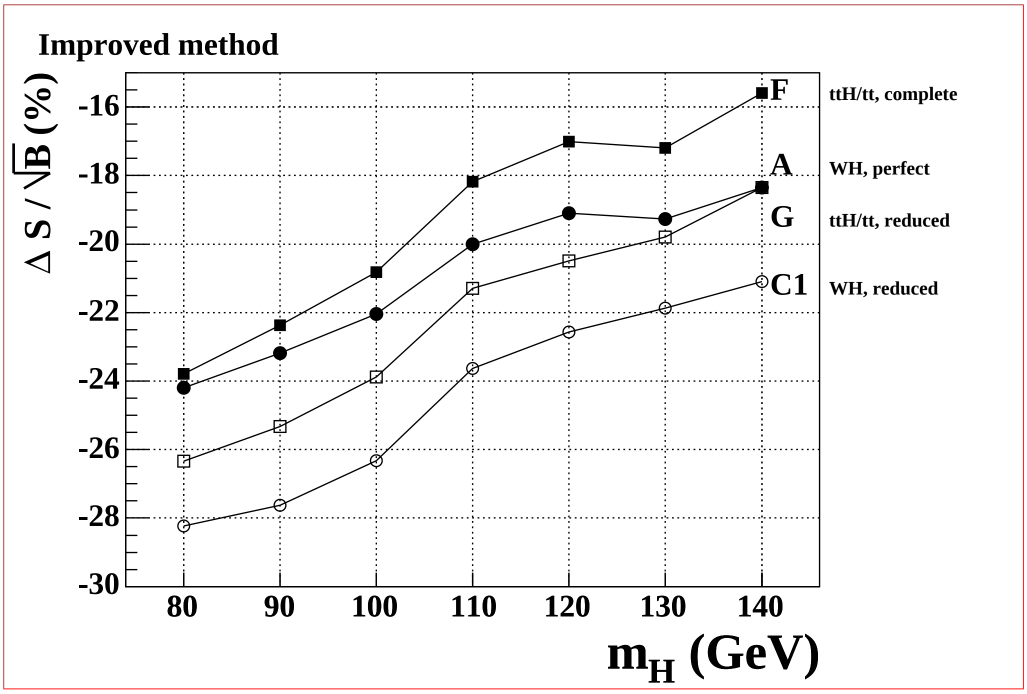

Figure 10.8: Category II—Significances relative to the 'perfect layout' (configuration ∅) for the improved analysis.

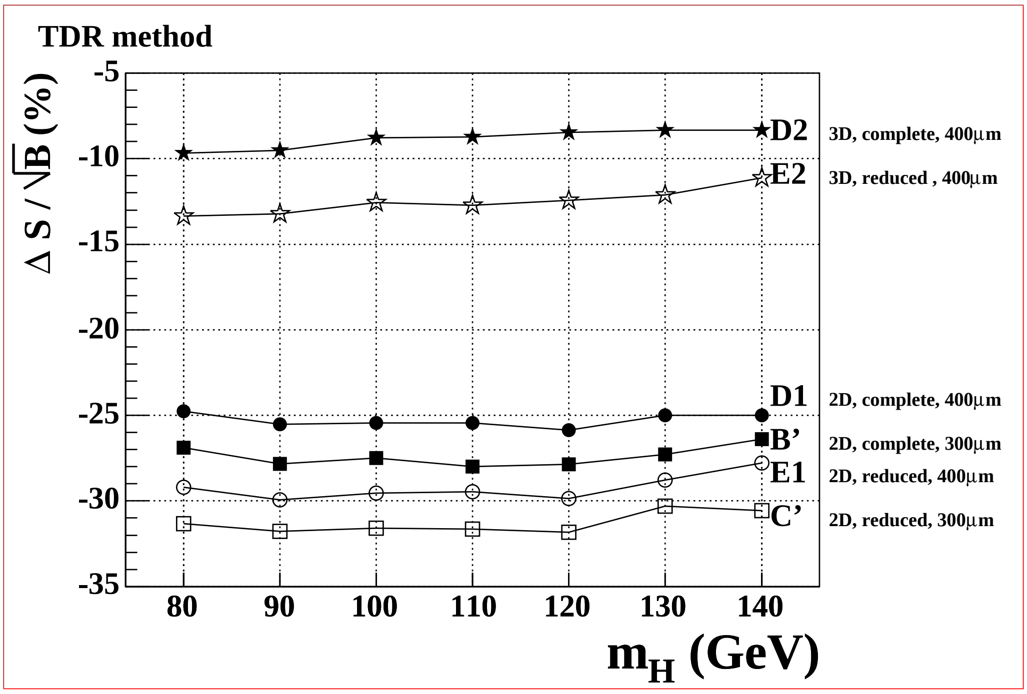

Figure 10.9: Category III—Significances relative to the 'perfect layout' (configuration ∅) for the TDR reconstruction method.

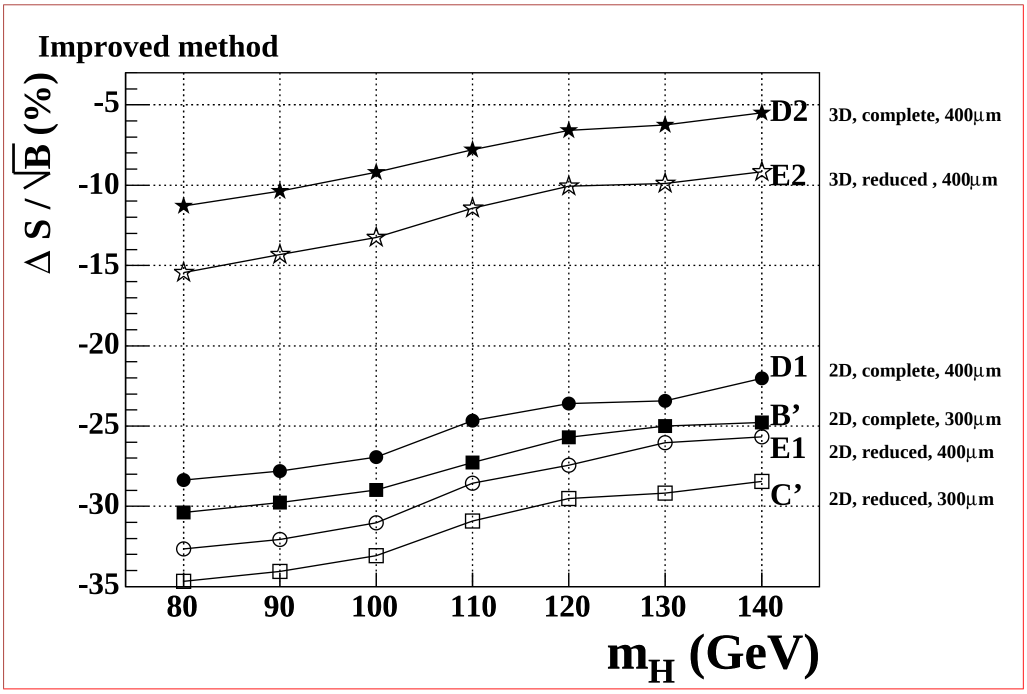

Figure 10.10: Category III—Significances relative to the 'perfect layout' (configuration ∅) for the improved analysis.

Table 10.3: TDR reconstruction: Expected events for an integrated luminosity of 30 fb^{-1}, the selection of a 120 GeV Higgs boson, and different detector configurations.

TDR-Method

Configuration	0	A	C1	C2	A'	B'	C'	D1	D2	E1	E2	F	G
$\varepsilon_{\mathrm{t\bar{t}H^0}}$ (%)	0.88	0.99	1.02	1.06	1.01	1.04	1.08	1.03	0.92	1.05	0.94	0.98	1.00
$\mathcal{P}^b_{\mathrm{jjb}}$	60.7	55.3	54.3	52.3	54.4	52.8	51.7	53.7	58.8	52.7	58.0	56.2	55.7
$\mathcal{P}^b_{\ell\nu\mathrm{b}}$	61.6	58.1	57.4	56.4	57.6	56.8	56.0	57.4	60.3	56.6	59.8	58.4	58.1
$\mathcal{P}^b_{\mathrm{H^0\to b\bar{b}}}$ (all)	27.2	23.3	22.5	21.2	22.7	21.7	20.8	22.3	25.7	21.4	25.0	23.8	23.3
$\mathcal{P}^b_{\mathrm{H^0\to b\bar{b}}}$ (win)	50.4	45.0	44.0	42.1	44.3	42.8	41.4	43.6	48.3	42.5	47.5	46.7	45.1
$\mathrm{t\bar{t}H^0}$	27.8	31.5	23.5	33.9	32.2	33.1	34.4	32.6	29.3	33.6	29.9	31.3	31.8
$\mathrm{t\bar{t}b\bar{b}}$ (QCD)	131.2	178.3	191.0	209.1	186.6	199.9	215.5	191.8	147.1	205.8	155.3	172.7	180.3
$\mathrm{t\bar{t}jj}$	44.7	196.7	249.8	353.5	229.2	300.7	391.1	260.4	87.3	336.7	113.5	183.0	216.9
$\mathrm{t\bar{t}b\bar{b}}$ (EW)	16.6	21.7	22.8	24.8	22.5	23.9	25.7	23.2	18.6	24.7	19.3	21.3	21.9
total bkg.	192.5	396.7	463.6	587.4	438.3	524.5	632.3	475.4	253.0	567.2	288.1	377.0	419.1
$S/\sqrt{B}$	2.01	1.58	1.09	1.40	1.54	1.45	1.37	1.49	1.84	1.41	1.76	1.61	1.55
$\sigma_{\mathrm{Poisson}}$	1.89	1.51	1.04	1.34	1.47	1.39	1.32	1.43	1.75	1.36	1.68	1.54	1.49

Table 10.4: Improved analysis: Expected events for an integrated luminosity of 30 fb^{-1}, the selection of a 120 GeV Higgs boson, and different detector configurations.

Improved method													
Configuration	0	A	C1	C2	A'	B'	C'	D1	D2	E1	E2	F	G
$\varepsilon_{\mathrm{t\bar{t}H^0}}$ (%)	1.43	1.66	1.99	1.80	1.70	1.76	1.84	1.73	1.50	1.80	1.54	1.63	1.66
$\mathcal{P}^b_{\mathrm{jjb}}$	63.1	57.3	56.5	54.4	56.5	54.8	53.7	55.7	61.4	54.6	60.5	58.6	57.9
$\mathcal{P}^b_{\ell\nu\mathrm{b}}$	67.6	64.5	64.1	62.9	64.0	63.4	62.5	63.6	66.4	63.0	66.0	64.9	64.5
$\mathcal{P}^b_{\mathrm{H^0\to b\bar{b}}}$ (all)	28.9	24.4	23.6	22.3	23.8	22.9	21.9	23.4	27.1	22.4	26.3	24.9	24.4
$\mathcal{P}^b_{\mathrm{H^0\to b\bar{b}}}$ (win)	50.9	45.2	44.3	42.5	44.4	43.0	41.8	43.7	48.6	42.7	47.8	45.9	45.3
$\mathcal{P}^b_{\mathrm{H^0\to b\bar{b}}}$ (LH)	53.5	48.1	47.4	45.6	47.4	45.9	44.8	46.8	51.7	45.7	50.9	49.1	48.4
$\mathrm{t\bar{t}H^0}$	45.6	52.7	54.2	57.2	54.1	56.1	58.3	55.0	47.9	56.8	49.0	51.7	52.7
$\mathrm{t\bar{t}b\bar{b}}$ (QCD)	166.0	235.5	252.1	284.2	250.6	271.9	294.1	260.9	187.5	278.6	198.3	225.2	235.8
$\mathrm{t\bar{t}jj}$	63.1	246.9	309.6	444.4	293.5	384.1	494.9	334.4	105.9	423.5	136.3	215.3	266.2
$\mathrm{t\bar{t}b\bar{b}}$ (EW)	21.0	28.2	29.7	32.5	29.3	31.7	33.9	30.5	23.4	32.5	24.2	27.1	28.4
total bkg.	250.1	510.6	591.4	761.1	573.4	687.7	822.9	625.8	316.8	734.6	358.8	467.6	530.4
$S/\sqrt{B}$	2.88	2.33	2.23	2.07	2.26	2.14	2.03	2.20	2.69	2.09	2.59	2.39	2.29
$\sigma_{\mathrm{Poisson}}$	2.74	2.25	2.16	2.01	2.18	2.07	1.97	2.13	2.57	2.03	2.48	2.30	2.21

Table 10.5: Significances for the different b-tagging parameter sets.

TDR method

m_{H^0} (GeV)	80	90	100	110	120	130	140
Configuration	Significance $S/\sqrt{B}$						
TDR, $\mathrm{R_j} = 100$, $\mathrm{R_c} = 10$							
$\emptyset$	5.2	4.3	3.4	2.8	2.0	1.3	0.7
from $\mathrm{W}^{\pm}\mathrm{H}^0$, no pile-up							
A	4.1	3.4	2.7	2.2	1.6	1.1	0.6
B1	3.4	2.9	2.3	1.8	1.3	0.9	0.5
B2	3.8	3.2	2.5	2.0	1.5	1.0	0.5
B3	3.7	3.1	2.4	2.0	1.4	1.0	0.5
B4	2.9	2.3	1.9	1.5	1.1	0.7	0.4
C1	3.9	3.2	2.6	2.1	1.1	1.0	0.6
C2	3.6	3.0	2.4	1.9	1.4	0.9	0.5
from $\mathrm{W}^{\pm}\mathrm{H}^0$, low luminosity pile-up							
A’	4.0	3.3	2.6	2.1	1.5	1.0	0.6
B’	3.8	3.1	2.5	2.0	1.5	1.0	0.5
C’	3.6	2.9	2.3	1.9	1.4	0.9	0.5
from $\mathrm{W}^{\pm}\mathrm{H}^0$, low luminosity pile-up, $400\,\mu$m pitch							
D1	3.9	3.2	2.6	2.1	1.5	1.0	0.5
D2	4.7	3.9	3.1	2.5	1.8	1.2	0.7
E1	3.7	3.0	2.4	1.9	1.4	0.9	0.5
E2	4.5	3.7	3.0	2.4	1.8	1.2	0.6
from $\mathrm{t\bar{t}H^0/t\bar{t}}$, no pile-up							
F	4.1	3.5	2.7	2.2	1.6	1.1	0.6
G	4.0	3.3	2.7	2.1	1.6	1.0	0.6

Table 10.6: Significances for the different b-tagging parameter sets.

Improved method

m_{H^0} (GeV)	80	90	100	110	120	130	140
Configuration	Significance $S/\sqrt{B}$						
TDR, $\mathrm{R_j} = 100$, $\mathrm{R_c} = 10$							
$\emptyset$	7.4	6.1	4.9	3.9	2.9	1.9	1.1
from $\mathrm{W}^{\pm}\mathrm{H}^0$, no pile-up							
A	5.6	4.7	3.8	3.1	2.3	1.6	0.9
B1	4.9	4.0	3.2	2.5	2.0	1.3	0.8
B2	5.2	4.3	3.5	2.9	2.2	1.5	0.8
B3	5.1	4.2	3.4	2.8	2.1	1.5	0.8
B4	4.1	3.3	2.7	2.2	1.6	1.1	0.6
C1	5.3	4.4	3.6	2.9	2.2	1.5	0.9
C2	5.0	4.1	3.4	2.7	2.1	1.4	0.8
from $\mathrm{W}^{\pm}\mathrm{H}^0$, low luminosity pile-up							
A’	5.4	4.5	3.7	3.0	2.3	1.5	0.9
B’	5.2	4.3	3.5	2.8	2.1	1.4	0.8
C’	5.0	4.0	3.3	2.7	2.0	1.4	0.8
from $\mathrm{W}^{\pm}\mathrm{H}^0$, low luminosity pile-up, $400\,\mu$m pitch							
D1	5.3	4.4	3.6	2.9	2.2	1.5	0.9
D2	6.6	5.5	4.5	3.6	2.7	1.8	1.0
E1	5.0	4.1	3.4	2.8	2.1	1.4	1.0
E2	6.3	5.2	4.3	3.4	2.6	1.7	0.9
from $\mathrm{t\bar{t}H}^0/\mathrm{t\bar{t}}$, no pile-up							
F	5.7	4.7	3.9	3.2	2.4	1.6	0.9
G	5.5	4.5	3.7	3.0	2.3	1.5	0.9

11 The high luminosity scenario

This chapter describes the potential of the $t\bar{t}H^0$ channel under high luminosity conditions using the ATLFAST simulation.

11.1 Performance of detector and reconstruction

At the LHC design luminosity of 10^{34} $cm^{-2}s^{-1}$ on average 23 minimum-bias events will be overlaid with a physics event of interest. This *pile-up* of events degrades the energy and momentum resolution of the detector sub-systems and affects the reconstruction of tracks and calorimeter clusters. The performance of ATLAS in high luminosity conditions was studied in fully simulated events and parameterized in ATLFAST [39].

To account for the larger background the trigger thresholds must be raised. This reflects in higher p_T cuts in the preselection of events in the $t\bar{t}H^0$ analysis: The p_T-threshold are raised from 20 GeV to 30 GeV for jets, and from 25 GeV to 30 GeV for electrons. The minimal p_T for muons can be kept at the level of 20 GeV. Since the track resolution is worse at high luminosity, the b-tagging efficiency is expected to decrease from 60% to 50% for the same rejection factors $R_j = 100$ and $R_c = 10$.

11.2 Reconstruction and selection at high luminosity

The two methods of reconstructing the top quarks, described in Chapter 9.1 and 9.2, are applied to the events simulated with high luminosity conditions using the tighter cuts described above.

The reconstructed top masses in signal events for the TDR and the improved reconstruction method are displayed in Figure 11.1, and results from a fit to the mass distributions are given in Table 11.1. The resolution for the reconstructed top masses is on average 1.7 GeV worse than at low luminosity.

At masses of the Higgs boson between 80 GeV and 100 GeV the fits for low luminosity and high luminosity give similar values for the width of the signal peak within the errors. For $m_{H^0} > 100$ GeV the signal peak becomes a bit broader under high luminosity conditions. Some example signal spectra and the fit parameters for the TDR and the improved reconstruction method are shown in Figures 11.2 and 11.3 and in Tables 11.2 and 11.3.

Taking into account the general decrease in the mass resolutions, the cuts on the reconstructed masses are loosened. The acceptance window for the jj-candidates is changed

Table 11.1: Resolution of the reconstructed top quarks at low and at high luminosity for the TDR and the improved reconstruction in $t\bar{t}H^0$ events with $m_{H^0} = 120$ GeV.

	'TDR' reconstruction		Improved reconstruction	
	low lumi	high lumi	low lumi	high lumi
σ_{jjb} (GeV)	7.7	9.2	10.4	13.4
$\sigma_{\ell\nu b}$ (GeV)	8.6	9.3	10.4	12.1

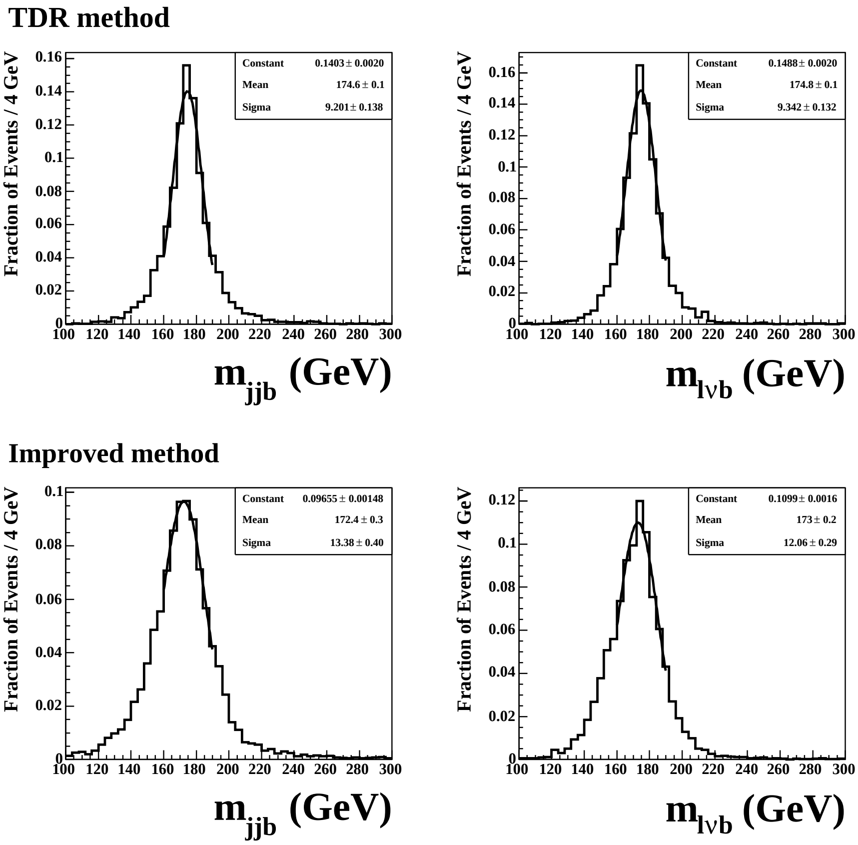

Figure 11.1: Reconstructed top masses in high luminosity conditions in $t\bar{t}H^0$ events with $m_{H^0} = 120$ GeV. Top row: TDR reconstruction method, bottom row: improved reconstruction method.

from 20 GeV to 25 GeV. The window for the reconstructed top quark masses is increased from 20 GeV to 23 GeV. The cut on m_{bb} is loosened from $m_{H^0}^{fit} \pm 30$ GeV to $m_{H^0}^{fit} \pm 45$ GeV to account for the decreased resolution at higher m_{H^0}. The changes of these cuts enhance the reconstruction efficiency to similar values as the reconstruction at low luminosity. The new mass cuts are summarized in Table 11.4.

The efficiencies in the steps of the analysis and the reconstruction purities are given in Table 11.5 for the TDR method and in Table 11.6 for the improved method. The efficiency after preselection (requiring one lepton and six jets of which four are b-tagged), is about one third of the efficiency at low luminosity due to tighter p_T cuts and a reduced b-tagging efficiency of 50%. The efficiency for reconstructing two top quarks is the product of the probability to find solutions for the neutrino momentum and the probability to find at least one jj-candidate inside the m_{jj} mass window. As a result of the generally worse resolutions at high luminosity, these two probabilities are smaller than for the low luminosity case, and the chance of successfully reconstructing two top quarks is reduced by a factor of 1.3. The efficiency of the cut on the reconstructed top-quark masses is similar to the low luminosity case, due to the increased mass cuts. The efficiency for the m_{bb} cut is higher at high luminosity because the cut window is increased considerably from 30 GeV to 45 GeV. This window was chosen to compensate for the smaller efficiency of the preselection cuts and to keep sufficiently large enough statistics for the final likelihood selection for events inside the mass window.

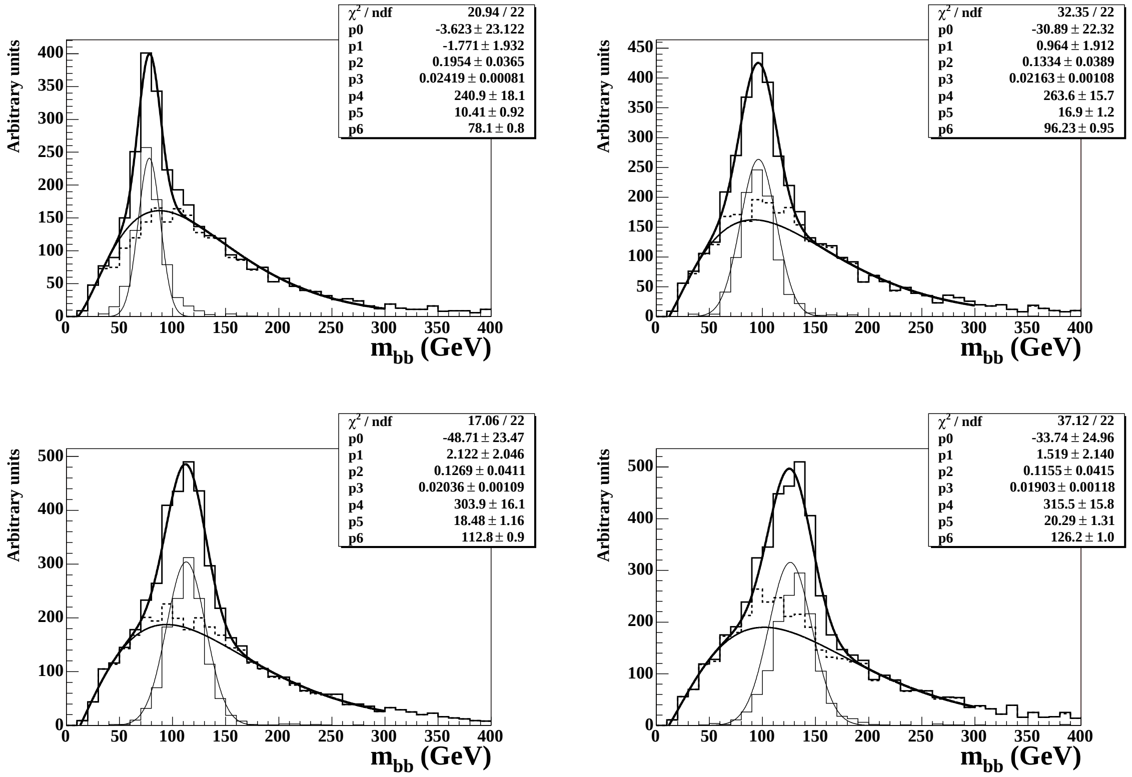

Figure 11.2: Fitted mass spectra of signal events for TDR reconstruction for $m_{\mathrm{H}^0} = 80, 100, 120, 140$ GeV. The thick line is the resulting fit to the complete spectrum in the range 10 GeV $< m_{\mathrm{bb}} <$ 300 GeV. The two thin lines show the fits to the combinatorial permutations (dashed histogram) and to the correctly reconstructed events (Gaussian-shaped histogram with thin line). The fit parameters p0–p6 correspond to the parameters in Equation (9.4) in the same order.

Table 11.2: Results for the parameters describing the Gaussian part of Equation 9.4 in signal events.

TDR method, high luminosity				
m_{H^0}(GeV)	$m_{\mathrm{H}^0}^{\mathrm{fit}}$(GeV)	$\Delta m_{\mathrm{H}^0}^{\mathrm{fit}}$(GeV)	σ(GeV)	$\Delta\sigma$(GeV)
80	78.1	0.8	10.4	0.9
90	87.3	0.8	12.4	0.9
100	96.2	0.9	16.9	1.2
110	103.6	0.9	16.5	1.3
120	112.8	0.9	18.5	1.1
130	121.3	0.9	18.7	1.2
140	126.2	1.0	20.3	1.3

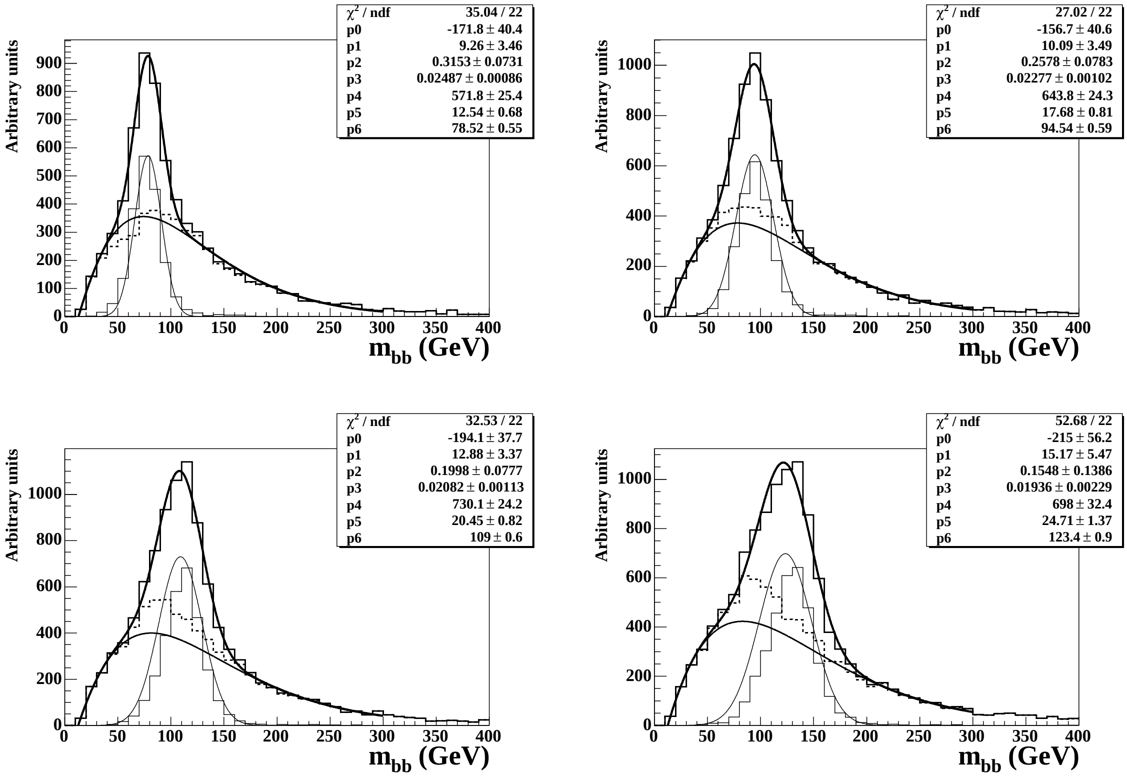

Figure 11.3: Fitted mass spectra of signal events for improved reconstruction for $m_{\mathrm{H}^0} = 80, 100, 120, 140$ GeV. The thick line is the resulting fit to the complete spectrum in the range 10 GeV $< m_{\mathrm{bb}} <$ 300 GeV. The two thin lines show the fits to the combinatorial permutations (dashed histogram) and to the correctly reconstructed events (Gaussian-shaped histogram with thin line). The fit parameters p0–p6 correspond to the parameters in Equation (9.4) in the same order.

Table 11.3: Results for the parameters describing the Gaussian part of Equation 9.4 in signal events.

Improved method, high luminosity				
m_{H^0}(GeV)	$m^{\mathrm{fit}}_{\mathrm{H}^0}$(GeV)	$\Delta m^{\mathrm{fit}}_{\mathrm{H}^0}$(GeV)	σ(GeV)	$\Delta\sigma$(GeV)
80	78.5	0.5	12.5	0.7
90	86.6	0.5	14.5	0.7
100	94.5	0.6	17.7	0.8
110	101.1	0.6	19.9	0.9
120	109.0	0.6	20.5	0.8
130	118.0	0.8	20.9	1.1
140	123.4	0.9	24.7	1.4

Table 11.4: Changes in the mass cuts used in the TDR reconstruction method (The cut on m_{bb} is also used in the improved analysis).

	high lumi	low lumi
m_{jj}	25 GeV	30 GeV
m_{jjb}	20 GeV	23 GeV
$m_{\ell\nu\mathrm{b}}$	20 GeV	23 GeV
m_{bb}	30 GeV	45 GeV

Table 11.5: TDR reconstruction method at high luminosity: Efficiencies after each step of the analysis for $m_{\mathrm{H}^0} = 120$ GeV. The relative efficiencies with respect to the previous step are given in parenthesis.

Cut	$\mathrm{t\bar{t}H^0}(120)$ (%)	$\mathrm{t\bar{t}b\bar{b}}$(QCD) (%)	$\mathrm{t\bar{t}jj}$ (%)	$\mathrm{t\bar{t}b\bar{b}}$(EW) (%)
1ℓ, 6 jets (4b)	1.2	0.5	3.1×10^{-3}	0.5
2 tops reconstructed	0.6 (46.6)	0.2 (45.5)	1.0×10^{-3} (33.3)	0.2 (45.7)
m_{t} inside mass window	0.4 (78.6)	0.15 (73.2)	0.7×10^{-3} (67.4)	0.16 (74.8)
m_{bb} inside mass window	0.3 (61.0)	0.06 (37.5)	0.3×10^{-3} (45.8)	0.07 (41.3)

Table 11.6: Improved reconstruction method at high luminosity: Efficiencies after each step of the analysis for $m_{\mathrm{H}^0} = 120$ GeV. The relative efficiencies with respect to the previous step are given in parenthesis.

Cut	$\mathrm{t\bar{t}H^0}(120)$ (%)	$\mathrm{t\bar{t}b\bar{b}}$(QCD) (%)	$\mathrm{t\bar{t}jj}$ (%)	$\mathrm{t\bar{t}b\bar{b}}$(EW) (%)
1ℓ, 6 jets (4b)	1.2	0.5	3.1×10^{-3}	0.5
2 tops reconstructed	0.95 (79.5)	0.36 (77.3)	2.0×10^{-3} (62.7)	0.4 (76.7)
m_{bb} inside mass window	0.62 (65.1)	0.14 (39.5)	1.0×10^{-3} (23.6)	0.15 (42.8)
$fLH > 0.35$	0.54 (87.9)	0.09 (66.8)	0.6×10^{-3} (61.2)	0.11 (70.3)

The reconstruction purity for b-jets is compared to the low luminosity values in Table 11.7. The purities are listed for events in the whole m_{bb} spectrum ('all'), for events inside the m_{bb} window ('win') and, in the case of the improved method, after the cut on the final likelihood ('*fLH*'). The purities at high luminosity are worse by only about 5% for b-jets associated to the top quarks and for b-jets from the decay of the Higgs boson considering events from the whole mass spectrum. The purity for b-jets from the Higgs boson for events inside the m_{bb} window is 10% worse at high luminosity (which corresponds to a relative decrease of about 20%). This is mainly due to the relaxed m_{bb} cut.

Finally, Tables 11.8 and 11.9 lists the expected event rates for high luminosity conditions for the TDR and the improved method. The assumed integrated luminosity is 100 fb^{-1} which corresponds to one year data taking at design luminosity. The significances $S/\sqrt{B}$ are very similar to the values obtained in Table 9.4 (page 73) and Table 9.13 (page 90) for three years at low luminosity ($\mathcal{L} = 30\ \mathrm{fb}^{-1}$). Figure 11.4 shows a graphical representation of expected significances for $\mathcal{L} = 100\ \mathrm{fb}^{-1}$ and $\mathcal{L} = 300\ \mathrm{fb}^{-1}$ at high luminosity conditions and for $\mathcal{L} = 30\ \mathrm{fb}^{-1}$ at low luminosity conditions. With 300 fb^{-1} the significance $S/\sqrt{B}$ is larger than five for $m_{\mathrm{H}^0} < 120$ GeV.

Table 11.7: Reconstruction purities for b-jets in signal events with $m_{\mathrm{H}^0} = 120$ GeV. The TDR and improved reconstruction method are compared at high and low luminosity.

Purity	$\mathcal{P}^b_{\mathrm{jjb}}$ (all) (%)	$\mathcal{P}^b_{\mathrm{jjb}}$ (win) (%)	$\mathcal{P}^b_{\ell\nu\mathrm{b}}$ (all) (%)	$\mathcal{P}^b_{\ell\nu\mathrm{b}}$ (win) (%)	$\mathcal{P}^b_{\mathrm{b\bar{b}}}$ (all) (%)	$\mathcal{P}^b_{\mathrm{b\bar{b}}}$ (win) (%)	$\mathcal{P}^b_{\mathrm{b\bar{b}}}$ (fLH) (%)
High luminosity							
TDR	48	56	47	57	27	42	—
Improved	47	56	54	63	28	41	44
Low luminosity							
TDR	48	61	50	62	27	50	—
Improved	50	63	55	68	29	51	54

Table 11.8: The TDR reconstruction method at high luminosity conditions. Expected events for the analysis of Higgs boson masses between 80 GeV and 140 GeV for an integrated luminosity of 100 fb^{-1}.

m_{H^0} (GeV)	80	90	100	110	120	130	140
$\varepsilon_{\mathrm{t\bar{t}H}^0}$ (%)	0.17	0.20	0.22	0.24	0.27	0.27	0.281
$\mathrm{t\bar{t}H}^0$	60.6	52.1	44.7	36.5	28.4	18.6	10.4
$\mathrm{t\bar{t}b\bar{b}}$ (QCD)	143.8	143.9	143.5	142.2	141.0	137.0	135.0
$\mathrm{t\bar{t}jj}$	47.1	47.1	45.2	45.8	45.8	45.8	45.8
$\mathrm{t\bar{t}b\bar{b}}$ (EW)	14.5	15.5	16.0	16.6	17.1	16.9	16.5
total bkg.	205.4	206.5	204.7	204.6	203.9	199.7	197.3
$S/\sqrt{B}$	4.2	3.6	3.1	2.6	2.0	1.3	0.7
$\sigma_{\mathrm{Poisson}}$	4.0	3.4	3.0	2.4	1.9	1.2	0.7

Table 11.9: The improved reconstruction and analysis method at high luminosity conditions. Expected events for the analysis of Higgs boson masses between 80 GeV and 140 GeV for an integrated luminosity of 100 fb^{-1}.

m_{H^0} (GeV)	80	90	100	110	120	130	140
$\varepsilon_{\mathrm{t\bar{t}H}^0}$ (%)	0.37	0.41	0.46	0.51	0.54	0.55	0.57
$\mathrm{t\bar{t}H}^0$	128.2	108.5	93.0	77.5	57.7	37.5	20.8
$\mathrm{t\bar{t}b\bar{b}}$ (QCD)	218.9	229.0	233.9	244.7	231.2	226.9	209.1
$\mathrm{t\bar{t}jj}$	98.8	105.2	109.1	106.5	92.3	83.9	80.0
$\mathrm{t\bar{t}b\bar{b}}$ (EW)	23.3	26.3	27.1	29.0	27.9	27.8	26.6
total bkg.	341.0	360.5	370.1	380.2	351.4	338.6	315.7
$S/\sqrt{B}$	6.9	5.7	4.8	4.0	3.1	2.0	1.2
$\sigma_{\mathrm{Poisson}}$	6.5	5.4	4.6	3.8	2.9	1.9	1.1

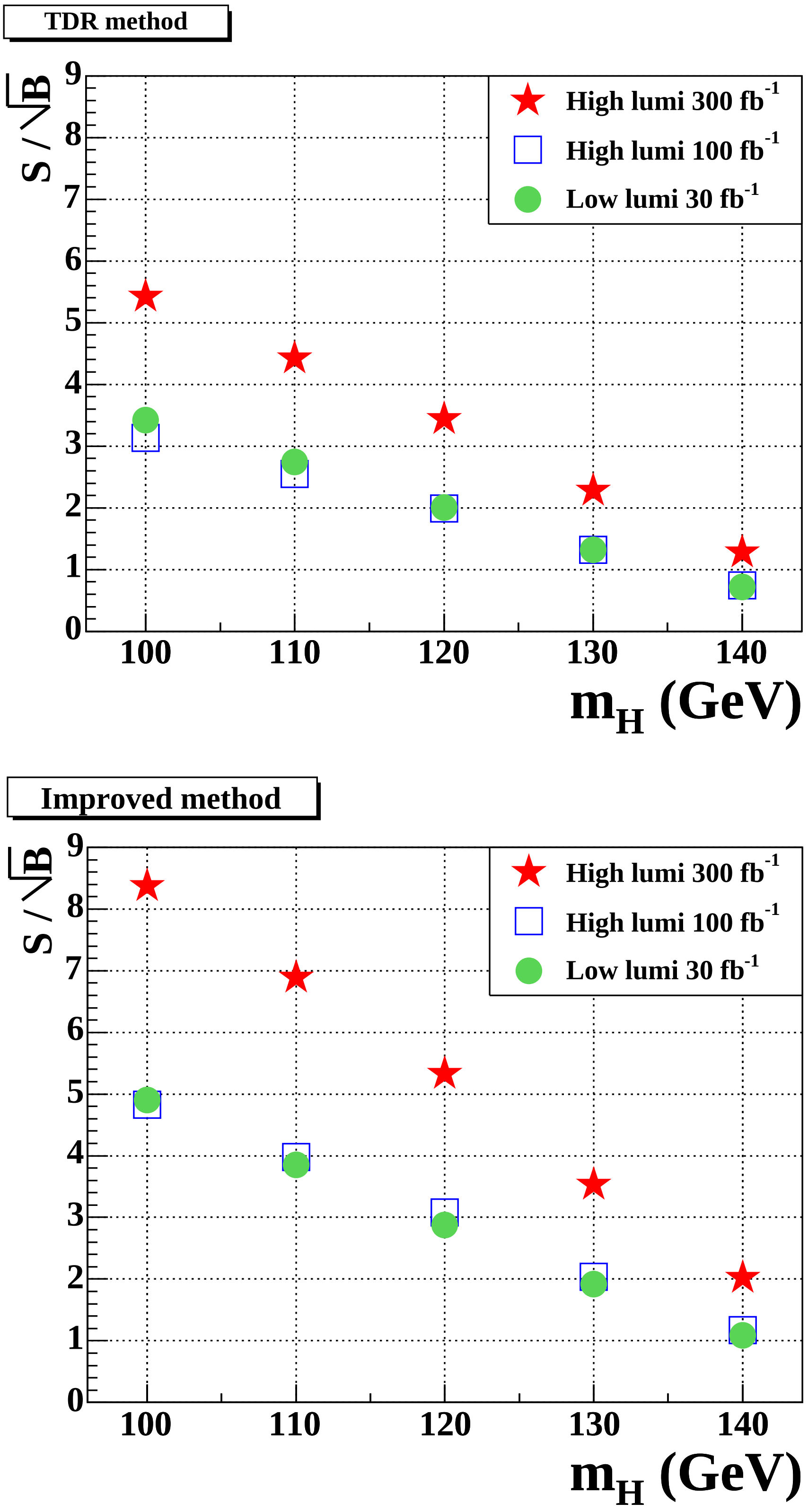

Figure 11.4: Significances $S/\sqrt{B}$ for Higgs masses between 100 and 140 GeV. Results for 30 fb^{-1} at low luminosity conditions are compared to results at high luminosity conditions for 100 fb^{-1} and 300 fb^{-1}.

12 Full simulation

The results in the preceding sections are obtained with the fast simulation of the ATLAS detector. The fast simulation with ATLFAST allows for generating a huge number of events with modest computing power. In contrast, the full GEANT 3 [38] based detector simulation and event reconstruction are very CPU time consuming so that only a few hundred thousand Monte Carlo events can be simulated in a reasonable amount of time. Nevertheless, some issues must be studied in full simulation, since some quantities are not available in ATLFAST or implemented in a simplified way (*e.g.*, reconstruction of tracks, b-tagging).

The study with fully simulated events serves two purposes:

1. re-evaluation of the parameterized fast simulation of the ATLAS detector with the latest detector layout,
2. investigation of the $\mathrm{t\bar{t}H^0}$ channel with an impact parameter based b-tagging algorithm.

Fully simulated events in the $\mathrm{t\bar{t}H^0}$ channel were already used in the TDR study in 1999, but only for signal events and using 'perfect' b-tagging $\varepsilon_\mathrm{b} = 100\%, \mathrm{R_j} = \mathrm{R_c} = \infty$. In the context of the ATLAS data challenges (DC 1) [60] in 2002, fully simulated and reconstructed $\mathrm{t\bar{t}H^0}$ events were produced with four times more statistics (20 k events) and for different detector layouts. In addition, fully simulated background events are available, too. The data challenges are a collaboration-wide effort to validate the ATLAS computing and data model, the software suite, and to ensure the correctness of the technical choices to be made. In later stages the integration into the GRID computing context [61] will be made. The new b-tagging parameterizations described in Section 10 offer the chance to apply b-tagging algorithms to the fully reconstructed events and to compare with the results with the parameterization of the fast simulation.

Another interesting question is whether information from a fully simulated b-tagging can be used to improve the background rejection of misidentified $\mathrm{t\bar{t}}$+light jets events.

Table 12.1 details the data sets used for this study. The 'initial' detector is subject to deferrals described in Section 7.6 and has only two pixel layers. The 'full' detector describes the final layout of ATLAS, except for the pixel detector which is simulated with two and three pixel layers.

Table 12.1: Data samples for the full simulation study.

Process	Run	Size	Detector
$\mathrm{t\bar{t}H^0}$	2308	20 k	initial
$\mathrm{t\bar{t}H^0}$	2310	20 k	full, 2 layers
$\mathrm{t\bar{t}H^0}$	2311	20 k	full, 3 layers
$\mathrm{t\bar{t}}$+jets	2309	100 k	initial
$\mathrm{t\bar{t}}$+jets	2312	20 k	full, 2 layers
$\mathrm{t\bar{t}}$+jets	2313	20 k	full, 3 layers

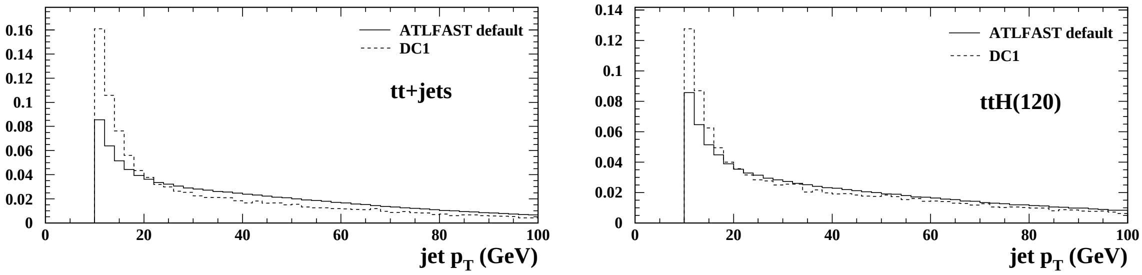

Figure 12.1: Distribution of the jet transverse momentum in samples used in sections 8 to 11 and samples from the ATLAS data challenges. The events are processed with the fast simulation, and the histograms are normalized to Unity.

12.1 Processing fully simulated events

In the reconstruction and analysis chain, events from full simulation are treated in the same way as those from fast simulation. There is only one extra step. Before applying the jet-calibration from ATLFAST an additional calibration is applied to the energy of fully reconstructed jets in order to compensate detector effects (*e.g.*, gaps, non-compensation) which are not apparent in the fast simulation. Therefore, before applying the jet calibration from ATLFAST, an additional calibration is applied to compensate detector effects [62].

There is a complication when comparing fully simulated events with those from the fast simulation. The full simulation events from the ATLAS data challenges were generated with different settings in PYTHIA. The multi-interaction scheme was changed to the one that is used by the CDF collaboration to model minimum bias events. The new scheme assumes a varying impact parameter and hadronic matter overlap ([40], PYTHIA switches `MSTP(82)=4`, `PARP(82)=2.2`). The effect from this change is an increase in the multiplicity of low-p_T jets, most prominent in $t\bar{t}$ events, as can be seen from Figure 12.1. Hence, a larger amount of $t\bar{t}$ events is expected to survive the selection cuts, and it will be difficult to compare the expected event rates and mass distributions of the DC 1 samples with those obtained in previous sections. Therefore, the DC 1 samples are also processed by ATLFAST, so that fast and full simulation can be compared with the same events.

The full reconstruction does not yet provide lepton identification and proper calibration of the missing transverse momentum. Therefore, electrons, muons, and p_T^{miss} are taken from the fast simulation. Although a complete treatment using only full simulation and reconstruction would be preferable, the described procedure still gives meaningful results, since the performance of the $t\bar{t}H^0$ channels is dominated by the quality of reconstruction and b-tagging of the six jets.

The study of fully simulated events is done in two steps. First, the fast and full simulation are compared in terms of mass resolution and efficiencies of the cuts used in the analysis (Section 12.4). Three detector layouts are used in order to compare the detector performance in the initial phase with the one of the 'complete' detector. The fully simulated events are also reconstructed using an impact-parameter based b-tagging algorithm described below.

In the second step the additional information from the 'b-ness' of a jet, provided by the b-tagging algorithm, is explored in order to reduce further the reducible $t\bar{t}jj$ background.

All studies involving fully simulated events are carried out with the TDR reconstruction method. The statistics of the samples is not large enough to allow for proper generation

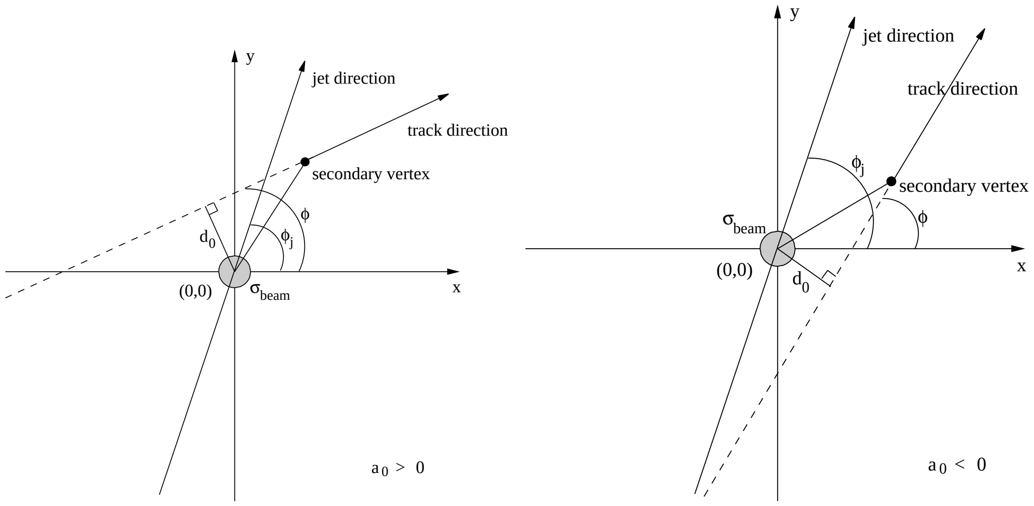

Figure 12.2: Definition of the impact parameter.

of reference histograms needed for the likelihood reconstruction and analysis. In principle, the reference histograms used in previous sections could be applied. But since fully simulated background events are available from the PYTHIA generator only, and are generated with different settings, affecting p_T and multiplicity distributions, non-optimal results are expected.

12.2 The b-tagging algorithm

This section describes the algorithm which is used for b-tagging in the full simulation samples [59]. It takes advantage of the lifetime of B-hadrons contained in b-jets. B-hadrons decay at a certain distance from the primary vertex, so that tracks originating from the decay have a non-zero distance of closest approach, d_0, to the primary vertex. Charm-jets also contain lifetime information, but not as distinct as b-jets.

The impact parameter of a track with respect to the jet axis is defined by (Figure 12.2)

$$a_0 = \begin{cases} +|d_0| & \text{if} \quad d_0 \sin(\phi_j - \phi) > 0 \\ -|d_0| & \text{if} \quad d_0 \sin(\phi_j - \phi) < 0. \end{cases}$$

The impact parameter is weighted by its error combined with the beam spread σ_{beam}. The new quantity is called impact parameter significance S_{a_0}:

$$S_{a_0} = \frac{a_0}{\sqrt{\sigma_{a_0}^2 + \sigma_{\text{beam}}^2}}.$$

The distribution of the significances of tracks in b-jets, c-jets, and u-jets is shown in Figure 12.3. Tracks in b-jets have a tail at larger values of the impact parameter significance which is more prominent than for c-jets or light jets. A weight function ω is calculated from the track significances:

$$\omega = \sum_{j=1}^{n} \ln \omega_j,$$

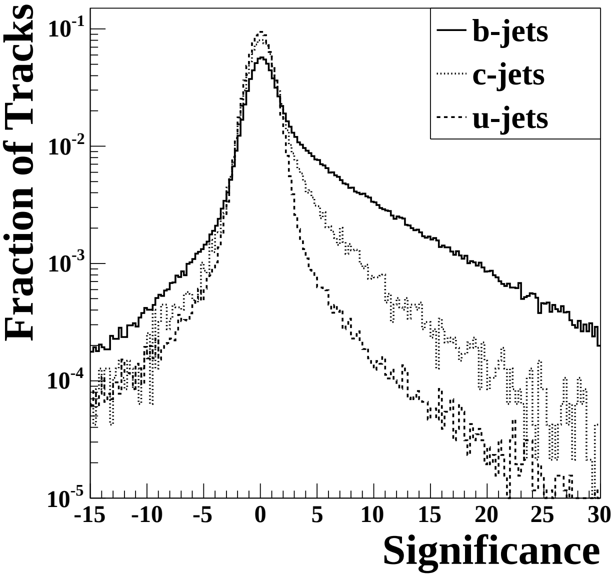

Figure 12.3: Distribution of impact parameter significances in $t\bar{t}H^0$ events simulated with the complete detector layout.

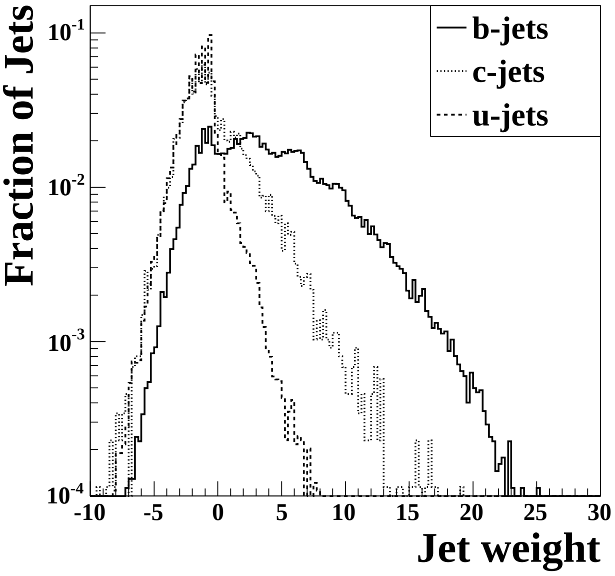

Figure 12.4: Distribution of jet weights in $t\bar{t}H^0$ events simulated with the complete detector layout.

where $\omega_j = f_b(S_{a_0})/f_u(S_{a_0})$, and f_b, f_u are the normalized distributions of the impact parameter significances. The sum runs over all tracks in the jet. The resulting distribution of weights (Figure 12.4) discriminates nicely between the jet flavors, with b-jets having large and u-jets having small weights. A cut is then applied at a certain value ω_b. Jets with $\omega \geq \omega_b$ are tagged as b-jets. The choice of ω_b defines the efficiency ε_b and rejection factors against light- and c-jets. In this analysis a jet is tagged as b-jet if $\omega > 2$. This corresponds to an average efficiency of $\varepsilon_\mathrm{b} = 0.6$.

12.3 b-tagging and normalization of fully simulated $\mathrm{t\bar{t}}$ events

The $\mathrm{t\bar{t}}$ samples contain mainly $\mathrm{t\bar{t}jj}$ events and only a small fraction of true $\mathrm{t\bar{t}b\bar{b}}$. The sample is therefore strongly reduced by the requirement of four b-tagged jets. In the studies with fast simulation a sample of 20 M $\mathrm{t\bar{t}jj}$ events was generated. These statistics are not available with full simulation, the samples listed in Table 12.1 contain 20 k or 100 k events. Applying a b-tagging algorithm would therefore yield very small Monte Carlo statistics and large statistical errors for the $\mathrm{t\bar{t}}$ background (after all cuts less than 10 Monte Carlo events would remain): For example, with $\varepsilon_\mathrm{b} = 0.6, \mathrm{R_j} = 100$ the probability for a $\mathrm{t\bar{t}jj}$ event to survive the cut $N_b = 4$ is $P = 0.6^2 \cdot 0.01^2 = 36 \cdot 10^{-6}$ (assuming the jets jj are u, d, s or g-jets). To enlarge statistics, in events with less than four b-jets, the light and c-jets are mistagged until the total number of b-tagged jets is at least four. The jets are chosen randomly, but they must lie in $|\eta| < 2.5$. In the case of full simulation, the fake b-jets must also be given a jet weight. The weight ω is chosen randomly according to the probability density function of $\omega > 2$ for light jets and c-jets as shown in Figure 12.4, and the jet weights correspond to the detector layout of the sample. Events where jets are mistagged with this procedure are called *forced*$_n$-jets in the following, because they are forced to contain n b-tagged jets.

The *forced*$_n$-jets must be normalized properly, taking into account the efficiencies of b-tagging and mistagging. The normalization weight $\mathcal{N}$ must be calculated for each event, because the probability of containing at least four b-tagged jets (either true b-jets or misidentified light or c-jets) depends on the number of b-jets, light jets and c-jets in the event. The normalization factor is the sum of probabilities of all possible combinations to find n b-tagged jets, provided there are N_b b-jets, N_c c-jets and N_j jets of other flavors, a (constant) b-tag efficiency ε_b and rejection factors $\mathrm{R_c}$ and $\mathrm{R_j}$. If $\mathrm{R_j}$ and $\mathrm{R_c}$ were constant, the combinatorial multiplicity could simply be taken into account with binomial coefficients. But in the general case the rejection factors are functions of the p_T of the jet. Hence, the rejection probability is different for each jet and the total probability must be calculated explicitly for each possible combination:

$$\begin{aligned}\mathcal{N}_\mathrm{event} &= P_{tot}(N_\mathrm{b}, N_\mathrm{j}, N_\mathrm{c}, n - N_\mathrm{b})\\ &= \sum_{i=0}^{N_\mathrm{b}} P_\mathrm{b}(N_\mathrm{b}, i) \times P_\mathrm{jc}(N_\mathrm{j}, N_\mathrm{c}, n - i),\end{aligned}$$

where

$$\begin{aligned}P_\mathrm{b}(N_\mathrm{b}, i) &= \binom{N_\mathrm{b}}{i} \times \varepsilon_\mathrm{b}^i \times (1 - \varepsilon_\mathrm{b})^{N_\mathrm{b} - i},\\ P_\mathrm{jc}(N_\mathrm{j}, N_\mathrm{c}, m) &= \sum_{k=0}^{m} P_\mathrm{j}(N_\mathrm{j}, k) \times P_\mathrm{c}(N_\mathrm{c}, m - k),\end{aligned}$$

Table 12.2: Test of the normalization procedure. Expected events for $\mathcal{L} = 30\ \text{fb}^{-1}$ and the selection for $m_{\text{H}^0} = 120$ GeV after preselection ('pre'), after reconstruction of the m_{bb} spectrum ('all'), and inside the m_{bb} mass window ('win').

Process	$\text{t}\bar{\text{t}}\text{jj}$			$\text{t}\bar{\text{t}}$+jets			$\text{t}\bar{\text{t}}\text{H}^0$		
'default'	pre	all	win	pre	all	win	pre	all	win
ATLFAST b-tag	456.9	131.3	44.7	1260.2	459.7	133.3	119.1	56.6	27.8
forced$_4$+*forced*$_5$	445.3	143.2	46.1	1183.1	457.4	137.2	114.8	57.7	29.1
$\Delta_{\text{rel.}}$ (%)	−2.5	9.1	3.1	−6.1	−0.5	3.0	−3.6	1.8	4.4
Process	$\text{t}\bar{\text{t}}\text{jj}$			$\text{t}\bar{\text{t}}$+jets			$\text{t}\bar{\text{t}}\text{H}^0$		
'initial'	pre	all	win	pre	all	win	pre	all	win
ATLFAST b-tag	2338.9	690.8	216.9	3430.0	1132.6	356.1	149.1	68.1	31.8
forced$_4$+*forced*$_5$	2253.7	730.0	233.5	3376.0	1170.1	367.6	146.6	72.1	35.3
$\Delta_{\text{rel.}}$ (%)	−3.6	5.7	7.7	−1.6	3.4	3.2	−1.7	5.9	11.3

and (x = j or c)

$$P_x(N_x, r) = \begin{cases} \sum\limits_{l=0}^{N_x} \left(1 - \frac{1}{\text{R}_x(l)}\right) & \text{if r=0,} \\ \sum\limits_{Comb.} \left[\left\{ \prod\limits_{s \in Comb.} \frac{1}{\text{R}_x(s)} \right\} \left\{ \prod\limits_{t \notin Comb.} \left(1 - \frac{1}{\text{R}_x(t)}\right) \right\} \right] & \text{if r>0,} \end{cases}$$

where the last sum runs over all possible combinations to choose r jets out of N_x jets, s runs over the set of jets selected for that very combination, and t runs over the set of jets not selected in that combination.

It is sufficient to generate two sets, *forced*$_4$ and *forced*$_5$, because the probability to find more than five b-jets is negligible. The normalization procedure is tested with three high-statistics samples from the fast simulation: $\text{t}\bar{\text{t}}\text{jj}$ (contains no $\text{t}\bar{\text{t}}\text{b}\bar{\text{b}}$), $\text{t}\bar{\text{t}}$+jets (both $\text{t}\bar{\text{t}}\text{jj}$ and $\text{t}\bar{\text{t}}\text{b}\bar{\text{b}}$), and $\text{t}\bar{\text{t}}\text{H}^0$ with $m_{\text{H}^0} = 120$ GeV. Each sample is reconstructed with the TDR reconstruction method, first using the default ATLFAST b-tagging, then forcing each event to contain four and five b-jets with the method described above. Two b-tagging parameterizations are used: The 'default' with $\varepsilon_{\text{b}} = 0.6$, $\text{R}_{\text{c}} = 10$, $\text{R}_{\text{j}} = 100$, and the p_T-dependent parameterization for the initial layout derived from $\text{t}\bar{\text{t}}\text{H}^0/\text{t}\bar{\text{t}}$ events. The results are listed in Table 12.2. In general, the agreement between the procedures is better than 10%. In the $\text{t}\bar{\text{t}}$+jets sample, which is relevant for the results in the full simulation study, the agreement is even at the 5% level. In conclusion, the approximation of 'forcing' the events to the desired number of b-tagged jets with proper normalization gives acceptable results compared to the default random-tag procedure.

12.4 Comparison between fast and full simulation

This section compares the steps of the reconstruction and analysis and mass resolutions in fast and fully simulated events.

12.4.1 Simplified b-tagging

In order to compare fast and full simulation without the influence of different b-tagging procedures, the simplified, random b-tagging with $\varepsilon_{\text{b}} = 60\%$, $\text{R}_{\text{j}} = 100$, $\text{R}_{\text{c}} = 10$ is applied

Table 12.3: Left: Reconstructed masses and resolutions in fast and full simulation. A simplified b-tagging is used as described in the text. Right: Efficiencies in the steps of the reconstruction. The relative efficiencies with respect to the previous step are given in parenthesis. The efficiencies marked with an asterisk are given with respect to the preselection (1ℓ, 6 jets (4b)) and are not taken into account separately in the cumulative efficiency, since they are included in the cut '2 tops reconstructed'.

$\mathrm{t\bar{t}H^0}$	R2308+2310+2311 Fast	Full
m_{jjb}	174.6 ± 0.2	175.1 ± 0.2
$\sigma_{m_{\mathrm{jjb}}}$	6.9 ± 0.2	7.4 ± 0.2
$m_{\ell\nu\mathrm{b}}$	174.2 ± 0.3	174.7 ± 0.2
$\sigma_{m_{\ell\nu\mathrm{b}}}$	9.4 ± 0.3	7.9 ± 0.2
m_{bb}	108.0 ± 2.1	117.7 ± 2.4
$\sigma_{m_{\mathrm{bb}}}$	20.3 ± 2.5	22.5 ± 4.8

Cut	Fast (%)	Full (%)
1ℓ, 6 jets(4b)	3.9	3.5
Sol. for $\mathrm{W} \rightarrow \ell\nu$ exists*	2.8 (72.8)	2.5 (71.5)
m_{jj} candidate*	3.2 (81.9)	2.8 (80.3)
2 tops reconstructed	2.3 (60.1)	2.0 (56.7)
m_{t} inside mass window	1.9 (80.1)	1.6 (78.2)
m_{bb} inside mass window	0.9 (49.0)	0.7 (46.6)

to the signal samples, run 2308, run 2310, and run 2311. Since tracking is not important with the simplified b-tagging, the three runs are combined to increase the statistics.

Table 12.3 shows results of fits to the reconstructed top quark and Higgs boson masses. The width of the fully hadronically decaying top quark and the Higgs boson is a bit broader for fully simulated events. The resolution of the semileptonically decaying top quark is slightly worse in events simulated with ATLFAST. There is no significant difference between fast and full simulation in the peak position of the top quark masses. However, the peak in the m_{bb} distribution in fully simulated events is closer to the generated Higgs boson mass compared to events from ATLFAST. This difference can be explained by the additional jet calibration mentioned in Section 12.1 which must be applied in the full simulation to account for detector deficiencies. Since the calibration to compensate for physics effects under-estimates the jet energies, as discussed in Section 9.1.5.2, one can conclude that the additional full simulation calibration over-estimates the energies. In total, over- and under-estimation almost cancel, and the mass peak is reconstructed close to the expected mass. The calibration issue is not so distinct in the top quark masses, because the reconstruction forces them to be as close to m_{t} as possible (c.f. Equation 9.3 on page 63).

The comparison of the cut efficiencies reveals no significant difference between fast and full simulation. Slightly smaller efficiencies of mass cuts can be attributed to the larger widths of m_{jjb} and m_{bb}.

12.4.2 Realistic b-tagging

In this section the b-tagging algorithm described in Section 12.2 is applied to fully simulated $\mathrm{t\bar{t}H^0}$ and $\mathrm{t\bar{t}}$+jets events. Three samples are investigated: events simulated with the full detector layout and three pixel layers ('full 3L'), the full layout with two pixel layers ('full 2L'), and the initial detector layout.

Table 12.4 shows the results from fits to the reconstructed masses of the top quarks in $\mathrm{t\bar{t}H^0}$ and $\mathrm{t\bar{t}}$+jets events and to the peak of the reconstructed Higgs boson mass in $\mathrm{t\bar{t}H^0}$ events. The mass spectra are displayed in Figures 12.5 to 12.9. In general, there is agreement between full and fast simulation in the peak position and width of the reconstructed masses of the top quark. In fully hadronic decays of the top quarks, involving three reconstructed jets, one observes again a slightly broader width in fully simulated events. Although one would expect some correlation between the mass resolution and the detector

Table 12.4: Reconstructed masses and resolutions in fast and full simulation for three detector layouts.

$t\bar{t}H^0$	R2308 (initial)		R2310 (full, 2L)		R2311 (full, 3L)	
	Fast	Full	Fast	Full	Fast	Full
m_{jjb}	174.5 ± 0.3	174.3 ± 0.3	174.6 ± 0.2	174.5 ± 0.3	174.5 ± 0.3	175.4 ± 0.3
$\sigma_{m_{\mathrm{jjb}}}$	7.1 ± 0.3	6.9 ± 0.3	6.4 ± 0.2	7.5 ± 0.3	6.8 ± 0.3	7.9 ± 0.3
$m_{\ell\nu\mathrm{b}}$	174.4 ± 0.4	174.5 ± 0.4	173.5 ± 0.4	173.2 ± 0.4	175.2 ± 0.5	174.2 ± 0.3
$\sigma_{m_{\ell\nu\mathrm{b}}}$	9.5 ± 0.5	8.5 ± 0.4	9.5 ± 0.5	9.7 ± 0.6	7.9 ± 0.3	8.4 ± 0.4
m_{bb}	—	—	111.1 ± 2.0	114.2 ± 2.2	105.5 ± 3.7	111.2 ± 3.0
$\sigma_{m_{\mathrm{bb}}}$	—	—	15.1 ± 2.3	18.9 ± 3.9	23.0 ± 4.9	19.0 ± 4.2
$t\bar{t}$+jets	R2309 (initial)		R2312 (full, 2L)		R2313 (full, 3L)	
	Fast	Full	Fast	Full	Fast	Full
m_{jjb}	174.4 ± 0.2	174.5 ± 0.3	173.3 ± 0.5	174.7 ± 0.5	174.6 ± 0.5	174.0 ± 0.7
$\sigma_{m_{\mathrm{jjb}}}$	8.2 ± 0.3	8.7 ± 0.4	8.3 ± 0.8	7.9 ± 0.7	7.9 ± 0.7	8.1 ± 0.7
$m_{\ell\nu\mathrm{b}}$	173.7 ± 0.3	174.2 ± 0.4	173.9 ± 0.6	174.7 ± 1.0	174.2 ± 0.5	175.9 ± 0.5
$\sigma_{m_{\ell\nu\mathrm{b}}}$	9.4 ± 0.3	9.3 ± 0.4	9.9 ± 1.0	11.0 ± 1.2	8.2 ± 0.4	7.7 ± 0.5

Table 12.5: Efficiencies after each step of the selection for $m_{\mathrm{H}^0} = 120$ GeV with fast and fully simulated $t\bar{t}H^0$ and $t\bar{t}$ events. The relative efficiencies with respect to the previous step are given in parenthesis. The efficiencies marked with an asterisk are given with respect to the preselection (1ℓ, 6 jets (4b)) and are not taken into account separately in the cumulative efficiency, since they are included in the cut '2 tops reconstructed'.

$t\bar{t}H^0$ events						
Detector	Initial		Full, 2L		Full, 3L	
Cut	Fast (%)	Full (%)	Fast (%)	Full (%)	Fast (%)	Full (%)
1ℓ, 6 jets (4b)	5.0	4.6	5.0	4.7	4.7	5.1
Sol. for W → $\ell\nu$ exists*	3.7 (74.0)	3.4 (74.0)	3.7 (74.1)	3.5 (74.3)	3.4 (73.0)	3.7 (73.5)
m_{jj} candidate*	4.0 (80.3)	3.6 (79.2)	4.1 (82.0)	3.7 (79.2)	3.7 (79.6)	4.0 (79.4)
2 tops reconstructed	3.0 (60.7)	2.6 (57.5)	3.0 (60.5)	2.8 (58.7)	2.7 (58.3)	3.0 (58.3)
m_{t} inside mass window	2.3 (76.7)	2.1 (77.6)	2.4 (80.1)	2.1 (76.7)	2.2 (78.8)	2.3 (78.8)
m_{bb} inside mass window	1.1 (46.1)	0.9 (42.7)	1.2 (48.5)	1.0 (48.5)	1.0 (46.2)	1.1 (47.5)

$t\bar{t}$+jets events						
Detector	Initial		Full, 2L		Full, 3L	
Cut	Fast (%)	Full (%)	Fast (%)	Full (%)	Fast (%)	Full (%)
1ℓ, 6 jets (4b)	0.02	0.01	0.02	0.01	0.02	0.01
Sol. for W → $\ell\nu$ exists*	(73.9)	(73.8)	(75.6)	(73.8)	(76.0)	(74.7)
m_{jj} candidate*	(82.8)	(80.3)	(81.2)	(80.5)	(80.0)	(82.0)
2 tops reconstructed	(61.2)	(59.4)	(60.4)	(59.6)	(60.6)	(60.2)
m_{t} inside mass window	(76.1)	(74.3)	(81.3)	(74.1)	(80.4)	(72.3)
m_{bb} inside mass window	(31.1)	(34.1)	(34.4)	(29.3)	(29.7)	(36.5)

'completeness' in the sequence initial layout → full 2L → full 3L, the fitted widths rather reveal a statistically fluctuating behavior and larger events samples are necessary to make a clear statement about this dependence. Only m_{jjb} in signal events shows a tendency of improving mass resolution if the amount of material in the Inner Detector is reduced due to detector deferrals.

In signal events the peak of the reconstructed m_{bb} spectrum could not be fitted in the sample simulated with the initial detector layout due to ill-behaving statistical fluctuations near the peak region. The remaining two samples show that in fully simulated events the peak of the m_{bb} distribution is reconstructed at larger values and closer to the simulated Higgs boson mass. This observation was already discussed in the previous section. The fitted widths are comparable with those obtained with high statistics samples in Section 9.1.5, but suffer from quite large statistical errors.

The absolute and relative efficiencies of cuts in the steps of the reconstruction and selection are listed in Table 12.5. The relative efficiencies, written in parenthesis, show agreement between fast and full simulation. The overall selection efficiency is smaller in fully simulated events, and a significant discrepancy shows up in the $t\bar{t}$+jets samples. For these events, only relative efficiencies are listed after the preselection. The difference is introduced by the preselection cuts, requiring one isolated lepton and six jets of which four are tagged as b-jets. The lepton is taken from the fast simulation in both cases, so the difference must originate from the jet reconstruction. A significant difference is observed in the number of reconstructed jets in fast and full simulation, refer to Figure 12.10. A smaller number of jets is reconstructed in fully simulated events, which explains the smaller efficiency of the cut '$N_{\mathrm{jet}} \geq 6$'. The impact on the preselection efficiency is more distinct in $t\bar{t}$+jets events, since the probability of mistagging at least two light jets as b-jets depends strongly on the total number of jets. The reason for the smaller jet multiplicity can be traced back to different thresholds of the minimal p_T for jet reconstruction in fast and full simulation. Jets were reconstructed in ATLFAST if they have a transverse momentum larger than 10 GeV, and in the full simulation if the transverse momentum exceeds 12 GeV. For a proper comparison of the jet multiplicities in fast and full simulation, the p_T threshold should be *smaller* in the full simulation, since the energy reconstruction suffers from additional detector effects which are not simulated in ATLFAST. On the other hand, the threshold has an impact only on jets with relatively small p_T, and the agreement is much better if only jets with $p_T > 20$ GeV are counted, the minimal p_T required in this analysis (Figure 12.11). However, in the simulation chain light jets are mistagged as b-jets before energy calibration, and the calibration factors for b-jets are larger than those for light jets. Thus, mistagged light jets are more likely to pass the p_T threshold of 20 GeV, and so the preselection efficiency is influenced also by the multiplicity of jets which have transverse momentum slightly below this threshold.

12.5 Background reduction with information from b-tagging

The fast simulation labels jets as being b-jets, c-jets or light jets, but it does not tell the level of 'b-ness'. In contrast, the real b-tagging algorithm used in full simulation calculates a continuous weight for each jet. A jet is marked 'b-jet' if the weight ω is above a chosen threshold. The value of the threshold is determined by the requested b-tagging efficiency.

The jet weight provides additional means to suppress the reducible $t\bar{t}jj$ background. $t\bar{t}jj$ events, where the additional jets do not originate from b-quarks, can only survive the preselection cuts if at least two light or c-jets are mistagged as b-jets. Such jets generally

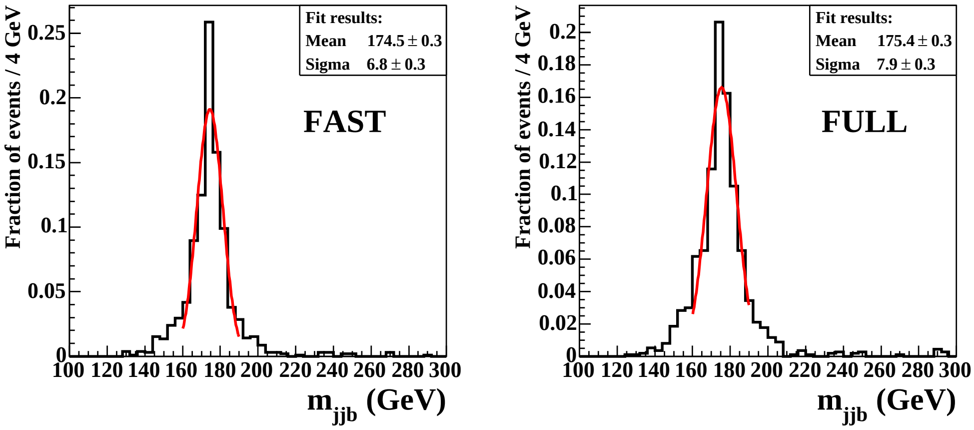

Figure 12.5: Mass distribution of reconstructed $t \longrightarrow jjb$ decays in $t\bar{t}H^0$ events (R2311).

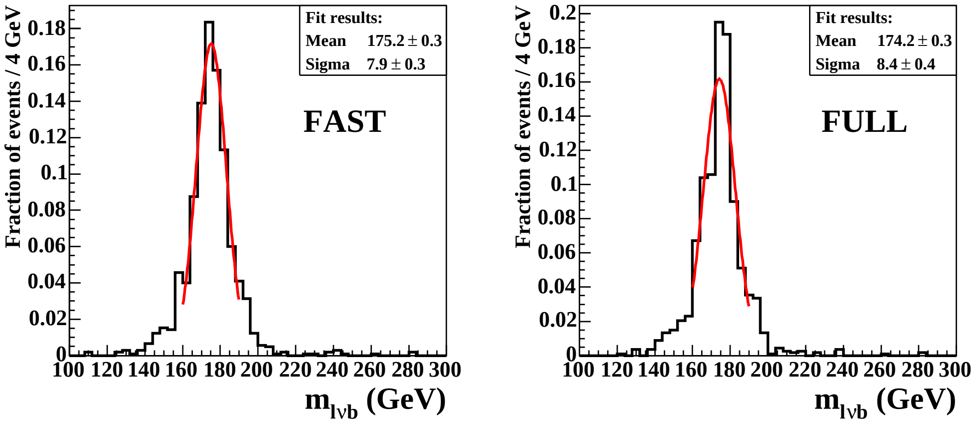

Figure 12.6: Mass distribution of reconstructed $t \longrightarrow \ell\nu b$ decays in $t\bar{t}H^0$ events (R2311).

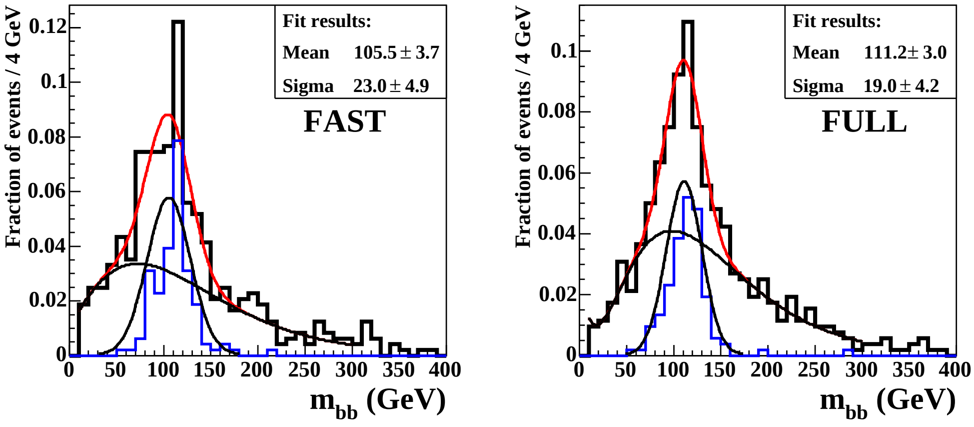

Figure 12.7: Mass distribution of reconstructed $H \longrightarrow b\bar{b}$ decays in $t\bar{t}H^0$ events (R2311).

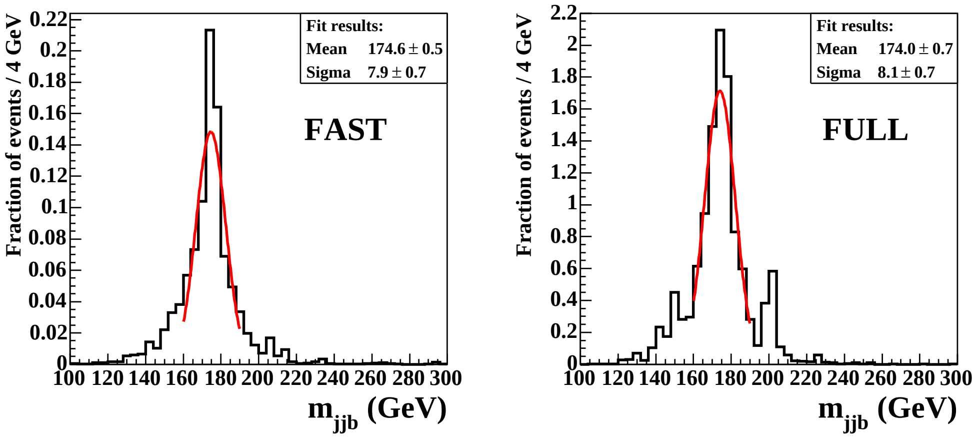

Figure 12.8: Mass distribution of reconstructed t $\longrightarrow$ jjb decays in t$\bar{\text{t}}$ events (R2313).

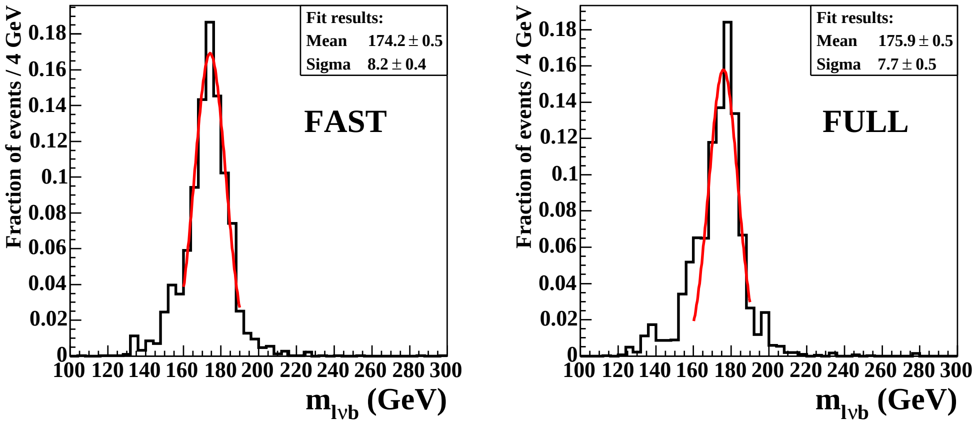

Figure 12.9: Mass distribution of reconstructed t $\longrightarrow \ell\nu$b decays in t$\bar{\text{t}}$ events (R2313).

have smaller weights than true b-jets.

A new variable Ω is constructed in order to discriminate the t$\bar{\text{t}}$jj background further. Ω is the sum of weights of the four b-jets assigned to the decays of the top quarks and the Higgs boson,

$$\Omega = \sum_{\substack{i=\mathrm{b}_{\mathrm{t}_1},\mathrm{b}_{\mathrm{t}_2},\\ \mathrm{b}_{1,\mathrm{H}},\mathrm{b}_{2,\mathrm{H}}}} \omega_i .$$

The distribution of Ω for t$\bar{\text{t}}$H^0 and t$\bar{\text{t}}$+jets events is shown in Figure 12.12. To investigate if this variable can be used to improve the sensitivity, the efficiency of a cut on Ω for t$\bar{\text{t}}$H^0 and t$\bar{\text{t}}$+jets events is determined for many positions of the cut. Then the following two assumptions are made: The efficiency of the cut is the same for the t$\bar{\text{t}}$H^0 signal and the t$\bar{\text{t}}$b$\bar{\text{b}}$ background (ε_1), the efficiencies are the same for the TDR reconstruction method and the improved reconstruction and selection method. The efficiency ε_2 for t$\bar{\text{t}}$+jets events is corrected for the fact that the fully simulated t$\bar{\text{t}}$+jets samples contain both t$\bar{\text{t}}$jj and t$\bar{\text{t}}$b$\bar{\text{b}}$

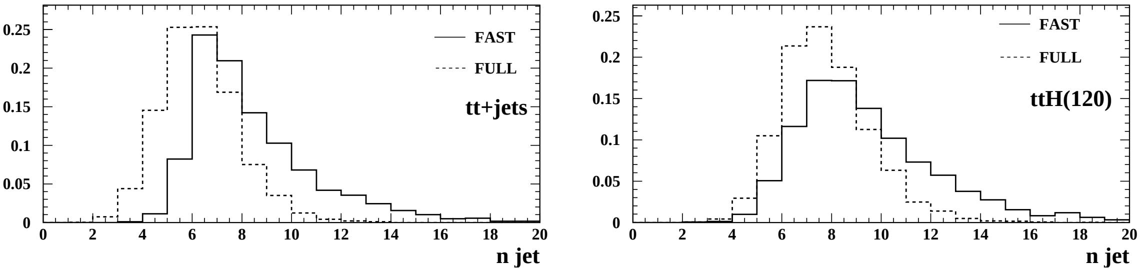

Figure 12.10: Distribution of the jet multiplicity in fast and full simulation, normalized to Unity. No p_T cut is applied, except for the jet reconstruction threshold.

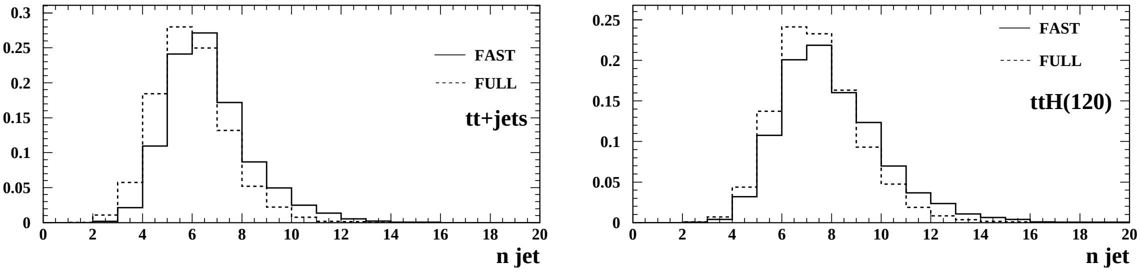

Figure 12.11: Distribution of the jet multiplicity in fast and full simulation with $p_T > 20$ GeV, normalized to Unity. All necessary jet calibration routines are applied.

Table 12.6: Comparison of expected event rates (for low luminosity and fast simulation) with and without a cut on *Ω*.

TDR method			Improved method		
Process	default	$\times\varepsilon_{1,2'}$	Process	default	$\times\varepsilon_{1,2'}$
$t\bar{t}H^0$	27.8	26.0	$t\bar{t}H^0$	45.6	42.7
$t\bar{t}b\bar{b}$	147.8	138.4	$t\bar{t}b\bar{b}$	187.1	175.1
$t\bar{t}jj$	44.7	22.8	$t\bar{t}jj$	63.1	32.3
total bkg.	192.5	161.2	total bkg.	250.2	207.3
$S/\sqrt{B}$	2.0	2.1	$S/\sqrt{B}$	2.9	3.0

events (efficiency $\varepsilon_{2'}$). The efficiencies are then applied to the results of the fast simulation with high statistic event samples: The expected events rates for $t\bar{t}H^0$, $t\bar{t}b\bar{b}$ (QCD and EW) are multiplied by ε_1 and the event rate for $t\bar{t}jj$ events is multiplied by $\varepsilon_{2'}$. The optimal cut maximizes $S/\sqrt{B}$, and is found to be $\Omega > 16$. This cut yields $\varepsilon_1 = 94\%$ and $\varepsilon_{2'} = 51\%$. The improvements gained by applying a cut on Ω are shown in Table 12.6. Although the reducible $t\bar{t}jj$ background is lowered by a factor of two, the significance $S/\sqrt{B}$ is enhanced by just 4–5%. This is due to the fact that the reducible background is only a small fraction of the total background. However, the reduction makes the sensitivity become less dependent on uncertainties of the background prediction. Improvements in the b-tag, *e.g.*, the use of a three-dimensional b-tagging algorithm, may improve the sensitivity further.

12.6 Conclusions on full simulation

In this study, fully simulated signal and background events of the $t\bar{t}H^0$ channel were investigated for the first time in ATLAS using a b-tagging performance anticipated for

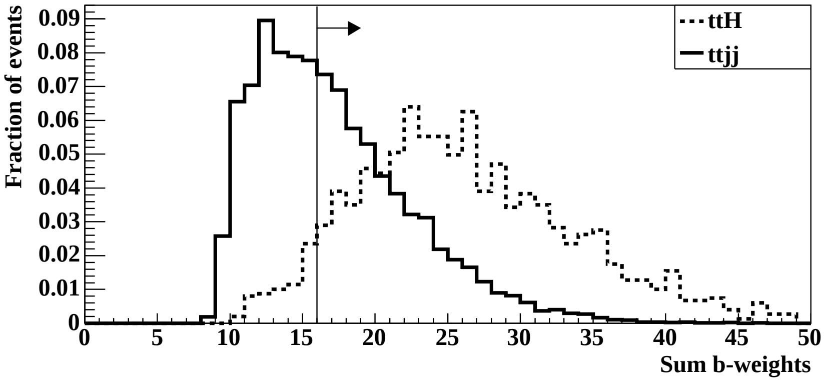

Figure 12.12: Normalized distributions of the sum of weights Ω. The vertical line with the arrow indicates the optimal cut.

the real experiment. The fast simulation is found to be a proper approximation of fully simulated events in terms of mass resolutions and relative efficiencies of cuts applied in the different steps of the selection for $t\bar{t}H^0$ events.

Differences are observed in the jet energy scales and the number of reconstructed jets with small p_T. In the future, a careful adjustment of the jet p_T threshold in fast and full simulation is important to give compatible predictions of the $t\bar{t}$+jets background rate.

The investigation of an impact-parameter based b-tagging algorithm shows that the jet b-weight provides useful information. It can be used to reduce the remaining $t\bar{t}$+light jets background by a factor of two.

13 Implication of results

This chapter presents some studies by other parties which use results from this thesis. Brief summaries are given here, and more details can be found in the supplied references.

13.1 Measurement of the Higgs boson coupling parameters

Once a signature from a Higgs boson is discovered at the LHC and the mass is fixed, the next task is to study in detail the remaining properties of the Higgs boson. Measurements of the coupling parameters of the Higgs boson to fermions and bosons provide a way to test the predictions of the Standard Model. In Reference [63] a global fit is performed based on data from ATLAS studies of a Standard Model Higgs boson in the range $m_{\mathrm{H}^0} = 110$ GeV to 190 GeV in order to estimate the accuracy with which the couplings can be measured. The following channels are considered:

Gluon fusion with $\mathrm{H}^0 \to \mathrm{Z}^0\mathrm{Z}^0$, $\mathrm{W}^\pm\mathrm{W}^\pm$ and $\gamma\gamma$, weak boson fusion with $\mathrm{H}^0 \to \mathrm{Z}^0\mathrm{Z}^0$, $\mathrm{W}^\pm\mathrm{W}^\pm$, $\gamma\gamma$ and $\tau^+\tau^-$, associated production $\mathrm{W}^\pm\mathrm{H}^0$ with $\mathrm{H}^0 \to \mathrm{W}^\pm\mathrm{W}^\pm$ and $\gamma\gamma$, associated production $\mathrm{Z}^0\mathrm{H}^0$ with $\mathrm{H}^0 \to \gamma\gamma$, and associated production $\mathrm{t\bar{t}H}^0$ with $\mathrm{H}^0 \to \gamma\gamma$, $\mathrm{W}^\pm\mathrm{W}^\pm$ and $\mathrm{b\bar{b}}$. The $\mathrm{t\bar{t}H}^0$ channel provides the only direct access to the H-b Yukawa coupling.

A 10% uncertainty is assumed for the background prediction in the $\mathrm{t\bar{t}H}^0$ channel. One result of the study is that with 300 fb^{-1} at high luminosity the relative branching ratio

$$\Gamma_{\mathrm{b}}/\Gamma_{\mathrm{W}} = \frac{BR(\mathrm{H}^0 \to \mathrm{b\bar{b}})}{BR(\mathrm{H}^0 \to \mathrm{W}^+\mathrm{W}^-)}$$

can be measured with a precision better than 60% (Figure 13.1). The measurement of the relative coupling is shown in Figure 13.2 for the same luminosity. A precision of 40% for the ratio $g^2(\mathrm{H},\mathrm{b})/g^2(\mathrm{H},\mathrm{W})$ can be reached for $m_{\mathrm{H}^0} < 130$ GeV. With some theoretical assumptions it is also possible to measure the absolute couplings, but it turns out that the errors on the H-b coupling are large ($> 75\%$) even with 300 fb^{-1}.

13.2 Determination of the CP state of a light Higgs boson

Once searches for Higgs bosons have established a signal at the LHC, it must be clarified whether the observed states are Higgs Bosons described by the Standard Model or by extended models. In the Standard Model there is one CP-even scalar Higgs boson, but many extensions predict the existence of additional CP-odd scalars. In models with two Higgs doublets each of the neutral bosons has a well defined CP quantum number, but there are models where CP properties can mix, *e.g.*, in models with more than two Higgs doublets or the Complex Minimal Supersymmetric Model CMSSM [17].

The possibility of measuring the CP state of a light Higgs boson is studied in [64]. Two issues are addressed:

1. Discrimination between pure CP-even and CP-odd quantum number,

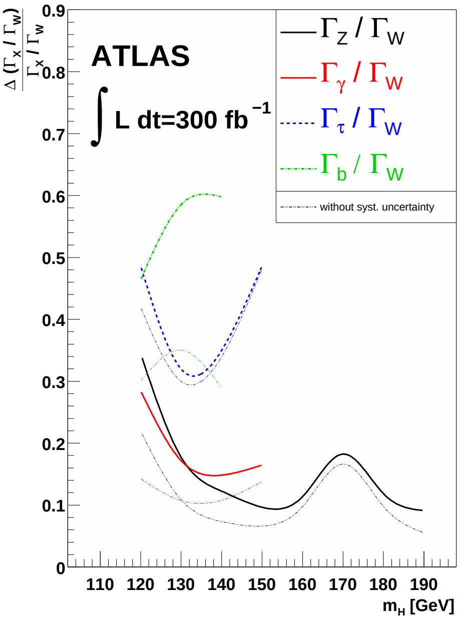

Figure 13.1: Relative error for the measurement of relative branching ratios [63].

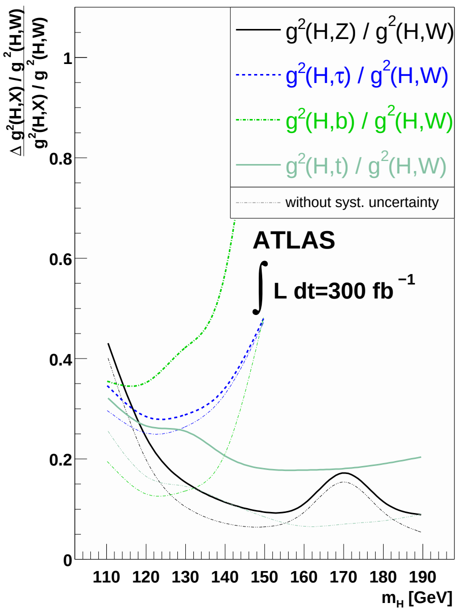

Figure 13.2: Relative error for the measurement of relative couplings [63].

2. measurement of the mixing parameter α if states Φ are realized with

$$\Phi = \mathrm{H} + \alpha \cdot \mathrm{A},$$

where H and A correspond to CP-even and CP-odd Higgs bosons.

The analysis makes use of Optimal Observables [65] in order to benefit from the full kinematic event information which is slightly different for $\mathrm{t\bar{t}h}$ and $\mathrm{t\bar{t}A}$ production.

The CP nature of the Higgs boson can be measured with a confidence larger than 96% up to $m_{\mathrm{H}^0} = 130$ GeV and for $\mathcal{L} = 300\ \mathrm{fb}^{-1}$.

In case a mixed state is realized, the mixing parameter α can be measured at the 68% confidence level for values of α in the vicinity of 1, refer to Figure 13.3. In all other cases only upper or lower limits can be set.

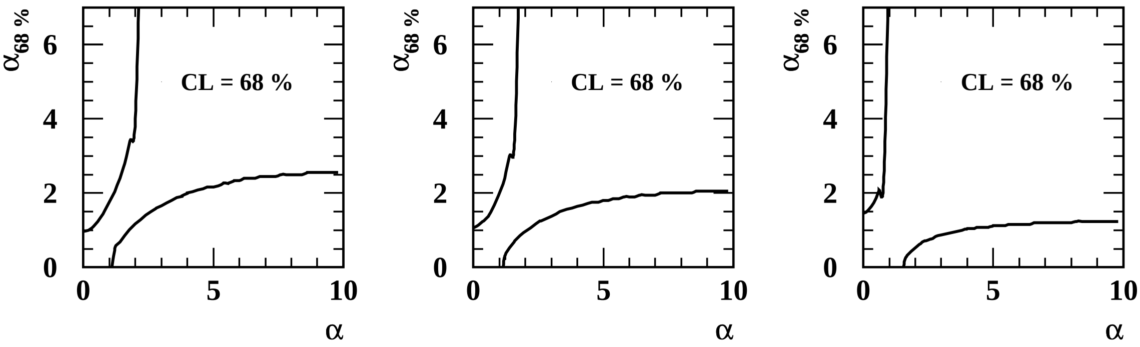

Figure 13.3: Confidence belts for the mixing parameter α for $m_h = 110$ GeV (left), $m_h = 120$ GeV (middle), and $m_h = 130$ GeV (right) with the improved analysis method and $\mathcal{L} = 300\ \mathrm{fb}^{-1}$.

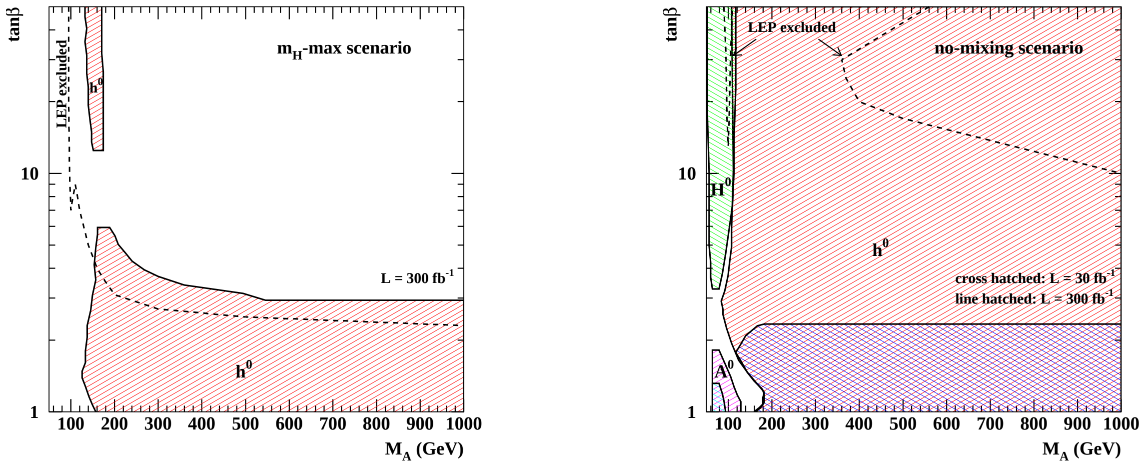

Figure 13.4: Discovery potential of the $t\bar{t}H^0$ channel in the m_{h^0}-max scenario (left) and the no-mixing scenario (right). The gap at $m_{A^0} \approx 100$ GeV and the region in the upper right corner in the right-hand figure is not excluded by the LEP experiments.

13.3 Discovery potential for the MSSM

Supersymmetry is an attractive extension to the Standard Model, and for the special case of the MSSM many studies have already been performed to explore the parameter space of the model. On Born-level, the phenomenology of the MSSM Higgs sector is described by two parameters, $\tan\beta$ and m_A, but loop corrections containing SUSY partners of the Standard Model particles are important and introduce another five parameters. To allow for two-dimensional graphical representations of scans over the $(\tan\beta, m_A)$ parameter space, usually four benchmark scenarios are considered in which the five loop correction parameters are fixed [26]. The results from the Standard Model $t\bar{t}H^0$ study can be reinterpreted to estimate the discovery potential of the production of either of the three neutral MSSM Higgs bosons in association with a pair of top quarks [66]. The benchmark scenarios presented here are the m_{h^0}-max and the no-mixing scenario. In the m_{h^0}-max scenario the parameters are chosen to get the maximum possible Higgs boson mass as a function of $\tan\beta$. The no-mixing scenario contains no mixing in the stop sector and results typically in small masses for the lightest CP even Higgs boson h^0. The parameters $\tan\beta$ and m_A for which the h^0, H^0, and A^0 can be discovered are shown in Figure 13.4 for integrated luminosities of 30 fb^{-1} and 300 fb^{-1}.

In the m_{h^0}-max scenario only the h^0 can be seen with 300 fb^{-1}. Discovery is possible for $\tan\beta < 3$ and $m_A > 150$ GeV and in a small island for $\tan\beta > 12$ and m_A between 140 GeV and 170 GeV. However, most of the discovery region is already excluded by the LEP experiments. In the no-mixing scenario all three neutral Higgs bosons can be seen with 300 fb^{-1}. Observation of the h^0 is possible in most of the parameters space between $m_{h^0} = 100$ GeV and $m_{h^0} = 1$ TeV and $\tan\beta$ between 1 and 50. The H^0 will show up only if m_A is between 60 GeV and 120 GeV and $\tan\beta > 3.5$. The A^0 can be seen only in a small region around $m_A = 100$ GeV and $\tan\beta = 1$ to 2. The h^0 and A^0 can also be seen with 30 fb^{-1}, but in much smaller regions of the parameter space. Again, most of the parameters for which the neutral Higgs bosons are detectable are already excluded by the LEP experiments. The h^0 might be observed for large m_A and $\tan\beta$, where the $t\bar{t}H^0$ channel closes a hole not covered by the LEP searches. Of course, the overall sensitivity of ATLAS to MSSM Higgs bosons is enlarged by the combination with other channels [66].

Part III

Decay-mode independent searches for neutral Higgs bosons with OPAL at LEP

14 Introduction

The Higgs boson has been haunted for extensively by the LEP experiments, and some analyses are still to be finished three years after end of data taking. The searches cover a wide spectrum of models, the Standard Model being the most prominent one. Exploring Z^0H^0 production with decays of the Higgs boson into $b\bar{b}$ and $\tau^+\tau^-$, the combination of results from the four LEP experiments culminates in a lower limit of 114.4 GeV for the mass of the Standard Model Higgs boson [16]. Searches for neutral Higgs bosons beyond the Standard Model exist for several models:

- Flavor-independent searches: General Two Higgs Doublet models [17, 67] or composite models predict hadronically decaying Higgs bosons, but not necessarily into b-quarks. The four LEP experiments have conducted searches in the four-jet ($q\bar{q}q\bar{q}$), missing energy ($q\bar{q}\nu\bar{\nu}$), and leptonic ($q\bar{q}\ell^+\ell^-$) channel, without exploiting the flavor of the jets. A combined mass limit of 112.9 GeV is obtained [68].

- Invisible decaying Higgs boson: In Majoron models [69], for some part of the parameter space in supersymmetric theories, or in models with extra dimensions [70, 71, 72] the decay of a Higgs boson into 'invisible' particles (*e.g.*, neutralinos) can become dominant. Searches are performed for acoplanar leptons or jets in the Z^0H^0 channel with $H^0 \rightarrow$invisible and $Z^0 \rightarrow q\bar{q}$ or $Z^0 \rightarrow \ell^+\ell^-$. Assuming Standard Model production cross section and exclusive invisible decays, the preliminary LEP combined mass limit is 114.4 GeV [73].

- Fermiophobic scenarios: In some Two Higgs Doublet models and in some other models the coupling of the Higgs boson to fermions is suppressed, so that the Higgs boson decays preferentially into a pair of bosons [74, 75]. Searches have been performed for the final states $Z^0H^0 \rightarrow q\bar{q}\gamma\gamma$, $\nu\bar{\nu}\gamma\gamma$, and $\ell^+\ell^-\gamma\gamma$, except for the ALEPH collaboration who conducted a global analysis of the di-photon state without discriminating between Z^0 decay modes. Assuming exclusive decays $H^0 \rightarrow \gamma\gamma$, a lower mass bound of 109.7 GeV is obtained [76].

- In the MSSM the h^0 and A^0 decay predominantly into $b\bar{b}$ and $\tau^+\tau^-$ for most of the parameter space. The Standard Model analyses can be used to search for h^0. In regions where the $b\bar{b}$ and $\tau^+\tau^-$ modes are suppressed, flavor-independent analyses are applied. Dedicates searches were developed to look for the CP-odd Higgs boson in the $e^+e^- \rightarrow h^0A^0$ mode. In the m_h^0-max-scenario scan of the parameters of the MSSM, the mass limits $m_{h^0} > 91.0$ GeV and $m_{A^0} > 91.9$ GeV are obtained [77].

- A search for light Higgs bosons h^0/A^0 in non-supersymmetric Two Higgs Doublet Models, produced in the Yukawa process $e^+e^- \rightarrow b\bar{b}h^0/A^0 \rightarrow b\bar{b}\tau^+\tau^-$, was performed in [78]. Limits on the production cross section were set for the range of Higgs bosons masses between 4 GeV to 12 GeV.

  (All limits are valid at the 95% confidence level.)

These searches have in common that they are optimized for a particular model of the Higgs sector, making use of specific properties of the Higgs boson in that model. For instance, in the Standard Model and MSSM the main decay mode is $h^0 \rightarrow b\bar{b}$, and tools such as b-tagging are utilized to isolate the signal from large background. If an alternative model predicts a different main decay mode, new dedicated analyses must be developed to explore the full sensitivity of the experiment. A step towards generalization are flavor-independent searches [79]. Basically, these are the Standard Model searches, but the requirement of b-tagged jets is dropped. This relaxation allows for interpretation of the results in more general 2HDM scenarios, but the assumption is still made that the Higgs boson decays predominantly into a pair of gluons or quarks (but not necessarily b-quarks). Table 14.1 summarizes the status of searches for neutral Higgs bosons at LEP.

The searches for neutral Higgs bosons, which have been performed up to now, share the assumption that the Higgs boson will manifest itself as a narrow peak on top of a broad mass spectrum from background processes. Even if Higgs bosons decayed only into final states to which present searches are sensitive, they could have escaped detection if they are spread over a large mass range. This could, for instance, be due to a single Higgs boson with a large decay width, or due to a large number of new scalar states populating a broad mass range. Two such scenarios which are based on these ideas are introduced in Section 15.3.

Therefore, all present Higgs searches are limited in the sense that they do not allow for interpretations in an arbitrary scenario. This is due to the restriction to specific decay modes and narrow mass peaks. These limitations lead to the idea of a much more general search for new scalar bosons, independent of any assumptions about the decays or the mass distribution. The advantage is that only one analysis needs to be developed, and the results can be interpreted in an arbitrary model. Such an analysis is presented in this part of the thesis.

Table 14.1: Status of combined searches for neutral Higgs bosons at LEP. Limits for the MSSM are obtained from representative scans. See the quoted references in the text for details.

Analysis	ALEPH	DELPHI	L3	OPAL	LEP combined	LEP status
Standard Model	111.5	114.3	112.0	112.8	114.4	final
Flavor-independent	109.3	109.6	111.6	109.4	112.9	preliminary
Invisible Higgs	114.1	113.0	107.6	107.0	114.4	preliminary
Fermiophobic Higgs	104.5	104.3	104.7	105.3	109.7	preliminary
h^0 (MSSM)	89.6	89.7	83.2	79.3	91.0	preliminary
A^0 (MSSM)	90.0	90.7	83.9	80.6	91.9	preliminary

15 Higgs physics at LEP

This chapter discusses the production modes and phenomenology of Higgs physics at LEP at center-of-mass energies $\sqrt{s} > m_{\mathrm{Z}^0}$ (‘LEP 2’).

15.1 The Standard Model Higgs boson

The main production process for neutral Higgs bosons at LEP 2 is the associated production $\mathrm{e}^+\mathrm{e}^- \to \mathrm{Z}^0\mathrm{H}^0$, where the Higgs boson is radiated off a virtual Z^0 boson (‘Higgs-strahlung’, Figure 15.1 left). The fusion processes $\mathrm{e}^+\mathrm{e}^- \to \nu\bar{\nu}\mathrm{H}$ and $\mathrm{e}^+\mathrm{e}^- \to \mathrm{e}^+\mathrm{e}^-\mathrm{H}$ have only a very small contribution (Figure 15.1 right).

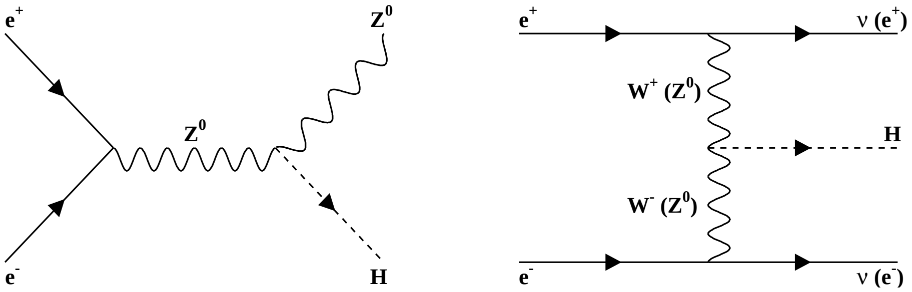

Figure 15.1: Production modes for neutral Higgs bosons in $\mathrm{e}^+\mathrm{e}^-$ collisions. Left: Higgs-strahlung, Right: Vector boson fusion.

At Born level, and neglecting the width of the Z^0, the cross section for Higgs-strahlung in the Standard Model is given by ([80])

$$\sigma_{\mathrm{ZH}} = \frac{G_F^2 m_{\mathrm{Z}^0}^4}{96\pi s}\left(v_e^2 + v_a^2\right)\lambda^{1/2}\frac{\lambda + 12 m_{\mathrm{Z}^0}^2/s}{(1 - m_{\mathrm{Z}^0}^2/s)^2}, \tag{15.1}$$

where $\sqrt{s}$ denotes the center-of-mass energy, v_e and v_a the vector and axial-vector coupling of an electron to the Z^0 boson, and $\lambda = (1 - m_{\mathrm{H}^0}^2/s - m_{\mathrm{Z}^0}^2/s)^2 - 4m_{\mathrm{H}^0}^2 m_{\mathrm{Z}^0}^2/s^2$ is a phase-space factor. The finite width of the Z^0 boson and radiation of photons in the initial state have considerable impact on the cross section [10], whereas the width of the Higgs boson in the mass range accessible at LEP is below 3 MeV for $m_{\mathrm{H}^0} < 100$ GeV and can safely be neglected in Equation 15.1. The cross section is depicted in Figure 15.2 as a function of m_{H^0} for fixed $\sqrt{s}$ (left-hand figure), and as a function of $\sqrt{s}$ for some fixed masses m_{H^0} (right-hand figure). Figure 15.2, left, shows the cross section with and without the effect of ISR and the finite Z^0 width. ISR enhances the cross section for small Higgs boson masses, and reduces it at larger m_{H^0}. The finite Z^0 width dilutes the kinematic edge at $m_{\mathrm{H}^0} = \sqrt{s} - m_{\mathrm{Z}^0}$, which is a sharp cut-off if one assumes a vanishing Z^0 width. The smaller picture zooms into the mass region of the kinematic limit. Although the cross section for $\mathrm{Z}^0\mathrm{H}^0$ production decreases rapidly above the kinematic limit, the cross section for $\mathrm{W}^+\mathrm{W}^-$ and $\mathrm{Z}^0\mathrm{Z}^0$ fusion is nevertheless almost one and two orders of magnitude smaller, respectively.

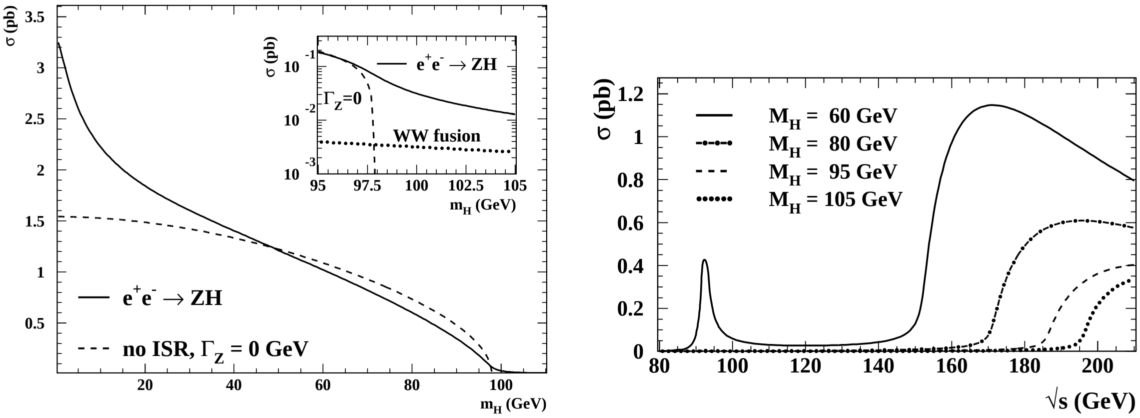

Figure 15.2: Left: Cross section for Higgs boson production as a function of m_{H^0} at $\sqrt{s} = 189$ GeV. Right: Cross section for Higgs boson production as a function of $\sqrt{s}$ for some masses m_{H^0}.

The spin-parity quantum numbers of the Higgs boson define the angular distribution of the Z^0 and H^0 boson in the Higgs-strahlung process. At high energies the Z^0 boson is produced with longitudinal polarization, and due to the 0^+ spin-parity of the Standard Model Higgs boson, the angular distribution follows the $(\sin^2\theta + \mathrm{const.})$ law:

$$\frac{\mathrm{d}\sigma}{\mathrm{d}\cos\theta} \sim \lambda \sin^2\theta + 8m_{\mathrm{Z}^0}^2/s, \tag{15.2}$$

where λ is the phase space factor from Equation 15.1, so that the distribution becomes flat in $\cos\theta$ at the kinematic threshold $(m_{\mathrm{H}^0} + m_{\mathrm{Z}^0})^2 = s$, where $\lambda = 0$.

The branching fractions into fermions and bosons of the Higgs (see Figure 3.3 in Section 3.1.1) and the Z^0 boson determine the topologies in which the SM Higgs boson is searched for at LEP 2. The Higgs boson decays predominantly into $\mathrm{b\bar{b}}$ (BR($\mathrm{H}^0 \to \mathrm{b\bar{b}}$) $\gtrsim 80\%$ for $2m_b < m_{\mathrm{H}^0} < 100$ GeV). The second largest branching fraction with $\approx 9\%$ is $\mathrm{H}^0 \to \tau^+\tau^-$. The Z^0 boson decays into $\mathrm{q\bar{q}}$ ($\approx$70%), $\nu\bar{\nu}$ ($\approx$20%), and $\ell^+\ell^-$ ($\approx$10%). Accordingly, the main search channels are the four-jet channel ($\mathrm{Z}^0 \to \mathrm{q\bar{q}}, \mathrm{H}^0 \to \mathrm{b\bar{b}}$ ($\approx$ 85%), total fraction 60%), the neutrino channel ($\mathrm{Z}^0 \to \nu\bar{\nu}, \mathrm{H}^0 \to \mathrm{b\bar{b}}$, 17%), the τ-channel ($\mathrm{Z}^0 \to \mathrm{q\bar{q}}$, $\mathrm{H}^0 \to \tau^+\tau^-$ and $\mathrm{Z}^0 \to \tau^+\tau^-, \mathrm{H}^0 \to \mathrm{b\bar{b}}$, 9%), and the lepton channels ($\mathrm{Z}^0 \to \mathrm{e}^+\mathrm{e}^-/\mu^+\mu^-$, $\mathrm{H}^0 \to \mathrm{b\bar{b}}$, 6%).

15.2 The Higgs sector in Two-Higgs-Doublet Models

Common extensions to the minimal Higgs sector of the Standard Model are general Two-Higgs-Doublet models [67] with five Higgs bosons $\mathrm{h}^0, \mathrm{H}^0, \mathrm{A}^0, \mathrm{H}^+$ and H^-. In this work, only the production of the lightest neutral CP-even Higgs boson, h^0, and the CP-odd Higgs boson, A^0, is discussed, because the production of the heavier H^0 at LEP is kinematically allowed only for a very small range of the parameter space. The h^0 is produced in $\mathrm{Z}^0\mathrm{h}^0$-strahlung, like the Standard Model Higgs boson, but with a cross section suppressed by a factor $\sin^2(\beta - \alpha)$. The A^0 can only be produced in association with the h^0 in the pair production process $\mathrm{e}^+\mathrm{e}^- \to \mathrm{h}^0\mathrm{A}^0$ (or in Yukawa production). The cross section is reduced by a factor $\cos^2(\beta-\alpha)\bar{\lambda}$ with respect to Standard Model $\mathrm{Z}^0\mathrm{H}^0$ production, where $\bar{\lambda} = \bar{\lambda}(s, m_{\mathrm{h}^0}, m_{\mathrm{A}^0}, m_{\mathrm{Z}^0})$ is a phase space factor accounting for the suppression of the P-wave cross section near the threshold. The bosons h^0 and A^0 decay mostly hadronically or into $\tau^+\tau^-$, but the dominant quark flavor depends on the model parameters α and β. The couplings relative to the Standard Model couplings as functions of α and β are:

$$\mathrm{h}^0 \to \mathrm{c\bar{c}} \sim \frac{\cos\alpha}{\sin\beta}, \quad \mathrm{h}^0 \to \mathrm{b\bar{b}} \sim -\frac{\sin\alpha}{\cos\beta}, \quad \mathrm{A}^0 \to \mathrm{c\bar{c}} \sim \cot\beta, \quad \mathrm{A}^0 \to \mathrm{b\bar{b}} \sim \tan\beta. \tag{15.3}$$

Searches for $\mathrm{Z}^0\mathrm{h}^0$ are the same as for Standard Model $\mathrm{Z}^0\mathrm{H}^0$ and the flavor-independent analyses. In addition, the process $\mathrm{Z}^0\mathrm{h}^0 \to \mathrm{Z}^0\mathrm{A}^0\mathrm{A}^0$, followed by $\mathrm{A}^0 \to \mathrm{b\bar{b}}$ is considered for those parts of the parameter space where the A^0 is light enough to allow for the decay $\mathrm{h}^0 \to \mathrm{A}^0\mathrm{A}^0$. In pair production, the channels $\mathrm{h}^0\mathrm{A}^0 \to \mathrm{b\bar{b}b\bar{b}}$, $\mathrm{h}^0\mathrm{A}^0 \to \tau\tau\mathrm{q\bar{q}}$ (and vice versa), and $\mathrm{h}^0\mathrm{A}^0 \to \mathrm{A}^0\mathrm{A}^0\mathrm{A}^0 \to \mathrm{b\bar{b}b\bar{b}b\bar{b}}$ were studied [81].

15.3 Continuous Higgs scenarios

Models predicting smooth and wide-spread mass distributions for the signal process instead of a peak have so far not been subject of research at the LEP experiments and present searches do not exclude these models. Two scenarios with continuous mass distribution, on which limits will be put in Section 17.3.2 for the first time, are described below.

15.3.1 The Uniform Higgs scenario

This model, as described in Ref. [82], assumes a broad enhancement over the background expectation in the m_X mass distribution for the process $\mathrm{e^+e^-} \to \mathrm{Z^0X}$. This enhancement is due to numerous additional neutral Higgs bosons h^0_i with masses $m_\mathrm{A} \leq m(\mathrm{h}^0_\mathrm{i}) \leq m_\mathrm{B}$, where m_A and m_B indicate the lower and upper bound of the mass spectrum. The squared coupling, $g^2_{\mathrm{Z^0h^0_i}}$, of the Higgs states h^0_i to the Z^0 is modified by a factor k_i compared to the Standard Model $\mathrm{Z^0H^0}$ coupling: $g^2_{\mathrm{Z^0h^0_i}} = k_i \cdot g^2_{\mathrm{Z^0h^0_{SM}}}$.

If the Higgs states are assumed to be closer in mass than the experimental mass resolution, then there is no need to distinguish between separate k_i (Figure 15.3). In this case the Higgs states and their reduction factors k_i can be combined into a coupling density function, $\tilde{K}(m) = \mathrm{d}k/\mathrm{d}m$. The model obeys two sum rules which in the limit of unresolved mass peaks can be expressed as integrals over this coupling density function:

$$\int_0^\infty \mathrm{d}m\, \tilde{K}(m) = 1 \tag{15.4}$$

$$\int_0^\infty \mathrm{d}m\, \tilde{K}(m) m^2 \leq m_\mathrm{C}^2, \tag{15.5}$$

where $\tilde{K}(m) \geq 0$ and m_C is a perturbative mass scale of the order of 200 GeV. The value of m_C is model dependent and can be derived by requiring that there is no Landau pole in the Higgs boson self-coupling up to a scale Λ where new physics occurs [82]. If neither a continuous nor a local excess is found in the data, Equation 15.4 can be used to place constraints on the coupling density function $\tilde{K}(m)$. For example, if $\tilde{K}(m)$ is assumed to be constant over the interval $[m_\mathrm{A}, m_\mathrm{B}]$ and zero elsewhere,

$$\tilde{K}(m) = \begin{cases} 1/\left(m_\mathrm{B} - m_\mathrm{A}\right) & \text{for } m_\mathrm{A} \leq m \leq m_\mathrm{B} \\ 0 & \text{elsewhere,} \end{cases} \tag{15.6}$$

then certain choices for the interval $[m_\mathrm{A}, m_\mathrm{B}]$ can be excluded. From this and from Equation 15.5 lower limits on the mass scale m_C can be derived.

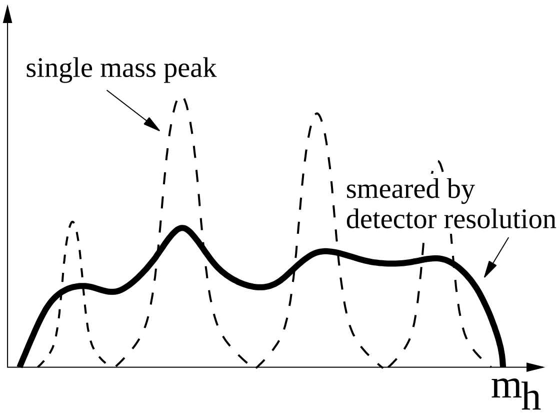

Figure 15.3: Sketch of mass distributions in the Uniform Higgs scenario.

15.3.2 The Stealthy Higgs scenario

This scenario predicts the existence of a new hidden scalar sector with additional $\mathrm{SU(3)_C} \times \mathrm{SU(2)_I} \times \mathrm{U(1)_Y}$ singlet fields (phions). The phions would not interact via the strong or electro-weak forces, thus coupling only to the Higgs boson [83]. Therefore, these singlets would reveal their existence only in the Higgs sector by offering invisible decay modes to the Higgs boson. The width of the Higgs resonance can become large if the number of such singlets, N, or the coupling ω is large, thus yielding a broad spectrum in the mass recoiling against the reconstructed Z^0. The interaction term between the Higgs boson and the additional phions in the Lagrangian is given by

$$\mathscr{L}_{\text{interaction}} = -\frac{\omega}{2\sqrt{N}} \vec{\varphi}^2 \phi^\dagger \phi, \tag{15.7}$$

where ϕ is the Standard Model Higgs doublet, ω is the coupling constant, and $\vec{\varphi} = (\varphi_1, \ldots, \varphi_N)$ is the N-plet of the new phions. An analytic expression for the Higgs width can be found in the limit $N \to \infty$:

$$\Gamma_{\mathrm{H}}(m_{\mathrm{H}}) = \Gamma_{\mathrm{SM}}(m_{\mathrm{H}}) + \frac{\omega^2 v^2}{32\,\pi\, m_{\mathrm{H}}}, \tag{15.8}$$

where v is the vacuum expectation value of the Higgs field. This expression is obtained by setting other model parameters to zero, including the mass of the phions [83]. The cross section for the Higgs-strahlung process can be parameterized by the Standard Model cross section for $\mathrm{Z}^0\mathrm{H}^0$ production modified by a Breit-Wigner distribution (a more detailed expression is given in Equations 9 and 10 of Reference [83]):

$$\sigma_{(\mathrm{e}^+\mathrm{e}^- \to \mathrm{Z}^0 + \not{E})} = \int \mathrm{d}s_I \sigma_{(\mathrm{e}^+\mathrm{e}^- \to \mathrm{Z}^0\mathrm{H}^0)}(s_I) \frac{\sqrt{s_I} \quad \Gamma(\mathrm{H}^0 \to \not{E})}{\pi \left((m^2_{\mathrm{H}^0} + s_I \Gamma(\mathrm{H}^0 \to \mathrm{all})^2 \right)}, \tag{15.9}$$

where s_I is the invariant mass of the decay products of the Higgs boson, $\Gamma(\mathrm{H}^0 \to \not{E})$ is the invisible decay width of the Higgs boson into phions, and $\Gamma(\mathrm{H}^0 \to \mathrm{all})$ is the total decay width. The differential cross section $\mathrm{d}\sigma/\mathrm{d}E_I$ is illustrated in Figure 15.4.

In section 17.3.2.3 limits are derived on the Stealthy Higgs model which can be compared to expected limits from dedicated $\mathrm{H}^0 \to$ invisible searches, which are estimated in Ref. [83] for the same scenario. By simulating signal spectra for different Higgs widths Γ_{H}, limits are set in the ω-m_{H} plane in the large N limit.

More stringent limits can be obtained from an analysis that is dedicated to the search for an invisibly decaying Higgs boson with large decay width, currently being performed using OPAL data at center-of-mass energies above m_{Z^0} [84].

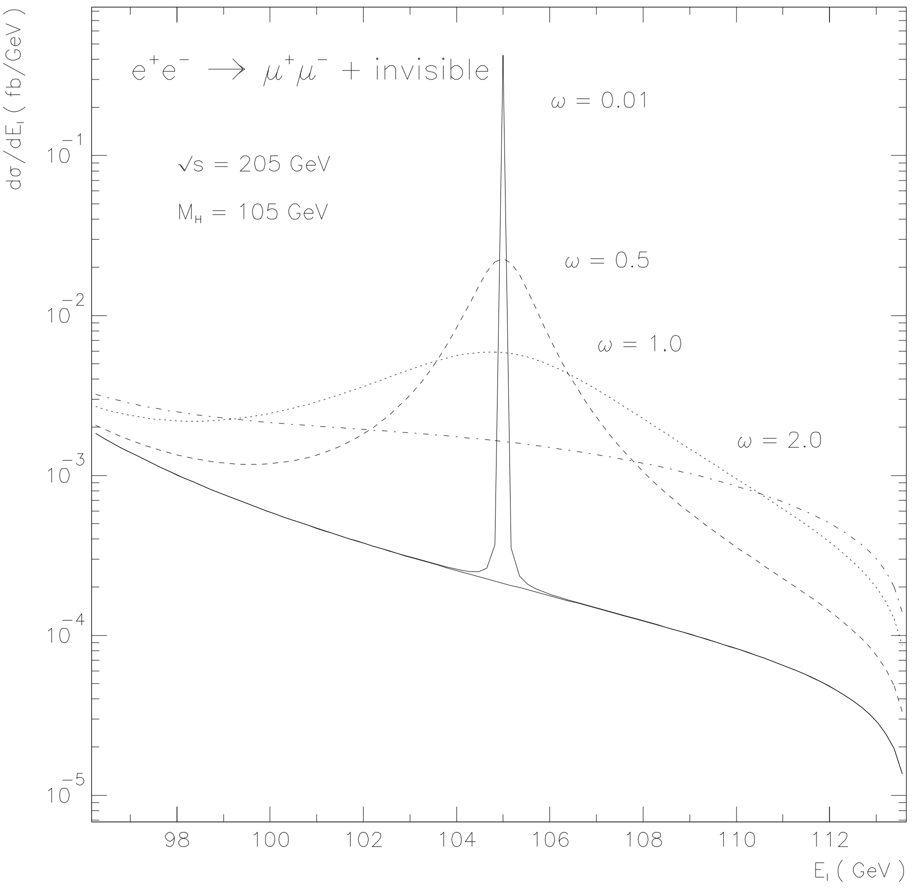

Figure 15.4: Differential cross sections in the Stealthy Higgs scenario [83].

16 The experiment

This chapter describes the accelerator and the experimental setup which recorded the data analyzed in this part of the thesis.

16.1 The LEP accelerator

The Large Electron Positron Collider LEP at CERN was operated from 1989 to 2000. The ring was 27 km in circumference and resided about 100 m below the surface. The electron and positron beams were brought to collision at four interaction points with the experiments ALEPH, DELPHI, L3, and OPAL (Figure 16.1). From 1989 to 1995 the accelerator was operated as a Z^0-boson factory, with center-of-mass energies around 91 GeV. Being on the Z^0-resonance, it was possible to study the production and the decays of the Z^0-boson with high statistics. After this LEP 1 phase the energy was increased step-by-step. Pairs of $W^\pm$ bosons were produced after reaching $\sqrt{s} = 161$ GeV, and the study of Z^0-pairs was feasible at energies above $\sqrt{s} = 183$ GeV. The highest energy of $\sqrt{s} = 209$ GeV was reached in 2000.

The LEP physics program consisted of electroweak precision measurements at the Z^0 resonance (LEP 1), accurate measurement of the $W^\pm$ boson mass, its branching ratios and triple gauge boson couplings, the study of Z^0-pair production, searches for signatures of physics beyond the Standard Model, and, of course, the search for Higgs bosons in the context of the Standard Model and in many other models.

16.2 The OPAL detector

The OPAL detector is an Omni Purpose Apparatus for LEP [85] (the present tense is used here, despite of the fact that OPAL doesn't exist any more). The different components of the detector measure the energy and momentum vector of the particles which are produced in e^+e^--collisions. The OPAL-detector measures 12 m in length, has a diameter of 10 m, and weights 3 000 tons. The detector is built concentrically around the beam pipe. It consists of parts to measure tracks from charged particles, a time-of-flight counter, calorimeters for energy and shower measurements, and a muon system. OPAL uses a right handed coordinate system. The z axis points along the direction of the electron beam and the x axis is horizontal pointing towards the center of the LEP ring. The polar angle θ is measured with respect to the z axis, the azimuthal angle ϕ with respect to the x axis. OPAL is shown in different views in Figures 16.2 and 16.3.

The detector is made of a cylindrical central part (barrel, $|\cos\theta| \lesssim 0.72$) and the cylinder caps or end-caps ($|\cos\theta| \gtrsim 0.72$). The innermost part of the barrel consists of the central tracking system, which is located inside a 4 bar pressure vessel. A 0.435 T solenoid field makes possible the measurement of the direction and momentum of tracks and particle identification via $\mathrm{d}E/\mathrm{d}x$. The tracking system serves also to reconstruct the primary vertex and secondary vertices. Outside the tracking system there is a time-of-flight counter, which is used as event trigger, for particle identification, and to reject cosmic particles penetrating the detector. Next are the electromagnetic and hadronic calorimeters which measure

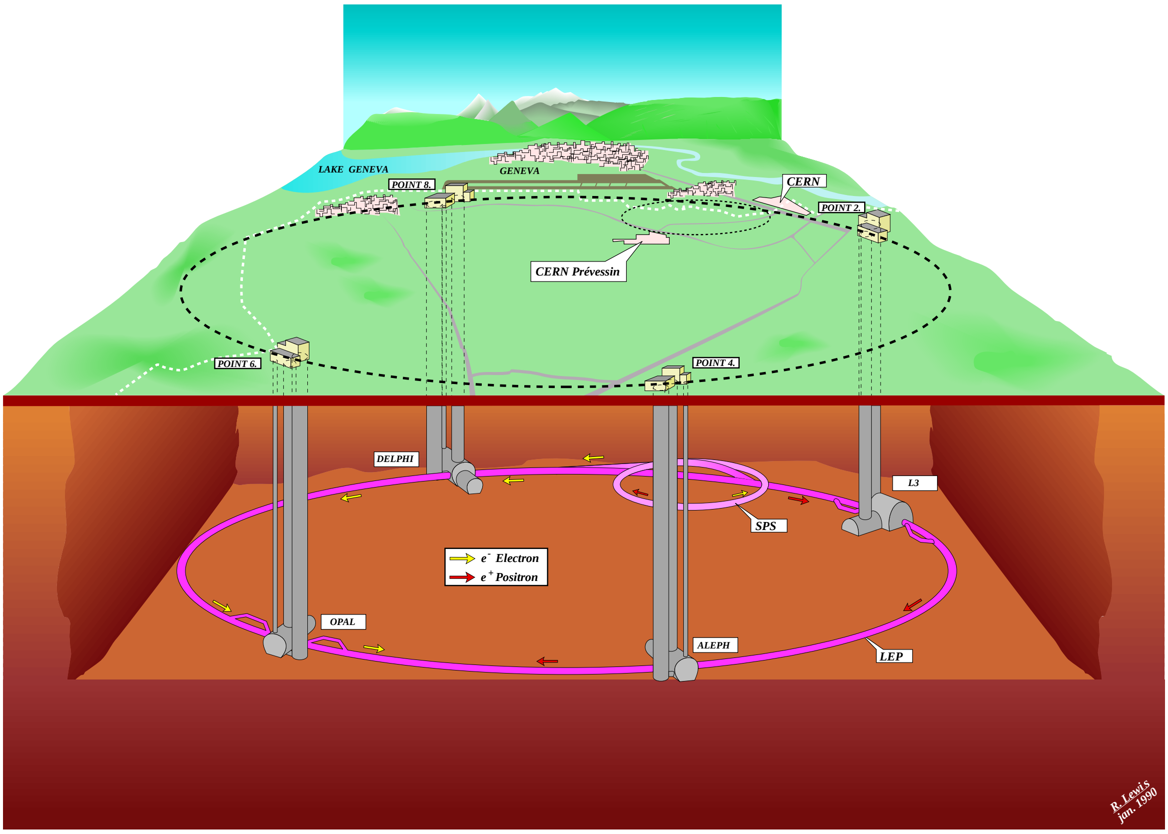

Figure 16.1: The LEP accelerator with the four experiments ALEPH, DELPHI, L3, and OPAL.

the energy and position of electrons and photons and hadronically decaying particles, respectively. The calorimeters are surrounded by the muon system, which covers the angular region up to $|\cos\theta| < 0.82$.

The end-caps house special forward detectors in order to measure particles which travel at small angles to the beam axis, as well as electromagnet and hadronic calorimeters and muon detectors in a region down to 47 mrad. Luminosity detectors monitor the delivered particle flux. In the following, the components of the OPAL detector are explained in more detail:

- The innermost part of the central tracking system, in close contact to the beam pipe, consists of a **silicon microstrip detector** (SI) with two layers of silicon counters. They have a resolution of 13 µm along the beam direction, and 5 µm in the r-ϕ plane. The **vertex detector** (CV) is a cylindric drift chamber with a length of 1 m and a diameter of 47 cm. There is an inner and an outer layer with 36 cells each. In the twelve innermost layers the sense wires are parallel to the z-axis, and in the outer six layers there are stereo wires with in inclination of 4° with respect to the wires of the inner layers. The track resolution is 50 µm in the r-ϕ plane. Next is the **jet chamber** (CJ) with good spatial resolution and the ability to measure the energy loss $\mathrm{d}E/\mathrm{d}x$ of tracks. The jet chamber extends to 4 m in length and 3.7 m in diameter. It is divided into 24 sectors, which are separated by a plane of anode wires. 159 sense wires per sector collect the charge from traversing charged particles.

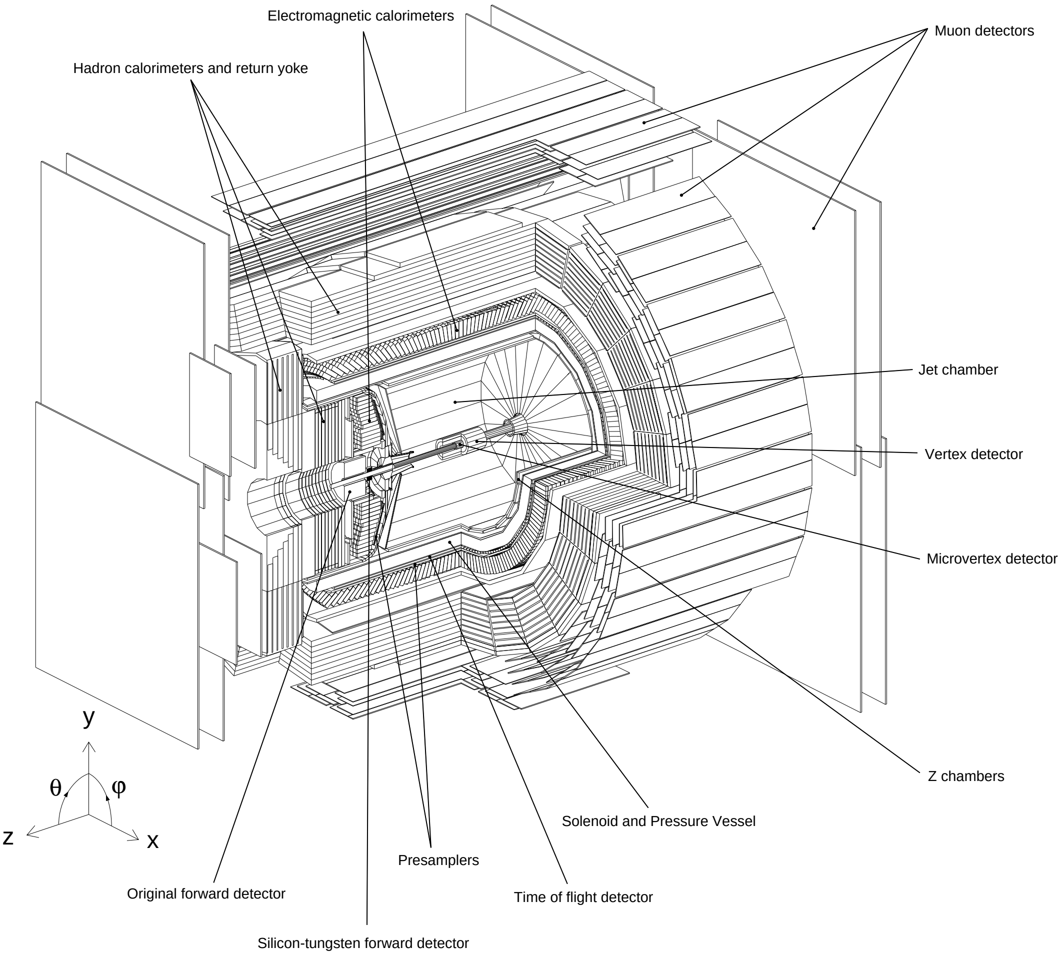

Figure 16.2: A survey of the OPAL detector.

For 98% of the 4π spatial angle a track leaves a signal in at least eight wires. The space coordinates from a particle are reconstructed from the known positions of the sense wires, drift time and charge measurement. The transverse momentum and the sign of the charge can be determined from the curvature of the track in the magnetic field. The resolution of the transverse momentum is given by

$$\frac{\sigma_p}{p_T} \approx 2\% \oplus 0.15\% \cdot p_T \qquad (p_T \text{ in GeV}). \tag{16.1}$$

The energy loss in the gas of the detector is calculated from the charge signal of consecutive wires. Particle identification is possible from the known expected energy loss of a given particle. The accuracy of the track measurement along the z-direction is enhanced by the ***z*-chambers** (CZ), surrounding CJ and CV. The z-chambers are composed of 24 drift chambers with a length of 4 m, a width of 40 cm, and a thickness of 5.9 cm. Each cell is divided into eight sub-cells with wires perpendicular to those of the track chambers.

- The **time-of-flight system**, located outside the pressure vessel, is formed from 160 scintillating counters with a length of 6.84 m. They are read out by photomultipliers. The system serves as event trigger and for measuring the time-of-flight of particles

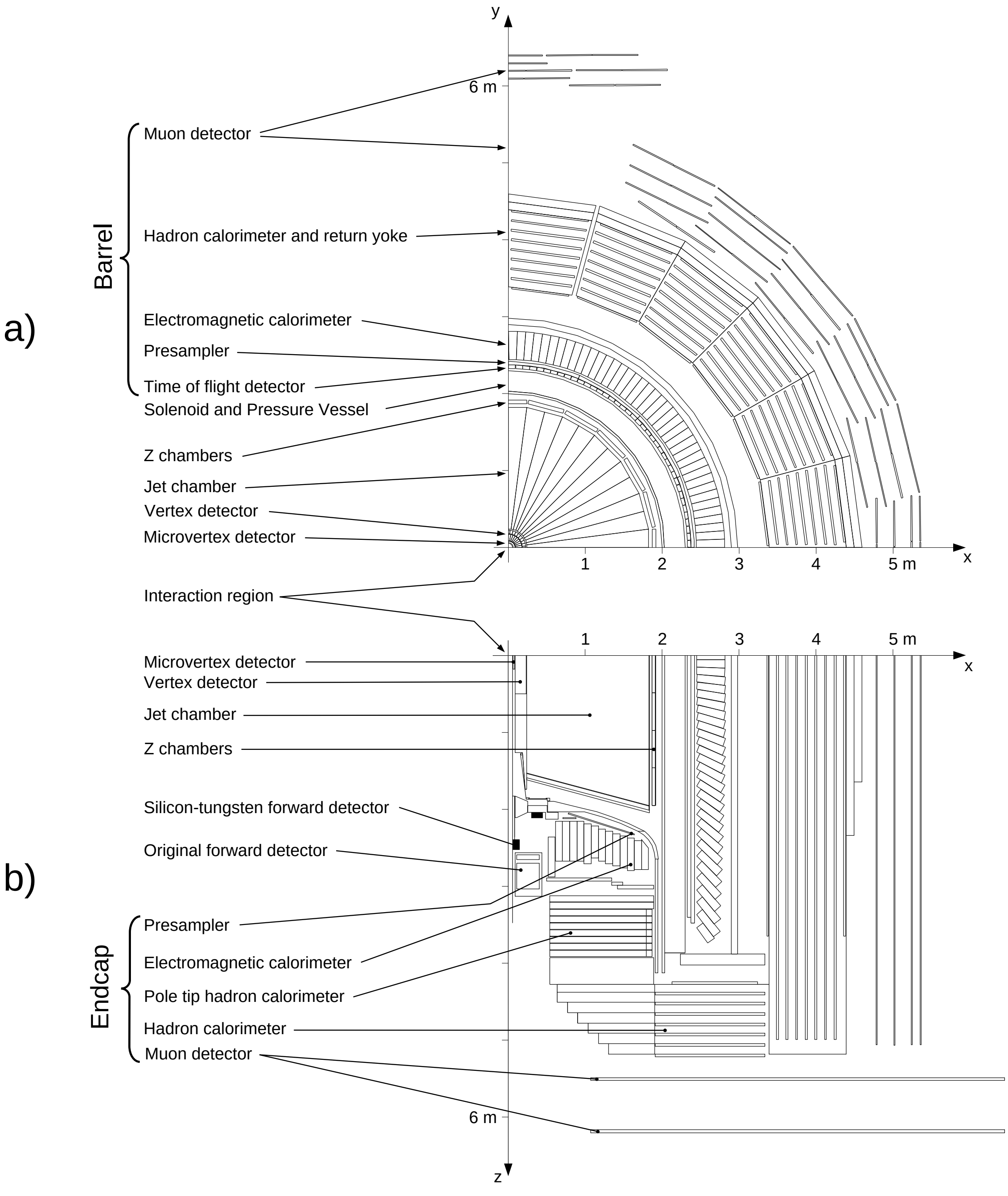

Figure 16.3: The detector in the *xy*- and in the *xz*-plane.

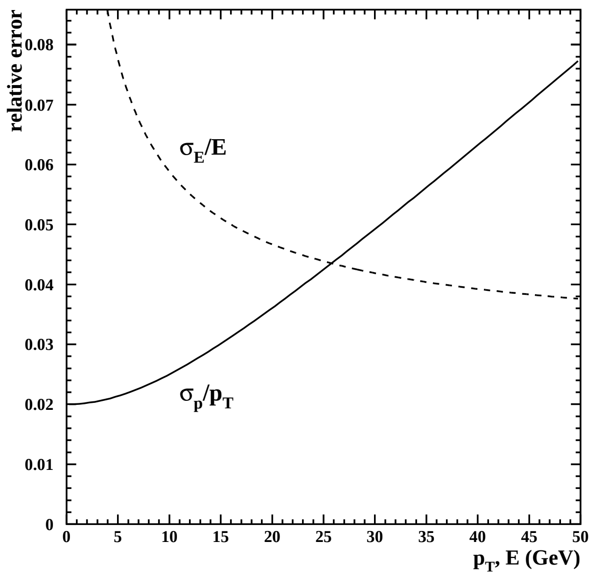

Figure 16.4: Energy resolution of ECAL and momentum resolution of the central tracking system.

from the interaction point. The time resolution is about 300 ps in the barrel region and 3 ns in the end-cap time-of-flight scintillators.

- The **electromagnetic calorimeter** measures the energy of electrons and photons in a range between some MeV and some hundred GeV by means of Čerenkov light which is emitted in electromagnetic showers. A total of 9 440 lead-glass blocks cover 98% of the angular region in the central region (EB) and the end-caps (EE). The active area of one block is about 10 × 10 cm^2. The amount of material corresponds to 24.6 radiation lengths. In the barrel, the blocks point to the interaction region, and have spatial resolution of ≈ 1 cm. The energy resolution is given by

$$\frac{\sigma_E}{E} \approx 3\% \oplus \frac{16\%}{\sqrt{E}} \qquad (E \text{ in GeV}). \tag{16.2}$$

  Figure 16.4 shows the energy resolution of the electromagnetic calorimeter and the momentum resolution of the tracking system. The resolution is dominated by the momentum measurement for electrons below 26 GeV, and by the energy measurement above 26 GeV.

  The presence of the pressure vessel and the magnet cause particles to shower already before reaching the ECAL. Therefore, a **presampler** (PB and PE) was installed in front of the ECAL to correct for the energy loss and to improve the discrimination between neutral pions and photons and between electrons and hadrons. In the barrel, it consists of streamer tubes, and in the end-caps of multi-wire chambers.

- The **hadronic calorimeter** around the ECAL measures the energy of hadrons and is used in the identification of muons. It is divided into the a barrel part (HB), an endcap part (HE), and a pole-cap part (HP). The HCAL is a sampling calorimeter with alternating layers of streamer tubes and iron. The diameter in the barrel is 1 m, and it serves also as return yoke for the magnetic field.

For accurate reconstruction of hadronic energy depositions information from HCAL and ECAL must be combined, because the ECAL has a thickness of 2.2 hadronic interaction lengths. The pole-cap calorimeters, built from similar multi-wire proportional chambers as the ones in the presampler, are used to measure energy depositions at small angles $|\cos\theta| = 0.91$ up to $|\cos\theta| = 0.99$.

- The hadronic calorimeter is enclosed by **muon detectors** (barrel: MB, end-caps: ME). They measure position and direction of particles that have not been absorbed by all other detectors (equivalent to 1.3 m of iron). In the central region, there are 110 drift chambers with a length of 1.2 m and a thickness of 90 mm. Large-size streamer chambers, covering a total of 2×150 m^2 and located at both ends of OPAL perpendicular to the beam axis, form the endcap muon detectors. Identification of muons is a result from the association of information from the muon system, hits in the outer layers of the hadronic calorimeter, and tracks measured in the inner detector.

- Special **forward detectors** are installed in the end-caps to detect activity at very small angles (40 bis 150 mrad) to the beam axis (Figure 16.5). Parts of it are also used to determine the luminosity with small-angle Bhabha scattering.

  The forward detector (FD) is a system of 35 layers of lead and scintillators with 24 radiation lengths, completed by a presampler. The energy resolution is $\sigma_E/E \approx 17\%/\sqrt{E}$. Proportional chambers and drift chambers measure the position and direction of charged particles.

  The **Gamma Catcher** (GC) is a ring-shaped sandwich of lead and scintillators with seven radiation-lengths, which measure photons and electrons with energy above 2 GeV.

  A **silicon-tungsten calorimeter** (SW: tungsten plates and double-sided silicon-strip counters) is used to measure Bhabha events at very low angles. With their help, the luminosity can be determined with an accuracy of 0.2%.

  A so called **MIP-plug** was installed in the region 200 mrad–43 mrad to measure minimal ionizing particles. It consists of four layers of plastic scintillators of 1 cm width.

Track parameters

The tracks of charged particles in the solenoid field is described by a helix, which is parameterized by five parameters. OPAL uses the following track parameters:

- $|\kappa| \equiv (2\rho)^{-1}$: ρ is the curvature of the track in the projection to r-ϕ.
- d_0: radial distance of the vertex to the point of closest approach (p.c.a) of the track to the vertex in the r-ϕ plane.
- z_0: z-coordinate of the track at the p.c.a.
- $\tan\lambda = \cot\theta$, θ is the polar angle of the track.
- ϕ_0: Azimuthal angle of the tangent to the track at the p.c.a.

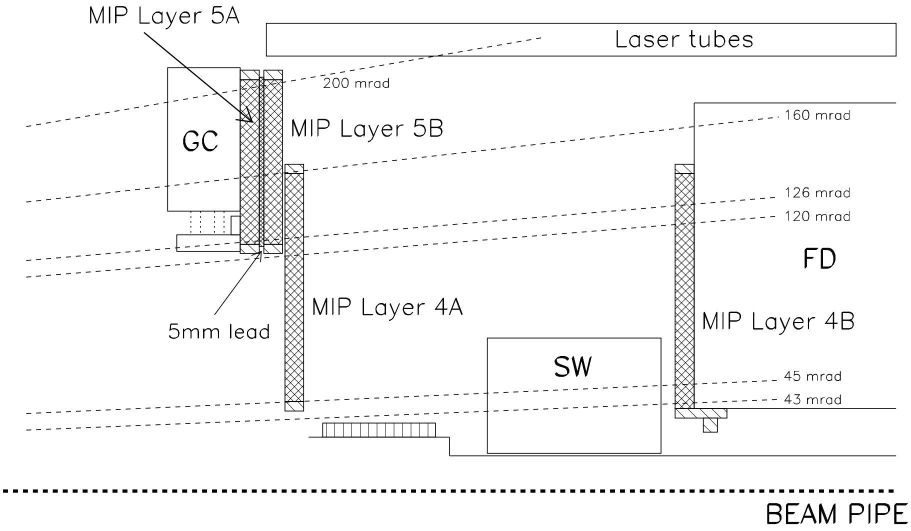

Figure 16.5: The components for detecting particles at small polar angles.

The track parameters in cartesian coordinates are then given by

$$\begin{aligned} p_{xy} &= 1.5 \cdot 10^{-4} \cdot |B_z/\kappa|, \\ p_x &= p_{xy} \cdot \cos\phi_0, \\ p_y &= p_{xy} \cdot \sin\phi_0, \\ p_z &= p_{xy} \cdot \tan\lambda. \end{aligned}$$

16.2.1 Event simulation

The physics processes are simulated on computers in order to study the properties of signal and background and to find optimal cuts to separate both. The first step of simulation consists of calculating the four-vectors of the outgoing particles in the wanted process for a great many of events, which is done according to theoretically predicted distributions of angles and energy. In hadronic events fragmentation of quarks and gluons into jets is simulated as well. As a second step, one simulates the flight of the particles through the detector. This is done with the GEANT 3-based GOPAL [86]. This program emulates the interaction of the transversing particles with the different materials in the components of OPAL. The response from the subdetectors serves as input to the same event reconstruction software which is used for real data. The output events can be handled in the same way as real data, but in addition it contains information about the true values of the generated particles (‘tree-information’). This is useful, for example, to compare reconstructed with generated quantities and to determine the resolution of, *e.g.*, reconstructed masses.

16.3 Data sets and Monte Carlo samples

The analysis is based on data collected with the OPAL detector at LEP during the runs in the years 1997 to 2000 at center-of-mass energies between 183 and 209 GeV (LEP 2). The parts of the detector relevant for the analysis were required to be fully functional (CJ, EB, EE, HS, HT, HP, MB, ME, FD, SW). The integrated luminosity used is 605.9 pb^{-1}, as detailed in Table 16.1.

Table 16.1: Overview of the analyzed integrated data luminosities.

Year	1997	1998	1999	1999	1999	1999	2000	2000
$\sqrt{s}$	183	189	192	196	200	202	202–206	206–209
$\int \mathcal{L}\,\mathrm{d}t$ (pb^{-1})	56.1	177.7	28.8	73.2	74.2	36.5	83.1	132.4

To estimate the detection efficiency for a signal from a new scalar boson S^0 and the amount of background from SM processes, several MC samples are used. Signal events are simulated for masses from 30 GeV to 110 GeV in a large variety of decay modes with the HZHA [87] generator. The signal efficiencies are determined for all possible decays of a Standard Model Higgs boson (quarks, gluons, leptons, photons), for the decays into 'invisible' particles (*e.g.*, Lightest Supersymmetric Particles) $\mathrm{S}^0 \to \chi_1^0\chi_1^0$ as well as for 'nearly invisible' decays, $\mathrm{S}^0 \to \chi_2^0\chi_1^0$, where the χ_2^0 decays into a χ_1^0 plus a photon or a virtual Z^0, and for decays $\mathrm{S}^0 \to \mathrm{A}^0\mathrm{A}^0$ with $\mathrm{A}^0 \to \mathrm{c\bar{c}}$, gg or $\tau^+\tau^-$, where A^0 is the CP-odd Higgs boson in supersymmetric extensions of the Standard Model. For simulation of background processes the following generators are used: BHWIDE [88], TEEGG [89] ($(\mathrm{Z}/\gamma)^* \to \mathrm{e^+e^-}(\gamma)$), KORALZ [90], KK2F [91] (both $\mu^+\mu^-(\gamma)$ and $\tau^+\tau^-(\gamma)$), JETSET [92], PYTHIA [92] ($\mathrm{q\bar{q}}(\gamma)$), GRC4F [93] (four-fermion processes), PHOJET [94], HERWIG [95], and Vermaseren [96] (hadronic and leptonic two-photon processes). For all Monte Carlo generators other than HERWIG, the hadronization is done using JETSET. The luminosity of the main background Monte Carlo samples is at least four times the statistics of the data for the two-fermion background, 50 times for the four-fermion background and five times for the two-photon background. The signal Monte Carlo samples contain 500–1000 events per mass and decay mode. The generated events are passed through a detailed simulation of the OPAL detector [86] and are reconstructed using the same algorithms as for the data.

17 Search for S^0Z^0

In this chapter searches for new neutral scalar bosons S^0, *e.g.*, Higgs bosons, with the OPAL detector at LEP are described. The new bosons are assumed to be produced in association with a Z^0 boson via the Bjorken process $e^+e^- \rightarrow S^0Z^0$ ('S^0-strahlung'). Throughout the chapter, S^0 denotes, depending on the context, any new scalar neutral boson, the Standard Model Higgs boson H^0_{SM} or CP-even Higgs bosons h^0 in models that predict more than one Higgs boson.

17.1 Introduction

The analyses are based on studies of the recoil mass spectrum in $Z^0 \rightarrow e^+e^-$ and $\mu^+\mu^-$ events. They are sensitive to all decays of S^0 into an arbitrary combination of hadrons, leptons, photons and invisible particles, and to the case of a long-lived S^0 leaving the detector without interacting. The analyses are applied to 605.9 pb^{-1} of LEP 2 data collected at center-of-mass energies in the range of 183 to 209 GeV. To cover the low mass range, this analysis is complemented by a similar work that analyses LEP 1 data [97]. In 1990 OPAL performed a decay-mode independent search for light Higgs bosons and new scalars using 6.8 pb^{-1} of data with center-of-mass energies around the Z^0 pole [98]. Assuming the Standard Model production cross section, a lower limit on the Higgs boson mass of 11.3 GeV was obtained. The full data set of the LEP 1 on-peak data are re-analyzed in [97] in order to extend the sensitive region to signal masses up to 55 GeV. Including the data above the Z^0 peak (LEP 2) with results from this work enlarges the sensitivity up to $m_{S^0} \sim 100$ GeV. The S^0 mass range between 30 and 55 GeV is covered by both the LEP 1 and the LEP 2 analysis.

The results are presented in terms of limits on the scaling factor k, which relates the S^0Z^0 production cross section to the Standard Model (SM) cross section for the Higgs-strahlung process:

$$\sigma_{S^0Z^0} = k \cdot \sigma_{H^0_{SM}Z^0}(m_{H^0_{SM}} = m_{S^0}), \tag{17.1}$$

where it is assumed that k does not depend on the center-of-mass energy for any given mass m_{S^0}. Since the analysis is insensitive to the decay mode of the S^0, these limits can be interpreted in any scenario beyond the Standard Model. Examples of such interpretations are listed in the following.

- The most simple case is to provide upper limits on the cross section or scaling factor k for a single new scalar boson independent of its couplings to other particles than the Z^0. It is assumed that the decay width is small compared to the detector mass resolution. In a more specific interpretation, assuming the S^0Z^0 production cross section to be identical to the Standard Model Higgs boson one, the limit on k can be translated into a lower limit on the Higgs boson mass[1].

---

[1] Dedicated searches for the Standard Model Higgs boson by the four LEP experiments, exploiting the prediction for its decay modes, have ruled out masses of up to 114.4 GeV [16].

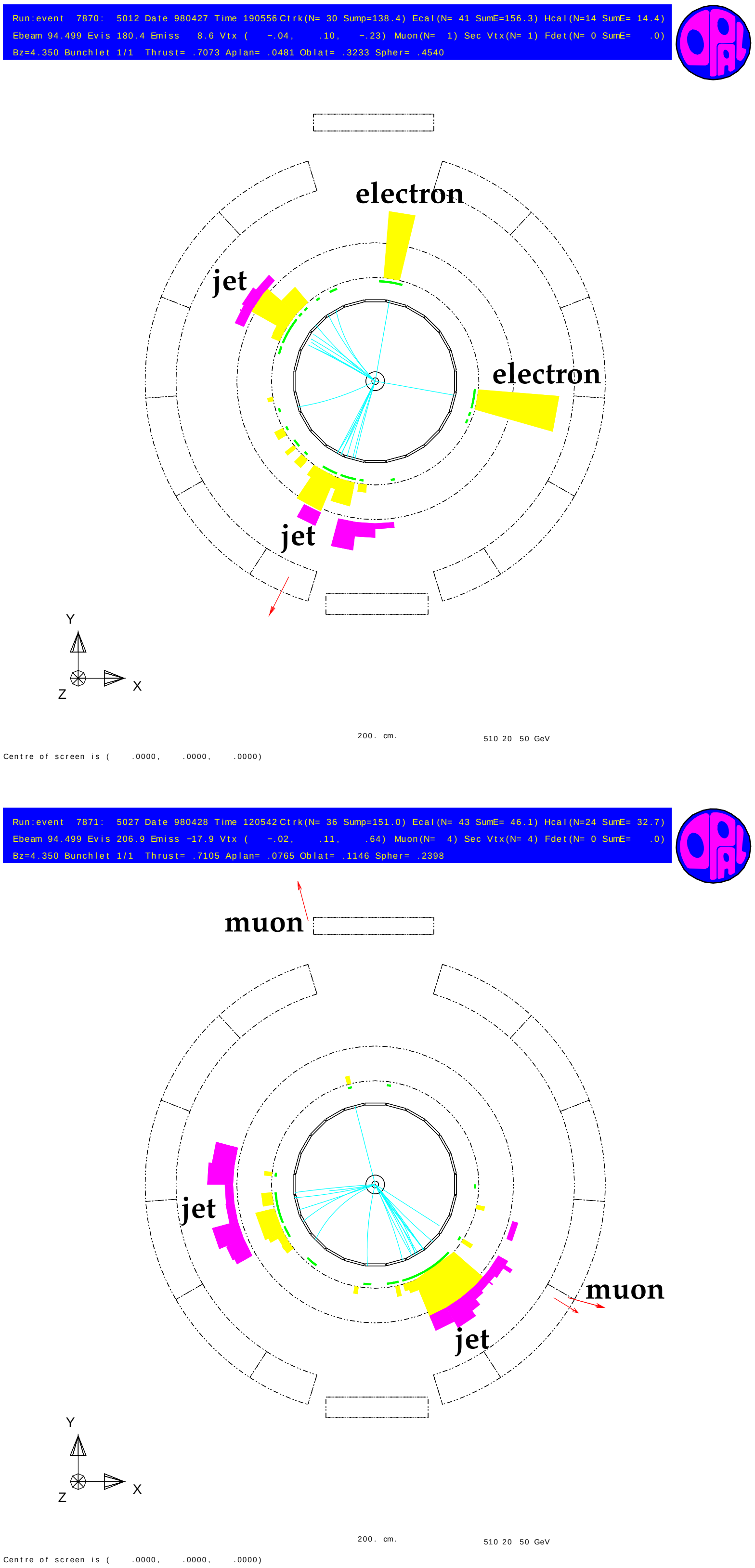

```
Run:event  7870:  5012 Date 980427 Time 190556 Ctrk(N= 30 Sump=138.4) Ecal(N= 41 SumE=156.3) Hcal(N=14 SumE= 14.4)
Ebeam 94.499 Evis 180.4 Emiss   8.6 Vtx (   -.04,     .10,    -.23)  Muon(N=  1) Sec Vtx(N= 1) Fdet(N= 0 SumE=    .0)
Bz=4.350 Bunchlet 1/1  Thrust= .7073 Aplan= .0481 Oblat= .3233 Spher= .4540
```

```
Centre of screen is (    .0000,    .0000,    .0000)
```

```
Run:event  7871:  5027 Date 980428 Time 120542 Ctrk(N= 36 Sump=151.0) Ecal(N= 43 SumE= 46.1) Hcal(N=24 SumE= 32.7)
Ebeam 94.499 Evis 206.9 Emiss -17.9 Vtx (   -.02,     .11,     .64)  Muon(N=  4) Sec Vtx(N= 4) Fdet(N= 0 SumE=    .0)
Bz=4.350 Bunchlet 1/1  Thrust= .7105 Aplan= .0765 Oblat= .1146 Spher= .2398
```

```
Centre of screen is (    .0000,    .0000,    .0000)
```

Figure 17.1: Event displays of simulated signal events in the electron (top figure) and muon channel (bottom figure).

- For the first time, limits are given not only for a single mass peak with small width, but also for a continuous distribution of the signal in a wide mass range. Such continua appear in several recently proposed models, *e.g.*, in the Uniform Higgs scenario and the Stealthy Higgs scenario described in Section 15.3.

17.2 Decay-mode independent searches for $e^+e^- \rightarrow S^0Z^0$

The event selection is intended to be efficient for the complete spectrum of possible S^0 decay modes. As a consequence it is necessary to consider a large variety of background processes. Suppression of the background aims at using no information from the particular decay of the S^0. The decays of the Z^0 into electrons and muons are the channels with highest purity and best mass resolution for m_{Z^0}, and therefore they used in this analysis. They are referred to as the electron and the muon channel, respectively. The signal process can be tagged by identifying events with an acoplanar, high momentum electron or muon pair with $m_{\ell\ell} \approx m_{Z^0}$. The term 'acoplanar' is used for lepton pairs if the two leptons are not consistent with forming a single plane with the beam axis. Figure 17.1 visualizes the topology of simulated signal events $e^+e^- \rightarrow Z^0H^0$ in the electron and muon channel. The event displays are generated with the Higgs boson decaying hadronically. Figure 17.2 gives a diagrammatic representation of the signal process.

Many of the standard processes at LEP 2 are background to the Z^0S^0 signal. They can be divided into several classes. Some classes can easily be suppressed by applying cuts on variables in which signal and background are clearly distinguishable. Some classes resemble the signal and are difficult to cut on efficiently. The relevant background classes are described in the following, and typical cross sections are listed in Table 17.1 on page 160:

- Two-fermion processes with initial state radiation (Figure 17.3). The cross section for two-fermion processes is enhanced, if the effective center-of-mass energy after radiating one or more photons in the initial state is equal to m_{Z^0}. The Z^0 boson is then on its mass shell, and the system of decay products of the Z^0 is imbalanced due to the radiated photon(s).

- In the electron channel, an additional background arises from the t-channel process $e^+e^- \rightarrow e^+e^-$. The cross section is large compared to the two-fermion s-channel process, but the usually small scattering angle provides a way to cut on this background.

- Some background processes with four fermions in the final state are shown in Figures 17.4–17.6. Z^0-pair production with at least one Z^0 decaying into e^+e^- or $\mu^+\mu^-$ is irreducible since the leptons are daughters of an on-shell Z^0 boson, whereas in $W^\pm$-pair production with both $W \rightarrow \ell\nu$ the leptons originate from different mother particles, and so the invariant $\ell^+\ell^-$ mass is generally not equal to the Z^0 mass.

- In two-photon processes (Figure 17.7) the electron and positron are scattered at very small angles. The cross section is large but the scattering angle is often not large enough for both electrons to leave the beam pipe and reach the detector.

To identify the signal process and reject background, the analysis proceeds as follows: It starts with a preselection of events that contain at least two charged particles identified as electrons or muons. A particle is marked as an electron or muon, if it is identified by at least one of the two methods:

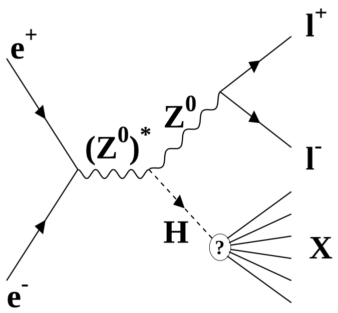

Figure 17.2: The signal process.

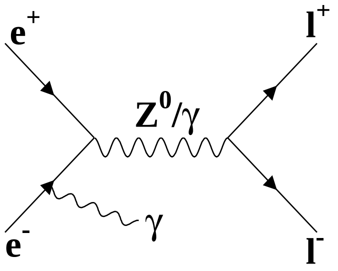

Figure 17.3: Two-fermion process with ISR.

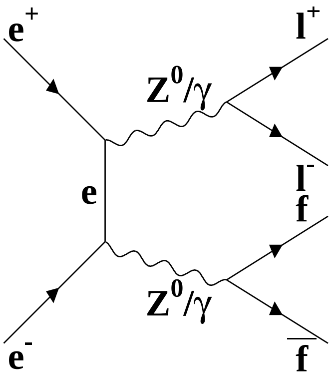

Figure 17.4: Z-pair production.

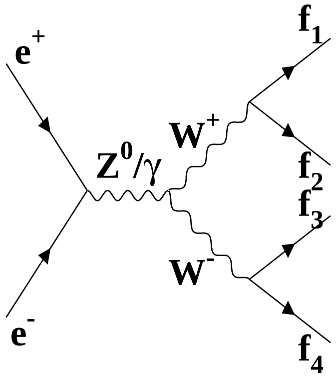

Figure 17.5: W-pair production.

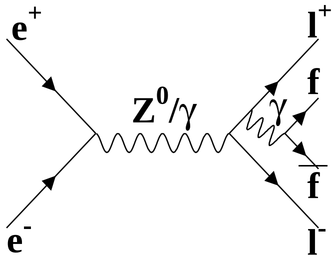

Figure 17.6: Four-fermion process from FSR.

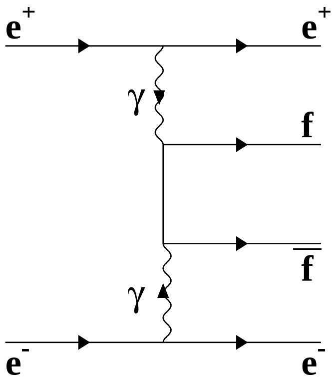

Figure 17.7: Two-photon process.

Table 17.1: Cross sections for background processes at selected center-of-mass energies. The $e^+e^-(\gamma)$ cross section is obtained for an angular cut $12.5 < \theta < 167.5°$. The 2-photon cross section is defined in [99].

$\sqrt{s}$ σ	183 GeV (pb)	189 GeV (pb)	200 GeV (pb)	206 GeV (pb)
$e^+e^-(\gamma)$	628	596	532	502
$\mu^+\mu^-(\gamma)$	8.5	8.0	7.5	7.0
$\tau^+\tau^-(\gamma)$	8.4	8.0	7.4	6.9
4-fermion	72.1	70.3	83.4	81.3
2-photon	1 827	1 843	1 876	1 961

- ◦ The standard OPAL procedures for electron and muon identification [100]. These routines were developed to identify leptons in a hadronic environment. Since the signal events contain primarily isolated leptons, a second method with a higher efficiency is also used:

- ◦ A track is classified as an electron if the ratio E/p is greater than 0.8, where p is the track momentum and E the associated electromagnetic energy. Furthermore the energy loss $\mathrm{d}E/\mathrm{d}x$ in the central tracking chamber has to be within the central range of values where 99% of the electrons with this momentum are expected. Muons are required to have $E/p < 0.2$ and at least three hits in total in the muon chambers plus the last three layers of the hadronic calorimeter.

The average efficiency and purity of the combined lepton identification are determined in a control sample of collinear di-lepton data events: One lepton is required to be identified by the procedures described above, and then the fraction of events is measured which have another identified lepton opposite to the tagged lepton. In these samples the average efficiency (purity) for muons is 97% (94%), and for electrons it is 90% (90%).

The two tracks must have opposite charge and high momentum. The selection requires $E_1 > 0.22 \cdot \sqrt{s}$, $E_2 > 0.11 \cdot \sqrt{s}$ for electrons and $p_1 > 0.22 \cdot \sqrt{s}$, $p_2 > 0.12 \cdot \sqrt{s}$ for muons, where E_1, p_1 and E_2, p_2 are the energy (measured in the ECAL) and momentum of the lepton with the higher and lower momentum, respectively.

The two leptons must be isolated from the rest of the event. The isolation angle α_{iso} of a lepton candidate is defined as the maximum angle for which the energy E_{cone} contained within a cone of half-angle α_{iso} around the direction of the lepton at the vertex is less than 1 GeV. E_{cone} is the energy of all tracks and electromagnetic clusters not associated to the lepton candidate within the cone, excluding the energy of the lepton itself. Leptons at small angles to the beam axis ($|\cos\theta| > 0.9$ in the electron channel and $|\cos\theta| > 0.94$ in the muon channel) are not used due to detector inefficiencies and mismodeling in this region. These cuts also serve to reduce the background from two-fermion and two-photon processes. Lepton candidates inside a 0.3° azimuthal angle to the anode planes of the jet chamber are ignored since they are not well described in the detector simulation. If more than one electron or muon pair candidate with opposite charge is found, the pair with invariant mass closest to m_{Z^0} is taken as Z^0 decay products.

The backgrounds to the $S^0\ \ell^+\ell^-$ signal are suppressed as described below. The cuts are listed in Table 17.2 and the number of events after each cut is given in Table 17.3. The distributions of the cut variables in data and Monte Carlo are shown in Figures 17.8 and 17.9 for data taken at $\sqrt{s} = 183$–209 GeV.

- ◦ The semileptonic decays of b- or c-mesons provide a source of leptons which can be misidentified as direct Z^0 decay products, *e.g.*, in events $Z^0Z^0 \rightarrow q\bar{q}\ell^+\ell^-$ or $W^+W^- \rightarrow qq'\ell\nu$. This background is reduced by requiring the leptons to be isolated from the rest of the event. One of the isolation angles of the two lepton candidates must be greater than 15° and the other one must be greater than 10°.

- ◦ The selection requires the invariant mass $m_{\ell\ell}$ of the lepton pair to be consistent with the Z^0 mass. Due to the limited detector mass resolution, invariant masses within $m_{Z^0} \pm 8$ GeV and $m_{Z^0} \pm 10$ GeV are accepted for the electron and the muon channel, respectively.

- The dominant background at this stage originates from leptonic Z^0 decays with photon radiation in the initial state so that the effective center-of-mass energy of the electron-positron pair after photon emission is close to the Z^0 mass ('radiative returns' to the Z^0 pole). These background events are characterized by an acolinear and sometimes acoplanar lepton pair and one or more high energy photons. Such events are rejected by a photon-veto: if there is only one cluster in the electromagnetic calorimeter not associated to a track and the energy E_{unass} of the cluster exceeds 60 GeV, then the event is rejected. Events with two tracks and more than 3 GeV energy deposition in the forward calorimeters (covering the polar angle region 47–200 mrad) are also vetoed.

- In two-photon processes, where the incoming electron and positron are scattered at low angles, usually one or both of the electrons are undetected. Events of this type usually have large missing momentum with the missing momentum vector, $\vec{p}_{\mathrm{miss}}$, pointing at low angles to the beam axis. In $(\mathrm{Z}/\gamma)^* \rightarrow \mathrm{e}^+\mathrm{e}^-, \mu^+\mu^-$ events with initial-state radiation the photons usually remain undetected at low angles. The requirement $|\cos\theta(\vec{p}_{\mathrm{miss}})| < 0.95$ reduces background from these two sources.

- In $(\mathrm{Z}/\gamma)^* \rightarrow \mathrm{e}^+\mathrm{e}^-, \mu^+\mu^-$ events without initial or final state radiation the leptons are produced in a back-to-back topology. These events are rejected by cutting on the acoplanarity angle ϕ_a which is defined as $\pi - \phi_{\mathrm{open}}$, where ϕ_{open} is the opening angle between the two lepton tracks in the plane perpendicular to the beam axis. The cut is $\phi_a > 0.15$—0.20 rad (depending on the center-of-mass energy).

- In the remaining background from two-photon processes and $(\mathrm{Z}/\gamma)^* \rightarrow \mathrm{e}^+\mathrm{e}^-, \mu^+\mu^-$ with initial-state radiation the leptons carry considerable momentum along the beam axis. These events are rejected by requiring $|p_1^z + p_2^z| < 50$ GeV where p_i^z are the z-components of the momentum of the two lepton candidates.

After these cuts a total of 54 events remain in the data of 183–209 GeV in the channel $\mathrm{Z}^0 \rightarrow \mathrm{e}^+\mathrm{e}^-$, with $46.9 \pm 0.6\,(\mathrm{stat.}) \pm 3.3\,(\mathrm{syst.})$ events expected from SM background (the evaluation of the systematic uncertainties is described in section 17.2.2). In the channel $\mathrm{Z}^0 \rightarrow \mu^+\mu^-$, 43 events remain in the data with $51.6 \pm 0.3\,(\mathrm{stat.}) \pm 2.6\,(\mathrm{syst.})$ expected from SM background. The quoted statistical errors denote the errors from the limited Monte Carlo statistics only. The statistical error of the expected background rates is $\sqrt{46.9} \approx 6.9$ in the electron channel and $\sqrt{51.6} \approx 7.2$ in the muon channel. The signal efficiency is at least 24% in the electron channel and at least 30% in the muon channel for S^0 masses between 30 and 90 GeV.

Table 17.2: A summary of the selection criteria.

$Z^0 \rightarrow e^+e^-, \mu^+\mu^-$		
0.	Preselection	see text
1.	Isolation of lepton tracks	$\max(\alpha_{\mathrm{iso}_1}, \alpha_{\mathrm{iso}_2}) > 15°$ $\min(\alpha_{\mathrm{iso}_1}, \alpha_{\mathrm{iso}_2}) > 10°$
2.	Invariant mass of the lepton pair	$\lvert m_{e^+e^-} - m_{Z^0} \rvert < 8$ GeV $\lvert m_{\mu^+\mu^-} - m_{Z^0} \rvert < 10$ GeV
3.	Photon veto	see text
4.	Polar angle of missing momentum vector	$\lvert \cos\theta(\vec{p}_{\mathrm{miss}}) \rvert < 0.95$ for $p_{\mathrm{miss}} > 5$ GeV
5.	Acoplanarity	$\phi_a > 0.15$–0.20 rad
6.	Momentum in z-direction	$\lvert p_1^z + p_2^z \rvert < 50$ GeV

Table 17.3: Cutflow table: Number of selected events after each cut. As an example the efficiencies for the signal process $S^0Z^0 \rightarrow b\bar{b}\,\ell^+\ell^-$ are also given. The efficiencies are the luminosity-weighted average of the values at 183–209 GeV.

$\sqrt{s} = 183$–209 GeV						
Cut	Data	Total bkg.	2-fermion	4-fermion	2-photon	Signal (m_{S^0}=90 GeV)
Electron channel						
Preselection	27708	28183.5	27720.0	378.0	85.5	49.1%
Lepton isolation	24176	24803.9	24410.6	314.3	79.0	42.1%
$M_{\ell\ell}$	708	639.1	547.9	73.0	18.2	37.7%
Photon-veto	470	477.1	393.8	67.9	15.4	37.7%
$\lvert \cos\theta_{p_{\mathrm{miss}}} \rvert$	118	106.3	57.4	45.7	3.2	34.8%
Acoplanarity	67	63.1	25.4	37.2	0.5	28.7%
$\lvert p_1^z + p_2^z \rvert$	54	46.9	12.8	33.7	0.4	28.7%
Muon channel						
Preselection	3042	3115.6	2818.8	212.2	84.6	64.7%
Lepton isolation	2866	2948.5	2669.5	195.9	83.1	55.7%
$M_{\ell\ell}$	803	842.4	733.3	88.5	20.7	49.3%
Photon-veto	575	629.3	532.0	80.9	16.4	49.3%
$\lvert \cos\theta_{p_{\mathrm{miss}}} \rvert$	111	101.5	45.8	52.3	3.4	45.5%
Acoplanarity	66	72.0	26.7	44.3	1.0	37.5%
$\lvert p_1^z + p_2^z \rvert$	43	51.6	12.2	38.6	0.8	37.5%

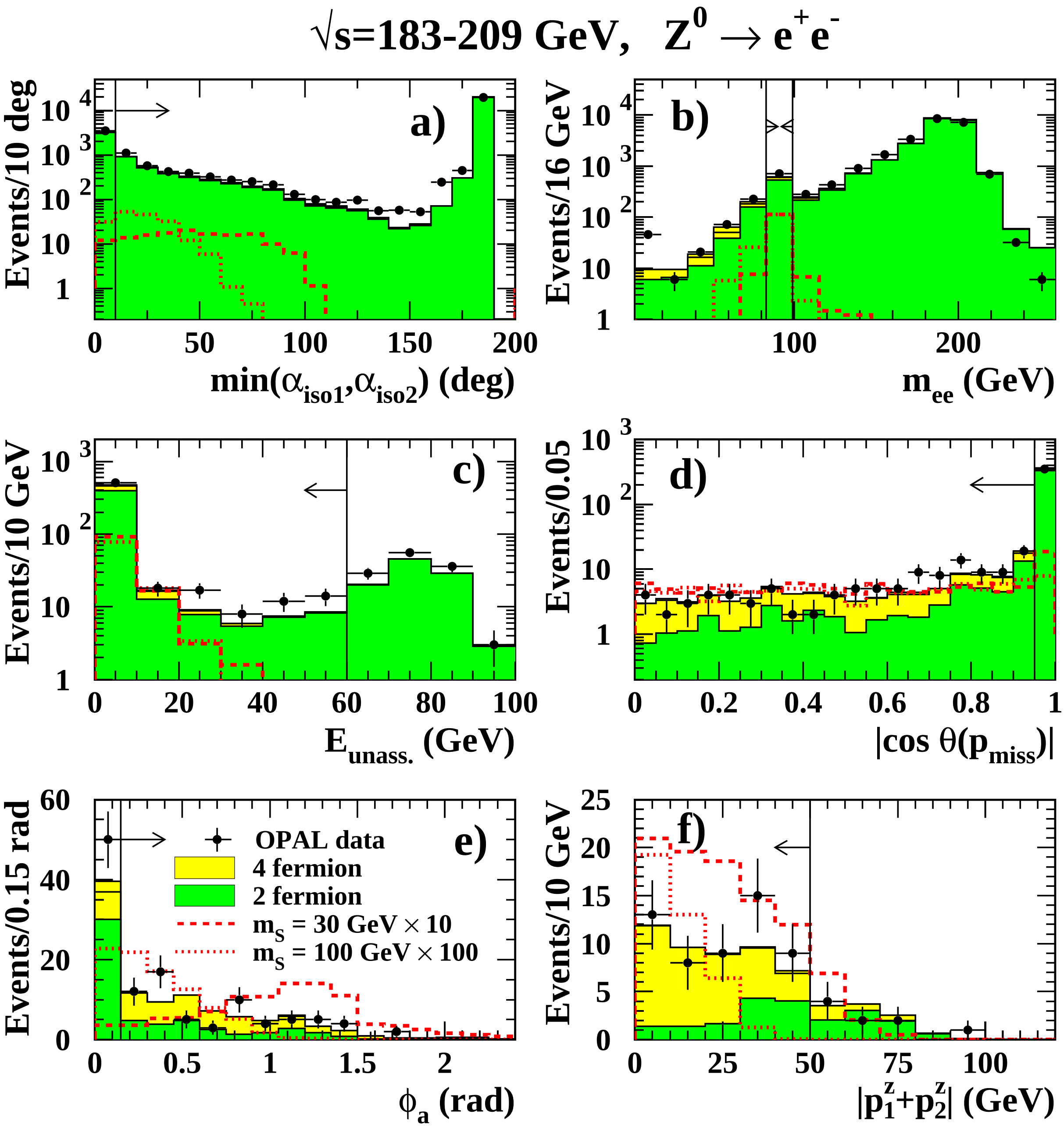

Figure 17.8: Cut variables for $Z^0 \to e^+e^-$ at $\sqrt{s} = 183$–209 GeV. The OPAL data are indicated by dots with error bars (statistical error), the four-fermion background by the light gray histograms and the two-fermion background by the medium gray histograms. The signal distributions from a 30 GeV S^0 are plotted as dashed lines and those from a 100 GeV S^0 as dotted lines, respectively. The signal histograms are normalized to 10 and 100 times of the Standard Model Higgs-strahlung cross section, respectively, and show the decays $S^0 \to gg$. Each variable is shown with the cuts applied before the cut on this variable is done, respecting the order of cuts in Table 17.3. The arrows indicate the accepted regions.

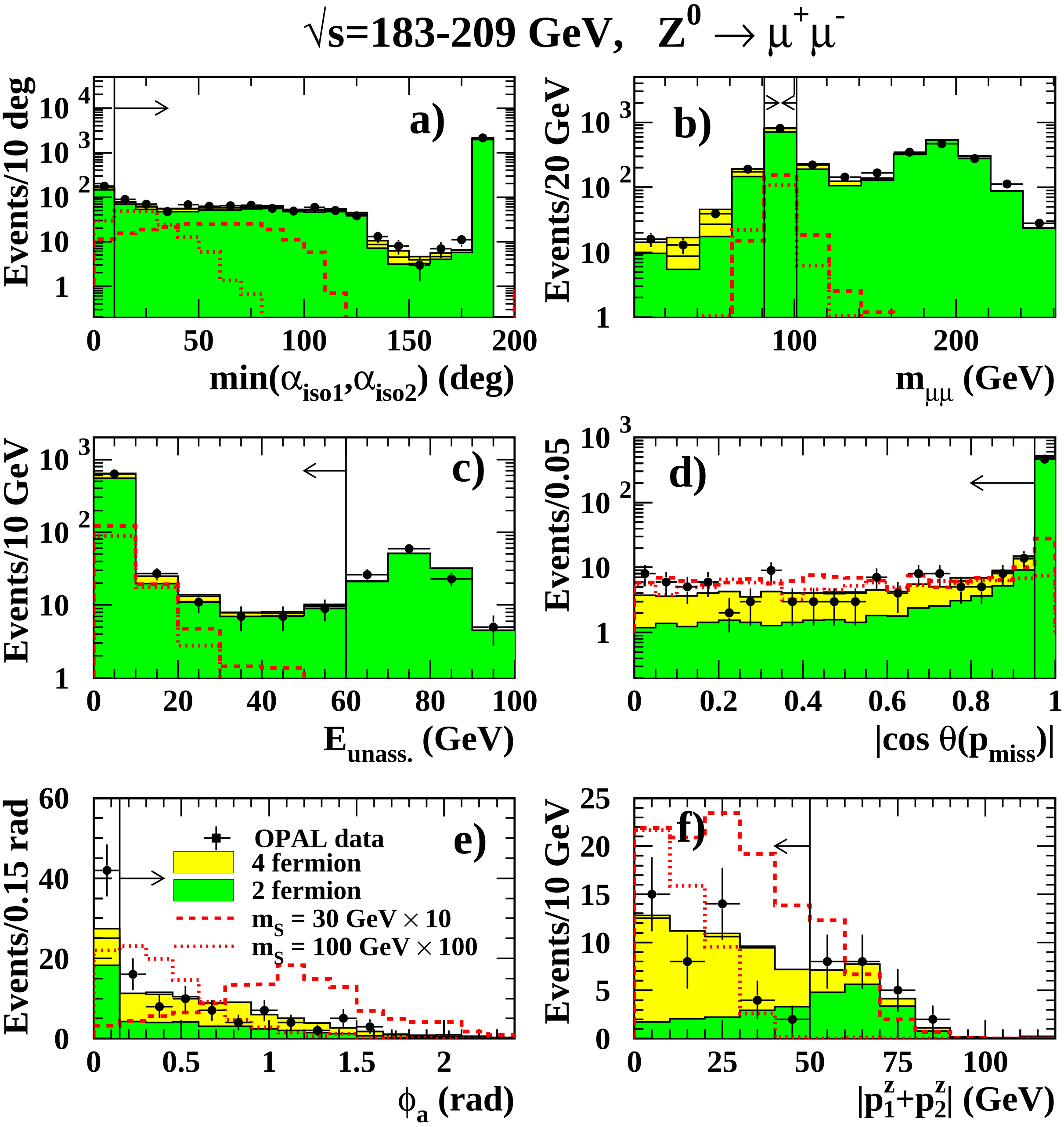

Figure 17.9: Cut variables for $Z^0 \to \mu^+\mu^-$ at $\sqrt{s}$ = 183–209 GeV. The OPAL data are indicated by dots with error bars (statistical error), the four-fermion background by the light gray histograms and the two-fermion background by the medium gray histograms. The signal distributions from a 30 GeV S^0 are plotted as dashed lines and those from a 100 GeV S^0 as dotted lines, respectively. The signal histograms are normalized to 10 and 100 times of the Standard Model Higgs-strahlung cross section, respectively, and show the decays $S^0 \to gg$. Each variable is shown with the cuts applied before the cut on this variable is done, respecting the order of cuts in Table 17.3. The arrows indicate the accepted regions.

Figure 17.10 shows the efficiency versus the S^0 mass at $\sqrt{s} = 202$–209 GeV for some example decays as well as the minimum efficiencies which are used in the limit calculation. The efficiencies for 183–202 GeV have similar values for $m_{S^0} < 100$ GeV. For the lower center-of-mass energies the efficiency decreases faster for higher masses due to kinematic effects, primarily the cut on the acoplanarity angle. Figure 17.11 shows the recoil mass spectrum for both channels summed from 183–209 GeV. The recoil mass squared is calculated from

$$m^2_{\mathrm{rec}} = \left(\sqrt{s} - E_{\ell\ell}\right)^2 - p^2_{\ell\ell}, \tag{17.2}$$

where $E_{\ell\ell} = E_{\ell_1} + E_{\ell_2}$ and $p_{\ell\ell} = |\vec{p}_{\ell_1} + \vec{p}_{\ell_2}|$ are the energy and the momentum sum of the two lepton tracks, and $\sqrt{s}$ is the center-of-mass energy. The momentum sum is calculated from the track momentum of the Z^0 decay products in the muon channel and from the track momentum and energy deposition of the electrons in the electromagnetic calorimeter in the electron channel. For electrons the momentum $\vec{p}$ is calculated from the energy, weighted by the respective momentum component: $p^{\mathrm{e}}_i = E \cdot p_i/|\vec{p}|$. This accounts for the fact that the energy of electrons can be measured with smaller error than the momentum at high energies (c.f. Figure 16.4). Due to the limited energy and momentum resolution, the calculated value of m^2_{rec} can be negative. Thus, the recoil mass is defined as $m_{\mathrm{rec}} = \sqrt{m^2_{\mathrm{rec}}}$ for $m^2_{\mathrm{rec}} \geq 0$ and $m_{\mathrm{rec}} = -\sqrt{-m^2_{\mathrm{rec}}}$ for $m^2_{\mathrm{rec}} < 0$..

17.2.1 Correction on background and signal efficiencies

The analysis makes use of a veto on activity in the forward calorimeters (see description of the photon veto). In data the veto could be triggered by randomly-occurring collisions of beam electrons with the beam-pipe walls or residual gas molecules inside the beam-pipe, or from detector noise. These effects are not modeled by the Monte Carlo. Thus, in all channels a correction is applied to the number of expected background events and the signal efficiencies. The correction factor is derived from the study of random beam crossings. The fraction of these events that fail the veto on activity in the forward region is 3.1%. Since the veto is applied only to events with two tracks, the corrections on the expected background in the actual analyses are typically only 1.8–3.5%. For the signal efficiencies the full correction is applied to the decay channels where appropriate.

17.2.2 Systematic uncertainties

Apart from statistical errors, there are systematic uncertainties which occur from imperfect modeling of Monte Carlo events. In the event generation, higher order corrections must be neglected at some level, and in the simulation the detector can not be simulated in every detail. These effects introduce imponderabilities to the prediction of signal and background properties. In this section several sources of uncertainties are studied.

- The systematic uncertainty of the lepton identification efficiency is studied in a control sample of events with two collinear tracks of which at least one is tagged as an electron or muon. The systematic uncertainty is obtained from the difference of the identification efficiencies for the other track between data and Monte Carlo.
- The tracking systematics are studied by changing the track resolution[2] in the Monte Carlo by a relative fraction of 5% in d_0 and ϕ and by 10% in z_0, κ and $\cot\theta$, which

---

[2] d_0 is the distance between the vertex and the point of closest approach of a track to the vertex in the r–ϕ plane, z_0 is the z-coordinate of the track at this point, and κ is its curvature.

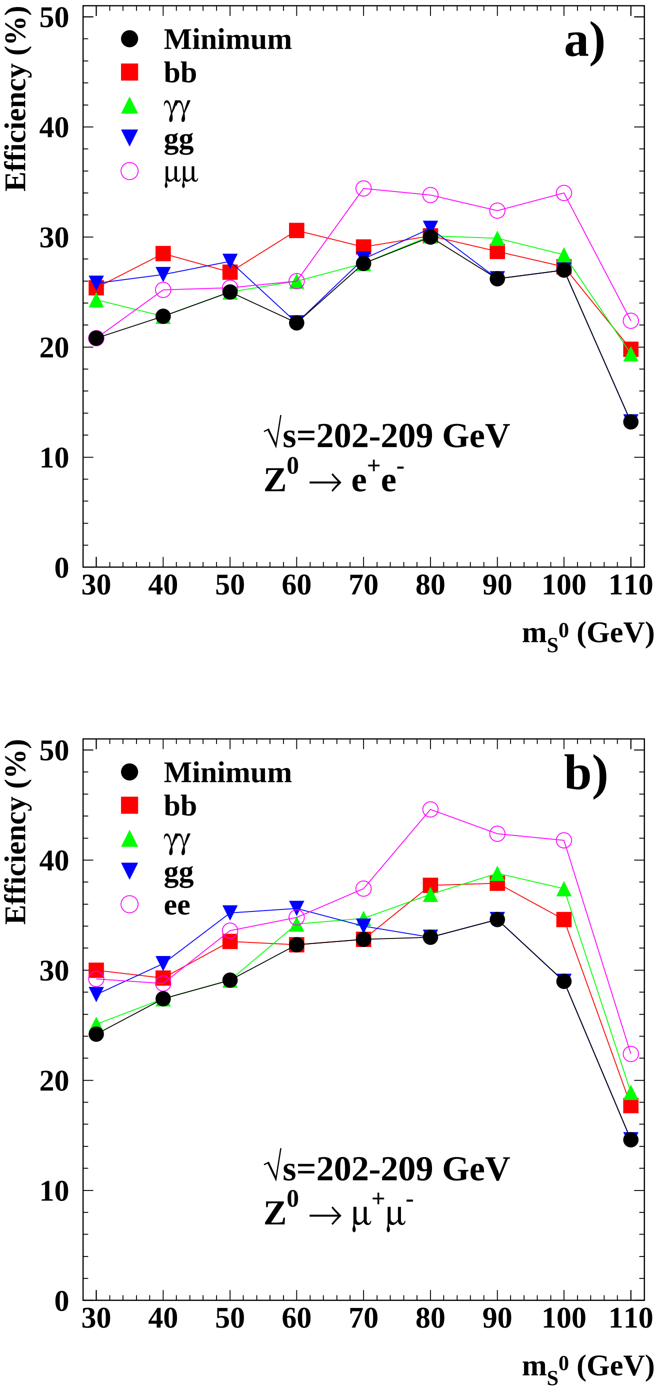

Figure 17.10: The efficiency versus the S^0 mass at $\sqrt{s} = 202$–209 GeV for a subset of decay modes of S^0 a) in the $Z^0 \to e^+e^-$ and b) $Z^0 \to \mu^+\mu^-$ channel. The minimum efficiencies which are used in the limits are given as well. For the other LEP 2 center-of-mass energies the signal efficiencies are similar.

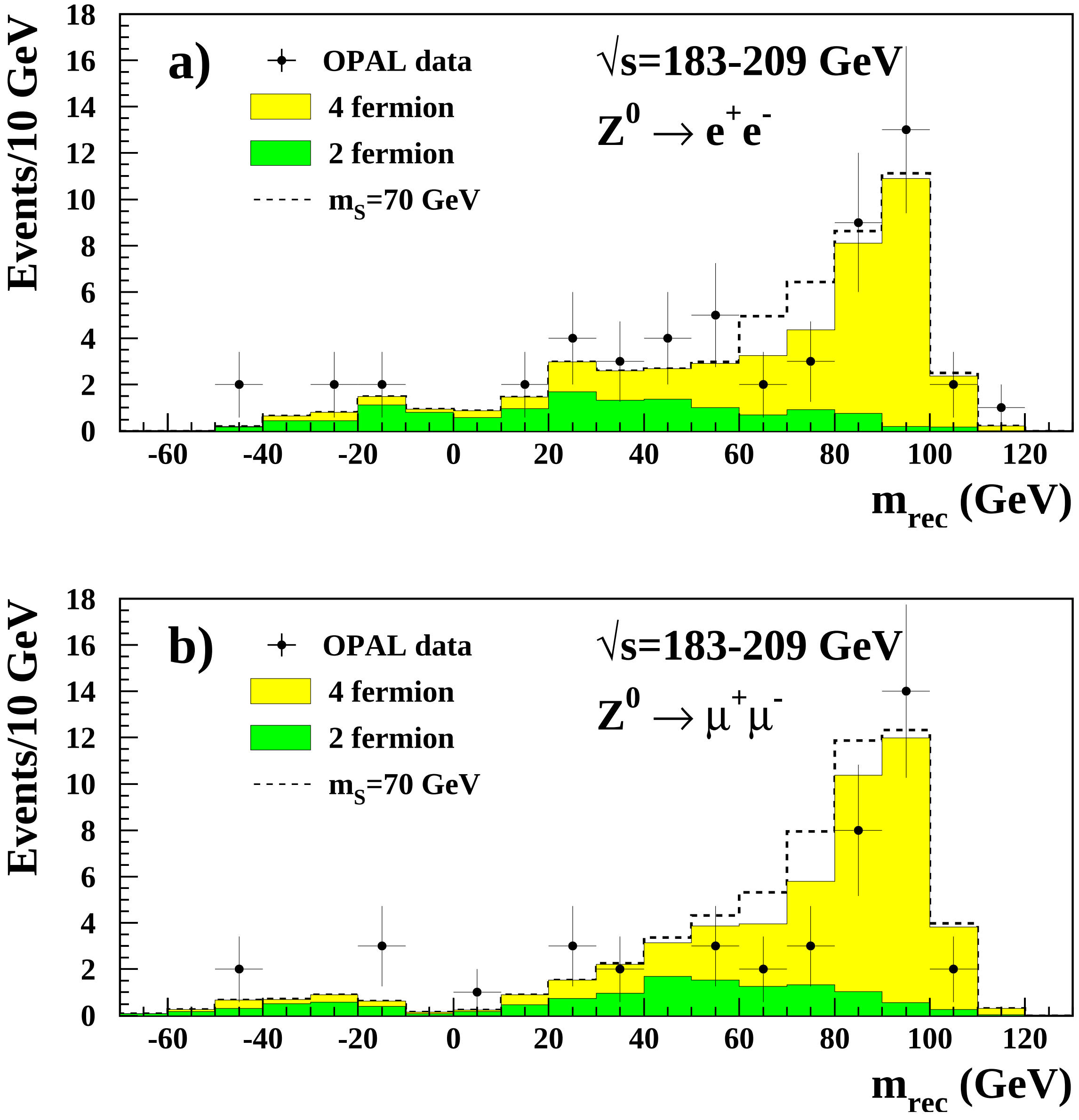

Figure 17.11: The recoil mass spectrum from 183–209 GeV a) for the decays $Z^0 \rightarrow e^+e^-$ and b) for $Z^0 \rightarrow \mu^+\mu^-$. OPAL data are indicated by dots with error bars (statistical error), the four-fermion background by the light gray histograms and the two-fermion background by the medium gray histograms. The dashed lines for the signal distributions are plotted on top of the background distributions with normalization corresponding to the excluded cross section from the combination of both channels.

corresponds to the typical difference in the resolution of these parameters in data and Monte Carlo. The difference in signal and background expectation compared to the one obtained from the unchanged track resolution is taken as the systematic uncertainty.

- The reconstruction of the energy deposition in the electromagnetic calorimeter and the momentum in the tracking system of the lepton candidates is investigated with the help of the mean values $\bar{x}_{dat}$ and $\bar{x}_{MC}$ of the distributions of p and E from the collinear lepton pair control sample for data and Monte Carlo expectation. The analyses are repeated with the cuts on p and E being changed by the difference $|\bar{x}_{dat} - \bar{x}_{MC}|$. The deviations in the number of expected events compared to the original cuts are taken as the systematic uncertainties.

- The uncertainty from the lepton isolation angle α_{iso} is studied in a control sample of $W^+W^- \rightarrow q\bar{q}\ell\nu$ events. The isolation of the lepton is compared in data and Monte Carlo. The cut on α_{iso} is then varied by the difference of the mean of the data and the Monte Carlo distributions of the control sample.

- Correct modeling of photon radiation is a crucial ingredient of the decay-mode independent searches. In the muon channel two different Monte Carlo generators are used for the two-fermion background, and the difference between the background prediction of the two generators is taken as the systematic uncertainty of the photon modeling. For the electron channel only one generator is available. Here, the uncertainty is determined from the comparison of the number of events in the data and Monte Carlo sets in a side band of the distribution of the lepton pair invariant mass where no signal is expected. This test is dominated by the statistical uncertainties of the side-band sub-sample.

- The four-fermion Monte Carlo samples do not account for low mass resonances (*e.g.*, $\rho, \omega, \phi, J/\psi$). Also, the electromagnetic coupling constant α_{em} is taken to be constant instead of depending on the momentum transfer q^2. To correct for the two effects a weight w is calculated from the recoil mass against the lepton system [101]. Each event contributes with its weight w_i. The uncertainty from this reweighting is assessed to be 50% of the change of the expected background after switching off the reweighting.

The evaluation of the systematic uncertainties at each single center-of-mass energy is limited by Monte Carlo statistics. Therefore, they are investigated for the total set of Monte Carlo samples with $\sqrt{s} = 183$–209 GeV. A detailed overview is given in Table 17.4. The uncertainties are assumed to be uncorrelated and the individual contributions are added in quadrature for the total systematic uncertainty.

Modeling of the radiative returns has a large impact on the total systematic uncertainty, both in the electron and the muon channel. In the electron channel the uncertainty from the isolation angle criterion and in the muon channel the uncertainty of the muon identification efficiency are also significant.

The numbers of expected background events, broken down by the different center-of-mass energies, are listed in Table 17.5 for the channels $Z^0 \rightarrow e^+e^-$ and $Z^0 \rightarrow \mu^+\mu^-$. The numbers include systematic errors discussed above and the statistical error from the limited Monte Carlo samples. Also the number of expected events from a 30 GeV Standard Model Higgs boson is shown.

Table 17.4: Systematic uncertainties for the background rate and signal efficiency. The relative uncertainties in the signal are shown for $m_{S^0} = 60$ GeV.

Source	electron channel Bkg.	electron channel Sig.	muon channel Bkg.	muon channel Sig.
Electron/muon-ID	1.3%	1.3%	2.8%	2.8%
Energy	1.2%	1.5%	1.9%	1.3%
Isolation angle	4.3%	2.8%	1.7%	2.0%
Trk. resolution	2.2%	1.3%	2.2%	1.1%
ISR/FSR	4.7%	—	2.3%	—
α_{em}	0.4%	—	0.2%	—
Luminosity	0.2%	—	0.2%	—
Total systematics	7.0%	3.7%	5.0%	3.8%
MC Statistics	3.1%	0.9%	1.7%	1.0%

Table 17.5: Summary of selected data events, background Monte Carlo and signal expectation for a 30 GeV Standard Model Higgs boson in the decay-mode independent searches. The first error is statistical and the second error is systematic.

$\sqrt{s}$ (GeV)	Data	Total bkg.	2-fermion	4-fermion	2-photon	Signal (m_{S^0}=30 GeV)
			Electron channel			
183	7	$3.6 \pm 0.1 \pm 0.3$	1.4	2.1	0.1	$0.91 \pm 0.02 \pm 0.03$
189	18	$13.7 \pm 0.4 \pm 1.0$	4.2	9.5	0.0	$2.42 \pm 0.04 \pm 0.09$
192	0	$2.2 \pm 0.1 \pm 0.2$	0.7	1.5	0.0	$0.37 \pm 0.01 \pm 0.01$
196	6	$5.7 \pm 0.2 \pm 0.4$	2.0	3.7	0.0	$0.87 \pm 0.01 \pm 0.03$
200	4	$4.8 \pm 0.2 \pm 0.3$	1.2	3.5	0.1	$0.81 \pm 0.01 \pm 0.03$
202	5	$2.5 \pm 0.1 \pm 0.2$	0.6	1.9	0.0	$0.39 \pm 0.01 \pm 0.01$
202–206	5	$5.0 \pm 0.2 \pm 0.4$	0.7	4.2	0.1	$0.86 \pm 0.01 \pm 0.03$
206–209	9	$9.4 \pm 0.3 \pm 0.7$	2.0	7.3	0.1	$1.34 \pm 0.02 \pm 0.05$
$\sum$	54	$46.9 \pm 0.6 \pm 3.5$	12.8	33.7	0.4	$7.97 \pm 0.06 \pm 0.25$
			Muon channel			
183	5	$4.4 \pm 0.1 \pm 0.2$	1.6	2.7	0.1	$1.20 \pm 0.01 \pm 0.05$
189	9	$13.7 \pm 0.1 \pm 0.7$	4.0	9.5	0.2	$2.96 \pm 0.03 \pm 0.11$
192	2	$2.5 \pm 0.1 \pm 0.1$	0.6	1.9	0.0	$0.46 \pm 0.01 \pm 0.02$
196	6	$6.1 \pm 0.1 \pm 0.3$	1.2	4.7	0.2	$0.96 \pm 0.01 \pm 0.04$
200	5	$5.7 \pm 0.1 \pm 0.3$	1.3	4.3	0.1	$0.89 \pm 0.01 \pm 0.03$
202	3	$2.9 \pm 0.1 \pm 0.1$	0.6	2.3	0.0	$0.43 \pm 0.01 \pm 0.02$
202–206	9	$6.0 \pm 0.1 \pm 0.3$	0.9	5.0	0.1	$1.00 \pm 0.01 \pm 0.04$
206–209	4	$10.3 \pm 0.1 \pm 0.5$	2.0	8.2	0.1	$1.53 \pm 0.02 \pm 0.06$
$\sum$	43	$51.6 \pm 0.3 \pm 2.5$	12.2	38.6	0.8	$9.43 \pm 0.06 \pm 0.37$

17.3 Results

The results of the decay-mode independent searches are summarized in Table 17.5, which compares the numbers of observed candidates with the background expectations. The total number of observed candidates from all channels combined is 97, while the Standard Model background expectation amounts to 98.5±0.7(stat.)±6.0(syst.). For each individual search channel there is good agreement between the expected background events and observed candidates. As no significant excess over the expected background is observed in the data, limits on the cross section for the Bjorken process $e^+e^- \rightarrow S^0Z^0$ are calculated.

The limits are presented in terms of a scale factor k, which relates the cross section for S^0Z^0 to the Standard Model one for the Higgs-strahlung process $e^+e^- \rightarrow H^0_{SM}Z^0$ as defined in Equation 17.1. The 95% CL upper bound on k is obtained from a test statistic for the signal hypothesis, by using the weighted event-counting method described in [102]: In each search channel, given by the different center-of-mass energies and the Z^0 decay modes considered, the observed recoil mass spectrum is compared to the spectra of the background and the signal. The latter is normalized to $\varepsilon \cdot \mathrm{BR} \cdot \mathcal{L} \cdot k \cdot \sigma_{H^0Z^0}$, where ε is the minimum signal detection efficiency out of all tested decay modes, BR is the branching ratio of the Z^0 decay mode considered in this channel and $\mathcal{L}$ is the integrated luminosity recorded for that channel. The efficiencies for arbitrary S^0 masses are interpolated from the efficiencies at masses for which Monte Carlo samples were generated. Every event in each of these mass spectra and each search channel is given a weight depending on its expected ratio of signal over background, s/b, at the given recoil mass. For every assumed signal S^0 mass these weights are a function of the signal cross section, which is taken to be k times the Standard Model Higgs cross section for the same S^0 mass. Finally, from the sum of weights for the observed number of events, an upper limit k^{95} for the scale factor is determined at the 95% confidence level.

The systematic uncertainties on the background expectations and signal selection efficiencies are incorporated using the method described in [56].

The limits are given for three different scenarios:

1. Production of a single new scalar S^0.
2. The Uniform Higgs scenario.
3. The Stealthy Higgs scenario.

In order to extend the sensitivity region to S^0 masses below ≈ 55 GeV, the results of this work are combined with results from a similar search which uses data from the Z^0 peak (LEP 1). The LEP 1 analysis is described in Ref. [97], and the weighted event-counting method described above is applied to combine the results.

17.3.1 Production of a single new scalar S^0

In the most simple interpretation of the combined results from the LEP 1 and LEP 2 search, a cross-section limit is set on the production of a new neutral scalar boson S^0 in association with a Z^0 boson. To calculate the limit, the mass distributions are used which are shown in Figure 17.11 and in Figure 4 of Ref. [97] for OPAL data, the expected background and the signal.

Figure 17.12 presents the limits obtained for scalar masses down to the lowest generated signal mass of 1 keV (in the LEP 1 search). They are valid for the decays of the S^0 into

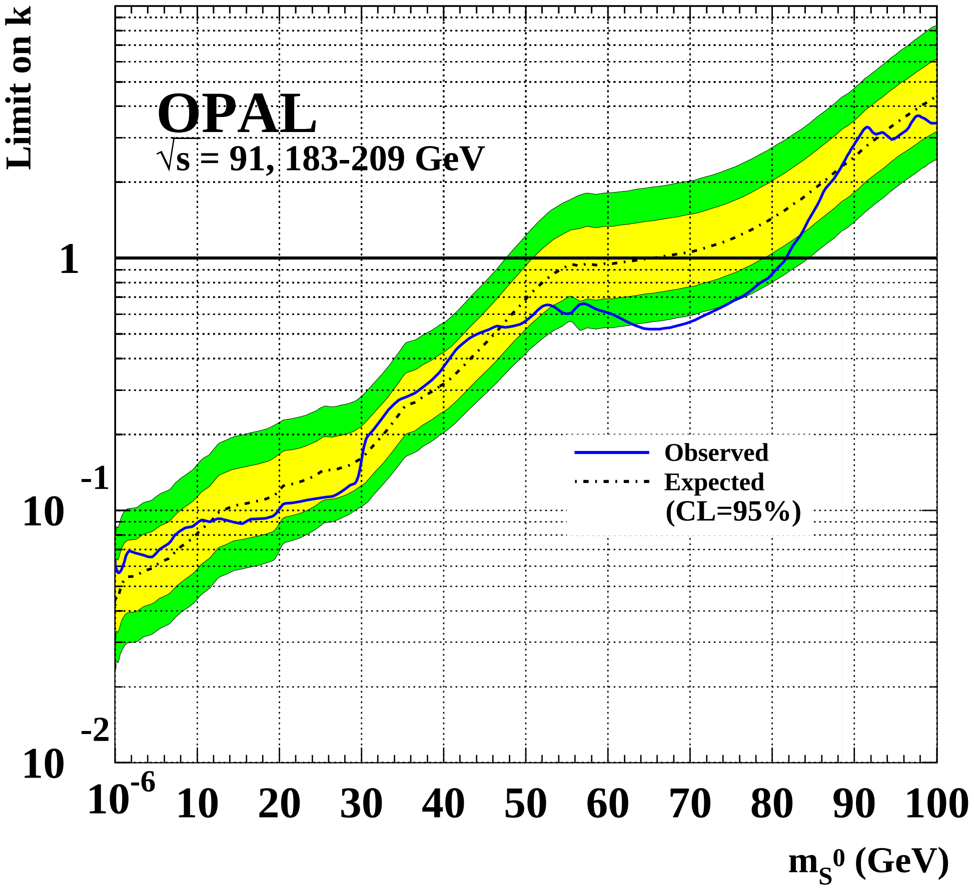

Figure 17.12: The upper limit on the scale factor k on the cross section for the production of a new scalar boson in the Higgs-strahlung-process (solid line). The dot-dashed line represents the expected median for background-only experiments. Both limits are calculated at the 95% confidence level. The dark (light) shaded bands indicate the 68% (95%) probability intervals centered on the median expected values. For masses $m_{S^0} \lesssim 1$ GeV the limits are constant. The lowest signal mass tested is 10^{-6} GeV.

hadrons, leptons, photons and invisible particles (which may decay inside the detector) as well as for the case in which the S^0 has a sufficiently long lifetime to escape the detector without interacting or decaying. The observed limits are given by the solid line, while the expected sensitivity, determined from a large number of Monte Carlo experiments with only background, is indicated by the dotted line. The shaded bands indicate the one and two sigma deviations from the expected sensitivity. Values of $k > 0.1$ are excluded for values of m_{S^0} below 19 GeV, whereas $k > 1$ is excluded from the data for m_{S^0} up to 81 GeV, independently of the decay modes of the S^0 boson. This means that the existence of a Higgs boson produced at the Standard Model rate can be excluded up to this mass even from decay-mode independent searches. For masses of the new scalar particle well below the width of the Z^0, *i.e.* $m_{S^0} \lesssim 1$ GeV, the obtained limits remain constant at the level of $k^{95}_{\text{obs.}} = 0.067$, and $k^{95}_{\text{exp.}} = 0.051$. Due to peculiarities of the analysis of LEP 1 data, which are detailed in [97], a decay of the S^0 into invisible particles plus photons can lead to a reduced sensitivity in the mass region where the sensitivity of the analyses is dominated by the LEP 1 data. If, of all things, 'invisible+photons' happens to be the dominant decay mode, the limits for $m_{S^0} \lesssim 55$ GeV as shown in Figure 17.12 have to be modified.

The discrepancy between the expected and the observed limits is within one standard

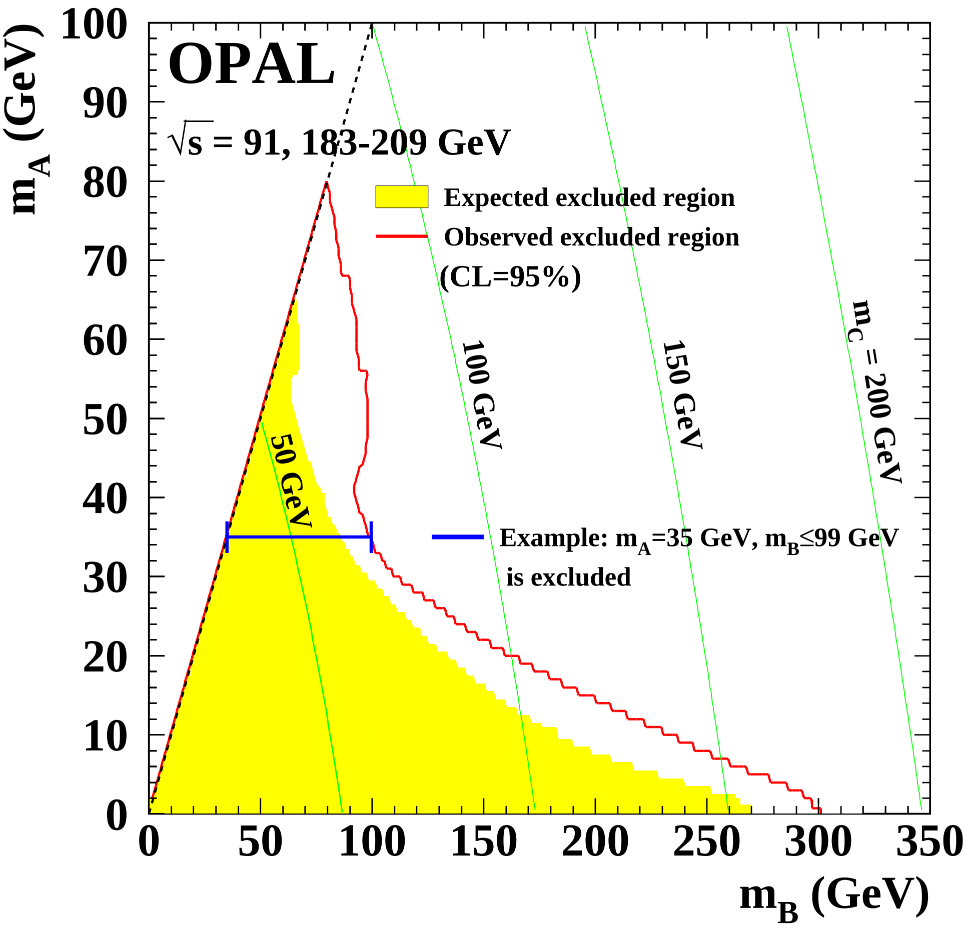

Figure 17.13: Exclusion limits for the Uniform Higgs scenario at the 95% confidence level. All mass intervals (m_A, m_B) within the area bordered by the dark line are excluded from the data. The shaded area marks the mass points which are expected to be excluded if there were only background. The light gray curves indicate isolines for several values of m_C. All intervals (m_A, m_B) to the right of each isoline are theoretically disallowed from Equation 15.5. By definition, only intervals (m_A, m_B) right to the dashed diagonal line are valid, *i.e.* $m_A \leq m_B$.

deviation for masses below 52 GeV and for masses above 82 GeV. The deviation of about two sigma in the mass range 52–82 GeV is due to a deficit of selected data events in the recoil mass spectrum of both the electron and muon channels.

17.3.2 Limits on signal mass continua

In this section limits are set on two scenarios described in Section 15.3 which predict continuous, wide-spread signal mass distributions.

17.3.2.1 The Uniform Higgs scenario

Signal spectra are simulated for the Uniform Higgs scenario for a constant coupling density $\tilde{K} = \mathrm{d}k/\mathrm{d}m =$ constant over the interval $[m_A, m_B]$ and zero elsewhere. Both the lower mass bound m_A and the upper bound m_B are varied between 1 GeV and 350 GeV (with the constraint $m_A \leq m_B$). In a similar way to the previous section an upper limit is obtained on the integral in Equation 15.4.

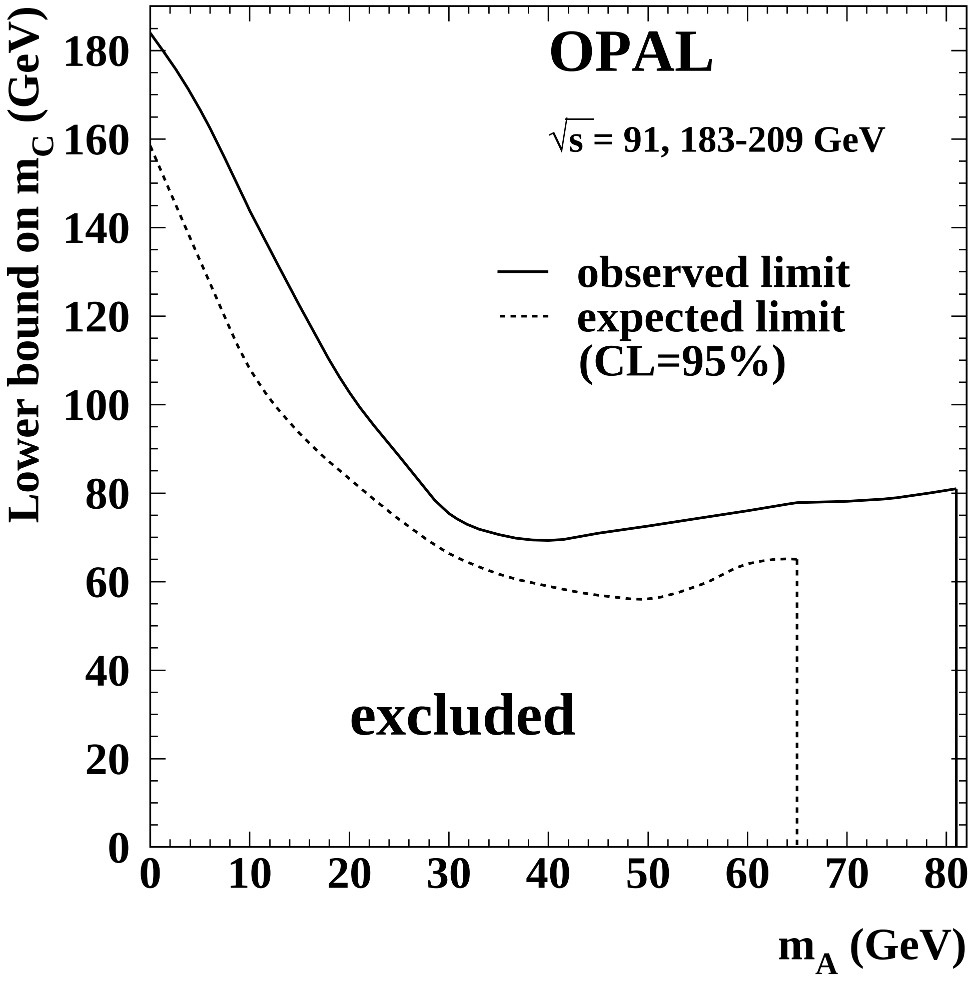

Figure 17.14: Exclusion limits on the perturbative mass scale m_C for constant $\tilde{K}$. The solid line represents the limits obtained from the data, and the dotted line shows the expected limit if there were only background. Values for m_C below the lines are excluded by this analysis at the 95% confidence level.

Figure 17.13 shows the mass points (m_A,m_B) for which the 95% CL limit on $\int \mathrm{d}m\,\tilde{K}$ is less than one. These are the signal mass ranges $m_A \leq m_{h_i^0} \leq m_B$ which can be excluded assuming a constant $\tilde{K}$.

If $m_A = m_B$, then the signal spectrum reduces to the mass distribution of a single boson. Excluded points on the diagonal $m_A = m_B$ are therefore the same masses as in Figure 17.12 for which $k < 1$. The horizontal line illustrates an example for excluded mass ranges: The line starts on the diagonal at $m_A = m_B = 35$ GeV and ends at $m_B = 99$ GeV. This value of m_B is the highest upper mass bound which can be excluded for this value of m_A. All mass ranges with an upper bound m_B below 99 GeV are also excluded for $m_A = 35$ GeV. The highest excluded value of $m_B = 301$ GeV is achieved for $m_A = 0$ GeV.

Using the two sum rules from Section 15.3.1, lower limits on the perturbative mass scale m_C can be derived. For each excluded value of m_A the highest excluded value of m_B is taken, and the lower bound of m_C is determined according to Equation 15.5. The excluded mass ranges for m_C, assuming a constant $\tilde{K}$, are shown in Figure 17.14.

Table 17.6: Bin-wise measurement of $\tilde{K}$ for the mass range 0–100 GeV with $\Delta m = 10$ GeV. To fit a theoretical distribution $\tilde{K}$ to these values, the correction matrix $\hat{C}$ from Table 17.7 must be applied first.

	Measurement of $\tilde{K}$ in bins of 10 GeV width									
Bin	1	2	3	4	5	6	7	8	9	10
Mass (GeV)	0–10	10–20	20–30	30–40	40–50	50–60	60–70	70–80	80–90	90–100
$\tilde{K} \times 10^3$ (GeV^{-1})	2.1	−2.4	−4.9	−2.8	−7.1	5.8	−33.5	−45.2	−18.6	200.2
$\Delta(\tilde{K})_{\mathrm{stat.}} \times 10^3$ (GeV^{-1})	2.9	4.4	4.8	6.4	14.3	23.7	21.7	30.5	66.9	166.4
$\Delta(\tilde{K})_{\mathrm{sys.}} \times 10^3$ (GeV^{-1})	0.9	0.9	0.6	0.5	1.3	3.3	4.5	7.0	16.5	37.4

17.3.2.2 Bin-by-bin limits

The limits presented in section 17.3.2.1 are specific to the case where the coupling density $\tilde{K}$ is constant in the interval $[m_\mathrm{A},\ m_\mathrm{B}]$ and zero elsewhere (Eq. 15.6). The data can also be used to exclude other forms of $\tilde{K}(m)$. To provide practical information for such tests, $\tilde{K}(m)$ is measured in mass bins with a width comparable to the experimental mass resolution. The typical resolution of the recoil mass in the LEP 1 analysis varies between 1 and 5 GeV in the mass region between 10 and 55 GeV. In the LEP 2 analysis the width is between 3 and 15 GeV for recoil masses between 20 and 100 GeV. The width becomes smaller at higher recoil masses. The results of the measurement of $\tilde{K}(m)$ are given in Table 17.6 together with the corresponding statistical and systematic uncertainties.

From these measured numbers of $\tilde{K}(m)$, one can obtain upper limits on the integral $\int \mathrm{d}m\, \tilde{K}(m)$ for any assumed shape of $\tilde{K}(m)$ using a simple χ^2 fitting procedure. To account for mass resolution effects, a correction matrix $\hat{C}$ is provided (Table 17.7). In order to test a theory which predicts a certain distribution of $\tilde{K}(m)$ in the 10 measured bins from Table 17.6, written as a vector $\vec{\kappa} = \left(\tilde{K}_1, \ldots, \tilde{K}_{10}\right)$, the values $\vec{\kappa}$ must first be corrected with the help of the matrix $\hat{C}$. Then the corrected vector $\vec{\kappa}' = \hat{C}\vec{\kappa}$ can be fitted to the measured values. In the fit the systematic uncertainties, which are small compared to the statistical errors, can be assumed to be fully correlated bin-by-bin.

17.3.2.3 The Stealthy Higgs scenario

Limits on the Stealthy Higgs scenario are set by simulating the reconstructed spectrum of a Higgs boson with a width according to Equation 15.8 and Ref. [83]. Since no generator is available which can handle a very large decay width of the Higgs boson in a consistent way, the shape of the broad spectrum $\mathcal{B}(x)$ is constructed from the sum of spectra from the available signal Monte Carlo with small decay width in a large mass range. Each spectrum is weighted according to the corresponding cross section, modified by a Breit-Wigner function to account for the large decay width and multiplied by the selection

Table 17.7: Correction matrix for mass resolution. For a given theory to be tested with a distribution of $\tilde{K}$ values in the 10 mass bins, $\tilde{\kappa} = \left(\tilde{K}_1, \ldots, \tilde{K}_{10}\right)$, the vector $\tilde{\kappa}$ has to be multiplied by the matrix $\hat{C}$ to account for mass resolution effects. The corrected vector $\tilde{\kappa}' = \hat{C}\tilde{\kappa}$ can then be fitted to the measured values of $\tilde{K}$ from Table 17.6.

$$\hat{C} = \begin{pmatrix}
0.33 & 0.04 & 0.02 & 0.01 & 0.00 & 0.00 & 0.00 & 0.00 & 0.00 & 0.00 \\
0.41 & 0.53 & 0.02 & 0.01 & 0.00 & 0.00 & 0.00 & 0.00 & 0.00 & 0.00 \\
0.17 & 0.27 & 0.11 & 0.04 & 0.01 & 0.00 & 0.00 & 0.00 & 0.00 & 0.00 \\
0.09 & 0.11 & 0.14 & 0.17 & 0.05 & 0.01 & 0.00 & 0.00 & 0.00 & 0.00 \\
0.00 & 0.05 & 0.17 & 0.21 & 0.28 & 0.09 & 0.01 & 0.00 & 0.00 & 0.00 \\
0.00 & 0.00 & 0.16 & 0.20 & 0.27 & 0.34 & 0.11 & 0.01 & 0.00 & 0.00 \\
0.00 & 0.00 & 0.11 & 0.14 & 0.16 & 0.29 & 0.37 & 0.09 & 0.01 & 0.00 \\
0.00 & 0.00 & 0.10 & 0.10 & 0.10 & 0.15 & 0.25 & 0.43 & 0.06 & 0.00 \\
0.00 & 0.00 & 0.09 & 0.07 & 0.07 & 0.08 & 0.11 & 0.27 & 0.46 & 0.03 \\
0.00 & 0.00 & 0.09 & 0.07 & 0.05 & 0.04 & 0.06 & 0.11 & 0.32 & 0.32
\end{pmatrix}$$

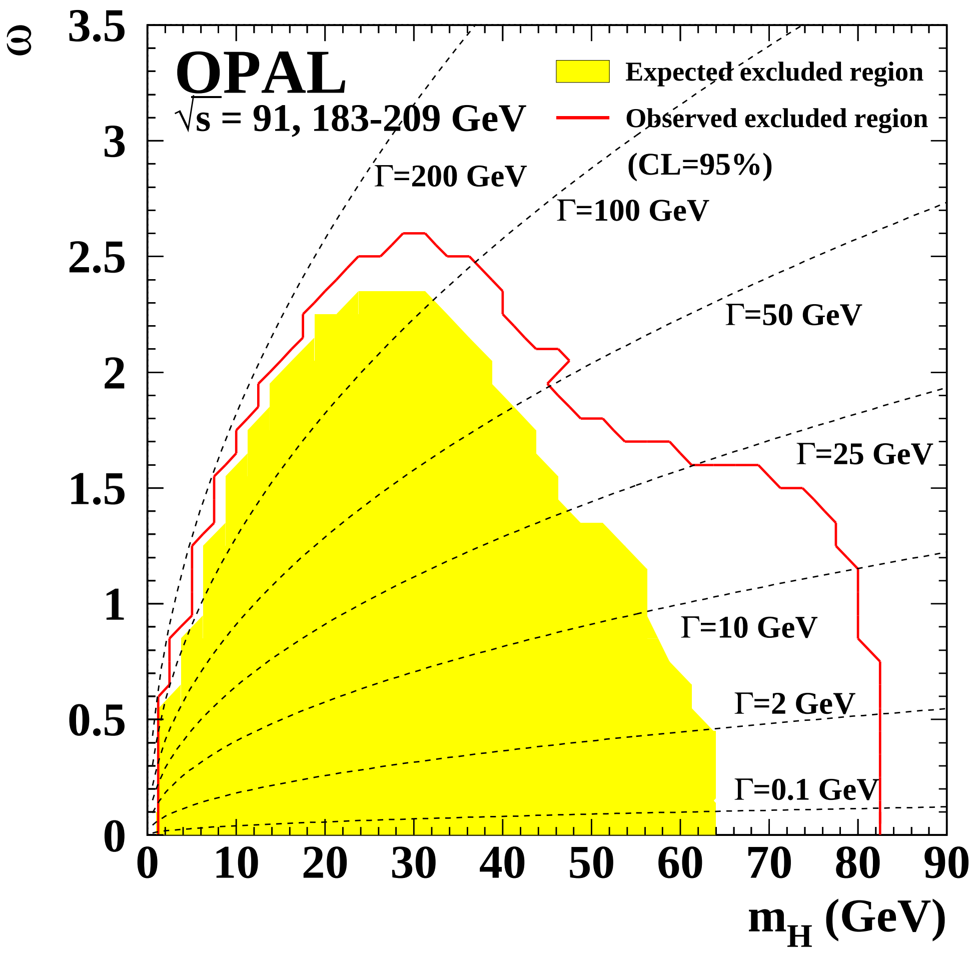

Figure 17.15: Excluded parameter regions for the simplified Stealthy Higgs scenario at the 95% confidence level. The solid line marks the region which is excluded from the data. The shaded area marks the region which would be excluded if the data corresponded exactly to the background-only prediction. The dashed lines indicate the Higgs width depending on m_{H} and ω.

efficiency of the signal mass for that spectrum:

$$\mathcal{B}(x) = \sum_{m_i} \mathrm{BW}(M_0, \Gamma, m_i) \times \sigma_{\mathrm{SM}}(m_i) \times \varepsilon(m_i) \times \mathcal{S}_{m_i}(x), \tag{17.3}$$

where $\mathrm{BW}(M_0, \Gamma, m_i)$ is the Breit-Wigner function at m_i with central value M_0 and width Γ, $\sigma_{\mathrm{SM}}(m_i)$ is the Standard Model cross section for $\mathrm{Z}^0\mathrm{H}^0$ production of mass m_i, $\varepsilon(m_i)$ is the selection efficiency for that mass, and $\mathcal{S}_{m_i}(x)$ is a function which describes the signal shape of mass m_i. For a given coupling ω the width Γ can easily be calculating using Equation 15.8.

The excluded regions in the ω-m_{H} parameter space are shown in Figure 17.15. To illustrate the Higgs width according to Equation 15.8, for a given mass m_{H} and coupling ω 'isolines' for some sample widths are added to the plot. The vertical edge in the exclusion contour at $m_{\mathrm{H}} = 81$ (62) GeV in the observed (expected) limits reflects the detector mass resolution in Δm: For a fixed mass m_{H} the exclusion power is the same for all couplings ω that yield $\Gamma_{\mathrm{H}} \lesssim \Delta m$, and the limits for $\omega \to 0$ reproduce the limits for a single narrow S^0 in Figure 17.12. The maximal excluded region of the coupling ω is achieved for masses around 30 GeV, where ω can be excluded up to $\omega = 2.7$. For lower masses the sensitivity drops due to the rapidly increasing width of the Higgs boson, and for higher masses due to the decreasing signal cross section.

17.4 Conclusions

Searches for new neutral scalar bosons S^0 decaying to hadrons of any flavor, to leptons, photons, invisible particles and other modes have been performed based on the data collected at $\sqrt{s} = 183$ to 209 GeV by studying the recoil mass spectrum of $\mathrm{Z}^0 \to \mathrm{e}^+\mathrm{e}^-, \mu^+\mu^-$ in $\mathrm{S}^0\mathrm{Z}^0$ production. No significant excess of candidates in the data over the expected Standard Model background has been observed. Therefore, upper limits on the production cross section for associated production of S^0 and Z^0, with arbitrary S^0 decay modes, were set at the 95% confidence level. To do so, the results of this work were combined with another decay-mode independent search applied to LEP 1 data. Upper limits in units of the Standard Model Higgs-strahlung cross section of $k < 0.1$ for 1 keV $< m_{\mathrm{S}^0} <$ 19 GeV and $k < 1$ for $m_{\mathrm{S}^0} <$ 81 GeV were obtained. In further interpretations, limits on broad continuous signal mass shapes to which previous analyses at LEP had no or only little sensitivity were set for the first time. Two general scenarios in the Higgs sector were investigated: A uniform scenario, when the signal arises from many unresolved Higgs bosons, and a Stealthy Higgs model, when the Higgs resonance width is large due to large Higgs-phion couplings.

Thanks to the generality of the decay-mode independent searches, the combined LEP 1 and LEP 2 limits could already be used in other interpretations to fill gaps were no other direct search is sensitive, *e.g.*, in the low mass range of CP violating MSSM scenarios [103], and for setting limits on non-standard HZZ couplings, when the Higgs boson decays exclusively into $\tau^+\tau^-$ [16].

18 Summary

Searches for Higgs bosons play an important role at past and present particle accelerators and motivate the planning and construction of future accelerators, *e.g.*, the Large Hadron Collider or a new Linear Collider. At present, the best limit on the mass of the Standard Model Higgs boson is available from the LEP experiments which seized taking data in the year 2000. Non-observation of the SM Higgs boson motivated the investigation of more exotic scenarios, but the mechanism of mass generation is still unclear.

Current experiments, with sensitivity for Higgs boson masses in the vicinity of or above the LEP limits, are located at the Fermilab $\mathrm{p\bar{p}}$ Tevatron collider. However, with the expected integrated data luminosity it will be difficult to observe a Higgs boson of mass 115 GeV before the LHC starts in 2007. The LHC is a machine for Higgs discovery. It will be possible to observe a Standard Model Higgs boson in the whole mass range between the LEP limit of 114.4 GeV and the mass scale of 1 TeV where new physics is likely to show up. The LHC experiments are also sensitive to models with more complex Higgs sectors and to alternatives to the Higgs mechanism.

This thesis presented two search strategies for Higgs bosons, one for a Standard Model Higgs boson with the ATLAS experiment at the future LHC collider, and the other a very general search for new scalar bosons with the OPAL experiment at LEP.

18.1 Study of $\mathrm{t\bar{t}H^0}$ with $\mathrm{H^0 \rightarrow b\bar{b}}$ with ATLAS

The first part of the thesis described a simulation of the production of the Standard Model Higgs boson in association with a pair of top quarks. If the mass $m_{\mathrm{H^0}}$ is below $\sim$ 135 GeV, this will be the only channel to observe the dominant decay $\mathrm{H^0 \rightarrow b\bar{b}}$ at LHC. This channel gives an important contribution to the overall discovery potential for a light Higgs boson. Furthermore, it is an important benchmark channel for the b-tagging performance of ATLAS. In this thesis, $\mathrm{t\bar{t}H^0}$ production was studied using new and more precise Monte Carlo generators and a realistic parameterization of b-tagging in ATLAS. It was demonstrated that earlier studies led to too optimistic results in terms of significances $S/\sqrt{B}$. Therefore, an improved reconstruction and selection method was developed, which is based on multivariate likelihood techniques. The new analysis results in a substantial improvement of the observability of the SM Higgs boson in the $\mathrm{t\bar{t}H^0}$ channel with significances being 45% larger on average compared to the method used in earlier studies. This result is also important for the potential of the $\mathrm{t\bar{t}H^0}$ channel in MSSM Higgs boson searches. For the first time, the full simulation study included also background processes. It was shown that it is possible to improve the signal to background separation further by using additional information from the b-tagging algorithm. Since the background prediction in the channels suffers from large theoretical uncertainties, a method was developed to measure the background shape and rate from data and using only little information from Monte Carlo generators. With this procedure the background can possibly be described with an uncertainty of less than 10% with $\mathcal{L} = 30\ \mathrm{fb}^{-1}$.

18.2 Search for S^0Z^0 with OPAL

At LEP, there were numerous searches for neutral Higgs bosons, not only in the context of the Standard Model, but also in the MSSM and more exotic scenarios. They all searched for a mass peak at the kinematic limit and in particular decay modes of the Higgs bosons. If there are new particles not foreseen in the Standard Model to which the Higgs boson can decay to, or if the Higgs boson has a broad mass distribution, it could have been missed by earlier searches. This motivated the search with LEP 2 data presented in the second part of this thesis. This analysis is the most general search for Higgs boson or other new scalar bosons carried out at LEP, because it makes no assumptions about the decay modes. The new bosons can be produced in association with a Z^0 boson, and information is used only from the recoil momentum and decay products of the Z^0 to separate a possible signal from backgrounds. In addition, the analysis was designed to have high efficiency over a broad mass range so that the search is also sensitive to the case of scalar bosons with a large spread in mass. No hint for the presence of a signal was found, and limits on several models were set. The results were combined with an analysis of LEP 1 data in order to enlarge the sensitive mass regions. Due to their generality, the searches allow for interpretations in arbitrary models. Three models were chosen to set limits: The case of the Standard Model Higgs boson, which yields a limit of $m_{H^0} > 81$ GeV, and two models with broad continuous signal mass shapes, which have never been studied experimentally before. Finally, the results from the decay-mode independent searches were provided as measurements in bins of the recoil mass spectrum so that they can easily be used to set limits on any other model were new scalar bosons are radiated off a Z^0 boson in e^+e^- collisions and for which no dedicated searches exist.

Decay-mode independent searches for the Higgs boson will not be possible at hadron colliders, but they will be powerful tools at a new linear collider. Studies in the TESLA Technical Design Report [104] conclude that a Higgs boson that couples to the Z^0 boson, in almost any conceivable extended Higgs boson scenario, can be observed at TESLA in Z^0H^0 production through the recoil mass method, independent of its decay.

Bibliography

[1] K. Hagiwara *et al.*, *Review of Particle Physics*, Physical Review D **66** (2002) 010001, `http://pdg.lbl.gov`.

[2] M. Peskin and D. Schroeder, *Quantum field theory*. Westview Press, 1995.

[3] E. Noether, *Invariante Variationsprobleme*, Gött. Nachr. (1918) 235.

[4] T. Chen and L. Li, *Gauge Theory of Elementary Particle Physics*. Oxford Science Publications, 1984.

[5] A. Pich, *Quantum chromodynamics*, `hep-ph/9505231`.

[6] Super-Kamiokande Collaboration, Y. Fukuda *et al.*, *Evidence for oscillation of atmospheric neutrinos*, Phys. Rev. Lett. **81** (1998) 1562, `hep-ex/9807003`.

[7] S. L. Glashow, *Partial symmetries of weak interactions*, Nucl. Phys. **22** (1961) 579.

[8] P. W. Higgs, *Broken symmetries and the masses of gauge bosons*, Phys. Rev. Lett. **13** (1964) 508 — F. Englert and R. Brout, *Broken symmetry and the mass of gauge vector mesons*, Phys. Rev. Lett. **13** (1964) 321 — G. S. Guralnik, C. R. Hagen, and T. W. B. Kibble, *Global conservation laws and massless particles*, Phys. Rev. Lett. **13** (1964) 585 — P. W. Higgs, *Spontaneous symmetry breakdown without massless bosons*, Phys. Rev. **145** (1966) 1156 — T. W. B. Kibble, *Symmetry breaking in non-abelian gauge theories*, Phys. Rev. **155** (1967) 1554–1561.

[9] F. Mandl and G. Shaw, *Quantum field theory*. John Wiley & Sons, 1984.

[10] E. Gross, G. Wolf, and B. A. Kniehl, *Production and decay of the Standard Model Higgs boson at LEP-200*, Z. Phys. **C63** (1994) 417.

[11] M. Spira and P. M. Zerwas, *Electroweak symmetry breaking and Higgs physics*, `hep-ph/9803257`.

[12] A. Djouadi, J. Kalinowski, and M. Spira, *HDECAY: A program for Higgs boson decays in the standard model and its supersymmetric extension*, Comput. Phys. Commun. **108** (1998) 56, `hep-ph/9704448`.

[13] K. Riesselmann, *Limitations of a Standard Model Higgs boson*, `hep-ph/9711456`.

[14] M. J. G. Veltman, *Second threshold in weak interactions*, Acta Phys. Polon. **B8** (1977) 475.

[15] LEP Collaboration, *A combination of preliminary electroweak measurements and constraints on the Standard Model*, `hep-ex/0312023`.

[16] ALEPH, DELPHI, L3 and OPAL Collaboration, R. Barate *et al.*, *Search for the standard model Higgs boson at LEP*, Phys. Lett. **B565** (2003) 61, `hep-ex/0306033`.

[17] J. Gunion, H. Haber, G. Kane, and S. Dawson, *The Higgs Hunter's Guide*. Addison-Wesley Publishing Co., 1990.

[18] E. Witten, *Dynamical breaking of supersymmetry*, Nucl. Phys. **B188** (1981) 513 — S. Dimopoulos, S. Raby, and F. Wilczek, *Supersymmetry and the scale of unification*, Phys. Rev. **D24** (1981) 1681 — S. Dimopoulos and H. Georgi, *Softly broken supersymmetry and SU(5)*, Nucl. Phys. **B193** (1981) 150 — N. Sakai, *Naturalness in supersymmetric 'GUTs'*, Zeit. Phys. **C11** (1981) 153.

[19] H. P. Nilles, *Supersymmetry, supergravity and particle physics*, Phys. Rept. **110** (1984) 1.

[20] M. Drees, *An introduction to supersymmetry*, `hep-ph/9611409` — I. Simonsen, *A Review of minimal supersymmetric electroweak theory*, `hep-ph/9506369`.

[21] H. Murayama, *Supersymmetry Phenomenology*, `hep-ph/0002232`.

[22] S. P. Martin, *A supersymmetry primer*, `hep-ph/9709356`.

[23] M. Kuroda, *Complete Lagrangian of MSSM*, `hep-ph/9902340`.

[24] H. E. Haber, *The status of the minimal supersymmetric standard model and beyond*, Nucl. Phys. Proc. Suppl. **62** (1998) 469–484, `hep-ph/9709450`.

[25] The LEP working group for Higgs boson searches, *Searches for the neutral Higgs bosons of the MSSM: Preliminary combined results using LEP data collected at energies up to 209 GeV*, `hep-ex/0107030`.

[26] M. Carena, S. Heinemeyer, C. E. M. Wagner, and G. Weiglein, *Suggestions for benchmark scenarios for MSSM Higgs boson searches at hadron colliders*, Eur. Phys. J. **C26** (2003) 601, `hep-ph/0202167`.

[27] ATLAS Collaboration, *ATLAS detector and physics performance. Technical design report. Vol. 2*, CERN-LHCC-99-15 (1999).

[28] ATLAS Collaboration, E. Richter-Wąs and M. Sapiński, *Search for the SM and MSSM Higgs boson in the* $t\bar{t}H, H \to b\bar{b}$ *channel*, Acta Phys. Polon. **B30** (1999) 1001–1040, ATL-PHYS-98-132.

[29] E. Farhi and L. Susskind, *Technicolor*, Phys. Rept. **74** (1981) 277.

[30] M. Spira, *QCD effects in Higgs physics*, Fortschr. Phys. **46** (1998) 203, `hep-ph/9704448`.

[31] E. Richter-Wąs, *Prospects for the observability of the WH and ZH, H→bb channel in 14 TeV pp and 2 TeV* $p\bar{p}$ *collisions (*ET_{miss} *+ bb final state*, ATL-PHYS-2000-023 — E. Richter-Wąs, *Revisiting the observability of the WH and ZH, H→bb channel in the 14 TeV pp and 2 TeV* $p\bar{p}$ *collisions (lbb and llbb final states*, ATL-PHYS-2000-024.

[32] ATLAS Collaboration, S. Asai *et al.*, *Prospects for the Search of a Standard Model Higgs Boson in ATLAS using Vector Boson Fusion*, SN-ATLAS-2003-024.

[33] CMS Collaboration, M. Della Negra *et al.*, *CMS: The Compact Muon Solenoid: Letter of intent for a general purpose detector at the LHC*, CERN-LHCC-92-3.

[34] LHCb Collaboration, S. Amato *et al.*, *LHCb technical proposal*, CERN-LHCC-98-4.

[35] ALICE Collaboration, P. Giubellino, *The ALICE detector at LHC*, Nucl. Instrum. Meth. **A344** (1994) 27.

[36] ATLAS HLT/DAQ/DCS Group, *ATLAS High-Level Trigger, Data Acquisition and Controls*, ATLAS TDR-016.

[37] ATLAS Collaboration, F. Gianotti and P. Jenni, *Physics impact of staging ATLAS detector components*, ATL-GEN-2001-002 (2001).

[38] *GEANT–Detector Description and Simulation Tool*, CERN Program Library Long Writeup W5013.

[39] E. Richter-Wąs, D. Froidevaux, and L. Poggioli, *ATLFAST 2.0: A fast simulation package for ATLAS*, ATL-PHYS-98-131.

[40] T. Sjöstrand, L. Lönnblad, and S. Mrenna, *Pythia 6.2 physics and manual*, hep-ph/0108264.

[41] B. Kersevan and E. Richter-Wąs, *The Monte Carlo Event Generator AcerMC 1.0 with Interfaces to PYTHIA 6.2 and HERWIG 6.3.*, Comput. Phys. Commun. **149** (2003) 142, hep-ph/0201302.

[42] T. Sjöstrand, *The lund Monte Carlo for jet fragmentation and e^+e^- physics: Jetset version 6.2*, Comput. Phys. Commun. **39** (1986) 347.

[43] G. Marchesini and B. R. Webber, *Monte Carlo simulation of general hard processes with coherent QCD radiation*, Nucl. Phys. **B310** (1988) 461.

[44] M. Spira, *The HQQ program*, http://people.web.psi.ch/spira/hqq/ — M. Spira, *QCD effects in higgs physics*, Fortsch. Phys. **46** (1998) 203, hep-ph/9705337.

[45] W. Beenakker *et al.*, *Higgs radiation off top quarks at the Tevatron and the LHC*, Phys. Rev. Lett. **87** (2001) 201805, hep-ph/0107081.

[46] L. Reina, S. Dawson, and D. Wackeroth, *Associated Higgs boson production with heavy quarks at hadron colliders: Impact of NLO results*, hep-ph/0110299.

[47] D. Froidevaux and E. Richter-Wąs, *Is the channel $H^0 \to b\bar{b}$ observable at LHC?*, Z. Phys. **C67** (1995) 213.

[48] Brückman, P. and Richter-Wąs, E., *How well can we reconstruct continuum background*, ATL-PHYS-2002-025 (2002).

[49] K. Cranmer, *UWStatTools v2.2*, http://www-wisconsin.cern.ch/physics/software.html#stats.

[50] E. Richter-Wąs, private communication.

[51] S. Corread, V. Kostioukhine, J. Levêque, A. Rozanov, and J. de Vivie, *b-tagging with DC1 data*, ATL-COM-PHYS-2003-049 (2003).

[52] *The ONETOP generator*, http://www.pa.msu.edu/~pineiro/onetop/onetop_welcome.html.

[53] S. Slabospitsky and L. Sonnenschein, *TopReX generator (version 3.25): Short manual*, Comput. Phys. Commun. **148** (2002) 87, hep-ph/0201292.

[54] V. Drollinger, *Reconstruction and Analysis Methods for Searches of Higgs Bosons in the Decay Mode $H^0 \to b\bar{b}$ at Hadron Colliders*, IEKP-KA/01-16 — V. Drollinger, T. Müller, and D. Denegri, *Searching for Higgs Bosons in Association with Top Quark Pairs in the $H^0 \to b\bar{b}$ Decay Mode*, IEKP-KA/2001-23, CMS NOTE 2001/054.

[55] J. Cammin and M. Schumacher, *The ATLAS discovery potential for the channel* $\mathrm{t\bar{t}H^0}$, $\mathrm{H^0 \to b\bar{b}}$, ATL-PHYS-2003-024 (2003).

[56] R. Cousins and V. Highland, *Incorporating systematic uncertainties into an upper limit*, Nucl. Instrum. Meth. **A320** (1992) 331.

[57] T. Junk, *Confidence level computation for combining searches with small statistics*, Nucl. Instrum. Meth. **A434** (1999) 435, hep-ex/9902006.

[58] H. Hu and J. Nielsen, *Analytic Confidence Level Calculations Using the Likelihood Ratio and Fourier Transform*, in ‘Workshop on Confidence Limits’, CERN-2000-005, F. James, L. Lyons, and Y. Perrin, eds., 2000, p. 109.

[59] J. Levêque, *Recherche d’un boson de Higgs léger produit en association avec une pair de quarks top dans l’expérience ATLAS.* PhD thesis, Université de la Méditerranée Aix-Marseille II, 2003.

[60] ATLAS collaboration, *The ATLAS Data Challenges*, http://atlas.web.cern.ch/Atlas/GROUPS/SOFTWARE/DC/.

[61] I. Foster and C. Kesselman, *The GRID: Blueprint for a New Computing Infrastructur.* Morgan Kaufmann Publ., 1999 — *The GLOBUS project*, http://www.globus.org — *The LHC Computing Grid*, http://lcg.web.cern.ch — R. W. L. Jones, *ATLAS computing and the GRID*, Nucl. Instrum. Meth. **A502** (2003) 372.

[62] Camarena, P. and others, *Calibrated jets for combined ntuple*, http://ific.uv.es/~camarena/jet.html.

[63] M. Duehrssen, *Prospects for the measurement of Higgs boson coupling parameters in the mass range from 110–190 GeV*, ATL-PHYS-2003-03 (2003).

[64] S. Hochkeppel, *Untersuchung zur Bestimmung der CP-Natur neutraler Higgs-Bosonen im Prozess $t\bar{t}H^0$ bei ATLAS*, Master’s thesis, Physikalisches Institut der Universität Bonn, 2003.

[65] M. Diehl and O. Nachtmann, *Optimal observables for the measurement of three gauge boson couplings in* $e^+e^- \to W^+W^-$, Z. Phys. **C62** (1994) 397.

[66] M. Schumacher, *MSSM interpretation of ATLAS Higgs searches*, ATLAS note in preparation.

[67] W. Hollik, *Nonstandard Higgs bosons in* $SU(2) \times U(1)$ *radiative corrections*, Z. Phys **C32** (1986) 291 — W. Hollik, *Radiative corrections with two Higgs doublets at LEP/SLC and HERA*, Z. Phys **C37** (1988) 569.

[68] The LEP working group for Higgs boson searches, *Flavour Independent Searches for Hadronically Decaying Neutral Higgs Bosons at LEP*, LHWG Note 2001-07 (2001) `hep-ph/0107034`.

[69] J. W. F. Valle, *Gauge theories and the physics of neutrino mass*, Prog. Part. Nucl. Phys. **26** (1991) 91.

[70] N. Arkani-Hamed, S. Dimopoulos, and G. R. Dvali, *The hierarchy problem and new dimensions at a millimeter*, Phys. Lett. **B429** (1998) 263, `hep-ph/9803315`.

[71] N. Arkani-Hamed, S. Dimopoulos, and G. R. Dvali, *Phenomenology, astrophysics and cosmology of theories with sub-millimeter dimensions and TeV scale quantum gravity*, Phys. Rev. **D59** (1999) 086004, `hep-ph/9807344`.

[72] I. Antoniadis, N. Arkani-Hamed, S. Dimopoulos, and G. R. Dvali, *New dimensions at a millimeter to a Fermi and superstrings at a TeV*, Phys. Lett. **B436** (1998) 257–263, `hep-ph/9804398`.

[73] The LEP working group for Higgs boson searches, *Searches for Invisible Higgs bosons: Preliminary combined results using LEP data collected at energies up to 209 GeV*, LHWG Note 2001-06 (2001) `hep-ph/0107032`.

[74] L. Brucher and R. Santos, *Experimental signatures of fermiophobic Higgs bosons*, Eur. Phys. J. **C12** (2000) 87–98, `hep-ph/9907434`.

[75] A. G. Akeroyd, *Fermiophobic Higgs bosons at the Tevatron*, Phys. Lett. **B368** (1996) 89, `hep-ph/9511347`.

[76] The LEP working group for Higgs boson searches, *Searches for Higgs Bosons Decaying into Photons: Combined Results from the LEP Experiments*, LHWG Note 2002-02 (2002).

[77] The LEP working group for Higgs boson searches, *Searches for the Neutral Higgs Bosons of the MSSM: Preliminary Combined Results Using LEP Data Collected at Energies up to 209 GeV*, LHWG Note 2001-04 (2001).

[78] OPAL Collaboration, G. Abbiendi *et al.*, *Search for Yukawa production of a light neutral Higgs boson at LEP*, Eur. Phys. J. **C23** (2002) 397–407, `hep-ex/0111010`.

[79] OPAL Collaboration, G. Abbiendi *et al.*, *Flavour Independent Search for Higgs bosons Decaying into Hadronic Final States in* e^+e^- *Collisions at LEP*, submitted to Phys. Letts **B**, OPAL Physics Note 525.

[80] G. Altarelli, T. Sjöstrand, and F. Zwirner eds., *Physics at LEP 2*, in CERN 96-01 (1996) — Erratum *ibid.* **C66** (1995) 321.

[81] OPAL Collaboration, G. Abbiendi *et al.*, *Two Higgs doublet model and model independent interpretation of neutral Higgs boson searches*, Eur. Phys. J. **C18** (2001) 425, `hep-ex/0007040` — ALEPH Collaboration, D. Decamp *et al.*, *Search for the neutral Higgs bosons of the MSSM and other two doublet models*, Phys. Lett. **B265** (1991) 475.

[82] J. Espinosa and J. Gunion, *A no-lose theorem for Higgs searches at a future linear collider*, Phys. Rev. Lett. **82** (1999) 1084.

[83] T. Binoth and J. van der Bij, *Influence of strongly coupled, hidden scalars on higgs signals*, Z. Phys. **C75** (1997) 17 — T. Binoth and J. van der Bij, *The stealthy higgs model at future linear colliders*, `hep-ph/9908256`.

[84] A. Ludwig, *Suche nach unsichtbar zerfallenden Higgs-Bosonen mit großer Zerfallsbreite mit dem OPAL-Detektor bei LEP2*, Master's thesis, Physikalisches Institut der Universität Bonn, 2003 — A. Ludwig, PhD thesis, in preparation.

[85] OPAL Collaboration, K. Ahmet *et al.*, *The OPAL detector at LEP*, Nucl. Instr. and Meth. **A305** (1991) 275 — OPAL Collaboration, B. Anderson *et al.*, *The OPAL silicon-tungsten calorimeter front end electronics*, IEEE Trans. Nucl. Sci. **41** (1994) 845 — OPAL Collaboration, S. Anderson *et al.*, *The extended OPAL silicon strip microvertex detector*, Nucl. Instr. and Meth. **A403** (1998) 326 — OPAL Collaboration, G. Aguillion *et al.*, *Thin scintillating tiles with high light yield for the OPAL endcaps*, Nucl. Instr. and Meth. **A417** (1998) 266.

[86] OPAL Collaboration, J. Allison *et al.*, *The Detector simulation program for the OPAL experiment at LEP*, Nucl. Instr. and Meth. **A317** (1992) 47.

[87] P. Janot in CERN 96-01 **Vol.2** (1996) 309.

[88] S. Jadach, W. Płaczek, and B. Ward in CERN 96-01 **Vol.2** (1996) 286.

[89] D. Karlen, *Radiative Bhabha scattering for singly tagged and untagged configurations*, Nucl. Phys. **B289** (1987) 23.

[90] S. Jadach, B. Ward, and Z. Wąs, *The Monte Carlo program KORALZ, version 4.0, for the lepton or quark pair production at LEP/SLC energies*, Comp. Phys. Comm. **79** (1994) 503.

[91] S. Jadach, B. Ward, and Z. Wąs, *The precision Monte Carlo event generator KK for two-fermion final states in* e^+e^- *collisions*, Comp. Phys. Comm. **130** (2000) 260.

[92] T. Sjöstrand, *High-energy physics event generation with PYTHIA 5.7 and JETSET 7.4*, Comp. Phys. Comm. **82** (1994) 74 — T. Sjöstrand, *PYTHIA 5.7 and JETSET 7.4: Physics and manual*, LU TP 95-20 (1995) `hep-ph/9508391`.

[93] J. Fujimoto *et al.*, *grc4f v1.1: a Four-fermion Event Generator for* e^+e^- *Collisions*, Comp. Phys. Comm. **100** (1997) 128 — J. Fujimoto *et al.* in CERN 96-01 **Vol. 2** (1996) 30.

[94] E. Budinov *et al.* in CERN 96-01 **Vol.2** (1996) 216 — R. Engel and J. Ranft, *Hadronic photon-photon interactions at high energies*, Phys. Rev. **D54** (1996) 4244.

[95] G. Marchesini *et al.*, *HERWIG: A Monte Carlo event generator for simulating hadron emission reactions with interfering gluons. Version 5.1 - April 1991*, Comp. Phys. Comm. **67** (1992) 465.

[96] J. Vermaseren, *Two photon processes at very high energies*, Nucl. Phys. **B229** (1983) 347.

[97] OPAL Collaboration, G. Abbiendi *et al.*, *Decay-mode independent searches for new scalar bosons with the OPAL detector at LEP*, Eur. Phys. J. **C27** (2003) 311, hep-ex/0206022.

[98] OPAL Collaboration, P. Acton *et al.*, *Decay mode independent search for a light Higgs boson and new scalars*, Phys. Lett. **B268** (1991) 122.

[99] The cross section is defined for events with 1 particle with $|\cos(\theta)| < 0.975$ and $p_T > 4$ GeV or 2 particles with $|\cos(\theta)| < 0.975$ and $p_T(\text{miss}) > 1.0$ GeV or 3 or 4 particles with $|\cos(\theta)| < 0.975$.

[100] OPAL Collaboration, G. Alexander *et al.*, *Measurement of the heavy quark forward-backward asymmetries and average B mixing using leptons in multi-hadronic events*, Z. Phys. **C70** (1996) 357 — OPAL Collaboration, G. Abbiendi *et al.*, *A measurement of R(b) using a double tagging method*, Eur. Phys. J. **C8** (1999) 217.

[101] M. Kobel, private communication.

[102] OPAL Collaboration, K. Ackerstaff *et al.*, *A search for neutral Higgs bosons in the MSSM and models with two scalar field doublets*, Eur. Phys. J. **C5** (1998) 19, hep-ex/9803019.

[103] OPAL Collaboration, The OPAL working group for Higgs boson searches, *Search for Neutral Higgs Bosons Predicted by CP Conserving and CP Violating MSSM Scenarios with the OPAL detector at LEP*, OPAL Physics Note 524 (2003).

[104] ECFA/DESY LC Physics Working Group Collaboration, J. A. Aguilar-Saavedra *et al.*, *TESLA Technical Design Report Part III: Physics at an e^+e^- Linear Collider*, hep-ph/0106315.

[105] F. Maltoni and T. Stelzer, *MadEvent: Automatic event generation with MadGraph*, hep-ph/0208156.

[106] T. Stelzer and W. Long, *Automatic generation of tree level helicity amplitudes*, Comput. Phys. Commun. **81** (1994) 357.

[107] H. Murayama, I. Watanabe, and K. Hagiwara, *HELAS: HELicity Amplitude Subroutines for Feynman diagram evaluations*, KEK-91-11.

A Feynman diagrams for signal and background in the $t\bar{t}H^0$ channel

Diagrams generated by MadGraph [105, 106, 107].

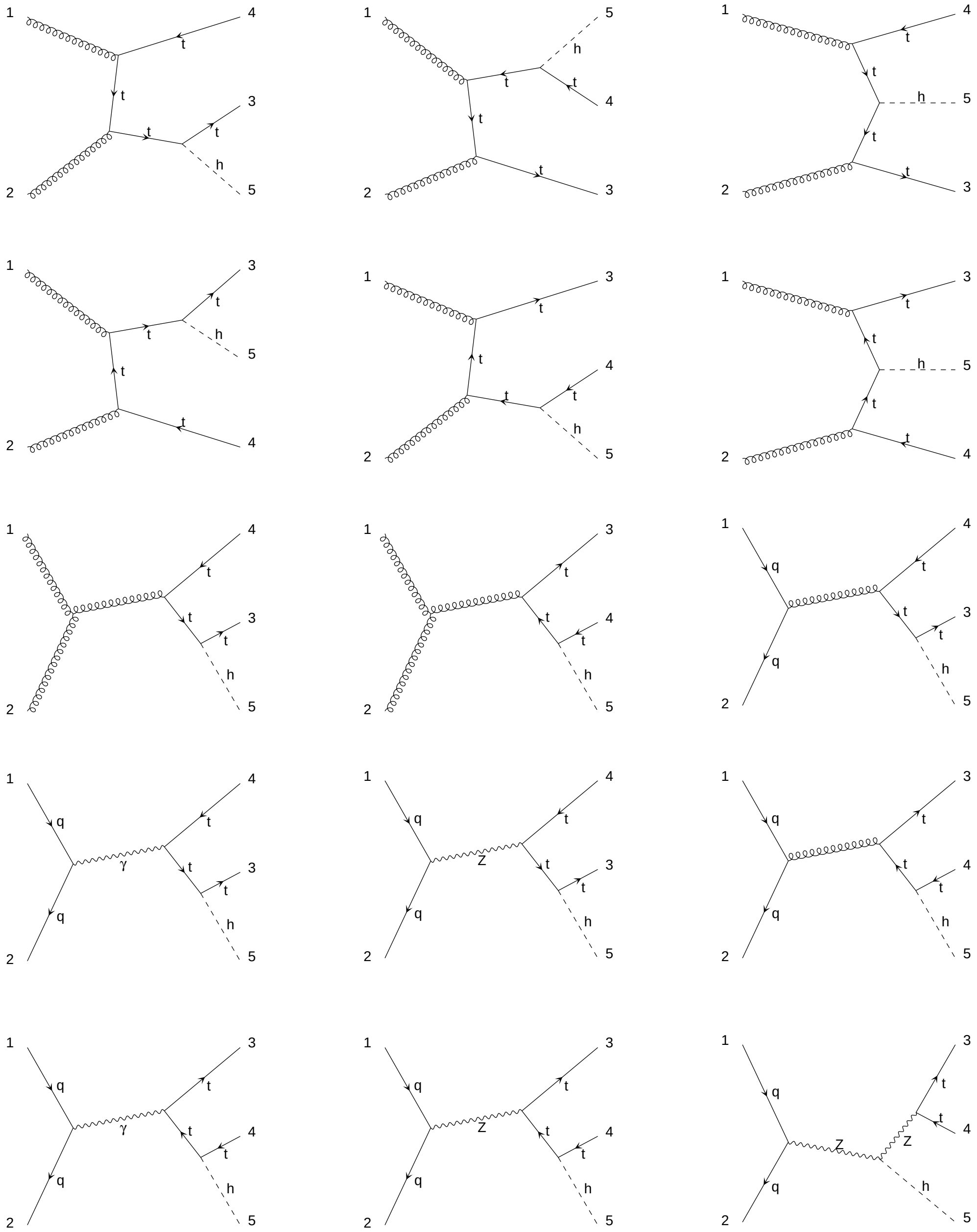

Figure A.1: The 15 Feynman leading-order diagrams for the $t\bar{t}H^0$ signal.

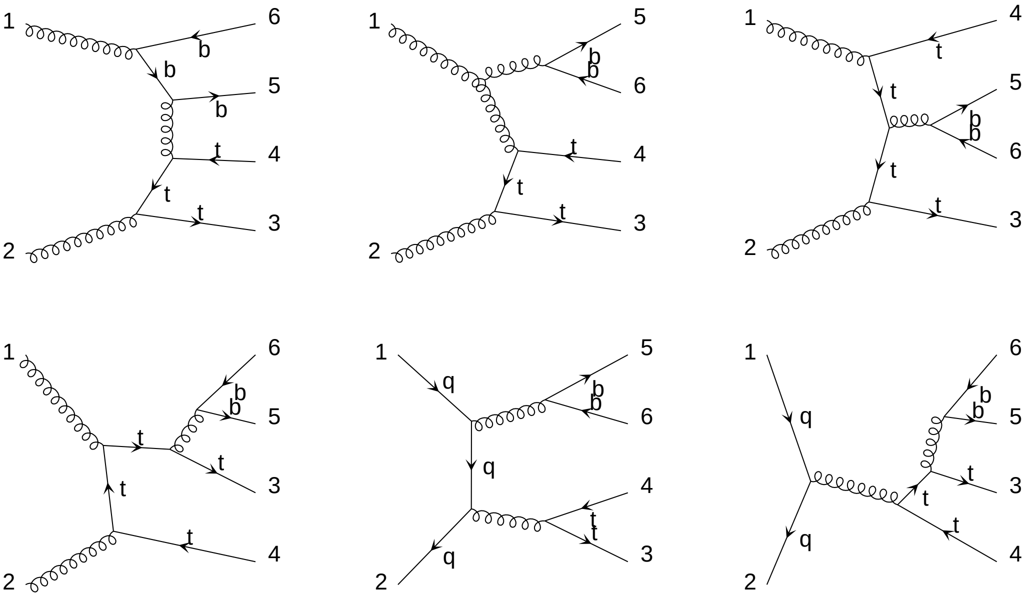

Figure A.2: A subset of the 38+7 Feynman leading-order diagrams for the gg,q$\bar{q}$ → t$\bar{t}$b$\bar{b}$ background.

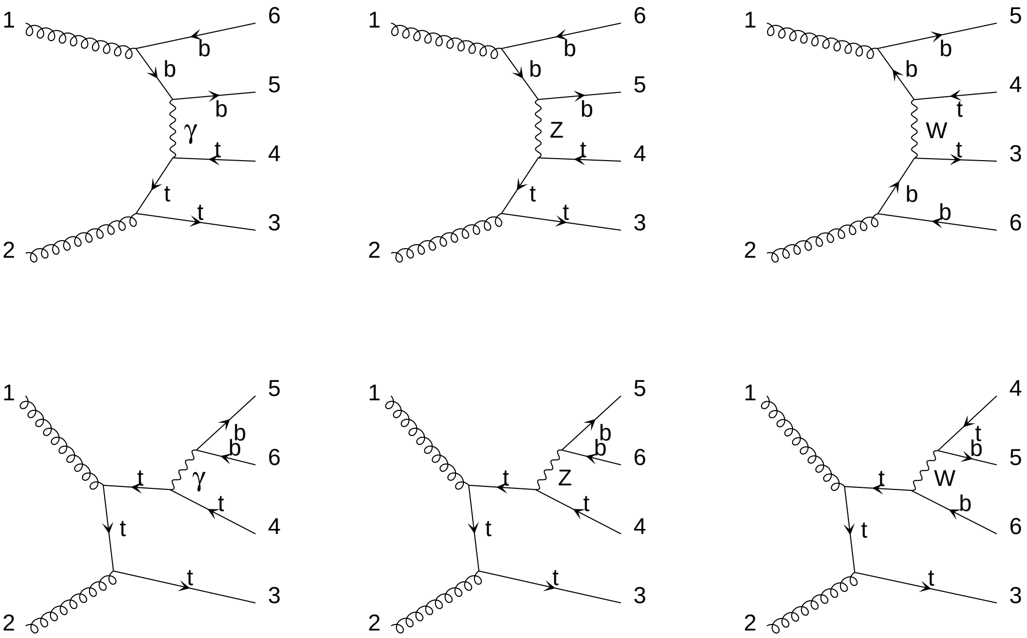

Figure A.3: A subset of the 72 Feynman leading-order diagrams for the gg→Z/γ^*/W→t$\bar{t}$b$\bar{b}$ background.

B The likelihood technique

The aim of a likelihood selection is to separate n_{class} different classes of events. Several input variables are combined into a single output variable. The output variable has better discrimination power between the event classes compared to subsequent cuts on each of the n_{var} input variables. For an event class j the distribution of each variable i follows a probability density function $f_i^j(x_i)$. The probability $p_i^j(x_i)$ of an event with value x_i in the variable i to belong to class j is given by

$$p_i^j(x_i) = \frac{f_i^j(x_i)}{\sum_{j=1}^{n_{\mathrm{class}}} f_i^j(x_i)}.$$

The distributions $f_i^j(x_i)$ must be normalized. One can normalize to the expected cross section for each class, $\int f_i^j(x_i)\,\mathrm{d}x_i = \sigma^j$, or to Unity, $\int f_i^j(x_i)\,\mathrm{d}x_i = 1$ (the latter is used in this thesis). For a class j the several variables are combined into a single event quantity $P^j(x_1, \ldots, x_{n_{\mathrm{var}}})$:

$$P^j(x_1, \ldots, x_{n_{\mathrm{var}}}) = \prod_{i=1}^{n_{\mathrm{var}}} p_i^j(x_i).$$

This quantity is normalized to Unity:

$$\mathcal{L}^j(x_1, \ldots, x_{n_{\mathrm{var}}}) = \frac{P^j(x_1, \ldots, x_{n_{\mathrm{var}}})}{\sum_{j=1}^{n_{\mathrm{class}}} P^j(x_1, \ldots, x_{n_{\mathrm{var}}})}.$$

If all input variables for a given class are uncorrelated the likelihood $\mathcal{L}^j(x_1, \ldots, x_{n_{\mathrm{var}}})$ is the probability of an event to belong to class j. If the variables are correlated, the likelihood can still be used to discriminate between several classes, but it can no longer be interpreted as a probability.

A cut is then applied, and an event is selected to belong to class j if the likelihood $\mathcal{L}^j(x_1, \ldots, x_{n_{\mathrm{var}}})$ is above the threshold $\mathcal{L}^j_{\mathrm{cut}}$. The choice of the cut determines the selection efficiency and purity.

Acknowledgments

Many people have contributed to my PhD studies with their help and guidance. I would like to take the opportunity to thank all of them.

First of all, I would like to thank my supervisor Prof. Dr. Michael Kobel. He offered me the possibility to work on these interesting subjects in the OPAL and ATLAS collaborations. His continuous support and guidance made my thesis an outstanding experience, and he gave me the opportunity to spend almost two years at CERN.

It is also a pleasure to thank Dr. Markus Schumacher for valuable advice, fruitful discussions and careful reading of all my manuscripts.

I am grateful to the coordinators of the ATLAS Higgs working group, Prof. Dr. Elżbieta Richter-Wąs and Prof. Dr. Karl Jakobs, for their support and for stimulating discussions.

I wish to thank Dr. Jessica Levêque, Dr. Jean-Baptiste de Vivie and Prof. Dr. Sasha Rozanov from Marseille for providing so much support with the ATLAS simulation.

Many thanks go out to all my friends and my colleagues in the Bonn OPAL, ATLAS, DØ and SiLAB group for the friendly atmosphere and all the help I received during the four years of my PhD studies. I also wish to thank my friends and colleagues at CERN for 21 interesting months in Geneva.

Finally, I sincerely thank my parents for giving me so much love and support.

Vielen Dank
Thank you
Merçi bien